Inelastic material response in multi-physics earthquake rupture simulations

Stephanie Wollherr

München 2018

Inelastic material response in multi-physics earthquake rupture simulations

Stephanie Wollherr

Dissertation zur Erlangung des
Doktorgrades an der Fakultät für Geowissenschaften
der Ludwig–Maximilians–Universität
München

vorgelegt von
Stephanie Wollherr

München, den 06.09.2018

Erstgutachter: Prof. Dr. Heiner Igel
Zweitgutachterin: Dr. Alice-Agnes Gabriel
Tag der mündlichen Prüfung: 18.12.2018

Summary

Dynamic rupture models are able to shed light on earthquake source dynamics where direct observations are rare or non-existent. These multi-physics simulations incorporate earthquake rupture along a fault governed by frictional constitutive laws, which is coupled to seismic wave propagation described by the linear elastic wave equation. To accurately model the earthquake process, numerical models need to include realistic material properties such as the ability of rocks to deform plastically. This dissertation extends the Arbitrary High Order Derivative Discontinuous Galerkin (ADER-DG) framework of the dynamic rupture software SeisSol to account for non-linear off-fault plasticity. The impact of plasticity on rupture dynamics and the emitted seismic wave field is investigated in realistic simulations motivated by past earthquakes on geometrically complex faults.

We first present the implementation of off-fault plasticity, which is verified in community benchmark problems and by three-dimensional numerical refinement studies. Motivated by the high efficiency of the implementation, we present a large-scale simulation of earthquake rupture along the segmented fault system of the 1992 Landers earthquake including plasticity. The results indicate that spatio-temporal rupture transfers are altered by plastic energy absorption, correlating with locations of geometrical fault complexity. In a next step, the model of the 1992 Landers earthquake is further extended to account for a new degree of realism among dynamic rupture models by incorporating high-resolution topography, 3D velocity structure, and viscoelastic attenuation in addition to off-fault plasticity. The simulation reproduces a broad range of observations including moment release rate, seismic waveform characteristics, mapped off-fault deformation patterns, and peak ground motions. We find that plasticity reduces the directivity effect and the spatial variability of peak ground velocities in comparison to the purely elastic simulation. In addition to this continental strike-slip earthquake, we investigate the effect of off-fault plasticity on source dynamics and seafloor deformation in a 3D subduction zone model of the 2004 Sumatra-Andaman earthquake. Simulated seafloor displacements are drastically altered by inelastic processes within the entire accretionary wedge, depending on fault-strike and the applied regional stress field, which potentially affects the tsunamigenesis. Finally, since these application scenarios show that rupture dynamics and the occurrence of off-fault plasticity are highly influenced by the assumed initial stresses and fault geometry, we propose a workflow to constrain dynamic rupture initial conditions with plasticity by long-term seismic cycling modelling. The exploited seismo-thermo-mechanical model provides a self-consistent slab geometry as well as initial stress and strength conditions that evolve according to the tectonic stress build-up and the temperature-dependent strength of the rocks. The geomechanically constrained subduction zone model suggests that the accretionary wedge is very close to plastic failure such that the occurrence of plastic strain hampers rupture to the trench, but locally increases the vertical seafloor uplift.

Contents

List of Figures

List of Tables

1 Introduction

The origin of earthquakes has been surrounded by many myths: While Greek philosophers regarded earthquakes as underground thunderstorms, mythologies blamed the wrath of their gods (Loki in the Norse mythology, Poseidon in the Greek mythology) or a giant catfish (Namazu in the Japanese mythology) to be the reason of the ground shaking. At the time of Enlightenment, the Great Lisbon earthquake in 1755 led to more physically motivated speculations of the origin of earthquakes such as electric shocks, specific constellations of the planets or the movement of underground cavities filled with gas. Inspired by observations following the devastating 1906 San Francisco earthquake, Reid formulated the famous elastic rebound theory in 1910 (Reid, 1910), which is still valid today. He describes earthquakes as a sudden release of gradually accumulated strain along a fracture (fault) in the Earths crust. With the rise of the plate tectonic theory in the 1960s, the slowly accumulating strain was linked to the tectonic loading at stuck plate boundaries.

During an earthquake, the accumulated strain is released as fracture energy, as heat and as radiated seismic waves. These waves travel throughout the earth and are responsible for the ground shaking that causes damage to buildings or other rigid structures. Earthquake-related hazard further includes the triggering of landslides, liquefaction of water-saturated sediments, fires initiated by the damage, as well as the formation of tsunamis. Due to Earth's complexity and the restricted possibilities to explore the Earth's interior directly, the exact location, time, and size of an earthquake remain unpredictable. This distinguishes earthquakes from other natural hazards such as tsunamis, floods, hurricanes, and volcanic eruptions that all are predictable to some extent on timescales of hours to days. In contrast to predicting earthquakes, probabilistic seismic hazard assessment provides the likelihood of exceeding a certain ground motion intensity within a given recurrence interval. It is based on the target sites seismotectonic conditions, historical seismicity, and ground motion prediction equations. The results build the basis for insurance policies and building codes in structural engineering that help to mitigate the consequences of earthquakes.

While the potential ground motions of a known seismic source have been extensively studied, the underlying earthquake source dynamics that control the intensity, the duration, and the extent of an earthquake, are still not fully understood. Important research questions with respect to the earthquake source comprise - but are not limited to - the conditions under which earthquakes initiate, propagate to neighbouring segments, and develop into devastating events, as well as the interdependence of the physical processes acting on and off the fault. By improving our knowledge of the fundamental earthquake dynamics we will be able to provide a better model of the earthquake source in seismic hazard analysis and source inversion methods.

The following sections give an overview of the constitutive models used to describe earthquakes, observations of on- and off-fault processes controlling them, as well as state of the art findings from numerical simulations modelling the earthquake source. The main objectives and outline of the thesis are described in the last section.

1.1 Earthquake source processes

There are several ways to accommodate for the movements of the plates within the lithosphere: As long as the boundary zone between plates is not stuck, plate movement is translated into continuous sliding along the interfaces, referred to as aseismic creep. However, if the fault interfaces are stuck due to friction, the build-up stresses might result in inelastic failure of the rock and eventually to coseismic slip.

The Mohr-Coulomb criterion is an important mathematical concept for describing either intact rock failure (fracture formation) or rock-on-rock frictional sliding (e.g., Byerlee, 1978; Yu, 2002). Within that framework, the fracture or frictional resistance is equal to the strength of the rock or the fault, respectively. Since earthquakes predominantly occur on pre-existing fault interfaces, they are often described as stick-slip frictional instabilities (Brace and Byerlee, 1966; Scholz, 1998). In the case of frictional sliding, the strength of the fault depends on the friction coefficient, cohesional forces between the interfaces, and the faults normal stress. Fault failure and hence slip arises whenever shear tractions overcome the strength of the fault.

Laboratory experiments show that the friction coefficient changes during slip, controlling the subsequent rupture evolution and therefore the earthquake dynamics. As a consequence, the study of frictional properties along natural fault zones and the description of frictional behaviour in empirical "friction laws" from observations and in laboratory experiments is of fundamental importance when studying earthquake source mechanics.

The simplest friction law that captures the evolution of the friction coefficient during slip is linear slip-weakening (Ida, 1972; Okubo and Dieterich, 1981). Initially, fault friction is at a static value (Byerlee, 1978). After shear tractions become large enough to overcome the fault strength and sliding begins, the friction coefficient linearly decreases with increasing slip distance until some constant dynamic value is reached. This concept is widely used in theoretical and numerical models describing shear crack propagation (Barenblatt, 1962; Ida, 1972; Andrews, 1976; Freund, 1979; Andrews, 1985).

While the linear slip-weakening law approximates fault strength variability during sliding, laboratory experiments suggest that the evolution of friction is much more complex: not only displacement but also time and slip velocity effects control the friction coefficient (Dieterich, 1972, 1978; Ruina, 1983). The static friction coefficient is found to be dependent on the sliding history, while the dynamic friction depends logarithmically on slip rate and a state variable. These dependencies were successfully described within the rate-and-state friction framework by Dieterich (1979); Ruina (1983). This constitutive relation provides a unified model to represent stable and unstable sliding phenomena observed on natural faults and in the laboratory, including the onset of slip instabilities, earthquake afterslip, and aseismic creep (Scholz, 1998), as well as the drastic decrease in frictional resistance at coseismic slip rates (e.g., Tsutsumi and Shimamoto, 1997; Di Toro et al., 2004).

Frictional resistance is further influenced by the geometry of the contact interface; geometrical irregularities along the fault are found over a large range of scales covering fault bends on kilometre to meter scale and small-scale roughness on meter to millimetre scale (Power et al., 1987; Okubo and Aki, 1987; Candela et al., 2012; Brodsky et al., 2016). Due to the geometrical roughness, fault interfaces only touch over a small fraction of their nominal contact area during low slip rates. At

sufficiently high slip rates, flash heating of these microscopic asperity contacts occurs which increases temperature and decreases frictional resistance (Rice, 2006; Beeler et al., 2008). This weakening process is likely the dominant mechanism determining the strength of a fault in the early stages of an earthquake (Goldsby and Tullis, 2011).

The strength of the fault can be further reduced in the presence of fluids: Rapid slip along the fault increases fluid pore pressure, which in turn decreases the effective normal stress and hence less shear stress is needed to cause the fault to fail (Wibberley and Shimamoto, 2005; Bizzarri and Cocco, 2006; Noda et al., 2009; Viesca and Garagash, 2015). This effect, called thermal pressurization, suppresses the temperature rise on the fault and may explain why melt products, such as pseudotachylyte, are not always observed on exposed fault surfaces (Noda et al., 2009).

Since these processes take all place within a narrow, localized shear zone of the fault, frictional sliding models provide a useful framework for interpreting earthquake source mechanisms on pre-existing faults. However, away from the primary slip interface, fault cores are often surrounded by a damage zone of fractured host rock (e.g., Scholz, 1989; Chester et al., 1993; Wibberley and Shimamoto, 2002; Sibson, 2003), as visualized in Fig. 1.1. Such a damage zone includes cracks, fractures, cleavages, veins, secondary faults and deformation bands of various lengths (Mitchell and Faulkner, 2009; Savage and Brodsky, 2011; Mitchell et al., 2011). The intensity of this damaged structure decreases with distance from the fault core (e.g., Chester and Logan, 1987).

Damage zones are found at many individual faults, such as the Carboneras fault in southeastern Spain (Faulkner et al., 2006), the Punchbowl fault in South California (Wilson et al., 2003), faults in the Volcanic Tablelands in eastern California (Scholz et al., 1993) and the Atacama fault zone in northern Chile (Mitchell and Faulkner, 2009). These non-necessary symmetric structures influence rupture dynamics, creating bimaterial interfaces (Ben-Zion and Sammis, 2003; Mitchell et al., 2011), and affect fluid flow properties due to the increased permeability of the host rock (Dimmen et al., 2017).

The origin of the damage zone is still under debate. One line of evidence suggests that off-fault damage around the fault core is generated at the rupture tip during coseismic slip. Stresses around the rupture tip are found to be sufficiently large to overcome the strength of the host rock and form new fractures or expand already existing ones (Irwin, 1957; Andrews, 1976; Rice, 1980). As such, inelastic processes during coseismic slip act as additional energy sinks since they contribute to the fracture energy of an earthquake (Andrews, 2005; Kanamori and Rivera, 2006). While frictional sliding forms the dominant part of the fracture energy, off-fault energy dissipation is found to be a non-negligible part with increasing slip and earthquake size (Di Toro et al., 2016; Nielsen et al., 2016; Nielsen, 2017). As a consequence, earthquake source models based on fault friction alone need to be complemented by inelastic failure off the principal slip interface to account for the correct energy balance when modelling physically-consistent earthquakes (Fialko, 2015; Nielsen, 2017).

1.2 Earthquake source simulations

Due to the lack of direct measurements and observations close to active faults, as well as the difficulty of reconstructing coseismic conditions in laboratory experiments, numerical models are an indispensable tool to study the earthquake source dynamics and the associated wave propagation. Numerical simulations provide a framework to test hypotheses and investigate the impact and hence the relative importance of different model parameters and assumptions.

While the radiation of seismic waves in the far field can be modelled by a single double-couple point source, this representation of an earthquake source is not suitable for large earthquakes or near-field

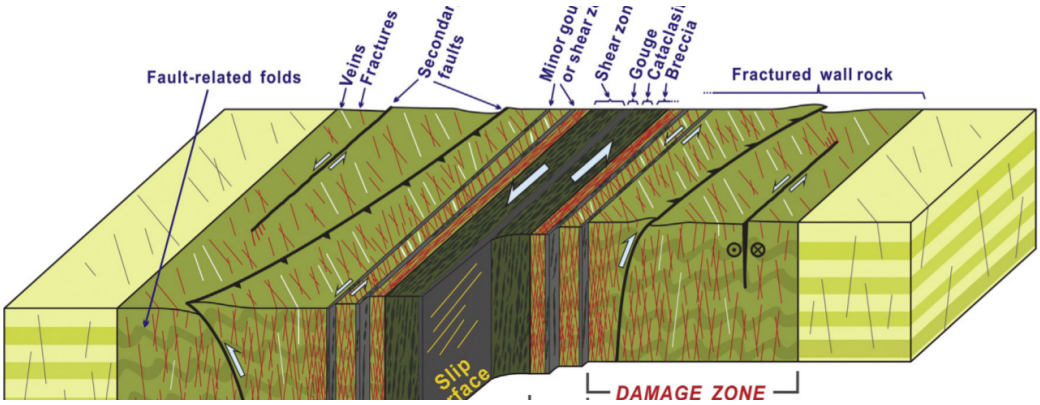

Figure 1.1: Conceptual fault structure modified after Choi et al. (2016). Slip is confined to a narrow shear zone surrounded by fault gauge. This fault core is enclosed by fractured wall rock forming the damage zone. The intensity of damage decreases with increasing distance to the fault core.

ground motion simulations which are dependent of the spatio-temporal details of the rupture process (Madariaga, 2007).

In contrast to single point sources, finite fault representations provide the possibility to account for the fault geometry and the temporal evolution of the rupture propagation. Within that framework, the fault geometry is discretized into subfaults. Each of these patches is then represented as one or a collection of point sources that might be defined by the slip, rupture velocity, and rise-time on that subfault. The kinematic source characteristics of earthquakes are commonly inferred from inversion of strong-motion, teleseismic and geodetic data (e.g. Wald and Heaton, 1994; Cotton and Campillo, 1995). However, inversion results are highly non-unique (Mai et al., 2007, 2016). Additionally, the resulting kinematic sources do not necessarily represent a physically consistent earthquake source, as they do neither consider the stress and strength of the fault prior to the earthquake nor its frictional characteristics. In contrast, dynamic rupture models are able to provide seismic wave propagation due to earthquake rupture along a fault governed by the Mohr-Coulomb failure criterion and friction laws as described in the previous section. In that manner, dynamic rupture evolves spontaneously in dependence of the fault geometry in conjunction with fault stress and strength.

Dynamic rupture models shed light to a wide range of different research questions: It has been shown that rupture can dynamically activate (jump) or branch into neighbouring faults under certain initial stress conditions, leading to cascading earthquakes within a system of faults (Harris and Day, 1993; Kame et al., 2003; Oglesby, 2008; Finzi and Langer, 2012b; Xu et al., 2015). These studies are crucial when quantifying the potential size of a future earthquake.

Further, simulation results confirm the influence of 3D velocity structures on ground motions. For instance, high ground motion amplifications at low-velocity basins such as the Los Angeles basin or the San Bernardino basin in Southern California can be investigated for different potential earthquake scenarios (Olsen et al., 2009; Lozos et al., 2015). These studies help to develop and improve ground motion prediction equations and building codes that sustain these amplified ground motions.

The velocity structure around the fault is found to also influence the rupture dynamics: damage zones around the fault with lower velocities than the intact host rock introduce multiple rupture fronts due to the seismic waves reflected at the velocity contrast (Harris and Day, 1997; Huang and Ampuero, 2011). These waves become trapped within the damage zone and contribute to the complexity of the earthquake source which might further affect the resulting ground motions.

The influence of fault geometry on rupture dynamics was investigated on various scales such as for branching (Aochi and Fukuyama, 2002) or double-bended fault geometries (Lozos et al., 2011) and small-scale rough faults (Xu and Ben-Zion, 2013). Fault geometry highly controls rupture propagation, as the orientation of the fault changes the normal and shear stress acting on the fault. Geometrical asperities can act as rupture barriers, controlling the extent and distribution of fault slip (Dunham et al., 2011b; Ulrich and Gabriel, 2017; Wollherr et al., 2018).

Most dynamic rupture models focus on frictional failure along a pre-existing fault but assume purely elastic material properties (e.g., Peyrat et al., 2001; Kozdon and Dunham, 2013; Galvez et al., 2014). Although the concept of inelastic processes was introduced much earlier into earthquake source modelling using so-called thick fault (Madariaga et al., 1998) or stress glut models (Andrews, 1976, 1999), it has only been recently that dynamic rupture simulations account for plastic failure off the fault (Andrews, 2005; Duan, 2008; Ma, 2008; Dunham et al., 2011a; Gabriel et al., 2013; Roten et al., 2016).

However, the implications are crucial. Accounting for off-fault plasticity in simulations highly reduces on-fault slip rates and, as a consequence, the simulated ground motions (Roten et al., 2014, 2017). By incorporating plastic processes around the rupture tip, rupture speed is decreased (Gabriel et al., 2013) and branch activation can be hampered (DeDontney et al., 2011). Additionally, the resulting surface displacement is enhanced by off-fault plasticity above dipping faults (Ma, 2008), which might essentially affect the generation of tsunamis in subduction zones earthquakes. All of these findings emphasize the importance of creating earthquake models that account for realistic material properties such as for off-fault plasticity to obtain reliable simulation results.

Dynamic rupture models are numerically challenging since they need to explicitly represent the displacement discontinuity across the fault surface. Several techniques were developed to incorporate the fault discontinuity, including the traction-at-split nodes (TSN) approach (e.g., Andrews, 1999) which is today used by a wide range of numerical methods (Dalguer and Day, 2007; Kaneko et al., 2008; Barall, 2009). Fault nodes within the TSN approach are doubled and each side of these so-called split-nodes experiences motion relative to its counterpart. Interactions between the halves of the split nodes occur exclusively through the tractions (frictional resistance and normal traction) acting between them, and these, in turn, are controlled by the jump conditions and a friction law. In contrast, numerical methods that naturally include discontinuities across element boundaries, such as Discontinuous Galerkin (DG) methods, have the advantage to directly include the frictional boundary conditions as modified numerical fluxes (De la Puente et al., 2009; Tago et al., 2012; Pelties et al., 2012).

Aside from the need to develop realistic numerical models, computational efficiency is another important aspect of earthquake source modelling. Earthquake processes occur on a variety of scales: from small scale processes govern frictional sliding along the fault in the millimetre to centimetre range, to strength drops at the earthquake rupture tip on the scale of meters, up to emitted seismic waves travelling over hundreds of kilometres. To accurately account for this range of spatial dimensions, dynamic rupture models can become very large, ranging from a million to over 200 millions of mesh elements in typical production runs (Breuer et al., 2014; Roten et al., 2016; Uphoff et al., 2017). The incorporation of realistic physics such as off-fault plasticity leads to an additional increase in computational costs. Numerical methods that are optimized for modern high-performance computing are essential to handle these multi-scale and multi-physics models that teach us about earthquake source dynamics and the resulting seismic wave field.

The dynamic rupture software package SeisSol, which has been developed at Ludwig Maximilian University of Munich over the last 12 years (Käser and Dumbser, 2006; Dumbser and Käser, 2006; De la Puente et al., 2009; Pelties et al., 2012; Breuer et al., 2014; Uphoff and Bader, 2016; Uphoff et al., 2017), is not only highly optimized for the latest supercomputer architectures but is also capable

to model earthquakes with a high degree of realism. SeisSol was first developed to model wave propagation with high-order accuracy in space and time using an Arbitrary High Order Derivative Discontinuous Galerkin (ADER-DG) method (Käser and Dumbser, 2006; Dumbser and Käser, 2006). Soon, the DG method, naturally including discontinuities across element boundaries, was recognized as an optimal framework for dynamic rupture problems (De la Puente et al., 2009; Pelties et al., 2012, 2014). SeisSol is able to combine complex fault geometries and topography due to its use of unstructured tetrahedral meshes and efficiently handles three-dimensional velocity structures, as well as viscoelastic attenuation effects. These model complexities make it possible to deploy the software for realistic earthquake rupture simulations like no other. The software is open-source (`github.com/SeisSol/SeisSol`), thus available to the entire scientific community. However, so far the ability of off-fault plastic deformation was a missing model component.

1.3 Main objectives and outline

The main objective of this work is to implement and investigate the complex non-linear effects of more realistic off-fault plastic material behaviour on rupture dynamics, subsequent wave propagation, and coseismic ground displacement. This topic is addressed from various perspectives: First, from a numerical and implementational point of view by developing an efficient computational scheme suitable for the already existing code structure of the dynamic rupture software SeisSol. Second, from an applicational point of view, modelling complex, segmented continental strike-slip fault systems and earthquakes along subduction zone interfaces. This work contributes to the development of the software package SeisSol, as well as the improved understanding of parameters and conditions influencing rupture dynamics, ground motions, and displacements in realistic multi-physics simulations.

Chapter 2 introduces a computationally efficient way to implement off-fault plasticity in modal DG methods. To ensure reliable simulation results, the implementation is verified against other software and detailed numerical refinement studies are presented. The results of the convergence analysis serve as numerical guidelines for the on-fault discretization of the realistic earthquake simulations in the subsequent chapters.

Chapter 3 presents large-scale dynamic rupture simulations of the 1992 Landers earthquake in South California, incorporating all available model complexities of SeisSol including off-fault plasticity. The model reproduces a broad range of observations of this earthquake, including off-fault deformation patterns and recorded peak ground motions. The simulation results demonstrate the potential of dynamic rupture simulations to improve the understanding of earthquake source observations and complement classic seismic hazard analysis.

Chapter 4 shows the up-to-now first 3D subduction zone model that includes off-fault plasticity. The model is an extension of the large-scale dynamic rupture scenario of the 2004 Sumatra-Andaman earthquake (Uphoff et al., 2017) which only accounted for purely elastic material properties. The simulation highlights that various factors, including the orientation of the principal stresses and fault geometry, determine whether plasticity increases or decreases seafloor displacement in comparison to the purely elastic scenario. The results have fundamental implications for understanding the generation of devastating tsunamis.

Chapter 5 is motivated by the strong dependence of earthquake rupture dynamics on initial stresses and fault geometry, as shown in the previous chapters. To overcome the difficulties in constraining appropriate initial conditions for dynamic rupture simulations, we present the coupling of SeisSol to a long-term seismic cycling model that captures the evolution of the fault zone and stresses over millions of years. The geomechanically constrained subduction zone models provide guidance for the

initial conditions of future earthquake models of megathrust ruptures.

Chapter 2 and 3 have been published or submitted to peer-reviewed journals as

- Wollherr, S., Gabriel A.-A., and Uphoff C. (2018). Off-fault plasticity in three-dimensional dynamic rupture simulations using a modal Discontinuous Galerkin method on unstructured meshes: implementation, verification and application, *Geophysical Journal International*, Vol. 214, 15561584, `https://doi.org/10.1093/gji/ggy213`

- Wollherr, S., Gabriel, A., and Mai, P. M. (2018). Landers 1992 reloaded: an integrative dynamic earthquake rupture model, *submitted to Journal of Geophysical Research: Solid Earth*

The work in Chapter 4 extends the Best Paper Award-winning publication

- Uphoff, C., Rettenberger, S., Bader, M., Madden, E. H., Ulrich, T., Wollherr, S., and Gabriel, A. A. (2017). Extreme scale multi-physics simulations of the tsunamigenic 2004 Sumatra megathrust earthquake. *Proceedings of the International Conference for High Performance Computing, Networking, Storage and Analysis, ACM*.

and will be part of a joint paper focusing on the geophysical analysis of the source dynamics of the 2004 Sumatra-Andaman Earthquake and the resulting tsunami generation.

A publication for the content of Chapter 5 is in preparation and will be eventually submitted to the Pure and Applied Geophysics Topical Volume "Physics of Megathrust Earthquakes". All chapters can be read independently.

2

Implementation, verification, and application of off-fault plasticity

Abstract

The dynamics and potential size of earthquakes depend crucially on rupture transfers between adjacent fault segments. To accurately describe earthquake source dynamics, numerical models can account for realistic fault geometries and rheologies such as nonlinear inelastic processes off the slip interface. We present implementation, verification, and application of off-fault Drucker-Prager plasticity in the open source software SeisSol (`www.seissol.org`). SeisSol is based on an arbitrary high-order derivative modal Discontinuous Galerkin (ADER-DG) method using unstructured, tetrahedral meshes specifically suited for complex geometries. Two implementation approaches are detailed, modelling plastic failure either employing sub-elemental quadrature points or switching to nodal basis coefficients. At fine fault discretizations the nodal basis approach is up to 6 times more efficient in terms of computational costs while yielding comparable accuracy. Both methods are verified in community benchmark problems and by three dimensional numerical *h*- and *p*-refinement studies with heterogeneous initial stresses. We observe no spectral convergence for on-fault quantities with respect to a given reference solution, but rather discuss a limitation to low-order convergence for heterogeneous 3D dynamic rupture problems. For simulations including plasticity, a high fault resolution may be less crucial than commonly assumed, due to the regularization of peak slip rate and an increase of the minimum cohesive zone width. In large-scale dynamic rupture simulations based on the 1992 Landers earthquake, we observe high rupture complexity including reverse slip, direct branching, and dynamic triggering. The spatio-temporal distribution of rupture transfers are altered distinctively by plastic energy absorption, correlated with locations of geometrical fault complexity. Computational cost increases by 7% when accounting for off-fault plasticity in the demonstrating application. Our results imply that the combination of fully 3D dynamic modelling, complex fault geometries, and off-fault plastic yielding is important to realistically capture dynamic rupture transfers in natural fault systems.

This chapter has been published in slightly altered form as Wollherr, S., Gabriel, A.-A., and Uphoff, C. (2018). Off-fault plasticity in three-dimensional dynamic rupture simulations using a modal Discontinuous Galerkin method on unstructured meshes: implementation, verification and application, *Geophysical Journal International*, Vol. 214, 1556–1584, `https://doi.org/10.1093/gji/ggy213`

2.1 Introduction

Understanding the physics of earthquake source processes enhances seismic hazard assessment for natural fault systems. Specifically, directivity effects as well as potential rupture transfers to adjacent fault segments are determined by earthquake source dynamics. However, the fundamentals of rupture dynamics are difficult to infer from observations. Numerical simulations pose a powerful tool to further our understanding of earthquakes rupturing (complex) faults.

In modelling earthquake rupture dynamics, the fault geometry in conjuncture with fault stress and strength constitute essential initial conditions, determining frictional failure, rupture propagation, and seismic wave emanation off the fault. Additionally, such models can describe the interaction of fault slip with the surrounding host-rock material, for example by considering off-fault plastic deformation.

Accounting for plastic rock failure causes inelastic energy dissipation which in turn influences rupture dynamics (e.g., Andrews, 1976, 2005; Kaneko and Fialko, 2011). Moreover, unreasonably high slip velocities on the fault are limited (Andrews, 2005; Dunham et al., 2011a). Plasticity also affects the source mechanical characteristics such as rupture speed and rupture style (e.g., Templeton and Rice, 2008; Duan and Day, 2008; Dunham et al., 2011a; Gabriel et al., 2013). For example, the transition from pulse-like to crack-like, as well as from sub- to supershear rupture may be delayed or even prevented by plastic material response.

Dynamic rupture simulations reveal that off-fault plastic yielding is enhanced by the interaction of rupture with a free surface boundary condition (Ma, 2008; Ma and Andrews, 2010). As a consequence, the formation of depth-dependent flower-like distribution of plastic strain is observed (Ma and Andrews, 2010), which is consistent with observations of damage zones in natural fault systems (e.g., Chester et al., 1993; Ben-Zion and Sammis, 2003; Mitchell and Faulkner, 2009). In addition, off-fault plasticity restricts shallow fault slip (Kaneko and Fialko, 2011; Erickson et al., 2017; Roten et al., 2017), contributing to the well-observed shallow slip deficit for strike-slip events (e.g., Fialko et al., 2005). Purely kinematic earthquake scenarios of the Southern San Andreas Fault (Roten et al., 2014), as well as spontaneous dynamic rupture on simplified planar faults (Roten et al., 2015) confirm that plasticity impacts peak slip rates, dominantly close to the free surface. As a result, peak ground velocities (PGVs) are reduced dramatically compared to purely elastic modelling.

Previous studies including plastic deformation are mostly based on planar fault geometries. However, geological observations reveal that natural faults are complex geometrical systems, which may include bends, branches, and distinct fault segments (e.g., King and Nabelek, 1985; Wesnousky, 1988, 2006). Accounting for full geometric fault complexity jointly with a homogeneous (regional tectonic) background stress state in the modelling domain leads to highly heterogeneous initial fault stresses, which influences rupture propagation (e.g., Aochi and Fukuyama, 2002; Gabriel and Pelties, 2014) and enhances plastic yielding (e.g., Dunham et al., 2011b).

Combining inelastic processes and complex fault geometries may crucially affect rupture transfers in terms of branching and dynamic triggering ("jumping"). For example, plasticity inhibits the activation of branching segments on compressional sides but promotes branching on extensional sides of strike-slip fault events (DeDontney et al., 2012). Considering 2D discontinuous, yet planar fault segments (step-over faults), off-fault plastic failure has been shown to effectively lengthen faults by enhancing coseismic slip and increasing the slip gradient at fault tips (Nevitt and Pollard, 2017).

In spite of off-fault plasticity being widely studied its numerical implementation remains challenging. Plastic material behaviour introduces a non-linear constitutive equation relating stress and strain. Incorporating this relation directly into the underlying wave equation requires distinct (non-linear) numerical methods and additional stabilisation techniques for solving this problem based on a damage

rheology description (e.g., Lyakhovsky and Ben-Zion, 2014). Alternatively, plasticity can be readily implemented in already existing numerical solvers of the linear wave equation via a predictor-corrector approach: First, an elastic trial stress state needs to be calculated and checked against the corresponding elastic yield surface. In a second step, the trial stress state is adjusted whenever this state exceeds the elastic domain, i.e. plastic deformation occurs. As a consequence, additional calculations are required for every time step and for the complete discretization space independent of plastic yielding actually occurring. Thus, incorporating plasticity can be computationally demanding. In particular, additional interpolation may become necessary to define stresses on all spatial discretization points e.g., in staggered-grid methods. For instance, Roten et al. (2016) report an increase of computational costs by 65% in comparison to a purely elastic simulation.

In addition, numerical solutions of plasticity models tend to be mesh-dependent regarding strain localization (e.g., Templeton et al., 2009; Dunham et al., 2011a), and thus require regularization. To ensure reliable simulation results with mesh refinement, numerical solvers need to be verified by convergence tests. However, detailed convergence studies of 3D dynamic rupture problems are generally scarce and are specifically missing with respect to heterogeneous on-fault initial conditions and off-fault plasticity.

Simulating dynamic rupture requires a discretized model of the area of interest, including a prescribed fault surface. Numerical methods based on hexahedral element discretization of the domain such as Finite Differences (e.g., Day, 1982; Dalguer and Day, 2007; Cui et al., 2010), Spectral Element Methods (Kaneko et al., 2008; Galvez et al., 2014) or Spectral Boundary Integral Equation Methods (e.g., Lapusta et al., 2000) are often restricted to planar fault models. The incorporation of curvilinear elements (Cruz-Atienza and Virieux, 2004; Kozdon et al., 2012; Zhang et al., 2014; Duru and Dunham, 2016) enables the discretization of geometrical heterogeneities such as fault roughness across fault segments, whereas fault branching remains challenging to incorporate. Finite Element (FE) Methods based on tetrahedral elements (e.g., Ma, 2008; Barall, 2009; Duan and Oglesby, 2006; Pelties et al., 2012) as well as Boundary Integral Equation (BIE) Methods (e.g., Rice, 1993; Aochi et al., 2000; Ando, 2016) are well suited for complex fault geometries. Discontinuous Galerkin (DG) and BIE methods are the only methods able to accurately handle intersecting faults (e.g., Tago et al., 2012; Pelties et al., 2012; Ando et al., 2017). However, the BIEM is restricted to purely elastic material properties. The (DG) method is therefore increasingly becoming attractive as a method of choice for representing Earth's complex structure in a high-order accurate manner (e.g., Wilcox et al., 2010; Tago et al., 2012; Pelties et al., 2012; Duru et al., 2017; Tavelli and Dumbser, 2018).

Here, we analyse numerical and physical characteristics of dynamic rupture simulations accounting for off-fault plastic yielding in direct conjunction with complex 3D fault geometry as well as heterogeneous initial stress and strength conditions. Such simulations pose high demands on numerical methods in terms of computational costs and mesh generation. Three-dimensional models featuring highly resolved fault zones, necessary to accurately capture the dynamic rupture process, exhibit quickly millions of degrees of freedom.

To this end, we present the implementation of plastic yielding in the open-source software package SeisSol via a Return Mapping Algorithm (e.g., Ortiz and Simo, 1986). SeisSol is based on an Arbitrary high-order DERivative Discontinuous Galerkin (ADER-DG) method (e.g., Dumbser and Käser, 2006; Pelties et al., 2012). The software package is highly optimized for the efficient use on modern high-performance computing infrastructure (Breuer et al., 2014; Heinecke et al., 2014; Breuer et al., 2015, 2016; Heinecke et al., 2016; Uphoff and Bader, 2016) enabling the simulation of realistic large-scale dynamic rupture models.

The remainder of this paper is structured as follows: In Sec. 2.2 we detail two distinct implementations of plastic material response based on a non-associated Drucker-Prager plastic yield criterion.

Both implementations are suitable for any high-order modal Discontinuous Galerkin approach and not restricted to the ADER-DG method. We verify both implementations in Sec. 2.3 in well-established community benchmarks for two naturally arising faulting mechanisms (Harris et al., 2009, 2011). In Sec. 2.4 we investigate the numerical convergence of key dynamic rupture parameters with mesh refinement and increasing polynomial order with respect to a reference solution. The setup includes depth-dependent initial stresses and plastic yielding, to reflect the current state-of-the-art of realistic dynamic earthquake simulations. The 3D *h*- and *p*-refinement study extends previous studies considering only elastic material response and homogeneous initial stress conditions (e.g., Day et al., 2005; Pelties et al., 2012). Both plasticity implementations are then analysed in terms of efficiency (computational cost) versus accuracy.

We demonstrate the specific advantages of the modal DG approach on unstructured meshes by presenting a large-scale 3D dynamic rupture earthquake scenario based on the 1992 Landers earthquake. We focus on the influence of inelastic material behaviour on rupture transfers across a geometrical complex fault system. Furthermore, we compare macroscopic earthquake source characteristics, such as peak slip rate and the distribution of slip in purely elastic versus plastically yielding simulations. Plasticity highly impacts 3D source dynamics, specifically at locations of geometrical complexities such as fault branches and fault bends. We critically discuss our numerical analysis as well as application example and conclude that it may be essential to combine fully 3D dynamic modelling, complex fault geometries, and off-fault plastic yielding to realistically capture dynamic rupture transfers in natural fault systems.

2.2 Methodology

In the first part of this section (Sec. 2.2.1) we summarize the governing equations, underlying numerical method, and recent optimization of the software package SeisSol (`www.seissol.org`) simulating spontaneous earthquake rupture coupled to elastic seismic wave propagation. We then detail the theory of non-associated Drucker-Prager plastic yielding and its numerical regularization (Sec. 2.2.2). In Sec. 2.2.3 we present two approaches for the numerical implementation of plastic yielding in modal Discontinuous Galerkin methods, and discuss their computational efficiency.

2.2.1 Spontaneous earthquake rupture within the ADER-DG framework

Numerical method solving the elastic wave equation

SeisSol numerically solves the weak form of the elastic wave equation in velocity-stress formulation. The underlying system of equations can be written in a compact matrix-vector form

$$\frac{\partial}{\partial t}\mathbf{Q}+\mathbf{A}\frac{\partial}{\partial x}\mathbf{Q}+\mathbf{B}\frac{\partial}{\partial y}\mathbf{Q}+\mathbf{C}\frac{\partial}{\partial z}\mathbf{Q}=\mathbf{0}, \tag{2.1}$$

for the solution $\mathbf{Q}=(\sigma_{xx},\sigma_{yy},\sigma_{zz},\sigma_{xy},\sigma_{yz},\sigma_{xz},u,v,w)^T$ including the stress tensor components σ_{ij} and the velocities u,v,w in x, y, z direction, respectively. The space-dependent Jacobian matrices $\mathbf{A},\mathbf{B},\mathbf{C}$ contain the Lamé parameters λ and μ as well as the density ρ, encapsulating the elastic material properties. A detailed definition can be found in Dumbser and Käser (2006).

For spatial discretization, a modal Discontinuous Galerkin (DG) approach is employed. The computational domain is subdivided into first-order tetrahedral elements τ_m and all material properties are constant within an element. To approximate the solution $\mathbf{Q}$ at a point $\mathbf{x}=(x,y,z)^T$ and at time t we

use a linear combination of orthogonal polynomial basis functions Φ_i, namely the Dubiner's basis functions (Cockburn et al., 2000), and time-dependent coefficients $\hat{\mathbf{Q}}_i(t)$:

$$\mathbf{Q}(\mathbf{x},t) = \sum_{i=1}^{L} \hat{\mathbf{Q}}_i(t)\ \Phi_i(\mathbf{x}), \tag{2.2}$$

with $L = (p+1)(p+2)(p+3)/6$ for polynomial degree p or order of accuracy $\mathscr{O} = p+1$. Multiplication of Eq. (2.1) by a test function Φ_k and integration over one element τ_m leads to the semi-discrete weak formulation. To evaluate the resulting mass, stiffness and flux matrices (see Dumbser and Käser, 2006) independently of the element shape of τ_m, all elements are transformed to a tetrahedral reference element τ_E. These matrices can then be pre-calculated analytically leading to a quadrature-free scheme (e.g., Atkins and Shu, 1996).

The exchange of information between elements is purely local, based on the concept of numerical fluxes established in Finite Volume methods: SeisSol uses the exact solution of the Riemann problem, namely the Godunov flux. This upwind flux poses a differential equation with discontinuous initial conditions (Toro, 1999; LeVeque, 2002). The numerical properties of the ADER-DG algorithm are extremely sensitive to the choice of flux function: The numerical dissipation and dispersion properties of the Godunov upwind flux have been widely studied (e.g., Hu et al., 1999; Käser et al., 2008; Hesthaven and Warburton, 2010). While numerical dissipation leads to a decay in waveform amplitudes of the marginally resolved wave numbers, numerical dispersion leads to a gradual separation of waves of different wave periods. Our ADER-DG scheme offers favourably low numerical dispersion properties, allowing to accurately recover phase velocities propagating over a large number of wavelengths (Käser et al., 2008). Numerical dissipation decreases with increasing polynomial degree and is stronger beyond a cut-off frequency that depends on the mesh size h and on the order of accuracy $\mathscr{O}$. The cut-off frequency is expected to be inversely proportional to the travel time of s-waves over a typical grid spacing $\approx h/\mathscr{O}/V_S$ (Pelties et al., 2014).

For the integration in time, the DG method is combined with an Arbitrary High Order DERivative (ADER) scheme (Titarev and Toro, 2002; Käser and Dumbser, 2006; Dumbser and Käser, 2006), which provides equivalent high-order accuracy as in space using a single explicit time integration step.

Dynamic rupture as internal boundary condition

De la Puente et al. (2009) and Pelties et al. (2012) incorporate non-linear frictional failure as internal boundary condition into SeisSol in two (2D) and three dimensions (3D). The Coulomb failure criterion and consecutive constitutive laws are enforced by solving a modified inverse Riemann problem on prescribed element interfaces (fault surfaces) in contrast to the typically applied traction at split-node approach (e.g., Andrews, 1999).

This requires, in distinction to the quadrature free approach used for solving the wave equation, the introduction of space-time quadrature points across dynamic rupture interfaces. The flux functions across those interfaces are integrated by quadrature based on $(p+2)^2$ Gaussian points (Stroud, 1971). These points are located within the triangular faces of the tetrahedral elements connected to the fault surface. Their distribution is visualized for p = 3 in Fig. 2.C.1 in Sec. 2.C. At these element internal points, we also enforce the Coulomb failure criterion of the frictional boundary condition. Numerical convergence towards a reference solution was demonstrated for sub-elemental treatment of the dynamic rupture boundary condition in Pelties et al. (2012). Fault initial stress and friction parametrizations are assigned individually to each quadrature point, resulting in an excellent agree-

ment with established numerical methods even under highly heterogeneous conditions (Pelties et al., 2014).

SeisSol is verified for a wide range of advanced dynamic rupture problems such as branched faults, dipping fault geometries, and laboratory-derived constitutive laws such as the rate-and-state friction law (Pelties et al., 2014). It allows for unstructured, tetrahedral mesh discretization, facilitating automatised mesh generation for naturally arising fault geometries, topography, and sub-surface structures. Additionally, local mesh refinement and coarsening allow for adaptive resolution, for example, to resolve the stress drop at the rupture tip in the cohesive zone (process zone) (Ida, 1972).

SeisSol's on-fault slip rates remain notably free of high-frequency oscillations (De la Puente et al., 2009; Pelties et al., 2012). The generation of such non-physical high-frequency modes may contaminate the solution over all space-time scales (Duan and Day, 2008). Due to the numerical properties of our flux higher frequency modes are subdued while the physically meaningful lower frequencies are minimally affected (see Sec. 2.2.1). This is advantageous for dynamic rupture simulations: spurious high-frequency oscillations are not generated in the vicinity of the fault and typical damping procedures as used by other methods (e.g., Rojas et al., 2008) do not need to be applied. The presence of spurious oscillations in DG schemes using a different flux, such as the non-dissipative central flux (Tago et al., 2012), suggests that on-fault solution behaviour is directly related to the properties of the numerical flux. Still, it remains unclear whether this behaviour results from the dissipative properties of the (modified) flux across the fault boundary elements (on-fault) or the upwind flux across non-frictional elements (off fault) - or both.

Computational optimization

SeisSol is optimized for the latest CPU architectures. It delivers high performance on a single compute node as well as on thousands of compute nodes in parallel. For example, SeisSol was one of the first software packages that were optimized for Intel's Knights Landing architecture (Heinecke et al., 2016). It exceeded 1 PFLOP/s performance on the SuperMUC supercomputer (Breuer et al., 2014), and it scaled up to 1.6 million compute cores of the Tianhe-2 supercomputer (Heinecke et al., 2014).

Recent optimization includes a hybrid OpenMP/MPI parallelization (Heinecke et al., 2014), high-performance compute kernels (Breuer et al., 2014), asynchronous I/O (Rettenberger and Bader, 2015; Rettenberger et al., 2016), and clustered local time-stepping (Breuer et al., 2016).

SeisSol is suitable for large-scale (spatial extent and modelling duration) earthquake simulations (Pelties et al., 2012; Heinecke et al., 2014; Gabriel and Pelties, 2014; Rettenberger et al., 2016; Weingärtner et al., 2016; Madden et al., 2017) including modelling challenges due to the geometrical complexity of the Earth, e.g., shallowly dipping megathrust faults, topography, 3D subsurface structure, and fault roughness (Ulrich and Gabriel, 2017; van Zelst et al., 2017).

All previous SeisSol dynamic rupture simulations were based on the assumption of purely elastic material properties. Motivated by the recent gain in efficiency, we present in this work the incorporation of the physics of plastic deformation into SeisSol.

2.2.2 Off-fault plastic yielding

This section provides an overview of the physics and the derivation of a numerical update scheme for off-fault plasticity. We first summarize a non-associated plasticity model widely used to describe plastic material behaviour of soils and rocks. We then discuss the required numerical regularization using viscoplasticity with a mesh-independent regularization factor. Finally, we describe the implementation of viscoplasticity via a Return Mapping algorithm into an existing dynamic rupture solver.

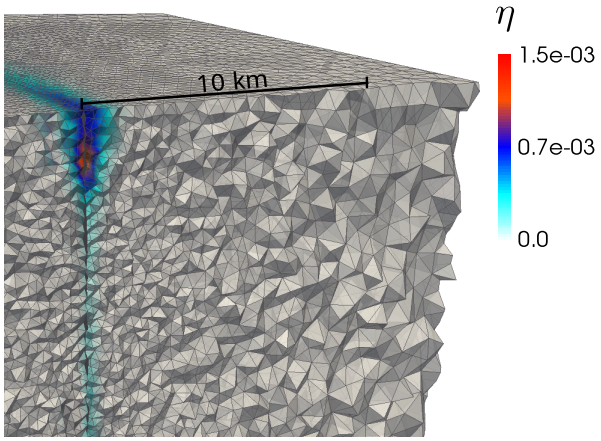

Figure 2.1: SeisSol's simulated accumulated plastic strain, as defined in Eq. (2.9), surrounding a strike-slip fault (TPV27, after 8 s of simulated time, see Sec. 2.3). At depth, plastic strain occurs mainly on the compressional side of the fault, but shifts to both fault sides close to the surface. SeisSol uses an unstructured tetrahedral mesh featuring coarsening away from the fault.

Non-associated Drucker-Prager plasticity

Plastic material response can be represented by a yield function F, which defines the onset of plastic yielding and thus limits the elastic domain of a material, and by a plastic potential function g defining the direction of the plastic strain rate (plastic flow) in case of plastic yielding. The corresponding plastic strain rate can be defined as the derivative of the flow rule with respect to the stress. In so-called associated plasticity models, e.g. used for metals and alloys (e.g., Vermeer and de Borst, 1984), the plastic strain increment is collinear to the normal of the yield surface, hence $g = F$. However, to model the plastic behaviour of soil and rocks, non-associated plasticity formulations are used, in which F and g are defined individually.

The total strain $\boldsymbol{\varepsilon}$ is the sum of an elastic strain component and a plastic strain component, $\boldsymbol{\varepsilon} = \boldsymbol{\varepsilon}^e + \boldsymbol{\varepsilon}^p$, whereas $\boldsymbol{\varepsilon} = \boldsymbol{\varepsilon}^e$ in case of pure elasticity. The stress increment can then be expressed by the time derivative of Hooke's law:

$$\dot{\sigma}_{ij} = \sum_{k,l} C_{ijkl}(\dot{\varepsilon}_{kl} - \dot{\varepsilon}^p_{kl}), \tag{2.3}$$

for the isotropic, elastic, fourth order stiffness tensor C. In the following, we derive the plastic strain increment

$$\sum_{k,l} C_{ijkl}\dot{\varepsilon}^p_{kl} = \lambda\,\delta_{ij}\left(\sum_k \dot{\varepsilon}^p_{kk}\right) + 2\mu\dot{\varepsilon}^p_{ij}, \tag{2.4}$$

where δ_{ij} is the Kronecker delta. We consider a plasticity model without dilatancy, i.e. no volumetric changes due to plastic yielding, such that $\sum_i \dot{\varepsilon}^p_{ii} = 0$ holds true.

The formulation employs a Drucker-Prager yield criterion which is defined as

$$\tau_c = c\,\cos(\phi) - \sigma_m\,\sin(\phi), \tag{2.5}$$

for cohesion c, an internal angle of friction $\phi = \tan^{-1}(\nu)$ with bulk friction ν, and mean stress $\sigma_m = (\sum_{i=1}^{3}\sigma_{ii})/3$, assuming compressional stresses to be negative. Defining the second invariant of deviatoric stresses s_{ij} as

$$I_2 = \frac{1}{2}\sum_{i,j} s_{ij}s_{ji} = \frac{1}{2}\sum_{i,j}(\sigma_{ij} - \delta_{ij}\,\sigma_m)(\sigma_{ji} - \delta_{ji}\,\sigma_m), \tag{2.6}$$

the yield function can be expressed as

$$F(\sigma) = \sqrt{I_2} - \tau_c. \tag{2.7}$$

If the current stress state σ reaches the elastic limit ($F(\sigma) = 0$), the plastic strain rate $\dot{\boldsymbol{\varepsilon}}^p$ is determined with the plastic potential function $g(\sigma) = \sqrt{I_2}$ as follows:

$$\dot{\varepsilon}_{ij}^p = \frac{1}{2\mu} \frac{\partial g(\sigma)}{\partial \sigma_{ij}} = \frac{1}{2\mu} \frac{s_{ij}}{2\sqrt{I_2}}. \tag{2.8}$$

With this, we define a so-called perfect plasticity model: The condition $F = 0$ is enforced strongly by instant multiplication of the deviatoric stresses with $\tau_c/\sqrt{I_2}$ when the yield surface is reached.

In case of plastic yielding, plastic strain at time t can be mapped into the scalar quantity $\eta(t)$ following Ma (2008):

$$\eta(t) = \int_0^t d\eta = \int_0^t \sqrt{\frac{1}{2}\dot{\varepsilon}_{ij}^p \dot{\varepsilon}_{ij}^p}. \tag{2.9}$$

Fig. 2.1 depicts exemplarily the accumulated plastic strain η surrounding a strike-slip fault in SCEC benchmark TPV27 (defined in Sec. 2.3).

Viscoplastic regularization

Perfect plasticity models, as discussed in the last section, are known to be mathematically ill-posed; their numerical solution tends to show mesh-dependent behaviour in case of strain localisation (e.g. De Borst et al., 1996; Templeton and Rice, 2008; Dunham et al., 2011a; Xu et al., 2012). Dias da Silva (2004) summarizes different approaches enabling Finite Element methods to produce mesh-independent results or, at least, to control mesh-dependencies. These include employing Cosserat media, gradient plasticity theories or the introduction of a rate-dependent material behaviour emulated by viscoplasticity. In the latter case, stresses are allowed to exceed the yield criterion and are subsequently relaxed to the yield surface over a specified amount of time (relaxation time).

In dynamic rupture simulations, viscoplastic relaxation is widely used to regularize the numerical implementation of off-fault plastic yielding (Andrews, 2005; Templeton and Rice, 2008; Duan, 2008; Dunham et al., 2011a; Xu et al., 2012; Gabriel et al., 2013). We employ hereafter a rate-dependent Duvaut-Lions (Duvaut and Lions, 1976) formulation of viscoplasticity, as specified for SCEC benchmark test problems (Harris et al., 2009; Barall and Harris, 2014). The viscoplastic strain rate is given as the differential equation

$$\dot{\varepsilon}_{ij}^{vp} = \frac{1}{2\mu T_v}(\sigma_{ij} - P_{ij}(\sigma)), \tag{2.10}$$

for the viscoplastic relaxation time $T_v > 0$ and projection P with

$$P_{ij}(\sigma) = \begin{cases} (\tau_c/\sqrt{I_2})\ s_{ij} + \sigma_m\ \delta_{ij} & \text{for } F(\sigma) \geq 0 \\ \sigma_{ij} & \text{for } F(\sigma) < 0. \end{cases} \tag{2.11}$$

Note, that $P_{ij}(\sigma)$ is the adjusted stress state in the rate-independent plasticity case with $\dot{\varepsilon}_{ij}^p$ defined in Eq. (2.8). In the absence of additional plastic yielding, viscoplastic regularization permits the current stress state σ_{ij} to reach the inviscid stress state $P_{ij}(\sigma)$ after a specified time T_v. In distinction to previous studies, we choose a constant relaxation time T_v independent of spatial discretization as detailed in the next section.

Implementation via a Return Mapping algorithm

Incorporating plasticity is commonly achieved via Return Mapping algorithms (e.g., Andrews, 2005, for dynamic rupture solvers), requiring the following steps:

First, a trial stress state $\boldsymbol{\sigma}^{\text{trial}}$ at time step t_{n+1} is calculated, which is based on the numerical solution of the wave equation coupled to frictional boundary conditions assuming purely elastic material properties (i.e. $\dot{\boldsymbol{\varepsilon}}^p = 0$ in Eq. (2.3)). Secondly, if $F(\boldsymbol{\sigma}^{\text{trial}}) < 0$, no plastic yielding occurs and the trial stress becomes the new stress, $\boldsymbol{\sigma}^{n+1} = \boldsymbol{\sigma}^{\text{trial}}$. In case of plastic yielding ($F(\boldsymbol{\sigma}^{\text{trial}}) \geq 0$), the stress state $\boldsymbol{\sigma}^{\text{trial}}$ is updated in a plasticity corrector-step by assuming non-zero plastic strain rates (i.e. $\dot{\boldsymbol{\varepsilon}}^p \neq 0$)

$$\sigma_{ij}^{n+1} = \sigma_{ij}^{\text{trial}} - 2\mu(\varepsilon_{ij}^{vp})^{n+1}. \tag{2.12}$$

To determine ε_{ij}^{vp} at t_{n+1} we need to integrate the viscoplastic strain rate in Eq. (2.10) over one time step. In classic Return Mapping algorithms an implicit backward Euler scheme is used for numerical integration (Simo et al., 1988). This approach has been presented for a viscoplastic rheology in dynamic rupture simulations by Dunham et al. (2011a). For the here presented plasticity formulation an update scheme based on a closed form integration of Eq. (2.12) is used (Andrews, 2005; Duan and Day, 2008). Therein, the problem is solved explicitly by assuming the projection P_{ij} to be constant over one time step.

The full derivation of the updated stress state σ_{ij}^{n+1} is detailed in Sec. 2.A and here summarized as

$$\sigma_{ij}^{n+1} = f^* s_{ij}^{\text{trial}} + \sigma_m^{\text{trial}} \delta_{ij}, \tag{2.13}$$

with the adjustment factor

$$f^* = (1 - \exp(-\Delta t / T_v)) \frac{\tau_c}{\sqrt{I_2}} + \exp(-\Delta t / T_v), \tag{2.14}$$

for time step width Δt. Combining Eq. (2.13) and Eq. (2.12) the viscoplastic strain is then defined as

$$(\varepsilon_{ij}^{vp})^{n+1} = \frac{1}{2\mu}(1 - f^*)\, s_{ij}^{\text{trial}}. \tag{2.15}$$

Due to the assumption of no change of volumetric plastic strain, the same mean stress before and after the plastic adjustment is preserved.

In previous studies, T_v in Eq. (2.14) is chosen to be of the order of the P- or S-wave travel time across the discretization length dx of the modelling domain (e.g. Duan, 2008; Ma and Andrews, 2010; Xu et al., 2012; Gabriel et al., 2013). This approach results in a discretization-dependent T_v, i.e. in a shorter relaxation time for meshes of smaller discretization lengths. However, the time step Δt, discretizing an explicit set of hyperbolic partial differential equations in time, needs to satisfy the Courant-Friedrich-Lévy (CFL) criterion to guarantee a stable numerical solution. In that case the time step is determined according to the fastest wave velocity in the medium and the smallest discretization length dx. Therefore, Δt itself introduces a mesh-dependent parameter into Eq. (2.14). Thus, throughout this study, we use a constant relaxation time $T_v = 0.03$ independent of the spatial discretization. This value has been chosen to regularize plasticity for typical dynamic rupture setups (Harris et al., 2011). Note, that this choice is not connected to a physical motivated description of viscoplasticity but is a purely numerical factor. We prove convergence towards a reference solution of this parametrization choice with increasing polynomial degree and decreasing mesh size in Sec. 2.4.

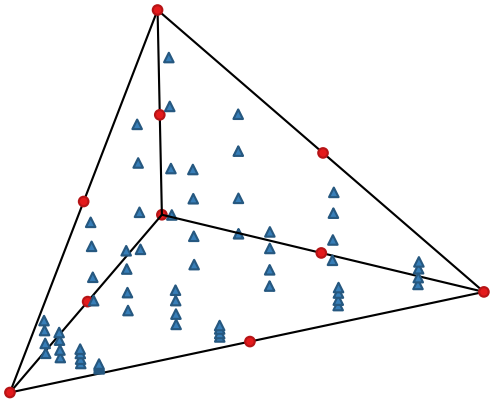

Figure 2.2: Reference tetrahedron with 64 quadrature points of the QP approach (blue triangles) and 10 nodal basis points of the NB approach (red circles) for polynomial degree $p = 2$. Both approaches achieve sub-element resolution. QPs cluster towards element edges.

2.2.3 Novel approaches for incorporating plasticity in modal DG schemes

In most numerical methods used for solving dynamic rupture problems, such as Finite Differences (FD) (e.g., Andrews, 2005; Kozdon et al., 2012), Finite Elements (FE) (e.g., Duan, 2008) or nodal high-order FE (e.g., Kaneko et al., 2008; Tago et al., 2012), the unknowns of the system of equations define the solution at mesh points (FD, FE) or at polynomial interpolation points within elements (nodal high-order FE). Such points can be readily used to evaluate a plastic yield criterion.

In SeisSol's modal approach the unknowns are given by the coefficients of a local polynomial expansion which are not associated with spatial points within an element. Hence, it is impossible to directly apply a nonlinear function at mesh or interpolation points.

We thus present in the following two implementation approaches for incorporating plastic yielding:

1. evaluation of the stress state at sub-elemental quadrature points (QPs),

2. switching to a system of nodal basis (NB) functions.

Both methods are fundamentally similar. The yield criterion is first evaluated at a set of sub-elemental points, followed by a projection of a non-polynomial function (the adjusted stresses) back to the polynomial space of the underlying high-order numerical discretization. To this end, our first approach approximates a L^2-projection using a quadrature rule, whereas the second approach uses interpolation. Both schemes can be generalized to any DG approach and are not restricted to the modal ADER-DG method of SeisSol. Even nodal methods need to decide whether the non-linearity is enforced at the present interpolation points or if a different set of points might be used.

We analyse both approaches in terms of efficiency (computational cost) in Sec. 2.2.3 and in terms of accuracy in Sec. 2.4.4.

Quadrature points approach

For both approaches, we need to retrieve a trial stress tensor σ^{trial} to be evaluated against the yield function F. We here detail the approximation of the required stress state at quadrature points (QPs) $\xi_1, \ldots, \xi_n$. This approach is referred to in the following as the QP approach.

The QPs are based on a multidimensional quadrature formulae of degree $(2n-1)$ for n^3 points for tetrahedral elements (Stroud, 1971) using Gauss-Jacobi polynomials of degree p. The number of QPs

increases with increasing p as $n_{\mathrm{QP}} = (p+2)^3$ corresponding to a quadrature of degree $2p+3$. Their distribution for $p = 2$ across a tetrahedral reference element is exemplarily visualized in Fig. 2.2. We achieve resolution of the solution distinctively higher than given by the vertices of the computational mesh. The trial stress is evaluated at every QP via the following matrix-matrix product:

$$\sigma_{iq}^{\mathrm{QP}} = \sum_{l=1}^{L} \Phi_l(\xi_i)\hat{Q}_{lq} =: \sum_{l=1}^{L} G_{il}\hat{Q}_{lq} \tag{2.16}$$

where $\hat{Q}_{lq} := (\hat{\mathbf{Q}}_l)_q$ is the coefficient of the l-th basis function in the polynomial expansion of the q-th quantity and $\mathbf{G}$ is a $n_{\mathrm{QP}} \times L$ matrix. We obtain the $n_{\mathrm{QP}} \times 6$ matrix σ^{QP}, which contains the stress tensor evaluated at every QP.

After checking the plastic yield criterion for each QP separately we adjust the stresses in case of plastic yielding using the update formula defined in Eq. (2.13). To recover the polynomial coefficients from the non-polynomial adjusted stresses σ^{new} we can make use of an L^2 projection for the q-th quantity requiring

$$\int_{\tau_E} \sigma_q^{\mathrm{new}}\, \Phi_l \, dV = \int_{\tau_E} \sum_{k=1}^{L} (\hat{Q}_{kq}^{\mathrm{new}}\Phi_k)\Phi_l \, dV, \tag{2.17}$$

for all basis functions Φ_l (i.e. the best polynomial representation of σ_q^{new} in the L^2 sense.) Due to the orthogonality of the basis functions, the integral on the right side of the equation is only non-zero for $k = l$. We can recover the coefficients $\hat{Q}_{lq}^{\mathrm{new}}$ of the polynomial representation by solving Eq. (2.17)

$$\hat{Q}_{lq}^{\mathrm{new}} = \frac{\int_{\tau_E} \sigma_q^{\mathrm{new}}\, \Phi_l \, \mathrm{d}V}{\int_{\tau_E} \Phi_l \Phi_l \, \mathrm{d}V} \approx \frac{\sum_{i=1}^{n_{\mathrm{QP}}} \sigma_{iq}^{\mathrm{new}}\, w_i \Phi_l(\xi_i) \, \mathrm{d}V}{\int_{\tau_E} \Phi_l \Phi_l \, \mathrm{d}V}, \tag{2.18}$$

where the integral in the numerator is approximated by quadrature using the same quadrature points $\xi_{\mathbf{i}}$ in conjunction with corresponding weights w_i. Hence, the choice of approximating the solution at the specific points ξ is motivated by the (numerical) evaluation of the integral in Eq. (2.18). The denominator is simply the (analytically precomputed) l-th entry M_{ll} of the diagonal mass matrix $\mathbf{M}$ as defined in Dumbser and Käser (2006). The L^2 projection can also be written as matrix-matrix product,

$$\hat{Q}_{lq}^{\mathrm{new}} = \sum_{i=1}^{n_{\mathrm{QP}}} \tilde{G}_{li}\sigma_{iq}^{\mathrm{new}}, \tag{2.19}$$

with the $L \times n_{\mathrm{QP}}$ matrix $\tilde{\mathbf{G}}$ with entries $\tilde{G}_{li} = \frac{1}{M_{ll}} w_i \Phi_l(\xi_i)$. Note, that both matrices $\mathbf{G}$ and $\tilde{\mathbf{G}}$ depend only on the reference element and the basis functions and can be precomputed.

Nodal basis approach

As an alternative formulation, we consider switching from SeisSol's modal to a nodal basis (NB) for incorporating plastic yielding. This approach provides polynomial coefficients representing the solution directly at a set of interpolation points which we may readily use to check the plastic yield criterion. To transform modal coefficients $\hat{Q}_{lq}$ to nodal coefficients $\sigma_{iq}^{\mathrm{NB}}$ defined at L points $\zeta_1, \ldots, \zeta_L$ we make use of a generalized Vandermonde matrix,

$$\sigma_{iq}^{\mathrm{NB}} = \sum_{l=1}^{L} \Phi_l(\zeta_{\mathbf{i}})\hat{Q}_{lq} =: \sum_{l=1}^{L} \mathscr{V}_{il}\hat{Q}_{lq}, \tag{2.20}$$

where $\mathscr{V}$ is a $L \times L$ matrix. In contrast to matrix $\mathbf{G}$ in Eq. (2.16), the Vandermonde matrix $\mathscr{V}$ is invertible, which allows to easily switch between different polynomial coefficients.

However, in order to ensure that computing the inverse of $\mathscr{V}$ is well-conditioned for a given set of basis functions, we use a special set of three-dimensional nodal points ζ_i (after Warburton (2006) and Hesthaven and Warburton (2010), script available at `https://github.com/tcew/nodal-dg/tree/master/Codes1.1/Codes3D`). The here presented approach is not restricted to this particular set of points but other choices might yield similar Lebesgue constants (Warburton, 2006). The main advantage of these points here is that they can easily be constructed on runtime avoiding the storage in additional files. The distribution of nodal points ζ_i is exemplary visualized for $p = 2$ inside the reference tetrahedron in Fig. 2.2. The number of nodal basis points $n_{\mathrm{NB}} = (p+1)(p+2)(p+3)/6$ conforms with the number of basis functions L for a given polynomial degree p.

In case of plastic yielding we adjust the stresses at the nodal basis points using Eq. (2.13) and obtain σ^{new}. An L^2 projection to the polynomial space as in Sec. 2.2.3 is not required since $\sigma_{iq}^{\mathrm{new}}$ is already polynomial. To reverse the adjusted nodal coefficients into the modal formulation, we use the inverse Vandermonde matrix $\mathscr{V}^{-1}$:

$$\hat{Q}_{lq}^{\mathrm{new}} = \sum_{i=1}^{L} \mathscr{V}_{li}^{-1} \sigma_{iq}^{\mathrm{new}}. \tag{2.21}$$

The Vandermonde matrix $\mathscr{V}$ and its inverse can be precomputed.

In comparison to the previously discussed QP approach, the NB algorithm requires to check the plastic yielding criterion at considerably less sub-element points, specifically for increasing polynomial degree p. Additionally, the points building the nodal basis are spatially equally distributed, in distinction to the quadrature points which cluster towards element edges (see Fig. 2.2). Since these points are located at the element interfaces, their distance to the fault does not change with polynomial order. In contrast, Gaussian integration points are located closer to the fault surface for higher polynomial orders. Larger pointwise adjustments due to higher stresses experienced may be applicable. We demonstrate in Sec. 2.4 that neither the choice of implementation approach nor the location of the integration points impair the physical solution quality.

Computational efficiency

Both approaches presented above make use of a code generator for highly efficient matrix multiplications to compute Eq. (2.16) and Eq. (2.19) or Eq. (2.20) and Eq. (2.21), respectively, in analogy to the optimization of viscoelastic rheologies in SeisSol (Uphoff and Bader, 2016).

It is challenging to unambiguously define an overhead in terms of time-to-solution caused by incorporating plastic yielding, as it depends on the number of elements that yield, in both space and time. In addition, the performance characteristics of the target hardware architecture may shift the relative computational efficiency of the plasticity kernel compared to the elastic kernel. As a proxy metric, we provide lower and upper bounds for the computational overhead per element and time step of both approaches with respect to the number of floating point operations (flops). We expect this to be meaningful because both kernels are generated using the same code generator.

As a lower bound estimate, we assume that the considered element is not yielding plastically: the yield condition is checked, but neither adjustment of the stress state nor mapping is required. The upper bound is based on the assumption of the element yielding plastically, therefore, requiring yield criterion evaluation, adjustment of the stress state, and mapping into the original modal polynomial coefficients at each point inside this element.

In practice, only a small percentage of all elements, mostly situated in the vicinity of the fault, will experience plastic deformation in realistic dynamic rupture simulations (see e.g. Fig. 2.1). Furthermore, plastic yielding is restricted to the few time steps in which the rupture front and emitted waves are passing by. Therefore, the upper bound definition overestimates the computational cost considerably for application purposes.

We determine the computational overhead by counting the number of flops per element and time step in the elastic kernel as well as in the plasticity kernel. For matrix-matrix multiplications, flops are automatically determined by the code generator. For simple loops (e.g. scalar times vector) we manually count flops in the loop body. Note, that the number of flops is hardware-specific (Uphoff and Bader, 2016). Here, we analyse the Haswell architecture, which is used, e.g., in the supercomputer SuperMUC, Phase 2 (`https://www.lrz.de/services/compute/supermuc/`). Furthermore, the number of flops in the elastic kernels has a slight dependence on the mesh generator, so we base the overhead on the average flops in the elastic kernel.

The estimated minimum overhead of the QP approach (Sec. 2.2.3) for varying polynomial degrees ranges between 23.9 % ($p = 2$) and 39.9 %, ($p = 5$), whereas the maximum increase of computational cost is estimated between 50.0 % and 79.1 %. For the NB approach (Sec. 2.2.3), the lower bound is considerably lower: between 4.5 % ($p = 2$) and 6.6 % ($p = 4$); as well as the upper bound estimate which ranges between 8.6 % and 13.1 % (Note that for NB, $p = 4$ has a larger relative overhead than $p = 5$). As a consequence, the NB approach is in general cheaper by up to a factor of 6.

Both approaches to incorporate plastic material response cause considerable computational overhead, as the number of QPs and the number of nodal coefficients grow with $\mathcal{O}(p^3)$. However, the NB approach requires considerably less points per element (see Fig. 2.2); hence it is computational more efficient at the cost of lower sub-elemental resolution. In Sec. 2.4 we analyse the accuracy of both approaches in a *h*- and *p*-refinement study of on-fault dynamics, shedding light onto the trade-off of computational cost versus accuracy.

For a typical dynamic rupture scenario (SCEC benchmark problem TPV26/27 with plasticity, as presented in Sec. 2.3.1) we measure a computational overhead of 12.5 % with the NB approach versus 46 % with the QP approach for polynomial degree $p = 3$. Computational performance (FLOP/s) is not affected by off-fault plasticity. In comparison, computational costs in the AWP-ODC code of Roten et al. (2016) using a finite difference method increases by 65 % for the same benchmark setup. Note, that AWP-ODC is less computational demanding with respect to time-to-solution for these type of benchmark problems.

2.3 Verification under realistic modelling assumptions

Two community benchmark problems established by the SCEC/USGS Spontaneous Rupture Code Verification Project (`http://scecdata.usc.edu/cvws/`, Harris et al. (2009, 2011)) combine off-fault plastic yielding with realistic fault geometries and heterogeneous initial conditions. In the following, we compare SeisSol to two state-of-the-art numerical methods in terms of synthetic ground motions and key dynamic rupture parameters for these two test problems.

In Sec. 2.3.1 we verify the implementation using a strike-slip fault as used in several previous studies with plasticity (e.g., Andrews, 2005; Templeton and Rice, 2008; Dunham et al., 2011a; Ma and Andrews, 2010). Additionally, asymmetric near-source ground motions induced by dipping faults (Oglesby et al., 2000) are of particular interest and challenging in terms of mesh generation and numerical stability: High stresses are induced due to rupture-free-surface interaction which have to

Symbol	Parameter	Value
V_p	P-wave velocity	6000 m/s
V_s	S-wave velocity	3464 m/s
ρ	Density	2670 kg/m^3
μ_s	Static friction coefficient	0.18
μ_d	Dynamic friction coefficient	0.12
D_c	Slip-weakening critical distance	0.3 m
d	Fault depth	0–20000 m
w	Fault width	0–40000 m
c_0	Frictional cohesion	
	$d \leq 5000$m	-4.0 MPa + 0.00072 $\times$ d MPa/m
	$d > 5000$m	0.4 MPa
t_0	Forced rupture decay time	0.5 s
r_{crit}	Nucleation patch radius	4000 m
P_f	Fluid pressure	9.8 $\times$ d MPa/m
$\Omega(d)$	Tapering coefficient	
	$d < 15000$ m	1.0
	15000 m $\leq d \leq$ 20000 m	(20000 m - d)/5000 m
	$d > 20000$ m	0.0
σ_n^0	Background normal stress	(-2.632.9267 $\times\Omega(d)$- 26.166) $\times$ d MPa/m
τ_n^0	Background shear stress	-6.07897$\times\Omega(d)\times$ d MPa/m
h	Smallest element edge length	250 m
p	Polynomial degree (space and time)	4
c_{plast}	Plastic cohesion	1.36 MPa
ν	Bulk friction	0.1934
T_v	Viscoplastic relaxation time	0.03 s

Table 2.1: Simulation parameters for SCEC benchmarks TPV26 (purely elastic) and TPV27 (with plasticity). The additional parametrization of viscoplasticity in TPV27 is denoted at the bottom.

be resolved in relatively small elements and enhance plastic yielding in the hanging wall (Ma, 2008, 2009).

The initial fault stress and strength conditions vary with depth in both benchmarks. Capturing these heterogeneities is crucial, since they may fundamentally affect rupture nucleation and propagation (Day, 1982; Boatwright and Quin, 1986; Oglesby and Day, 2002; Ripperger et al., 2007; Pelties et al., 2014). To accurately capture heterogeneous fault initial conditions, we assign initial stress values to each of DG's fault quadrature points, allowing sub-element sampling (Pelties et al., 2014).

We verify in the following the application of a high polynomial degree in conjuncture with larger elements for resolving smaller-scale heterogeneous initial conditions for strike-slip and for dipping fault geometries. We additionally demonstrate the sensitivity of on-fault dynamic rupture measurements to the resolution of the nucleation zone (cf. Galis et al., 2014). All results shown in this section are based on the QP plasticity implementation (Sec. 2.2.3). The QP and NB approach are shown to yield near-identical results in Sec. 2.B.

2.3.1 Strike-slip fault benchmark TPV26/27

Test problems TPV26 (elastic) and TPV27 (plasticity, with viscoplastic regularisation) incorporate rupture on a vertical strike-slip fault geometry differing with respect to elastic versus plastic rheol-

ogy assumptions. The fault frictional properties are governed by linear slip-weakening friction. For the viscoplasticity benchmark TPV27, initial stress loading is prescribed additionally off the fault throughout the domain.

Off-fault initial stresses need to be defined consistently with the stresses acting on-fault. Therefore, the commonly applied nucleation method of using an overstressed patch is not applicable for dynamic rupture simulations including plastic yielding. To initiate rupture, the fault is forced to break within a circular patch of radius r_{crit} around the hypocentre by gradually reducing the friction coefficient from its static to its dynamic value. In this manner, forced rupture is smoothly overtaken by spontaneous rupture which reduces numerical artefacts. The modelling parameters of both benchmarks are listed in Table 2.1.

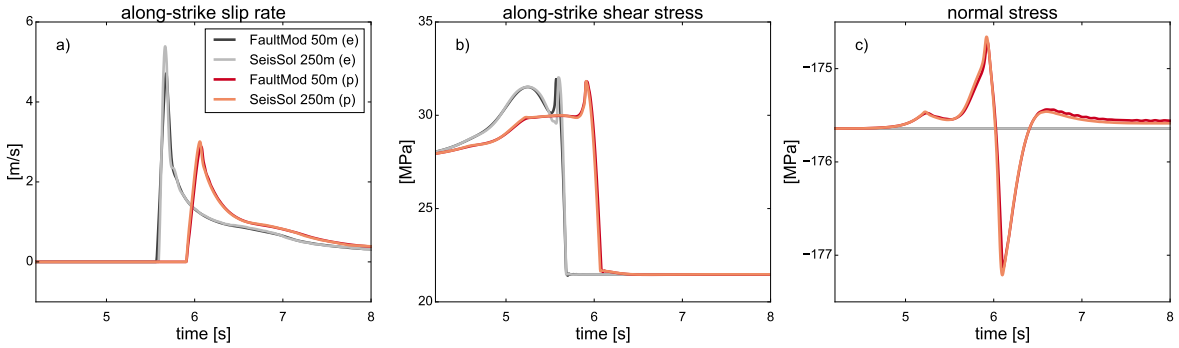

Figure 2.3: a) Along-strike slip rate, b) shear and c) normal stress at a fault location 10 km down-dip and 10 km along-strike for the benchmark problem TPV26 (purely elastic (e) , grey) and TPV27 (with plasticity (p), red). Lighter colours denote the ADER-DG SeisSol solution (using the QP approach), darker colours the FEM FaultMod solution.

We here verify SeisSol's results by comparing fault dynamics and ground motions to FaultMod, a well-established low-order FE software (Barall, 2009). FaultMod can handle hexahedral or tetrahedral elements to represent 3D geometries and material properties. Fault friction is implemented in FaultMod based on the traction-at-split-nodes method, featuring Newmark damping (Hughes, 2000), and an optional thin viscous layer surrounding the fault zone (Day et al., 2005; Dalguer and Day, 2007) to suppress spurious high-frequency oscillations. Thus, comparison to the undamped ADER-DG approach is specifically of interest.

We compare SeisSol's results of polynomial degree $p = 4$ and 250 m fault discretization to FaultMod's results with 50 m element edge length and polynomial degree $p = 2$. All meshes are coarsened away from the fault by a gradation rate of 1.06 (Simmetrix Inc., 2017) in order to reduce computational cost. The unstructured mesh used for this benchmark is depicted in Fig. 2.1.

Fig. 2.3 illustrates the overall agreement of SeisSol and FaultMod in terms of on-fault rupture dynamics for both, the elastic problem and the benchmark accounting for off-fault plasticity. Comparing on-fault slip rates (Fig. 2.3 a), we observe, that plastic yielding significantly reduces peak slip rate (here, by approx. 50%) and delays rupture arrival time (decreases rupture speed) as confirmed in various dynamic rupture models accounting for plastic energy dissipation (i.e. Andrews, 2005; Dunham et al., 2011a; Gabriel et al., 2013; Roten et al., 2015). In the elastic simulation, peak slip rate of SeisSol is slightly increased compared to FaultMod.

Remarkably, agreement improves distinctively when incorporating plastic material response. As we discuss in detail in Sec. 2.C, plasticity increases the cohesive zone width, the dynamic rupture problem inherent minimum length scale across which shear stress and slip rate vary abruptly (Day et al., 2005). For dynamic rupture models that include plastic yielding a high resolution at the fault

may be less crucial than commonly assumed: Analytical and numerical estimates based on purely elastic frameworks (in 2D) may underestimate the minimum length scale that needs to be resolved in a plastically yielding simulation (Sec. 2.C). This also impacts numerical convergence behaviour as we discuss in the next section.

The excellent agreement between SeisSol and FaultMod in terms of synthetic ground motions is shown in Fig. 2.4 for the purely elastic and the plastically deforming problem. SeisSol captures all features of horizontal, vertical and normal ground velocity time series even 20 km away from the fault where the mesh is already strongly coarsened to a maximum of 1300 m edge length. Within FaultMod's grid-doubling approach, the resolution is doubled from 50 m to 100 m in a distance of 10 element layers (500 m) from the fault. SeisSol resembles off-fault velocities obtained by the second-order method FaultMod, by using larger elements with polynomial degree $p = 4$, which illustrates the potential strengths of a high-order method also for plastically yielding materials. For the simulations including plasticity, we overall observe smaller peak ground velocities (PGVs) as a consequence of plastic deformation in the vicinity of the fault, consistent with recent studies (e.g., Roten et al., 2014). Even 20 km away from the fault, the effect of the delayed rupture arrival in the model with plasticity (Fig. 2.3) is visible as time shift of ground velocities (Fig. 2.4).

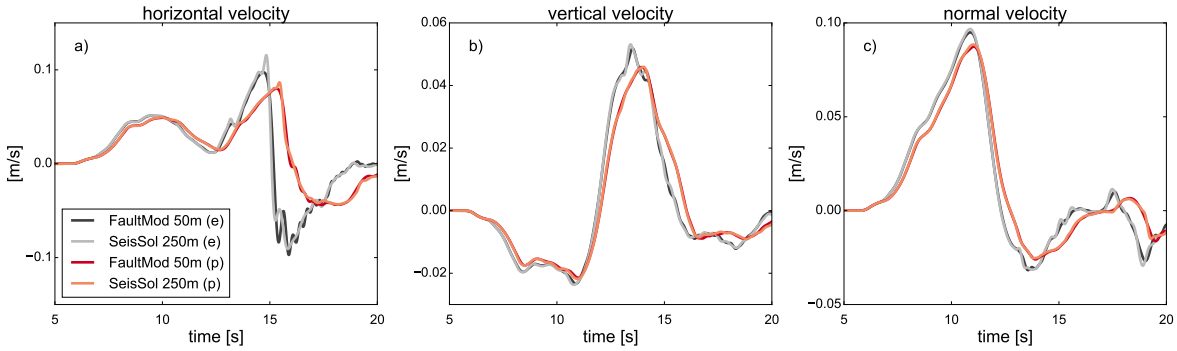

Figure 2.4: a) Horizontal, b) vertical and c) normal ground velocity time series at a location 20 km off-fault (near side) perpendicular to the epicentre for the purely elastic (e) and plasticity (p) strike-slip fault benchmark TPV26/27. Lighter colours denote the ADER-DG SeisSol solution (using the QP approach), darker colours the FEM FaultMod solution.

2.3.2 Dipping fault benchmark TPV12/13

Test problems TPV12 (elastic) and TPV13 (plasticity with viscoplastic regularisation) incorporate rupture on a 60-degree dipping normal fault based on the Solitario Canyon Fault at Yucca Mountain (Harris et al., 2009). All modelling parameters are summarized in Table 2.2. Rupture is initiated by prescribing a lower static coefficient of friction inside a predefined rectangular patch surrounding the hypocentre. In that way, the initial shear stress is greater than the yield stress and rupture initiates immediately after the simulation starts. Linear-slip weakening friction is assumed. The asymmetric unstructured tetrahedral mesh of the here presented solution of SeisSol exhibits a minimal element edge length of 250 m across the fault surface; its volume discretization is coarsened by a gradation rate of 1.06 with increasing fault distance (Simmetrix Inc., 2017).

In Fig. 2.5 we show the overall very good agreement of SeisSol with the solution of FaultMod. We additionally compare our solution with the high-order spectral element (SE) method SPECFEM3D (Kaneko et al., 2008), which is based on unstructured hexahedral meshes (Peter et al., 2011) and uses a traction-at-split-nodes approach to incorporate fault dynamics. As in FaultMod, SPECFEM3D damps

Symbol	Parameter	Value
V_p	P-wave velocity	5716 m/s
V_s	S-wave velocity	3300 m/s
ρ	Density	2700 kg/m^3
μ_s	Static friction coefficient	0.7
$\mu_{s,nuc}$	Static friction coefficient (inside nucleation patch)	0.54
μ_d	Dynamic friction coefficient	0.1
D_c	Slip-weakening critical distance	0.5 m
d	Fault depth	0-15000 m
w	Fault width	0-30000 m
c_0	Frictional cohesion	-0.2 MPa
P_f	Fluid pressure	$9.8 \times d$ MPa/m
σ_n^0	Background normal stress	
	($d <$13800 m)	-7.39001 $\times$ d MPa/m
	($d \geq$13800 m)	-14.42798 $\times$ d MPa/m
τ^0	Background shear stress	
	($d <$13800 m)	-0.549847$\cdot\sigma_n^0$
	($d \geq$13800 m)	0.0
A_{nuc}	Nucleation size	3 km $\times$ 3 km
h	Smallest element edge length	250 m
p	Polynomial degree in space and time	4
c_{plast}	Plastic cohesion	5.0 MPa
ν	Bulk friction	0.85
T_v	Viscoplastic relaxation time	0.03 s

Table 2.2: Simulation parameters for SCEC benchmarks TPV12 (purely elastic) and TPV13 (with plasticity). The additional parametrization of viscoplasticity in TPV13 is denoted at the bottom.

spurious oscillations by a thin layer of 1 or 2 Kelvin-Voigt elements surrounding the fault (Galvez et al., 2014). The fault discretization is 100 m for the FaultMod and 100 m for the SPECFEM3D solution, the latter with additional four sub-elemental integration points in each dimension.

Slip rate, shear stress, and normal stress (Fig. 2.5) are in equally good agreement. However, both, FaultMod and SPECFEM3D solutions, exhibit high-frequency oscillations most visible in the (relatively small) normal stress amplitudes, despite the implemented damping. Furthermore, we notice a small time shift in the arrival of the peak amplitudes for all three values of both high-order methods compared to FaultMod. Rupture arrival time is a sensitive indicator of numerical precision (Day et al., 2005). Both, SeisSol and SPECFEM3D, reach sub-element resolution of the nucleation patch causing a slightly faster rupture initiation in comparison to the low order method FaultMod.

2.4 Mesh and polynomial degree refinement study

The comparison of numerical methods in well-defined benchmark problems is a commonly used approach to verify dynamic (spontaneous) earthquake rupture implementations (e.g., Harris et al., 2011; Pelties et al., 2014). However, the convergence of the numerical solution with increasing mesh resolution (h-refinement) and increasing polynomial degree (p-refinement) cannot be guaranteed in such a manner.

A formal convergence analysis requires the analytical solution of the underlying problem. Analytical solutions to dynamic rupture problems have been proposed for a 2D self-similar crack (Kostrov,

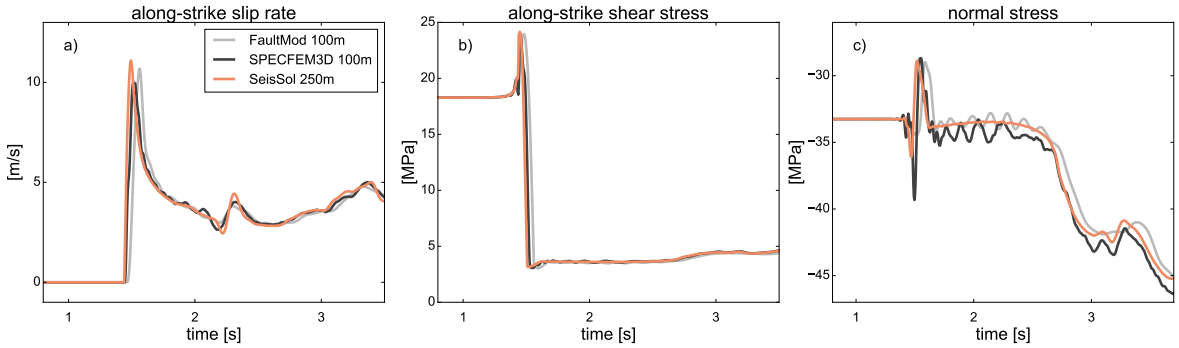

Figure 2.5: a) Along-strike slip rate, b) shear and c) normal stress at a fault location 1.5 km down-dip aligned with the hypocentre for benchmark TPV13. The ADER-DG SeisSol solution (using the QP approach) is shown in black, the FaultMod solution in grey, the SPECFEM3D solution in orange.

1964) or self-similar pulse (Nielsen and Madariaga, 2003), but are not available for typical application-based dynamic rupture simulations. Hence, a high-resolution reference solution which is invariant under additional discretization and polynomial refinement is commonly defined as stand-in for the exact solution (e.g., Day et al., 2005; Rojas et al., 2008; Pelties et al., 2012). In this manner, we provide helpful guidelines for the required fault resolution guaranteeing accurate on-fault physical results in the framework of dynamic rupture problems. In the following, the terms convergence and convergence rate refer to the given reference solution. We critically discuss this approach in Sec. 2.6.2.

Few refinement studies of this kind for dynamic rupture simulations have been presented in two dimensions (Rojas et al., 2008; Kaneko et al., 2008; Rojas et al., 2009; De la Puente et al., 2009; Huang and Ampuero, 2011) and three dimensions (Day et al., 2005; Pelties et al., 2012; Tago et al., 2012). All of them were based on idealised setups assuming homogeneous initial stresses, purely elastic material behaviour, and abrupt nucleation procedures. However, state-of-the-art dynamic rupture simulations emulate real fault properties using depth-dependent initial stresses (e.g., Ma and Andrews, 2010; Kozdon and Dunham, 2013; Heinecke et al., 2014), off-fault plasticity (e.g., Roten et al., 2015, 2016), and smoother nucleation procedures (e.g., Bizzarri, 2010; Roten et al., 2017).

Such models challenge convergence studies: For example, the assignment of initial fault stress and strength, as well as of the initial bulk stress, depends on the underlying discretization. Mesh refinement results in a higher sampling of the initial fields and smaller discontinuities in between neighbouring elements. Furthermore, the onset of rupture may be affected even by slight variations in the sampling of the nucleation conditions (Galis et al., 2014).

Here, we present an in-depth *h*- and *p*-refinement study of a three-dimensional dynamic rupture setup including now common modelling complexities: We combine elastic as well as plastic material response, following both plasticity approaches presented in Sec. 2.2.3, with depth-dependent initial stress conditions. To ensure consistency of the initial stress tensor in the bulk and on the fault, we employ a nucleation procedure smooth in space and time in contrast to over-stressed nucleation patches employed for previous convergence studies.

This section aims to provide hands-on guidelines in terms of the required resolution to ensure the accurate resolution of on-fault rupture dynamics of realistic, 3D dynamic rupture applications. To this end, we numerically investigate the convergence of key dynamic rupture parameters with mesh refinement and increasing polynomial order towards a reference solution. Furthermore, we analyse the size of the cohesive zone as the inherent length scale determining accurate resolution.

2.4.1 Models and procedure

We measure the root-mean square (RMS) error of dynamic rupture characteristics in comparison to a reference solution. The reference solution is generated using a small fault discretization h and high polynomial degree p (e.g., Day et al., 2005; Pelties et al., 2012). We ensure that the reference solution does not change with further mesh or polynomial refinement, i.e. accurately resolves the cohesive zone width as described in the next section.

In particular, we analyse rupture arrival time, peak slip rate amplitude, peak slip rate time, and the total amount of slip (final slip) on the fault surface. The numerical accuracy in resolving time-dependent parameters is particularly important for complex source dynamics involving rupture jumps and branching. Final slip represents an integrated value determined by rupture arrival time, peak slip rate amplitude and time, and rise time across the fault.

We base the following refinement study on SCEC benchmark problems TPV26 (elastic) and TPV27 (plastic) (see Sec. 2.3.1). To reduce computational cost we shorten the simulation time to 6.3 s and shrink the fault surface to 21 km $\times$ 30 km. The hypocentre is shifted to the centre of the new fault domain (at depth of 10.5 km) and we slightly decrease the size of the circular nucleation patch (r_{crit} =3.5 km) to account for the smaller fault area. All remaining modelling parameters, specifically the depth-dependence of initial stresses, are equivalent to Table 2.1.

We perform simulations with increasing polynomial degree of basis functions from $p = 2$ to $p = 5$ and decreasing fault mesh discretization from $h = 1061$ m to $h = 106$ m. The high-resolution reference solution is employing $p = 5$ and $h = 71$ m.

To quantify the accuracy of our results with respect to the reference solution we calculate the RMS errors at a total number of 362 on-fault locations ("receivers"). The RMS error is then normalised by the mean over all receivers of the reference solution, ensuring comparability with previous studies (Day et al., 2005; Pelties et al., 2012). The receivers are located at all fault grid points of the coarsest mesh ($h = 1061$ m). For our analysis, we excluded the nucleation patch, receivers within 1 km from the fault edges, and areas that rupture does not reach within the simulated time. For each simulation, the same points are evaluated independently of the mesh discretization and polynomial degree.

We emphasize, that point-wise measures are prone to large variations for any Galerkin type method since the equations are solved in an integral (weak) sense, with the largest variations being expected at the mesh vertices. Thus, our method is analysing the 'worst-case' solution evaluation. However, point-wise evaluation of rupture dynamics characteristics is commonly used for the interpretation of simulations.

We generate a set of fully regular triangles discretizing the fault surface (except the circular nucleation patch). This is achieved by first dividing the fault surface into quadrilateral elements of edge lengths $h/\sqrt{2} = 750$ m, 375 m, 250 m, 125 m, 75 m and 50 m. Then, each quadrilateral is subdivided into two triangles, resulting in fault discretizations of edge lengths $h = 1061$ m, 530 m, 354 m, 177 m, 106 m and 71 m. Thus, the mesh vertices of the coarsest discretization are a subset of the grid points of the finest discretization. In contrast, the volume mesh is fully unstructured, coarsened by a factor of 10% away from the fault up to a maximum edge length of $10h$. The regular fault discretization does not affect the generality of the results but facilitates evaluating exactly the same receiver locations (Pelties et al., 2012).

All meshes for the refinement tests are generated with the open-source software gmsh (Geuzaine and Remacle, 2009). All simulations of this section were conducted using SeisSol (`https://github.com/SeisSol`) with git hash `72596ff`.

2.4.2 Resolving the cohesive zone in 3D simulations with heterogeneous fault initial conditions

Dynamic rupture simulations have to accurately resolve a problem inherent length-scale, the cohesive zone width Λ which spans the part of the fault across which shear stress decreases from its static to its dynamic value. The width of the cohesive zone is decreasing with increasing rupture velocity (e.g., Day et al., 2005; Duan and Day, 2008).

We present a detailed analysis of the dynamic evolution of the cohesive zone width, along-strike and up-dip, under heterogeneous initial stress, and with and without off-fault plasticity in Sec. 2.C. We find, that the cohesive zone width varies considerably across the fault in dependence of the rupture speed which is determined by the depth-dependent initial stress, frictional properties, and propagation distance. Absolute rupture speed reaches a maximum of 3250 m/s in the purely elastic reference simulation, whereas rupture speed is limited to 3050 m/s in the reference simulation with plasticity. Both values are well below the theoretical terminal speed (p-wave speed) for 3D mixed mode rupture propagation (Bizzarri and Das, 2012) and below the s-wave speed of 3464 m/s. Specifically close to the free surface, the increase of cohesion rising frictional resistance, and the decrease of initial stresses result in very low rupture speeds leading to large cohesive zone widths. In general, off-fault plasticity leads to a distinctively larger cohesive zone width than under comparable purely elastic conditions since rupture propagates at lower speeds.

The minimum cohesive zone width for both setups, purely elastic and plastic material behaviour, is located at the largest distance from the hypocentre along-strike at a depth of 14.5 km where the absolute value of the depth-dependent initial stresses are highest. For the purely elastic case, the minimum cohesive zone with Λ^e_{min} is 162 m, which is considerably smaller than in previous convergence setups (Λ_{min} = 325 m in Day et al. (2005)). In the simulation with off-fault plasticity, this doubles to a width of Λ^p_{min} = 325 m. Consistent with previous studies (Day et al., 2005; Pelties et al., 2012; Tago et al., 2012), we also evaluate the median value of the cohesive zone width over all fault-receivers: $\bar{\Lambda}^e$ is 583 m and $\bar{\Lambda}^p$ is 722 m.

We follow Day et al. (2005) in defining a solution to be sufficiently close to the reference solution once the RMS errors reached the following thresholds: lower than 0.2 % for rupture arrival time, lower than 7 % for peak slip rate and lower than 1 % for final slip. In order to accurately resolve dynamic rupture characteristics (i.e. fulfilling the conditions described above), we determine the minimum required mesh resolution at the fault for a given polynomial degree p. The such defined mesh resolution may differ for different numerical methods. Assessing this resolution requires careful analysis in form of self-consistent refinement tests (see also Sec. 2.6).

The number of elements per median cohesive zone width are denoted by N_c (e.g., Day et al., 2005). Since the cohesive zone width changes dynamically with rupture speed, also N_c varies across the fault plane for a given discretization.

In the purely elastic convergence setup, we find N_c varying between 0.55 and 5.5 elements per median cohesive zone width $\bar{\Lambda}$ for discretizations between 1061 m and 106 m. In the simulations including plasticity, N_c falls in between 0.69 and 6.91 elements.

SeisSol resolves shear and normal stress at the fault at $(p+2)^2$ Gaussian quadrature points inside each fault triangle. Thus, the longest edge length h is itself discretized by $p+1$ additional points (see Fig. 2.C.1 in Sec. 2.C). As a result, the effective fault discretization is smaller than denoted by the grid spacing h and a higher resolution than denoted by N_c is achieved. We additionally introduce the number of sub-element points per median cohesive zone width $N_c^{sub} = N_c(p+1)$. For example, in a p = 5 simulation with N_c = 0.55 elements, the median cohesive zone width is effectively resolved by N_c^{sub} = 3.3 points. However, we will still present N_c as guidance to choose the corresponding required

h (m)	p	Rupture Arrival Time (%)	Final Slip (%)	Peak Slip Rate Time (%)	Peak Slip Rate (%)
1061	2	1.42	3.39	1.79	47.03
	3	0.60	2.87	0.89	35.10
	4	0.34	2.12	0.52	27.83
	5	0.24	2.03	0.45	22.58
530	2	0.44	1.56	0.64	30.63
	3	0.25	1.32	0.28	21.32
	4	0.18	0.99	0.24	16.04
	5	0.12	0.94	0.23	12.23
354	2	0.26	1.13	0.35	23.44
	3	0.15	0.95	0.18	15.54
	4	0.09	0.74	0.10	10.22
	5	0.08	0.69	0.11	6.57
212	2	0.12	0.63	0.16	15.61
	3	0.06	0.54	0.07	8.50
	4	0.04	0.41	0.07	4.48
	5	0.04	0.40	0.05	2.57
106	2	0.04	0.32	0.05	6.64
	3	0.03	0.28	0.03	2.60
	4	0.02	0.22	0.03	1.38
	5	0.02	0.21	0.03	1.04
71	5	3.90 s	1.67 m	4.03 s	2.98 m/s

Table 2.3: RMS errors of elastic refinement tests with varying discretization h and polynomial degree p. The bottom line denotes the mean over all receivers of the reference solution.

minimum mesh discretization. This approach also allows a direct comparison to low-order methods (e.g., Day et al., 2005).

The minimum required fault mesh resolution h for each polynomial degree p based on purely elastic convergence tests and including plastic yielding is reported in Sec. 2.4.3 and Sec. 2.4.4, respectively.

2.4.3 Convergence of 3D elastic dynamic rupture simulations with heterogeneous initial conditions

Absolute errors of on-fault measurements

The absolute RMS errors measured in the elastic refinement study are summarized in Table 2.3 and visualized in Fig. 2.6. The errors of the rupture arrival time, the peak slip rate time, the final slip, and the peak slip rate with respect to the reference solution are globally decreasing with mesh refinement and increasing polynomial degree. The smooth convergence of on-fault quantities towards the reference solution illustrates the robustness of the numerical method in handling heterogeneous initial conditions.

We note, that the minimum measured RMS error of rupture arrival time is only 0.02 % (h = 106 m and p = 4, 5). Even for the coarsest discretization and lowest polynomial degree (h = 1061 m and p = 2), the solution for rupture arrival time exhibits an error below 1.5% with respect to the reference solution. Equally low RMS errors can be found for peak slip rate time. In contrast, the RMS errors measured for the peak slip rate reach up to 47 % for the same polynomial degree and fault resolution. The RMS errors for final slip ranges between 3.39% (p = 2, h = 1061 m) and 0.21% (p = 5, h = 106 m).

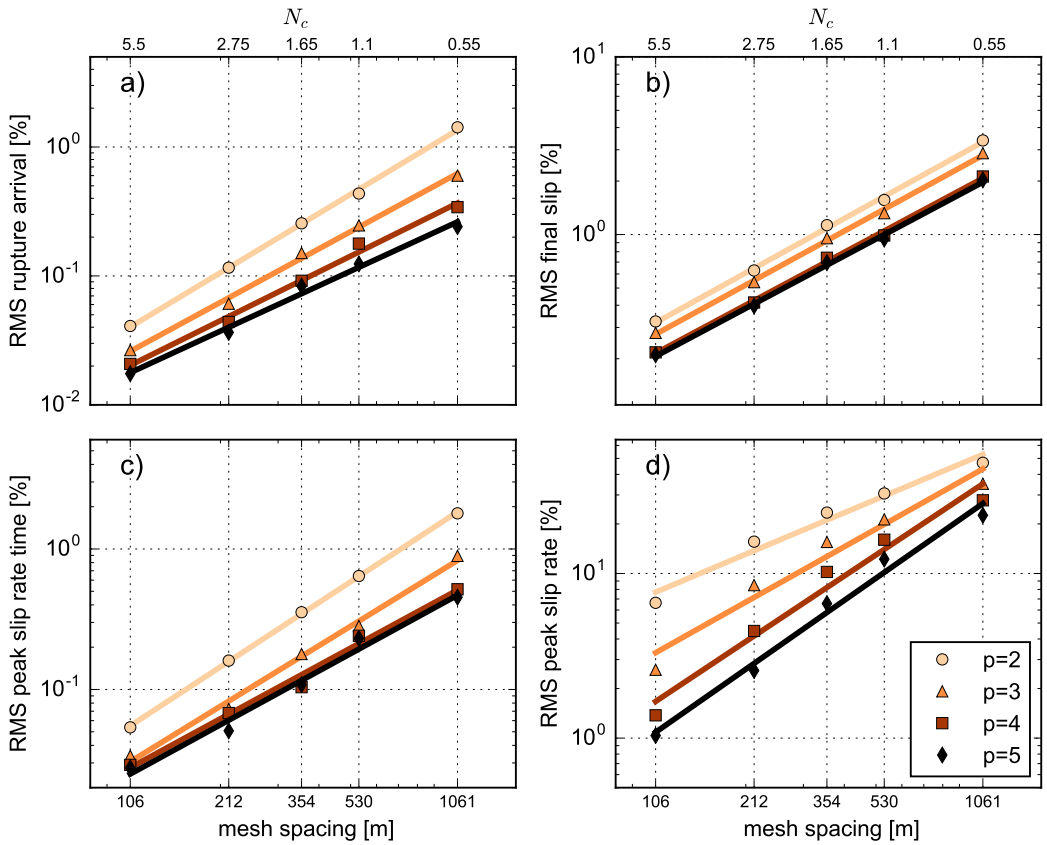

Figure 2.6: Refinement study results for purely elastic material behaviour and heterogeneous initial conditions. RMS errors with respect to the reference solution are shown for a) rupture arrival time, b) final slip, c) peak slip rate time, and d) peak slip rate. Markers denote the RMS errors in %, normalised by the mean over all receivers of the reference solution (h = 71 m, p = 5). Different colours and markers represent varying polynomial degrees. N_c denotes the number of elements per median cohesive zone for a given fault mesh spacing. The solid lines represent least square fits.

As an integrated value the RMS errors for final slip reflects the low RMS errors of the time-dependent quantities in conjuncture with the higher RMS errors of the peak slip rate.

Coarse (h- and p-) resolution highly impacts peak slip rate, which directly affects ground motion assessment. This suggests, that the measured peak value of slip rate is very sensitive to the sampling of the depth-dependent initial conditions and hence to the resolution of the fault. In distinction, the overall lower RMS errors of rupture arrival time, peak slip rate time, and final slip in our setup indicate that temporal and integrated fault characteristics are more robust: lower resolution of the cohesive zone still results in acceptable small RMS errors.

Using polynomial degrees p = 2, 3, solutions are sufficiently close to the reference solution for a minimum resolution of h = 106 m which corresponds to N_c = 5.5 (N_c^{min} = 1.53, N_c^{sub} = 16.5-22.0). For p = 4 a resolution higher than 212 m (N_c = 2.75, N_c^{min} = 0.76, N_c^{sub} = 13.75) and for p = 5 a resolution higher than 354 m (N_c = 1.65, N_c^{min} = 0.46, N_c^{sub} = 9.9) result in sufficiently small RMS errors. We note, that the convergence criteria for rupture arrival time and final slip are met already at much coarser discretizations. However, the RMS error of the peak slip rate is still too high for fulfilling all conditions for convergence towards the reference solution. In general we state, that the median cohesive zone width $\bar{\Lambda}$ needs to be resolved by approximately 5-6 (p = 2,3), 2-3 (p = 4) and

	p	Rupture Arrival Time	Final Slip	Peak Slip Rate Time	Peak Slip Rate
elastic	2	1.53	1.02	1.52	0.84
	3	1.38	1.01	1.43	1.12
	4	1.26	0.98	1.26	1.32
	5	1.17	0.98	1.27	1.39
plastic (QP)	2	1.67	1.13	1.74	0.68
	3	1.40	1.05	1.37	0.83
	4	1.33	1.01	1.06	0.91
	5	1.23	0.99	1.01	0.92
plastic (NB)	2	1.57	1.31	1.70	0.73
	3	1.16	1.07	1.26	0.85
	4	1.31	1.03	1.04	0.92
	5	1.28	1.01	1.04	0.93

Table 2.4: RMS error convergence rates with respect to the reference solution for varying polynomial degree p for the refinement studies with elasticity and with plasticity.

1-2 ($p = 5$) elements, or 22 ($p = 2$), 16.5 ($p = 3$), 13.75 ($p = 4$) and 9.9 ($p = 5$) sub-element points for purely elastic simulations featuring depth-dependent initial stress conditions.

Low-order convergence rates of on-fault measurements

The corresponding on-fault convergence rates are defined as the slope of a least square fit to the RMS values and are given in Table 2.4. The reported rates are defined with respect to the pre-defined reference solution and are therefore only representative for formal convergence of the numerical scheme if the reference solution is sufficiently close to the exact solution (which is unknown). For the following discussion, supplemented by the cohesive zone size analysis in Sec. 2.C, we assume that our high-resolution reference solution fulfils this requirement. Even though we observe clear h- and p-convergence towards the reference solution, the following specific characteristics of the convergence rates require special consideration:

Overall, no spectral convergence is achieved for on-fault dynamic rupture quantities. In particular, the reported convergence rates, ranging between 1.53 and 0.84, indicate that there is no high-order ($\geq$ 2) convergence for any of the dynamic rupture observables. Additionally, only peak slip rate exhibits increasing rates with higher polynomial order. Convergence rates for rupture arrival time, peak slip rate time, and slip do not clearly increase with increasing p.

Low-order (at most quadratic) convergence rates of dynamic rupture on-fault parameters have been previously reported (Rojas et al., 2008; Kaneko et al., 2008; Rojas et al., 2009; Pelties et al., 2012). Rojas et al. (2008), Kaneko et al. (2008) and Pelties et al. (2012) show that on-fault convergence rates achieved by high-order ("spectral") numerical methods do not exceed the reported rates of second-order methods (Day et al., 2005) for this type of refinement study.

A notable exception poses the convergence studies presented in Kozdon and Dunham (2013), O'Reilly et al. (2015), Duru and Dunham (2016), and Erickson et al. (2017): High-order convergence is achieved with respect to an a priori formulated analytical solution of a related but simplified problem (method of manufactured solutions (MMS)). We discuss a potential general limitation of convergence rates for dynamic rupture problems with respect to mathematical and numerical theory in Sec. 2.6.2.

2.4.4 Convergence of 3D dynamic rupture simulations with off-fault plasticity and heterogeneous initial conditions

We extend the elastic refinement study to account for plastic energy dissipation. Both of the implementation schemes presented in Sec. 2.2.3 are analysed. The RMS errors of the quadrature points (QP) based implementation approach are summarized in Table 2.5 and visualized in Fig. 2.7. The RMS errors of the nodal basis (NB) based implementation approach is given in Table 2.6 and Fig. 2.8. On-fault convergence rates (slopes) with respect to the reference solution are listed in Table 2.4.

For both approaches and all measured quantities, we observe h- and $p-$convergence. The observed smooth convergence of all measured on-fault quantities towards the reference solution illustrates the robustness of the numerical method while stresses are adjusted due to plastic yielding.

The RMS errors of rupture arrival time and peak slip rate time become very low (0.02 % and 0.04%, respectively) at high resolutions for both plasticity implementations. Overall, RMS errors do not exceed 10% even at the coarsest discretization and smallest polynomial degree under consideration. Notable is, that polynomial degrees 4 and 5 yield in general very similar absolute errors for both approaches, specifically at higher resolutions.

The required discretization to accurately resolve the cohesive zone width with plasticity differs to the purely elastic case. For the QP approach our results are sufficiently close to the reference solution at a minimum mesh resolution of h = 212 m (N_c = 3.41, N_c^{min} = 1.53, N_c^{sub} = 10.23) for polynomial degree p = 2, h = 354 m (N_c = 2.04, N_c^{min} = 0.92, N_c^{sub} = 8.16-10.2) for p = 3, 4, and approximately h = 530 m (N_c = 1.36, N_c^{min} = 0.61, N_c^{sub} = 8.16) for p = 5. The NB approach requires similar minimum on-fault resolutions, besides for p = 3 which requires a higher resolution of h = 212 m (N_c = 3.41, N_c^{min} = 1.53, N_c^{sub} = 13.64) than the corresponding polynomial degree in the QP approach.

Both plasticity implementations show non-spectral convergence for all on-fault quantities with respect to the reference solution, similar to the elastic refinement study in Sec. 2.4.3 (see also Sec. 2.6.2).

Accuracy vs. efficiency for off-fault plasticity implementation schemes

We shed light on the trade-off between accuracy and efficiency based on the refinement study of the QP and NB plasticity implementations. We aim to enable conclusions on a preferable scheme for a given dynamic rupture problem at hand. The reference solutions of both schemes (last row in Table 2.5 and Table 2.6), give near-identical results in terms of key dynamic rupture characteristics. As a consequence, the normalised RMS differences are well comparable.

The RMS errors of all on-fault quantities are in general smaller using the QP approach than the NB implementation. The largest difference can be found for p = 2 and h = 1061 m. The RMS error for rupture arrival is here 23% larger in the NB approach than in the QP approach (3.54% vs. 2.01%) since the QP approach approximates the non-linearity more accurately with respect to the L^2 norm which is in particular pronounced for low fault resolutions and low polynomial degrees. RMS errors for $p > 3$ and for a median cohesive zone width resolution (N_c) of more than 2.04 elements, are near equivalent for both plasticity implementations.

The convergence rates with respect to the reference solution reported in Table 2.4 are similar for all quantities in both approaches, in particular for polynomial degrees p = 4 and 5. The convergence rates of the time-dependent quantities decrease with increasing polynomial degree p. The slope of the least square fit to the RMS values of the peak slip rate is increasing with increasing p, while it saturates for both implementations at 1.0 for the final slip rate.

h (m)	p	Rupture Arrival Time (%)	Final Slip (%)	Peak Slip Rate Time (%)	Peak Slip Rate (%)
1061	2	2.01	4.94	2.48	10.34
	3	0.65	3.44	0.85	9.56
	4	0.38	2.45	0.46	9.12
	5	0.29	2.26	0.40	8.46
530	2	0.40	1.88	0.57	6.29
	3	0.20	1.52	0.27	6.89
	4	0.15	1.10	0.16	5.29
	5	0.13	1.03	0.14	4.06
354	2	0.22	1.33	0.28	5.63
	3	0.12	1.07	0.14	4.96
	4	0.09	0.81	0.11	3.66
	5	0.07	0.75	0.09	2.91
212	2	0.10	0.71	0.12	3.75
	3	0.06	0.59	0.08	2.80
	4	0.04	0.44	0.07	2.15
	5	0.03	0.42	0.06	1.77
106	2	0.04	0.36	0.04	2.06
	3	0.03	0.31	0.04	1.49
	4	0.02	0.23	0.04	1.16
	5	0.02	0.23	0.04	1.00
71	5	4.18 s	1.50 m	4.36 s	1.98 m/s

Table 2.5: RMS errors of QP plasticity refinement tests with varying discretization h and polynomial degree p. The bottom line denotes the mean over all receivers of the reference solution.

h (m)	p	Rupture Arrival Time (%)	Final Slip (%)	Peak Slip Rate Time (%)	Peak Slip Rate (%)
1061	2	3.54	8.03	3.92	11.26
	3	0.64	3.70	0.83	10.01
	4	0.36	2.46	0.40	9.24
	5	0.31	2.32	0.42	8.58
530	2	0.45	2.09	0.61	6.94
	3	0.28	1.57	0.33	6.89
	4	0.27	1.17	0.22	5.51
	5	0.22	1.08	0.17	4.16
354	2	0.32	1.42	0.35	5.83
	3	0.25	1.14	0.21	5.13
	4	0.16	0.86	0.14	3.71
	5	0.12	0.77	0.11	2.91
212	2	0.19	0.75	0.18	3.84
	3	0.13	0.61	0.12	2.81
	4	0.07	0.45	0.08	2.15
	5	0.05	0.42	0.06	1.76
106	2	0.07	0.36	0.07	2.06
	3	0.04	0.31	0.04	1.49
	4	0.02	0.24	0.04	1.17
	5	0.02	0.23	0.04	1.00
71	5	4.18 s	1.51 m	4.35 s	1.98 m/s

Table 2.6: RMS errors of NB plasticity refinement tests with varying discretization h and polynomial degree p. The bottom line denotes the mean over all receivers of the reference solution.

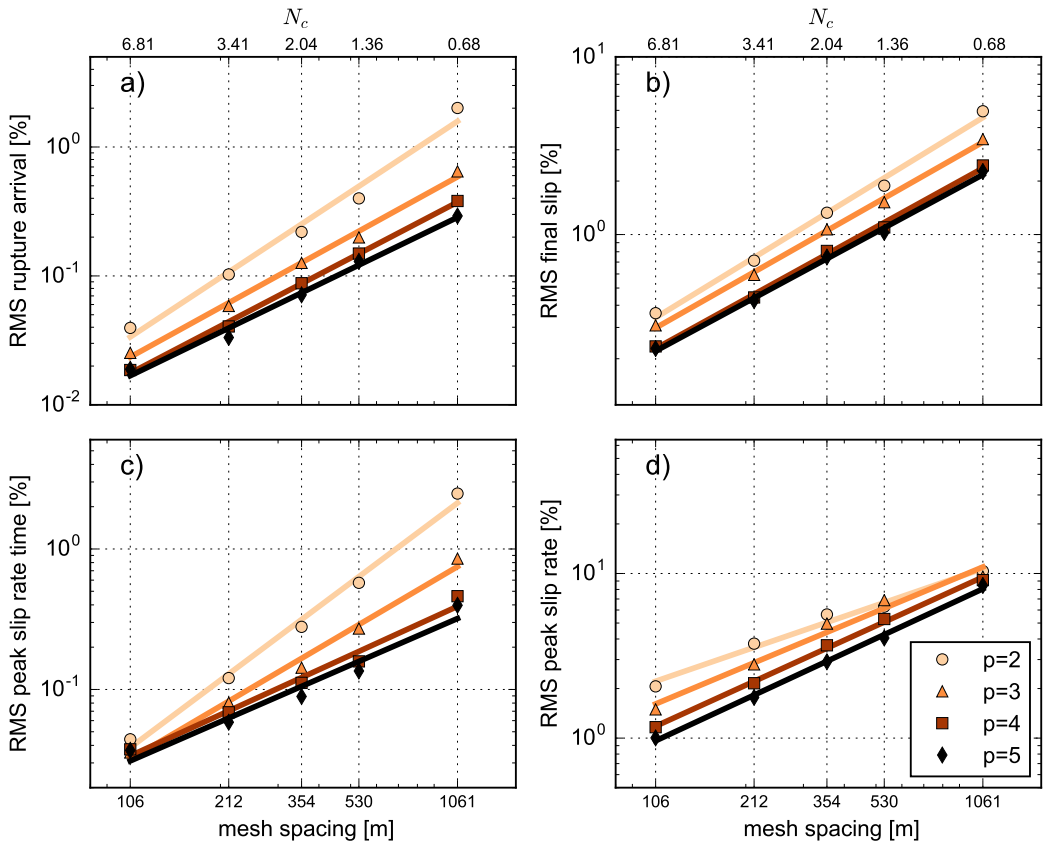

Figure 2.7: Refinement study results for plasticity implemented via the quadrature points (QP) approach. RMS errors with respect to the reference solution are shown for a) rupture arrival time, b) final slip, c) peak slip rate time, and d) peak slip rate. Markers denote the RMS error in %, normalised by the mean over all receivers of the reference solution (h=71 m, p = 5). Different colours and markers represent varying polynomial degrees. N_c denotes the number of elements per median cohesive zone for a given mesh spacing. The solid lines represent least square fits.

In terms of computational costs, the QP plasticity refinement study simulations are 24-79 % more expensive than the corresponding purely elastic simulations, depending on polynomial degree p and fault discretization length h. The NB plasticity approach is computationally distinctively less expensive, resulting in an increase of only 4.5-13% compared to the corresponding elastic models.

We conclude, that it is beneficial to use the QP plasticity approach for low mesh resolutions ($N_c <$ 1.36) and low polynomial degree ($p = 2$). In this case, it yields higher accuracy of on-fault dynamics. However, in all other cases, the NB plasticity approach pays off, i.e. is computational less expensive yielding comparably small RMS errors.

Effect of off-fault plasticity on dynamic rupture convergence

Fig. 2.9 compares slip rate over time for varying mesh discretizations and polynomial degrees for the refinement setups with elasticity and the two plasticity implementations. The figure highlights how recorded slip rates vary distinctively in terms of timing, peak, and encapsulated slip.

Time-dependent RMS errors, such as rupture arrival time and peak slip rate time, are significantly larger for coarse mesh discretizations (h = 1061 m) and low polynomial degrees (p = 2, 3) for the simulations with plasticity in comparison to the elastic results (Table 2.3, Table 2.5, Table 2.6 and

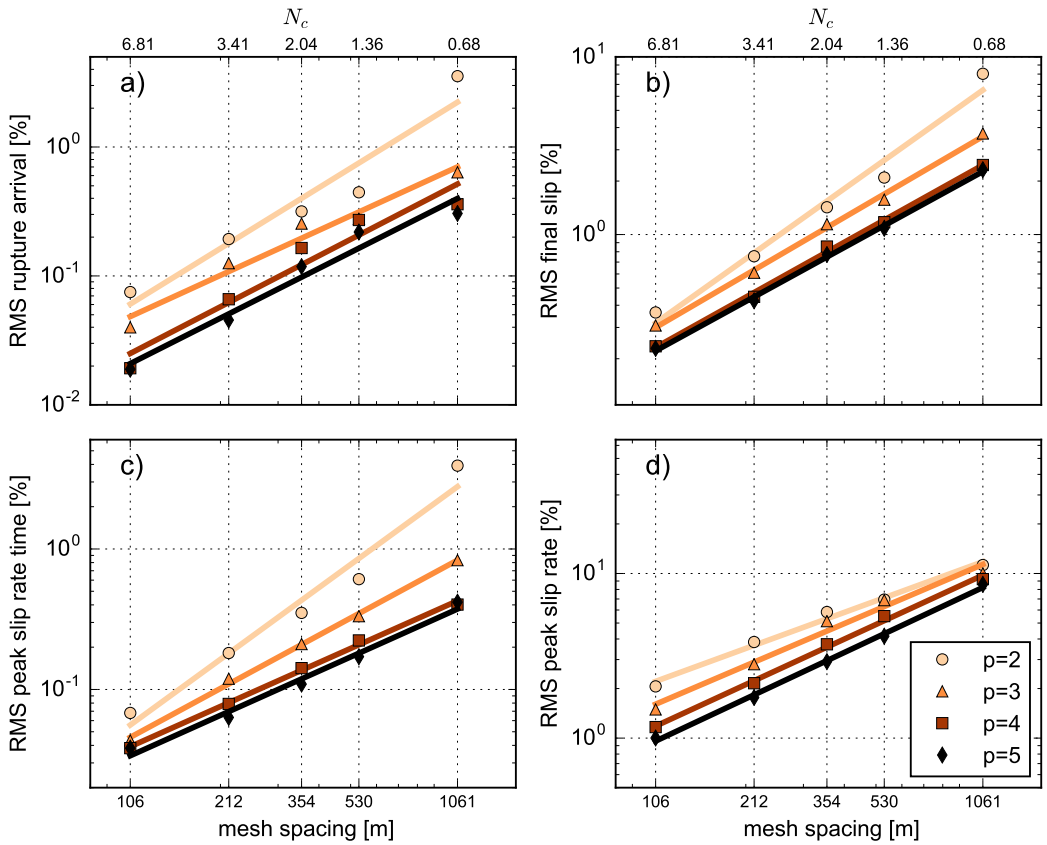

Figure 2.8: Refinement study results for plasticity implemented via the nodal basis (NB) approach. RMS errors with respect to the reference solution are shown for a) rupture arrival time, b) final slip, c) peak slip rate time, and d) peak slip rate. Markers denote the RMS error in %, normalised by the mean over all receivers of the reference solution (h=71 m, p = 5). Different colours and markers represent varying polynomial degrees. N_c denotes the number of elements per median cohesive zone for a given mesh spacing. The solid lines represent least square fits.

visualized in Fig. 2.9). In the models with pure elasticity rupture arrival time is already very consistent with the reference solution even for large on-fault discretization.

Remarkable are the small absolute RMS errors with respect to the reference solution for peak slip rate in the plastically yielding simulations: For all simulations with plasticity, the RMS errors fall in between 1-11 % (Table 2.5, Table 2.6) whereas the RMS error in the elastic case reaches up to 47 % (Table 2.3). Fig. 2.9 exemplarily visualizes the high variation of peak slip rate in the elastic case (up to 20 %) while differences with plasticity are below 7% even for the coarsest resolution.

With plasticity, rupture speed is decreased by off-fault energy absorption compared to elastic settings. The cohesive zone width does not shrink as pronouncedly as in elastic simulations with propagation along-strike (see Sec. 2.C and (Andrews, 2005)). As a result, the median cohesive zone width $\bar{\Lambda}$ is larger by up to a factor of 2 in the models with plastic yielding . Thus, $\bar{\Lambda}$ is naturally better resolved in the simulations with plasticity than in elastic models at comparable mesh discretization h and polynomial degree p.

Analysing the median cohesive zone width resolution N_c, which is independent of Λ, we find that less elements per cohesive zone width are required with plasticity to gain comparably small RMS errors of peak slip rate. This parameter is the most sensitive dynamic rupture characteristic in our

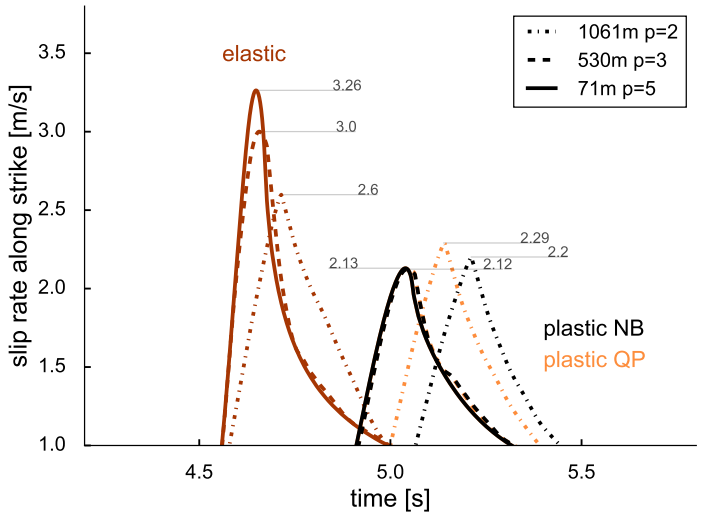

Figure 2.9: Exemplary slip rate measurements in the elastic (red) and plastic (orange QP approach, black NB approach) refinement tests. The time series are recorded at 11250 m along-strike and at 7500 m depth (location visualized by a triangle in Fig. 2.C.1 in Sec. 2.C). Three different mesh discretizations and polynomial degrees are marked by different line styles. Numbers indicate the peak slip rate of the corresponding curve. The dashed (530 m, $p = 3$) and solid lines (71 m, $p = 5$) align almost perfectly for both plasticity implementations.

analysis. Smaller RMS errors for peak slip rate in the models including plasticity can therefore be explained by a better resolution of Λ, plus a general regularizing effect of plasticity (smoother reference solution).

In contrast, we observe larger RMS errors for the time-dependent quantities (rupture arrival time, peak slip rate time) with plasticity than at equivalent N_c in the elastic case. This suggests, that time-dependent measurements are considerably impacted by (mesh-dependent) off-fault plastic energy dissipation. A higher resolution is required to resolve these quantities with the same accuracy as in a comparable elastic simulation.

In summary, the overall minimum required resolution of the cohesive zone width is 34.4-50% lower with plasticity due to the lower resolution required for the sensitive peak slip rate.

2.5 Landers fault system scenario with off-fault plasticity

We now aim to demonstrate the specific advantages of the modelling framework for large-scale earthquake simulations including various representations of natural complexity. To this end, a dynamic rupture scenario of the branched fault system hosting the 1992 Mw 7.3 Landers earthquake is presented. We analyse source dynamics at 3D multi-segment curved faults with and without plastic material response in terms of rupture transfers via dynamic triggering ("jumping") and direct branching. Furthermore, we compare peak slip rate, rupture arrival, and total slip distribution.

The Landers earthquake is a prominent example of an earthquake rupturing across a geometrically complex fault network. The cascading event activated at least five fault segments overlapping over approximately 80 km, demonstrating surprising interconnectivity. The Landers event raised awareness of unexpectedly large magnitude earthquakes enabled by rupture transfer mechanisms still not completely understood.

Based on high-quality observational data, the Landers earthquake has been investigated in great detail: Its slip distribution has been inferred from inversion of seismological and geodetic data (e.g., Wald and Heaton, 1994; Cotton and Campillo, 1995; Fialko, 2004b; Xu et al., 2016), as well as from geological perspectives (e.g., Wesnousky, 2006; Madden and Pollard, 2012; Madden et al., 2013) and in dynamic rupture simulations (e.g., Fliss et al., 2005; Peyrat et al., 2001; Aochi and Fukuyama, 2002; Tago et al., 2012). All these studies assume purely elastic behaviour of the material surrounding the fault.

Including off-fault plasticity in dynamic rupture simulations on a single planar fault revealed that the reduction of slip at shallow depth ("shallow slip deficit"), which has been observed in the Landers fault system amongst others (Fialko et al., 2005), can be partially related to near-surface plastic deformation (Kaneko and Fialko, 2011; Roten et al., 2017). Accounting for fault complexity in conjuncture with off-fault plasticity is expected to alter fault dynamics with respect to stress transfer and dynamic triggering of different segments.

We point out, that including off-fault plasticity (using the NB approach) only adds 7% of computational cost compared to a fully elastic production run. In the following, we restrict ourselves to the analysis of on-fault earthquake dynamics. A detailed analysis of induced ground motions and other off-fault observables is beyond the scope of this paper and will be addressed in future work.

2.5.1 Model setup

We base the dynamic rupture scenario on the fully elastic model presented in Heinecke et al. (2014), which has proven excellent scalability on some of the largest supercomputers worldwide. This allows the analysis of high-resolution rupture behaviour at full geometrical complexity directly coupled to seismic wave propagation. The model includes fault traces by Fleming et al. (1998) (white lines in Fig. 2.11) extended to 16 km in depth. The computational mesh accounts for regional topography and a 1D subsurface velocity structure, adapted from Graves and Pitarka (2010).

Previous dynamic rupture simulations of the Landers earthquake have failed to dynamically interconnect all fault segments (Pelties et al., 2012; Tago et al., 2012) or required initial stress or strength heterogeneities, such as principal stress angle rotation or weak step-over faults (e.g., Peyrat et al., 2001; Aochi and Fukuyama, 2002).

We here prescribe lateral homogeneous, but depth-dependent initial stress conditions throughout the modelling domain, in contrast to previous dynamic rupture scenarios assuming varying principal stress angles (e.g., Aochi et al., 2003a; Galvez et al., 2014, 2016). We assume a maximum principal stress orientation of 11 $^{\circ}$ North for the entire fault system, which has been found to optimally reproduce slip in geomechanical modelling (Madden et al., 2013). The lateral homogeneous stress generates a locally heterogeneous stress field due to the geometrical complexity of the fault. The amplitudes of the initial stress components as well as the friction parameters are chosen to match observed macroscopic earthquake characteristics, such as rupture duration and seismic moment, but are laterally homogeneous across the fault system. Stresses are consistent with commonly used dynamic rupture parametrization for strike-slip faults assuming that the axis of the intermediate principal stress is vertical. The amplitude ranges between 0 and 500 MPa, similar to what is assumed in Aochi et al. (2003a).

The parametrization of the linear slip-weakening frictional behaviour is constant across all fault segments. Friction parameters are based on laboratory experiments, assuming a static coefficient close to Byerlee's coefficient and a high stress drop to facilitate rupture transfer. In accordance with Sec. 2.4.1 we nucleate by smoothly enforcing rupture in a patch of radius 3450 m at the inferred hypocentre location (Hauksson et al., 1993).

	Parameter	Value
μ_s	Static coefficient of friction	0.55
μ_d	Dynamic coefficient of friction	0.15
D_c	Critical slip-weakening distance	0.6 m
c_0	Frictional cohesion	2 MPa
h	Smallest fault element edge length	100 m
p	Polynomial degree	3
ν	Bulk friction	0.55
T_v	Viscoplastic relaxation time	0.03s

Table 2.7: Constant on-fault model parameters for the 1992 Landers simulations.

All model parameters which are constant across the faults are summarized in Table 2.7. All depth-dependent initializations including the 1D velocity structure are visualized in Fig. 2.10. No stochastic variations nor asperities at the fault are included. This choice allows us to focus on the first-order effects of fault geometries oriented in a regional background stress field on rupture dynamics and transfers, which have been found to be a dominant factor in previous work (Gabriel and Pelties, 2014).

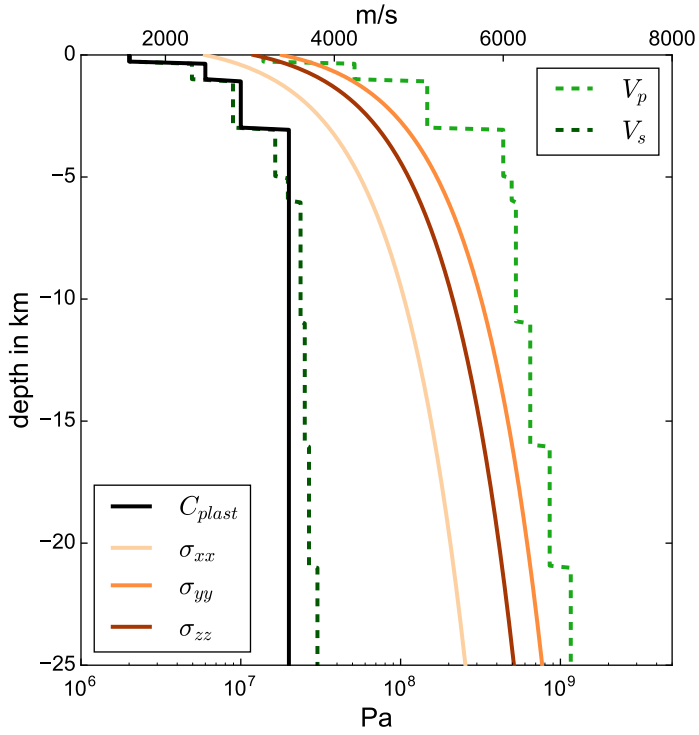

Figure 2.10: Depth dependent model parameters on- and off-fault. Principal initial stress components σ_{xx},σ_{yy},σ_{zz}, one-dimensional velocity structure for S- and P-waves (Graves and Pitarka, 2010) and plastic cohesion adapted from (Roten et al., 2015).

Off-fault plasticity requires a cohesion model of the host rock. Cohesion is material-dependent and altered by damage induced by previous earthquakes. Since these conditions are not well constrained, a wide range of damage levels and rock types may be included in earthquake simulations (Ma and Andrews, 2010; Roten et al., 2014, 2015).

Parameter	elastic	plastic	difference
Max. peak slip rate (m/s)	11.46	9.38	-22.17 %
Max. slip (m)	5.54	6.36	+12.9 %
Moment magnitude M_w	7.396	7.382	-0.19 %

Table 2.8: Comparison of on-fault macroscopic characteristics of the Landers earthquake scenarios with purely elastic and plastic material response.

In the Landers region, we may expect rather high cohesion as the main surficial rock type is granodiorite (Dibblee, 1967). As a consequence, we base our cohesion model on values for undamaged, granite-type rock (Roten et al., 2015). Additionally, cohesion is varied in depth aligned with the major zones of our velocity model (Fig. 2.10).

The cohesive zone width (Λ) varies greatly across the complex fault segments in this model. Therefore, we consider in the following the minimum cohesive zone width (Λ_{min}) instead of its average. We find Λ_{min} = 300 m in the elastic Landers scenario compared to 350 m in the corresponding simulation with plasticity. According to Sec. 2.4, Λ_{min} needs to be resolved by at least 1.5 elements for polynomial order $p = 3$ in the elastic case.

The mesh is discretized by tetrahedral elements constrained by an edge length of 100 m across the fault. We note, that on-fault resolution is increased by a factor of 2 in comparison to the mesh used in Heinecke et al. (2014), while the polynomial degree is decreased from 5 to 3. This discretization results in a sufficiently high resolution of the cohesive zone width (3 elements per Λ_{min} in the elastic case). To improve computational efficiency, the mesh features coarsening away from the fault by a gradation rate of 1.06 (Simmetrix Inc., 2017), which reduces the total mesh size from 191 million elements to 22 million elements.

A fully elastic simulation of a simulated time of 40 s requires 3 hours and 35 minutes on 240 MPI nodes, each using 28 OpenMP threads, on phase 2 of the supercomputer SuperMUC. The simulation's output is written in an asynchronous manner, reserving additional 16 nodes for output only (Rettenberger et al., 2016). 3D wavefield and plastic strain are written every second, 2D fault quantities are written every 0.1 s. Additionally, time series are recorded at 60 on-fault and 380 off-fault measuring points. The simulations with plasticity use the NB approach, which is beneficial for small fault discretizations (here, $h = 100$ m) and high polynomial degrees (here, $p = 3$), as discussed in Sec. 2.4.4. A full production run accounting for off-fault plasticity increases the computational cost by only 7.2% compared to an elastic simulation. The additional cost agrees well with the estimates given in Sec. 2.2.3.

2.5.2 Geometrically complex rupture dynamics with off-fault plasticity

In the following, we discuss the effects of off-fault plasticity on dynamic rupture across a curved, branched, and segmented fault system. We compare the key aspects of a fully elastic Landers earthquake scenario to one with plastic yielding. It is important to note, that off-fault plasticity does not change the closeness to failure across fault segments, as equivalent initial conditions are assigned in both models. Thus, all observed differences in rupture dynamics are caused by the adjustment of stresses around the fault.

Macroscopic source characteristics of both scenarios are compared in Table 2.8. The maximum peak slip rate is overall reduced due to off-fault plastic yielding, whereas maximum slip increases by almost 13%. Remarkably, the moment magnitude is almost identical in both scenarios.

Fig. 2.11 visualizes the accumulated plastic strain surrounding the fault system. Plastic strain accumulates in the vicinity of geometrical complexity, as fault branching points and upon abrupt changes of fault orientation, i.e. when the locally acting fault stresses change direction. Furthermore, plasticity is triggered at fault endings where rupture is not stopping smoothly.

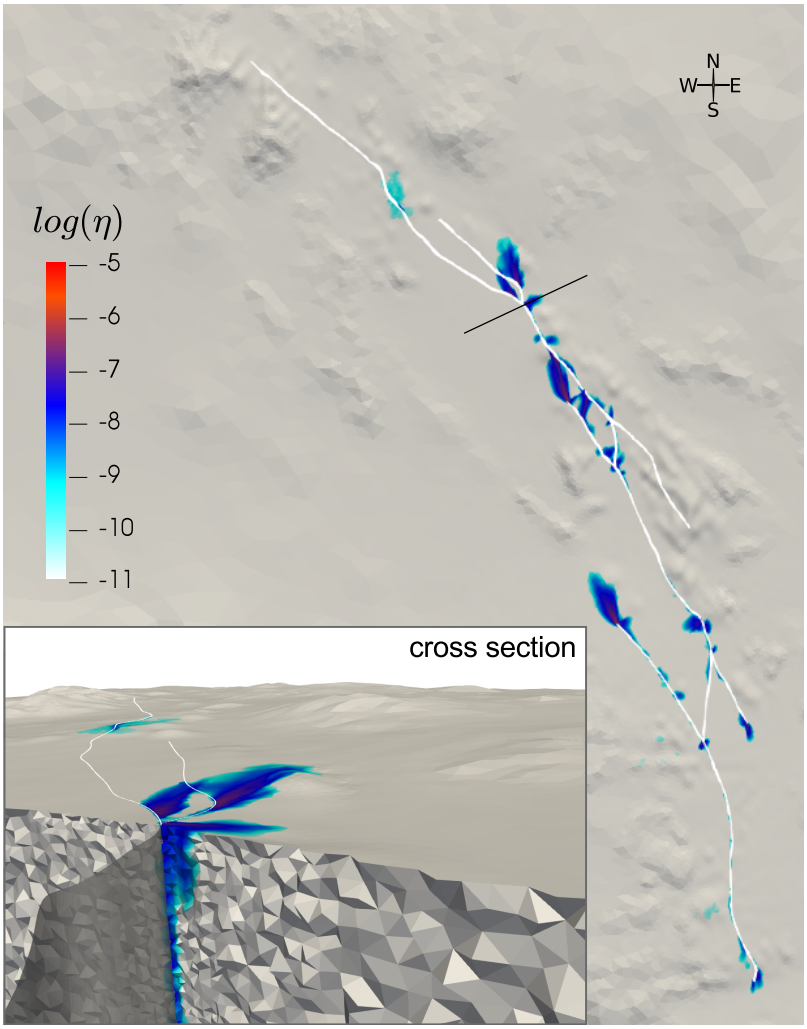

Figure 2.11: Map view of accumulated plastic strain (see Eq. (2.9)) in the Landers fault system scenario (fault traces in white). The inset shows a cross-section at a fault branching point marked by the black line in the main figure.

In the following, we discuss differences of the elastic and plasticity scenario in terms of rupture cascading, slip rates, and slip distribution. Rupture propagation in terms of slip rate across the full fault system is illustrated in Fig. 2.12 for both scenarios. Rupture path and rupture timing are very similar at the first segment, the Johnson Valley fault (JVF), up to 6 s of propagation time.

In both simulations, rupture at the Homestead Valley fault (HVF) is triggered dynamically by waves emitted by the failure of the preceding fault segment. However, fault zone plasticity affects not only the timing of rupture transfer but also its location: In the purely elastic model, we observe rupture transferring from the JVF to HVF after 6.8 s of propagation time. HVF is dynamically triggered (rupture ”jumps”) very close to the branching point with the Landers Kickapoo fault (LKF) (highlighted by a red rectangle in Fig. 2.12 at 7.1 s snapshot, left). In the simulation with plasticity, this rupture

jump is delayed to 7.4 s and shifted to a more distant location on HVF (highlighted by a red rectangle in Fig. 2.12 at 7.9 s, right). After 8 s of simulation time, we observe the evolution of multiple rupture fronts and back propagation of rupture at HVF in both simulations.

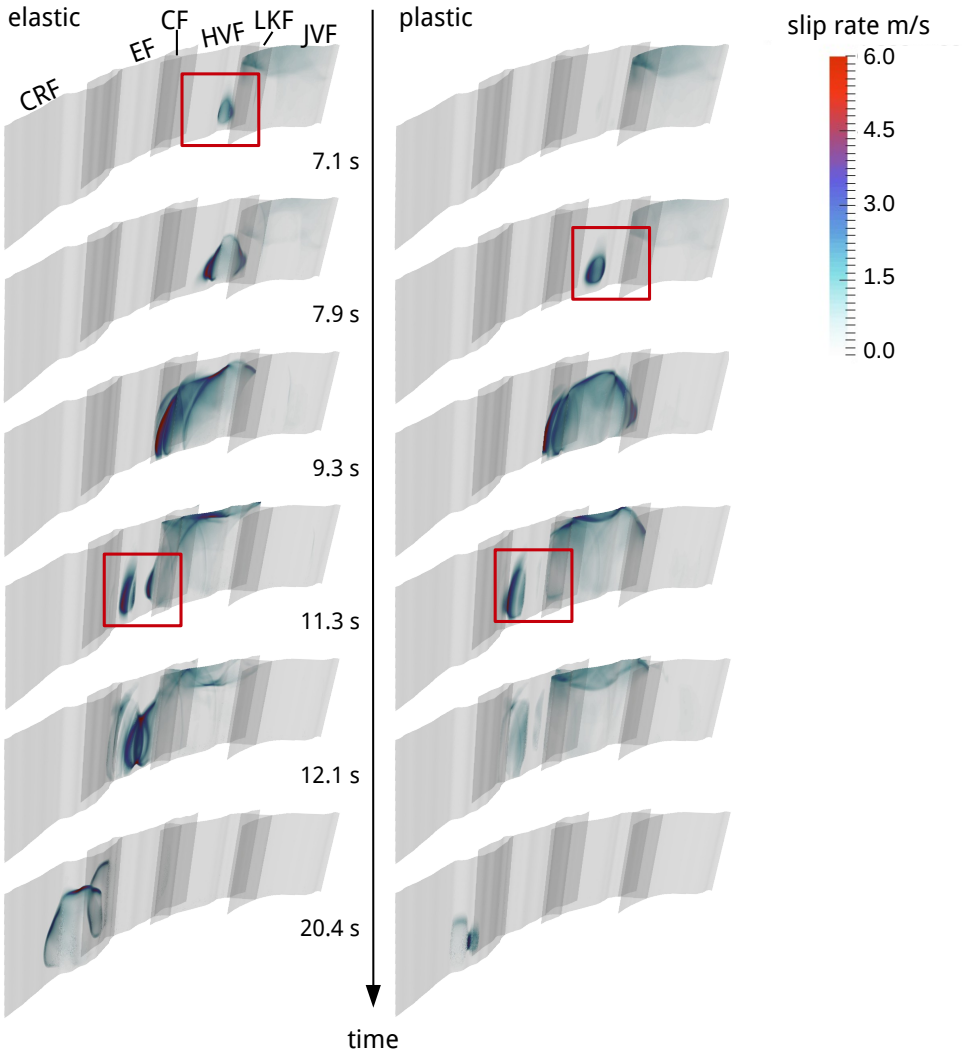

Figure 2.12: Temporal evolution of slip rate across the Landers fault segments (Johnson Valley Fault (JVF), Landers Kickapoo Fault (LKF), Homestead Valley Fault (HVF), the connecting fault segment (CF) between the Emerson Fault (EF) and Camp Rock Fault (CRF)). The purely elastic scenario (left) and the scenario with plastic material response (right) differ in rupture transfer location and mechanisms (dynamic triggering versus branching) and location, marked by red rectangles.

At around 11 s, rupture transfers from the HVF to the Emerson Fault (EF) by different mechanisms: In the elastic simulation rupture is branching directly onto the connecting fault (CF) segment between the HVF and the EF before jumping to the EF (highlighted by a red rectangle in Fig. 2.12 at 11.3 s, left). However, the accumulation of plastic strain in the vicinity of geometrical complexity, such as fault branching points, suppresses direct branching to CF. EF is instead dynamically triggered when we account for off-fault plastic yielding. At the EF, slip rate is considerably reduced due to plastic yielding (see Fig. 2.11) and rupture nearly arrests after 12.1 s.

The last fault segment, the Camp Rock Fault (CRF), is ruptured several seconds later compared to the elastic case. As a result of the plastic energy dissipation around the first segments (see JVF, LKF, and HVF in Fig. 2.11), the last two segments (EF and CRF) break only partially, specifically in regions of favourable orientation with respect to the background stress field.

The delay of rupture arrival as well as the damping of peak slip rate in the plasticity scenario become apparent in the time-series of slip rate recorded at on-fault locations at the JVF (r1), the HVF (r2), and the EF (r3) in Fig. 2.13. Peak slip rates are reduced by 32–48 %, rupture arrival is delayed by up to 1 s.

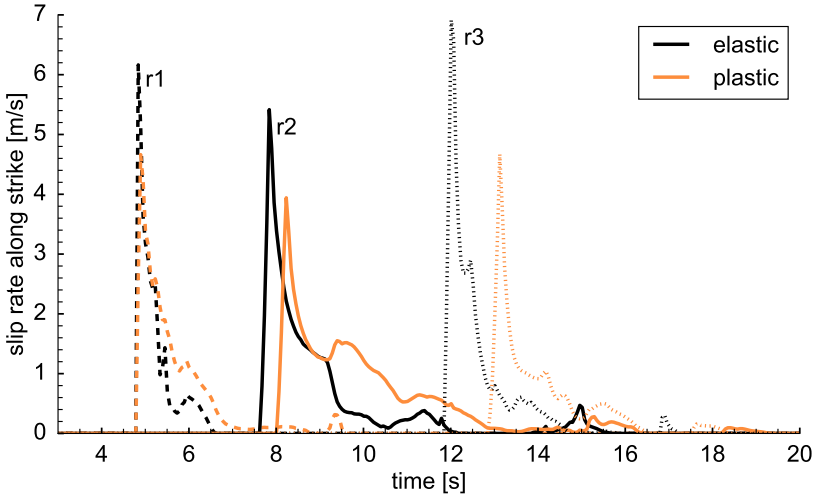

Figure 2.13: Time series of along-strike slip rate recorded at three points of the fault system (marked as r1, r2, r3 in Fig. 2.14). Grey denotes purely elastic, orange plastic material response. Similar line styles correspond to equivalent on-fault location.

Overall peak slip rate across the fault system for both simulations are compared in Fig. 2.14. We observe a general reduction of peak slip rates for plasticity, specifically across the JVF, HVF, and EF. The maximum peak slip rate across the entire fault is reduced by 22.17 % in the plasticity case (Table 2.8). In point-wise comparison, peak slip rate differs up to 47 %.

A reduction of peak slip rate is consistent with previous work in two- and three-dimensions (e.g., Andrews, 2005; Roten et al., 2015). In contrast to a planar fault setup, in which peak slip rate is mainly reduced near the surface (Roten et al., 2015), a reduction along the entire fault is possible when accounting for geometrical complexity of the fault. In particular, we observe a direct correlation of strong peak slip rate reduction and plastic strain accumulation (Fig. 2.14 and Fig. 2.11). Also, peak slip rate is drastically reduced at localized patches at the HVF and the EM. At such locations, the change of local on-fault stresses due to the change of geometrical orientation alters rupture path and speed which triggers plasticity.

The final slip distribution of both simulations is visualized in Fig. 2.15. Even though the seismic moment is very similar (Table 2.8), we observe higher, but more localized maximum slip due to plastic yielding. In both scenarios, maximum slip is occurring at the HVF, where we find 6.36 m in the simulation with plasticity and 5.54 m in the purely elastic simulation. Slip across the JVF and the HVF is overall higher with plasticity, even though peak slip rates and rupture speed are reduced. These findings are consistent with recent work on planar step-over faults (Nevitt and Pollard, 2017) in which a elasto-plastic continuum increased the maximum slip on the single fault segments in static finite element simulations.

We note, that the observed reduction of slip near the surface is not related to the complex fault geometry but rather to the decreasing bulk cohesion in combination with decreasing stresses towards the free surface: The interaction of rupture with the free surface triggers plastic yielding which in turn results in a higher plastic energy absorption with decreasing depth (Roten et al., 2015).

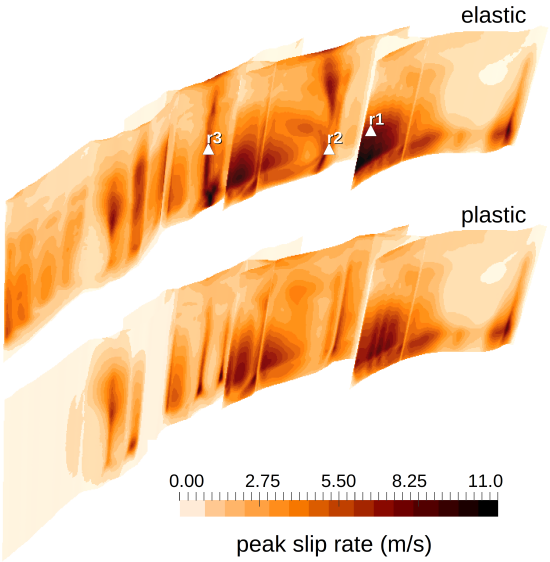

Figure 2.14: Peak slip rate of the Landers earthquake simulations with purely elastic (top) and plastic (bottom) material response. On-fault recording locations of Fig. 2.13 are marked by triangles.

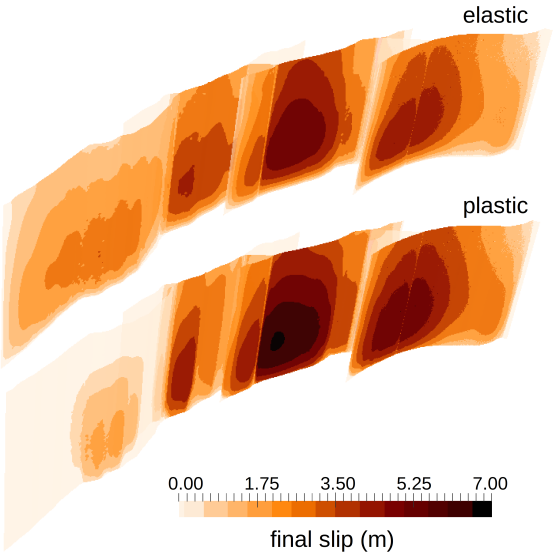

Figure 2.15: Accumulated slip of the Landers earthquake scenarios with purely elastic (top) and plastic (bottom) material response.

In summary, plasticity considerably affects rupture dynamics at complex fault geometries: Additionally to a reduction of rupture speed and peak slip rate as observed on planar faults, rupture path, transfer mechanisms, and slip distribution are altered. The effect of plasticity is highest wherever rupture is encountering geometrical fault complexity such as bending, branching or abrupt ending. At these locations, initial background stresses are highly altered by locally different fault orientations or rupture is stopped abruptly. These findings compare well to simulations accounting for smaller scale fault roughness (e.g., Dunham et al., 2011b; Ulrich and Gabriel, 2017), which find plastic strain accumulation even triggered by slight deviations of planarity. Most crucially, we find that the location and timing of rupture transfers may be distinctively affected in large-scale segmented fault systems.

2.6 Discussion

2.6.1 Damage rheologies for dynamic rupture problems

This study describes implementation, verification, and application of a widely-used proxy for plastic material deformation around rupturing faults for a high-order ADER-DG method. The main advantage of the plasticity approximation is to preserve the numerical method solving the linear elastic equations while reducing potentially unrealistic high stresses around the rupture tip, often observed in dynamic rupture simulations (Andrews, 2005; Dunham et al., 2011a). Here, we only update the stress state in a separate plasticity corrector step succeeding the elastic algorithm.

Within this approach, however, the material constitutive behaviour encapsulated by the elastic wave equation remains unchanged. Therefore, no direct effect of the damaged material response on seismic wave propagation can be modelled. In contrast, numerical models have been developed to consider the change of elastic moduli surrounding dynamic rupture (Xu et al., 2015; Lyakhovsky et al., 2016; Okubo et al., 2017; Thomas et al., 2017). These studies report additional effects, such as slip rate oscillations and as a consequence an increase of near-fault high-frequency radiation. However, continuum damage rheologies are currently restricted to 2D due to numerical challenges in solving the additional non-linear equations.

Future work could compare the effects of damage rheology versus plastic yielding, focusing on dynamic triggering and branching in complex fault systems. Such studies could shed light on how rupture transfer may interact with the reduced wave velocities in off-fault damage zones.

2.6.2 Convergence studies for dynamic rupture problems

Due to the lack of analytical solutions for dynamic rupture problems, we verify the here presented off-fault plasticity implementations in two complementary manners: First by comparing SeisSol's solution of a well-defined test problem to other state-of-the-art numerical methods (Sec. 2.3) and secondly by conducting h- and p-refinement studies for point-wise on-fault parameters with respect to a given reference solution (Sec. 2.4). The latter approach additionally constrains a minimum required resolution on the fault for accurately resolving source dynamics.

We point out, that the required resolution differs for different numerical approaches: e.g., Day et al. (2005) conclude, that for a Boundary Integral Method three points and for a second-order FD Method five points per cohesive zone width are sufficient to accurately resolve on-fault dynamics in elastic simulations with homogeneous initial stress conditions. However, in setups with heterogeneous on- and off-fault stresses, initial conditions depend on the underlying discretization. The analysis in Sec. 2.4.3 indicates, that peak slip rate is highly sensitive to the on-fault resolution of initial conditions, while other parameters such as rupture arrival time and peak slip rate time seem more robust. We expect similar effects for other numerical methods in setups with heterogeneous initial conditions.

Since no analytical solution exists for application-based simulations, the reported convergence rates in Sec. 2.4 highly depend on the choice of the reference solution. A suitable reference solution is commonly computed at a high mesh resolution and a high polynomial degree of basis functions, if applicable. However, if the reference solution still changes with further h- and p-refinement, the reported RMS errors may considerably underestimate the true error with respect to a solution with stable on-fault dynamics. As a consequence, the convergence rates (slope of the RMS regression lines with respect to the reference solution) might not be representative for the numerical scheme. The convergence analysis of Pelties et al. (2012) uses a reference solution with 354 m on-fault discretization, corresponding to a minimum cohesive zone width resolution of 0.91 elements. However, in this study we choose a distinctively higher resolution of the minimum cohesive zone width to ensure stable on-fault dynamics of the reference solution under heterogeneous initial conditions (2.28 mesh elements without and 4.58 mesh elements with plasticity).

2.6.3 Limitation of convergence rates for on-fault dynamic rupture

As discussed in Sec. 2.4.3 and Sec. 2.6.2 the here reported convergence rates are representative of analytical convergence of the numerical scheme only if the pre-defined stand-in reference solution is sufficiently close to an unknown exact solution. Specifically, asymptotic convergence behaviour is only expected for sufficiently small discretizations h. Supplemented by the cohesive zone size analysis

Sec. 2.C, we assume in the following discussion that the chosen high-resolution reference solution fulfils this requirement. We then discuss the origin of non-spectral convergence rates by interpreting rupture dynamics simulations in the framework of additional existing theoretical considerations. To our knowledge, a mathematical theoretical framework explaining the observed method-independent restriction of dynamic rupture problems to low-order convergence has not been published.

In general, the theoretical convergence rate of a numerical scheme is bounded by the degree of piecewise polynomials representing the projection space of the exact solution of the problem (Hesthaven and Warburton, 2010, Chapter 4.5, p. 87). In problems including high discontinuities or steep gradients, this degree might be distinctively smaller than the polynomial degree p of its numerical representation. In this case, an increase of p may not further increase the convergence rate. However, for realistic dynamic rupture problems, it is not possible to formulate an exact solution to establish a theoretical accuracy barrier for on-fault quantities. In fact, the origin of an eventual underlying general "shock-like" character of the dynamic rupture problem remains a topic of discussion.

Earlier studies suggest that the representation of the friction law causes an inherent non-smoothness of dynamic rupture problems (Rojas et al., 2008; Kaneko et al., 2008). The often used linear slip-weakening friction law, for example, poses a piecewise linear function. Its derivative exhibits singularities when slip equals zero and D_c (critical slip distance), yielding a discontinuity of slip acceleration despite smooth slip velocity and shear stress across the process zone (Ida, 1973). Previous attempts of analysing smoother friction law formulations, such as the rate-and-state friction law, indicate slightly increased convergence rates (Kaneko et al., 2008; Rojas et al., 2009; Nerger et al., 2014). However, for reaching spectral convergence properties fault resolutions several orders of magnitude higher than given by the cohesive zone size may be required.

Additionally, non-smoothness may be induced by the standard modification preventing tensile normal stresses $\sigma_n^{mod} = \min(0, \sigma_n)$ to avoid fault opening. Most dynamic rupture solvers, including SeisSol, allow slip to only occur in shearing directions (mode II and mode III fracture propagation). The formation of tensile cracks away from the prescribed fault surface has been accounted for (Dalguer et al., 2003; Dalguer and Day, 2009) but is numerically challenging to incorporate and awaiting convergence analysis. Plasticity is expected to prevent fault opening for a wide range of realistic material parameters (e.g., Dunham et al., 2011b; DeDontney et al., 2012), thus regularizing the solution. However, our convergence analysis with plasticity (Sec. 2.4.4) does not result in higher convergence rates than observed in the elastic study. The Return Mapping Algorithm uses a low-order operator splitting approach (e.g., Simo and Hughes, 2000) to solve for the elastic and plastic strain successively which may additionally limit the expected convergence to second order. We also note, that in the current implementation the plastic yield criterion is checked after a full-time increment Δt, while the dynamic rupture boundary condition is evaluated at each time integration point (Pelties et al., 2012).

Low-order convergence of dynamic rupture problems can be furthermore interpreted in the framework of Godunov's theorem (Godunov, 1959), predicting non-monotonicity in the vicinity of steep gradients of the solution for high-order linear solvers. SeisSol uses a linear upwind flux, the Godunov flux, which numerically dissipates oscillations, whether of numerical or physical origin. However, spectral convergence properties might be reduced to low order accuracy due to the manifestation of the well-known Gibbs phenomena in the vicinity of strong discontinuities (e.g., Hesthaven and Warburton, 2010, Chapter 5.6, p. 136). To overcome the limiting characteristics of linear high-order schemes at steep gradients, flux limiters, such as WENO schemes (Krivodonova, 2007; Dumbser et al., 2007; Hesthaven and Warburton, 2010), are promising approaches to avoid oscillations while preserving the overall high-order accuracy of the underlying method.

In contrast, high-order convergence can be established using the method of manufactured solutions (MMS) (e.g., Roache, 2002). Within this approach, the dynamic rupture problem is transformed into

a related problem for which an analytical solution is known a priori (e.g., Kozdon et al., 2012). Major simplifications of the boundary and interface conditions and the definition of additional source terms are required. Such solutions have been used to verify stability and convergence of a numerical method (Duru and Dunham, 2016; Erickson et al., 2017) without relying on numerical reference solutions. Nevertheless, the currently established manufactured solutions are too simplified to shed light on the convergence behaviour of typical dynamic rupture applications, in particular of ones including off-fault plasticity.

The in Sec. 2.4 reported low-order convergence rates of peak slip rate, peak slip rate time and final slip are consistent with previous dynamic rupture convergence studies (Day et al., 2005; Rojas et al., 2008; Pelties et al., 2012). As a notable exception, Day et al. (2005) and Pelties et al. (2012) report convergence rates higher than 2 for rupture arrival time. However, the therein reported absolute RMS errors of rupture arrival time are considerably higher than in this study: e.g., Pelties et al. (2012) report a RMS error of 2.79 % for $p = 3$ and $h = 1061$ m, while the RMS error of our solution is only 0.65% for the same polynomial order and fault resolution. In previous studies, increasing the fault resolution highly improves the rupture arrival time RMS error and therefore increases the slope of the last square fit, i.e. the convergence rates. We conclude that in contrast to the overstressed nucleation patch used in Day et al. (2005) and Pelties et al. (2012), the here smoothly initiated rupture seems to highly decrease rupture arrival time errors, specifically for lower resolutions.

We emphasize, that using a high-order scheme results in low dispersion properties (Dumbser and Käser, 2006), independently of the achieved order of accuracy. Furthermore, the absolute RMS errors decrease smoothly, even if high-order convergence is not reached.

A potential advantage in terms of computational efficiency when combining small elements with $p = 1$ at the fault with high-order discretization of the wave propagation part remains future work: computational cost per element increases roughly with $\mathcal{O}(p^6)$. However, hardware components are more efficiently employed at higher GFLOP/s counts leading to a non-linear relationship of p and time-to-solution.

2.6.4 Cohesive zone width estimation

The analysis of the cohesive zone width Λ in Sec. 2.C reveals a high spatio-temporal variability of Λ across the fault. The observed decrease of Λ with propagation distance for constant initial stress, as well as larger cohesive zone widths in corresponding plasticity simulations, is consistent with previous studies (Day et al., 2005; Duan and Day, 2008). Interestingly, our results indicate that an increase of frictional cohesion and decreasing initial stresses lead to an increase of Λ at shallow depths in both, elastic and plastically yielding simulations. The interplay of the cohesive zone width with free surface effects remains to be investigated in detail. In general, our results imply that cohesive zone width estimates based on 2D linear fracture mechanics (e.g., Andrews, 1976; Day et al., 2005) needs to be treated with care for setups including additional complexities such as heterogeneous stresses, frictional cohesion, 3D geometries, and plasticity.

2.6.5 Realistic parametrization of the Landers earthquake scenario

The demonstrator dynamic rupture scenario based on the 1992 Landers earthquake reproduces fairly well some of the main observed source characteristics: within the observed total rupture duration of around 24 s the rupturing fault segments produce a magnitude $M_w = 7.3$ earthquake. Not well constrained initial parameters are prescribed as simple as possible.

We observe that the orientation of the Camp Rock Fault (CRF) hinders rupture propagation when accounting for plasticity due to high plastic energy dissipation across the previous fault segments. However, observations indicate that rupture reached the surface of most of the Northern part (e.g., Wald and Heaton, 1994; Hernandez et al., 1999; Milliner et al., 2015). Including additional fault weakening mechanisms, such as velocity weakening friction laws, thermal pressurization (Noda et al., 2009), and thermal decomposition (Platt et al., 2015) could help to sustain rupture at this fault segment. An alternative strategy is prescribing a different orientation of the regional stress field or different friction parameters across the CRF (e.g., Aochi and Fukuyama, 2002).

The depth-dependent cohesion model is based on a 1D approximation of granite-type rock (Roten et al., 2015). Hoek-Brown parameters are used to calculate equivalent cohesion for a variety of rock types classified by their rock strength and the level of damage. Nevertheless, cohesion remains ill-constrained, as it strongly depends on the damage level of the host rock, which is potentially varying along and away from the fault. We observe, that the choice of cohesion highly influences the fault dynamics and the evolution of plastic strain around the fault. Similar effects are reported for ground motions (e.g., Ma and Andrews, 2010; Roten et al., 2014). Damaged zones near the surface or in the close vicinity of faults may imply very small values of cohesion values, additionally influencing dynamic rupture transfer mechanisms. As lower cohesion values imply a lower yield surface for plasticity, off-fault plastic yielding would be triggered more easily, impeding sustained rupture propagation and transfer to subsequent segments.

2.7 Conclusions

We detail two implementation schemes for off-fault plasticity for the three-dimensional dynamic rupture software package SeisSol. Both approaches incorporate plastic material response at sub-element resolution; namely at three-dimensional quadrature points (QP) or at nodal basis (NB) coefficients. The presented approaches are applicable to any modal Discontinuous Galerkin method. The algorithms are formulated as matrix-matrix products which can be efficiently calculated, e.g., via an offline code generator (Uphoff and Bader, 2016). The NB approach is in general cheaper by up to a factor of 6, as it uses considerably less points than the QP approach, but allows lower sub-elemental resolution. Plasticity is numerically regularized by a mesh-independent viscoplastic relaxation time T_v.

We verify our approaches first by comparison to SCEC community benchmark solutions combining off-fault plastic yielding with realistic fault geometries and heterogeneous initial conditions. Remarkably, on-fault agreement improves distinctively when incorporating plastic material response. Off-fault comparison verifies high-quality solutions calculated on large elements while using high-polynomial degrees also for plastically deforming materials.

To reflect the current state-of-the-art of realistic large-scale dynamic earthquake simulations, we provide for the first time 3D dynamic rupture *h*- and *p* refinement studies including depth-dependent initial stresses and off-fault plasticity. The observed general smooth convergence of on-fault dynamics towards the reference solution illustrates the robustness of the numerical method. We establish hands-on guidelines for the minimum required on-fault resolution to accurately resolve source dynamics. For dynamic rupture models with plastic yielding a high resolution at the fault may be less crucial than commonly assumed: In comparison to an elastic simulation, plasticity increases the cohesive zone width due to decreasing rupture speed and increasing plastic yielding close to the free surface. Plasticity additionally regularises the peak slip rate, which is very sensitive to the cohesive zone width resolution in purely elastic simulations. A too coarse fault resolution seems to highly impact the peak slip rate, which directly affects ground motion assessment. However, the required resolution

for time-dependent quantities, such as rupture arrival time and peak slip rate time, increases in setups with plasticity. In summary, the overall minimum required resolution of the cohesive zone width is 34%-50% lower with plastic yielding, mainly due to the lower resolution required for the sensitive peak slip rate.

In terms of accuracy, the two presented implementations for plasticity give almost identical results for a cohesive zone resolution of more than 2.04-2.75 mesh elements (10.2-12.24 sub-elemental points) for $p > 2$. In these cases, it is beneficial to use the NB approach due to its higher computational efficiency. For polynomial degree $p = 2$ and lower resolution of the cohesive zone, the QP approach yields higher accuracy since the projection to the polynomial space is more accurate with respect to the L^2 norm than in the NB approach. On-fault convergence rates with respect to the reference solution do not depict spectral convergence in both cases. We critically discuss a possible theoretical limitation of dynamic rupture to low-order convergence rates.

We demonstrate the influence of non-elastic material behaviour on rupture transfers across a geometrical complex fault system. The earthquake scenario based on the 1992 Landers event reveals that plasticity considerably affects rupture dynamics across complex fault geometries. Plastic strain accumulates at deviations of the rupture path from planarity, e.g., at changes of fault strike orientation, branching, or segment endings. In particular, we observe direct correlation of strong peak slip rate reduction and plastic strain accumulation. As a consequence, the spatio-temporal distribution of rupture transfers is distinctively altered by off-fault plastic energy dissipation. Off-fault plasticity reduces the peak slip rate by up to 50 % and delays rupture arrival across the entire fault and to a larger extent than reported for scenarios on planar faults (Roten et al., 2015). In the simulation with plasticity, slip is found to be locally higher but accumulated across a smaller area. As a result, moment magnitudes are comparable with and without plasticity, even though the rupture path differs dynamically. We find that the cohesive zone width varies considerably across the fault system, implying that a minimum inherent length scale may be sought to be resolved instead of an average.

Our study emphasizes the importance to combine fully 3D dynamic modelling, complex fault geometries, and off-fault plastic yielding to realistically capture dynamic rupture transfers between fault segments and further the understanding of the activation of fault branches and the potential for dynamic triggering of adjacent fault segments.

Acknowledgements

The work presented in this chapter was supported by the German Research Foundation (DFG) (project no. KA 2281/4-1, AOBJ 584936/TG-92), by the Bavarian Competence Network for Technical and Scientific High Performance Computing (KONWIHR), project GeoPF (Geophysics for PetaFlop Computing), by the Volkswagen Foundation (project ASCETE – Advanced Simulation of Coupled Earthquake-Tsunami Events, grant No. 88479) and by the European Union's Horizon 2020 research and innovation program under grant agreement No. 671698. Computing resources were provided by the Leibniz Supercomputing Centre (LRZ, projects no. h019z, pr63qo, and pr45fi on SuperMUC). The authors thank Dave A. May and Kenneth C. Duru for fruitful discussions. The manuscript benefited from valuable reviews and comments by R. Ando and an anonymous reviewer.

Additional information

2.A Derivation of a closed-form update formula for the return mapping algorithm

After solving the dynamic rupture problem for purely elastic material behaviour, we update the elastic trial stress state in case of plastic yielding ($F(\sigma) \geq 0$). We calculate the additional change in stress due to plasticity, assuming the trial stress state $\sigma_{ij}^{\text{trial}}$ at the beginning of the time step. The goal is to derive the updated stress state σ_{ij}^{n+1} solving the following equation:

$$\dot{\sigma}_{ij} = -2\mu\dot{\varepsilon}_{ij}^{p} = -\frac{1}{T_v}(\sigma_{ij} - P_{ij}(\boldsymbol{\sigma})), \tag{2.22}$$

where $\dot{\varepsilon}_{ij}^{p} \neq 0$ is defined by the flow rule given in Eq. (5.4).

We first multiply this equation by the integrating factor $\exp(-(t_{n+1}-t)/T_v)$ and then perform integration over the time interval of $\Delta t = t_{n+1} - t_n$ to get:

$$\sigma_{ij}^{n+1} = \exp(-\Delta t/T_v)\ \sigma_{ij}^{\text{trial}} + \int_{t_n}^{t_{n+1}} \exp(-(t_{n+1}-t)/T_v)\frac{1}{T_v}P_{ij}(\boldsymbol{\sigma})\ dt. \tag{2.23}$$

Note, that we make use of the relation

$$\int_{t_n}^{t_{n+1}} (\dot{\sigma}_{ij} + \frac{1}{T_v}\sigma_{ij})\ \exp(-(t_{n+1}-t)/T_v)\ dt =$$
$$\int_{t_n}^{t_{n+1}} \frac{\partial}{\partial t}[\sigma_{ij}\exp(-(t_{n+1}-t)/T_v)]\ dt = \sigma_{ij}^{n+1} + \exp(-\Delta t/T_v)\ \sigma_{ij}^{\text{trial}}, \tag{2.24}$$

to derive Eq. (2.23). Assuming $P_{ij}(\boldsymbol{\sigma})$ to be constantly equal to $P_{ij}(\boldsymbol{\sigma}^{\text{trial}})$ over the time interval $[t_n, t_{n+1}]$, the integral in Eq. (2.23) can be approximated as

$$\int_{t_n}^{t_{n+1}} \frac{1}{T_v}\exp(-(t_{n+1}-t)/T_v)\ dt\ P_{ij}(\boldsymbol{\sigma}^{\text{trial}}) = (1-\exp(-\Delta t/T_v))\ P_{ij}(\boldsymbol{\sigma}^{\text{trial}}). \tag{2.25}$$

Combining now Eq. (2.23) and Eq. (2.25) and inserting P_{ij} as defined in Eq. (2.11) results in:

$$\begin{aligned}\sigma_{ij}^{n+1} &\approx \exp(-\Delta t/T_v)\ \sigma_{ij}^{\text{trial}} + (1-\exp(-\Delta t/T_v))\left(\frac{\tau_c}{\sqrt{I_2}}\ s_{ij}^{\text{trial}} + \sigma_m^{\text{trial}}\delta_{ij}\right) \\ &= ((1-\exp(-\Delta t/T_v))\frac{\tau_c}{\sqrt{I_2}} + \exp(-\Delta t/T_v))\ s_{ij}^{\text{trial}} + \sigma_m^{\text{trial}}\delta_{ij},\end{aligned} \tag{2.26}$$

where we recover the adjustment factor f^* applied in Eq. (2.14).

2.B Verification of Quadrature Point versus Nodal Basis plasticity implementation

We compare the verification results of the two implementation approaches for off-fault plastic yielding presented in Sec. 2.2.3 for the benchmark setup TPV27 described in Sec. 2.3.1. The Quadrature Points

(QP) and the Nodal Basis (NB) implementation are employed to simulate plastic yielding around a strike-slip fault under heterogeneous initial stress conditions using an identical computational mesh and parametrization.

Fig. 2.B.1 depicts exemplarily slip rate and shear stress on the fault, as well as horizontal velocity off-fault at the same measuring locations as shown in Fig. 2.3 and Fig. 2.4 (which include the QP approach only). We compare both SeisSol solutions using h =250 m discretization and polynomial degree $p = 4$ to the second-order FE method FaultMod using $h = 50$ m. The near-perfect agreement of the QP and NB approach for on-fault dynamics and off-fault wave propagation include matching of the peak amplitude of the waveform in Fig. 2.B.1 (c), which varies from the FaultMod solution.

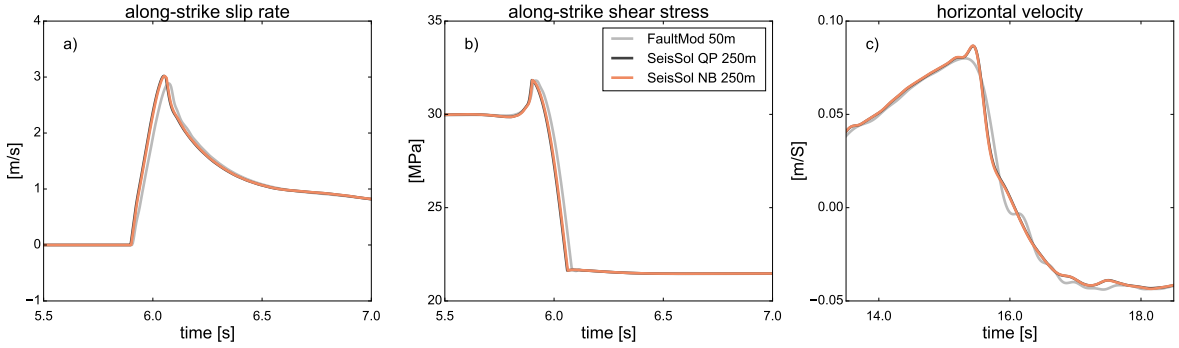

Figure 2.B.1: Comparison between FaultMod with a fault discretization of 50 m and SeisSol QP (black) and SeisSol NB (orange) with fault discretizations of 250 m for the benchmark problem TPV27. a) Along-strike slip rate and b) shear stress at a fault location 10 km down-dip and 10 km along-strike, c) horizontal velocity at a receiver 20 km off-fault. SeisSol's QP and NB approach to implement plastic yielding perform equally well.

Overall, both approaches yield very similar results and are in equally good agreement with FaultMod serving as method-independent comparison solution. A detailed quantitative analysis of the trade-off between computational cost and accuracy of both implementations is presented in Sec. 2.4.4.

2.C Cohesive zone width for the refinement studies

The cohesive zone (also known as breakdown or process zone) is defined as the area behind the rupture front in which shear stress decreases from its static to its dynamic value (Day et al., 2005). Across this portion of the fault, the slip rate and shear stress significantly change. Therefore, the width of the cohesive zone represents a dynamic rupture problem inherent length-scale which is crucial to accurately resolve. In this appendix, we determine the time- and location-dependent cohesive zone width Λ for the 3D dynamic rupture setup described in Sec. 2.4 for elastic and plastic material properties under depth-dependent initial stresses. All calculations are based on the reference (i.e. high-resolution) solutions employing $h = 71$ m at the fault and polynomial degree $p = 5$.

Fig. 2.C.1 visualises contour lines of the rupture front (RF) arrival time and the first point in time at which shear stresses reach their dynamic value (DS) across the fault for the plastically yielding convergence setup. The distance between contours at the same point in time (same colour) represents the cohesive zone width. Below 15 km depth, the shear stress is tapered to stop rupture smoothly at the end of the fault. The rupture front does not reach the free surface due to plastic energy dissipation and increasing frictional cohesion in the shallow part of the fault.

SeisSol's underlying numerical scheme defines shear and normal stress at two-dimensional quadrature points (QPs) located inside each tetrahedral element face which is linked to the fault, as discussed

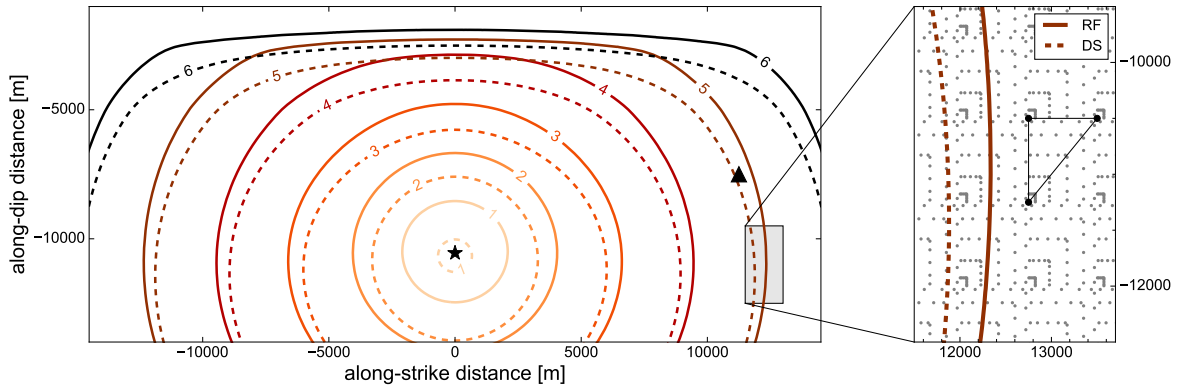

Figure 2.C.1: Contour plot of the rupture front (RF) arrival time (solid line) and the the first point in time at which shear stresses (DS) reach their dynamic value (dashed line), plotted at each second of the plasticity reference solution (QP approach) for the convergence test setup defined in Sec. 2.4. The star indicates the hypocentre, the triangle the location shown in Fig. 2.9. The zoom shows the distribution of SeisSol's integration points (QPs, gray) within one element for polynomial degree $p = 3$ for a $h = 1061$ m discretization at the fault. The black points denote the grid points of the mesh. The cohesive zone contours in the zoom are plotted at t =5 s.

in Sec. 2.2.1. The grey dots in the zoom-in of Fig. 2.C.1 visualize the distribution of QPs exemplarily for the lowest resolution we consider in the convergence analysis. Note, that the effective numerical discretization is distinctively higher than the mesh discretization, denoted by black dots. From Fig. 2.C.1 we see that the effective discretization at the fault can be approximated by the edge length of the mesh divided by $p+1$ additional integration points.

Fig. 2.C.2 depicts the spatio-temporal evolution of the cohesive zone width for a fixed depth along-strike and for a fixed along-strike location along-dip (capturing depth-dependent initial conditions) for the elastic and the plasticity reference solutions. The figure is plotted analogous to fig. 3 in Day et al. (2005).

In the elastic simulation (Fig. 2.C.2, grey), the cohesive zone decreases along strike: from 706 m at 2 s simulation time to 214 m once rupture reaches the end of the fault. This reflects the decreasing width of the cohesive zone with increasing rupture velocity, consistent with findings in Day et al. (2005). In contrast to the decreasing cohesive zone width for homogeneous initial stresses without frictional cohesion (Day et al., 2005), the cohesive zone width in our setup increases from 850 m to a maximum value of 2204 m at a shallow depth of -1800 m in the up-dip direction. The increasing frictional cohesion towards the free surface slows down rupture and results in a larger cohesive zone.

In the plastically yielding case (Fig. 2.C.2, orange), the cohesive zone width Λ decreases with propagation distance along-strike: from around 690 m just after nucleation to a minimum of 460 m. Note, that the minimal width reached is twice as large as in the purely elastic simulation. For up-dip rupture propagation the width increases from 901 m after nucleation to a maximum value of 1555 m (at a depth of -3000 m). This reflects a less-pronounced increase than in the elastic setup, while only in the latter rupture reaches the free surface.

The cohesive zone width Λ is overall smaller in purely elastic simulations than when accounting for off-fault plasticity. A natural exception poses the region close to the free surface, which does not rupture in the plastic simulations (and is excluded in the evaluation of convergence characteristics).

To determine the minimum required discretization for accurate (i.e. converged) on-fault solutions, we calculate the cohesive zone width at each on-fault location used in the convergence analysis of Sec. 2.4. To this end, the time difference (DS-RF) is multiplied by the rupture speed measured at each fault location under consideration.

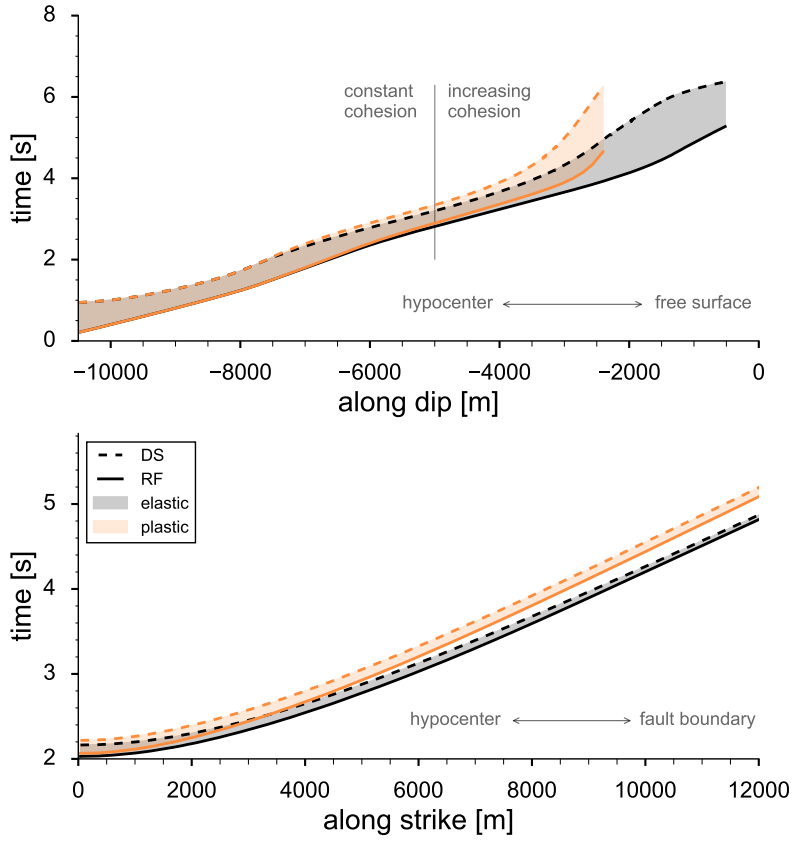

Figure 2.C.2: Cohesive zone width in dependence of rupture propagation distance and time (cf. fig. 3 Day et al. (2005)). Solid lines denote the rupture front (RF) arrival and dashed lines the dynamic shear stress (DS) arrival. Upper panel: along dip evolution at 0 m along-strike, lower panel: along-strike evolution at -10500 m depth. In grey the cohesive zone width of the purely elastic reference (high-resolution) solution is given, in orange the equivalent with off-fault plasticity.

Across all fault receivers, the minimum cohesive zone width is evaluated as $\Lambda^e_{min} = 162$ m in the elastic and $\Lambda^p_{min} = 325$ m in the simulation with plasticity. The median cohesive zone width is evaluated as $\bar{\Lambda}^e = 583$ m and $\bar{\Lambda}^p = 722$ m, respectively.

3

Landers 1992 "reloaded": an integrative dynamic earthquake rupture model

Abstract

The 1992 M_w 7.3 Landers earthquake is perhaps one of the best studied seismic events. However, many aspects of the dynamics of the rupture process are still puzzling, e.g. how did rupture transfer between fault segments? We present 3D spontaneous dynamic rupture simulations of a new degree of realism, incorporating the interplay of fault geometry, topography, 3D rheology, off-fault plasticity, and viscoelastic attenuation. The surprisingly unique scenario reproduce a broad range of observations, including final slip distribution, seismic moment-rate function, seismic waveform characteristics, and peak ground velocities, as well as shallow slip deficits and mapped off-fault deformation patterns. Sustained dynamic rupture of all fault segments in general, and rupture transfers in particular, put strong constraints on amplitude and orientation of initial fault stresses and friction. Source dynamics include dynamic triggering over large distances and direct branching; rupture terminates spontaneously on most of the principal fault segments. We achieve good agreement between synthetic and observed waveform characteristics and associated peak ground velocities. Despite very complex rupture evolution, ground motion variability is close to what is commonly assumed in Ground Motion Prediction Equations. We examine the effects of variations in modelling parameterization, e.g. purely elastic setups or models neglecting viscoelastic attenuation, in comparison to our preferred model. Our integrative dynamic modelling approach demonstrates the potential of consistent in-scale earthquake rupture simulations for augmenting earthquake source observations and improving the understanding of earthquake source physics of complex, segmented fault systems.

3.1 Introduction

The M_w 7.3 Landers earthquake of June 28, 1992 ruptured five distinct segments previously considered unconnected. Overlapping fault zones of 80 km length hosted large vertical slips, large surface strike-slip offsets and unusual high stress-drops (Kanamori et al., 1992; Sieh et al., 1993). Only

This chapter has been submitted in slightly altered form as Wollherr, S., Gabriel, A.-A., and Mai, P. M. (2018). Landers 1992 reloaded: an integrative dynamic earthquake rupture model, to the *Journal of Geophysical Research: Solid Earth*.

two segments of the strike-slip fault system slipped over their respective total length, the previously unknown Kickapoo fault and the Homestead Valley fault (Fig. 3.1), while only parts of the other involved fault segments ruptured. The Landers event raised awareness of unexpectedly large magnitude earthquakes hosted by complicated fault networks; in particular the dynamic rupture transfer mechanisms which pose pressing questions of fault mechanics. Distinct ground shaking was recorded by a dense network of seismometers (Campbell and Bozorgnia, 1994) including locations very close to the slipping faults (Chen, 1995; Sleep, 2012).

The wealth of observational data has been analysed to shed light on the slip distribution from inversion of seismological and geodetic data (e.g., Wald and Heaton, 1994; Cohee and Beroza, 1994; Freymueller et al., 1994; Cotton and Campillo, 1995; Fialko, 2004b; Xu et al., 2016) and to constrain rupture dynamics (e.g. Peyrat et al., 2001; Aochi and Fukuyama, 2002; Fliss et al., 2005; Heinecke et al., 2014; Wollherr et al., 2018). Together with detailed analysis of the recorded strong ground motions (e.g., Campbell and Bozorgnia, 1994), rupture transfer mechanisms (e.g., Wesnousky, 2006; Madden and Pollard, 2012; Madden et al., 2013), and potential energy release (e.g., Dreger, 1994; Wald and Heaton, 1994) a comprehensive picture of the source kinematics and macroscopic earthquake properties has been developed.

While the overall kinematics of the event are thought to be well understood, many observations regarding its complicated rupture dynamics are still unresolved. For instance, the Kickapoo-Landers fault unexpectedly connected the Johnson Valley fault and the Homestead Valley fault, which were previously assumed to be independent structures (Sowers et al., 1994). A well-recorded near-surface slip gap at the northern part of the Kickapoo fault, close to the junction to the Homestead Valley fault, suggests a disconnection between these faults. Thus, rupture is assumed to have propagated at depth and/or "jumped" via dynamic triggering to the adjacent fault segment (Spotila and Sieh, 1995). Across the entire fault system, the rupture front is found to propagate at highly variable speeds (Cotton and Campillo, 1995; Hernandez et al., 1999), slowing down at transitions between segments (Wald and Heaton, 1994) and in regions of high slip (Cohee and Beroza, 1994).

The orientation of geometrically complex faults in the tectonic stress field has a first-order impact on the mechanics of earthquakes and faulting (e.g., Kaven and Pollard, 2013). The Landers fault geometry is characterized by nearly vertical dip but exhibits strike rotation by about 30° from its original direction of nucleation (Bouchon and Campillo, 1998). Of particular interest is the fact that the northern fault segments, including the Emerson fault and Camp Rock fault, are not well oriented with respect to the regional stress field, indicating locally higher fault strengths and lower initial shear stresses. This leads to the hypothesis that large dynamic stress changes induced by rupture of the adjacent fault segments are necessary to overcome static friction at the northernmost faults (Bouchon and Campillo, 1998). In contrast, the lack of aftershocks and large fault offsets in conjunction with relatively shallow slip (Wald and Heaton, 1994), suggests that the Camp Rock fault was rather statically triggered shortly after the event (Sieh, 1996; Kaneda and Rockwell, 2009).

Physics-based dynamic rupture simulations allow investigating the full complexity of the earthquake source dynamics by numerically modelling a spontaneously propagating rupture on a prescribed fault surface. The space-time evolution of the rupture is thereby governed by initial stresses on the fault, a frictional constitutive law, and the bulk properties of the medium. Olsen (1997) presents the first dynamic rupture model of the Landers event using a single planar fault and initial stresses derived from the slip distribution of Wald and Heaton (1994). Consequently, their model features very heterogeneous on-fault stress conditions. This model is then subsequently refined in an iterative dynamic rupture inversion approach (Peyrat et al., 2001) and well reproduces recorded seismograms at selected sites for frequencies below 0.5 Hz.

However, simulations on single planar faults provide no insight on rupture transfer between fault segments. Also, rupture nucleation, propagation, and arrest are highly sensitive to variations in fault geometry. Dynamically, rupture is able to overcome fault bends, branch into or jump to adjacent fault segments only for specific fault pre-stresses, limited distances between adjacent fault segments and limited branching angles of connected faults (e.g., Harris and Day, 1993; Bhat et al., 2007; Oglesby, 2008; Lozos et al., 2011; DeDontney et al., 2012; Oglesby and Mai, 2012).

modelling complex fault geometries is challenging for numerical solvers since the detailed geometry must be honoured explicitly by the spatial discretization. Numerical schemes such as the Boundary Integral Equation Method (BIEM) (e.g., Aochi and Fukuyama, 2002; Ando et al., 2017), Finite Element Methods (FEM) based on tetrahedral elements (e.g., Barall, 2009) - including the Discontinuous Galerkin (DG) Method (e.g., Pelties et al., 2012; Tago et al., 2012) - or numerical methods using curvilinear elements (e.g., Duru and Dunham, 2016) are able to accurately represent non-planar fault geometries. We point out that the accurate representation of fault branches is restricted to methods that do not use a traction-at-split nodes approach (Andrews, 1999; Day et al., 2005; Dalguer and Day, 2007), like BIEM and DG methods.

Only a few dynamic rupture scenarios considered the complex fault geometry on which the Landers event occurred. A multi-segment geometry of the Landers fault zone is first integrated into a dynamic rupture model by Aochi and Fukuyama (2002) and Aochi et al. (2003b). By analysing the effects of varying principal stress directions and frictional parameters they conclude that rupture cannot propagate across all of the differently oriented fault segments assuming a single principal stress orientation. That is, the local tectonic setting and non-planar fault structure play the most significant role in this earthquakes generation and rupture process. However, the use of the BIEM restricted this study to fully elastic, homogeneous material properties. Additionally, the Landers earthquake serves as valuable validation and testing scenario, for example for demonstrating the geometrical flexibility of DG methods (Tago et al., 2012; Pelties et al., 2012; Breuer et al., 2014). However, these studies are not able to fully reproduce observations, as e.g. slip on all fault segments or regional seismogram recordings. While these studies incorporate realistic fault geometries and topography, realistic material properties, such as 3D subsurface structure and the possibility of plastic deformation, are missing.

In addition, significant fault-zone damage was observed for the Landers earthquake (e.g., Li et al., 1994a,b), motivating us to account for inelastic processes off the fault. Recent advances in processing high-resolution aerial photographs of near-fault deformation patterns reveal that off-fault deformation primarily correlates with fault complexity (Milliner et al., 2015). A significant slip reduction towards the shallow part of the faults is inferred, known as shallow slip deficit (SSD), which is often attributed to plastic deformation (Fialko, 2004b; Milliner et al., 2015; Gombert et al., 2018). Simulations on a non-planar yet single fault plane reveal that purely elastic simulations underpredict the SSD (Roten et al., 2017) as well as ground motions (Roten et al., 2014, 2015). Wollherr et al. (2018) includes the full geometrical complexity of the fault system in scenario calculations demonstrating that spatio-temporal rupture transfers are significantly altered by off-fault plasticity.

In this study, we develop an integrated dynamic source model for the multi-segment Landers earthquake based on physics-based HPC-enabled rupture simulations. Our dynamic source model incorporates a new degree of realism by integrating a comprehensive set of geological and geophysical information such as high-resolution topography, rotating tectonic stresses, 3D velocity structure, depth-dependent bulk cohesion, and a complex intersecting fault geometry. Unifying aforementioned complexities is enabled by using SeisSol (`www.seissol.org`, Dumbser and Käser (2006); Pelties et al. (2014)), a software package specifically suited for handling complex geometries and for the efficient use on modern high-performance computing infrastructure (e.g., Heinecke et al., 2014; Uphoff et al.,

2017). This work extends recent models presented in (Heinecke et al., 2014; Wollherr et al., 2018) which included complex fault geometries and off-fault plasticity but were restricted to 1D velocity structure, constantly oriented tectonic background stress and neglecting viscoelastic attenuation of the seismic wave field.

We find that the interplay of dynamic rupture transfers, geometric fault complexity, spatially smoothly varying pre-stress, 3D velocity structure, topography, viscoelastic attenuation, and off-fault plasticity pose unique conditions for a mechanically self-consistent dynamic source model. The such constrained simulation matches a broad range of regional and local observations, including fault slip, seismic moment release and ground motions. The presented model also contributes to the understanding of the shallow slip deficit, directivity effects and rupture branching and "jumping" under realistic conditions.

In the following, we first describe our modelling approach and the observational constraints considered. We then investigate the rupture characteristics of our preferred model in terms of rupture branching, dynamic triggering, moment-rate release, and final slip distribution in Sec. 3.3. We compare the ratio of shallow near-surface slip and deep slip (within the seismogenic zone) to recent inversion results based on a Bayesian approach (Gombert et al., 2018), as well as the modelled off-fault plastic strain distribution with near-field observations of fault zone width (Milliner et al., 2015). Analysing ground motions in terms of spatial distribution and shaking levels (e.g. peak ground motions) with respect to the observations proves an excellent quality of the synthetics produced by the dynamic rupture model. We lastly discuss the effects of variations in modelling parametrization, e.g. purely elastic setups or models neglecting viscoelastic attenuation, in comparison to our preferred model, as well as implications for understanding earthquake dynamics on segmented fault systems in Sec. 3.4.

3.2 Model

In the following, we describe our modelling approach and the observational constraints to construct a fully self-consistent dynamic rupture model of the 1992 Landers earthquake. Dynamic rupture evolves spontaneously according to the parametrization of frictional behaviour, initial fault stress state, and nucleation conditions on prescribed fault surfaces. The nonlinear interaction of rupture propagation and the emanated seismic wave field is further affected by the structural characteristics, such as material properties and topography of the modelling domain.

3.2.1 Structural model and numerical discretization

The Landers fault system consists of curved, branched, and segmented faults. We construct the geometry of the main fault segments from photometric images of fault surface traces (Fleming et al., 1998) that we extend to 15 km depth assuming purely vertical dip. The model includes five distinct non-planar fault segments connected over a total length of 80 km (see Fig. 3.1): the Johnson Valley fault (JVF) in the most southern part of the fault system, the Kickapoo fault (KF) connecting to the Homestead Valley fault (HVF), the Emerson fault (EF) including the connecting branch between the HVF and EF, and the Camp Rock fault (CRF) in the northernmost part. The fault surface intersects the local topography, leading to fault elevation differences of up to 1000 m. Our model incorporates DEM data of NASA's Shuttle Radar Topography Mission (SRTM) with 3-arc-seconds sampling (available from the U.S. Geological Survey `https://dds.cr.usgs.gov/srtm/version2_1/SRTM3/`,((Farr et al., 2007))), re-sampled to match a here chosen spatial topography discretization of 500 m. A cut-out of the resultant structural model is visualized in Fig. 3.2.

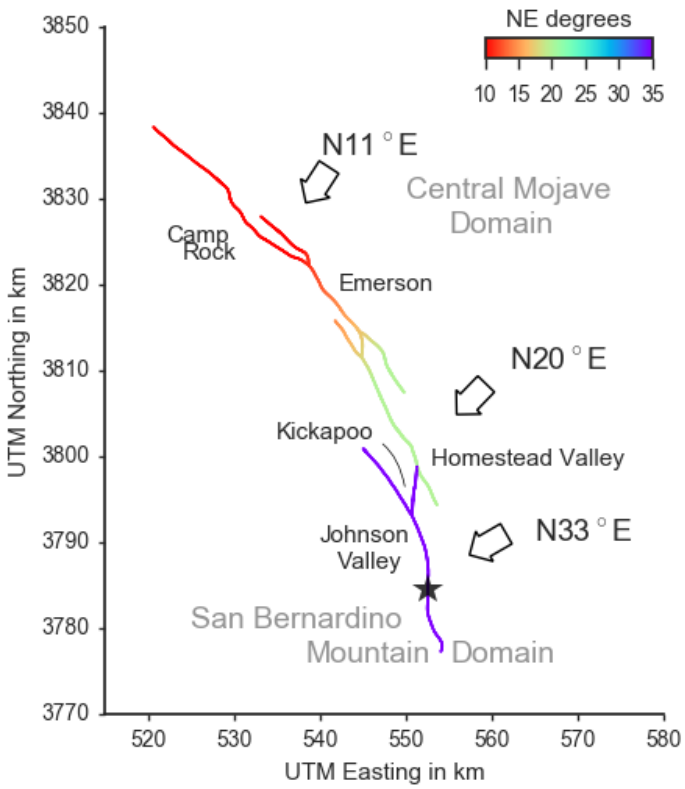

Figure 3.1: Mapped fault traces (Fleming et al., 1998) and assumed orientation of maximum compressional principal stress σ_1. The star marks the epicenter of the 1992 M_w 7.3 Landers earthquake.

In Wollherr et al. (2018) it was found, that the cohesive zone width may vary considerably across geometrically complex fault systems, implying that a minimum intrinsic scale length needs to be resolved instead of some average. For our here preferred scenario, we measure a minimum cohesive zone width of 155 m, located at the HVF at a depth of 8 km. Following the convergence tests conducted in Wollherr et al. (2018), a fault discretization of 200 m using polynomial basis functions of degree $p = 4$ or $\mathscr{O}5$ (corresponding to a minimum cohesive zone resolution of 0.78 m) sufficiently resolves the cohesive zone width to ensure convergence defined by Day et al. (2005). Due to the use of sub-elemental Gaussian integration points, the fault is efficiently discretized by a maximum distance of 33.3 m (effective minimum cohesive zone width resolution of 4.65 points). More details on the determination of the cohesive zone width and the required resolution are provided in Sec. 3.A.

We define a high-resolution model area surrounding the fault traces over a width and length of 270 km (east-west and north-south, respectively). Within this area, topography is represented by tetrahedral elements with 500 m edge length (Fig. 3.2), further refined by polynomial basis functions of degree $p = 4$ ($\mathscr{O}5$). Based on the locally refined and high-order spatio-temporal discretization, we resolve a maximum of 1.0 Hz in all analysed synthetic waveforms in Sec. 3.3.5 within 105 km distance to the fault trace. Synthetic measurements in the vicinity of low velocity basins resolve up to 1 Hz, while high frequencies up to 4.0 Hz are resolved within 10 km distance to the fault trace, Fig. 3.B.1 in Sec. 3.B illustrates the model's resolution exemplary for several stations with varying

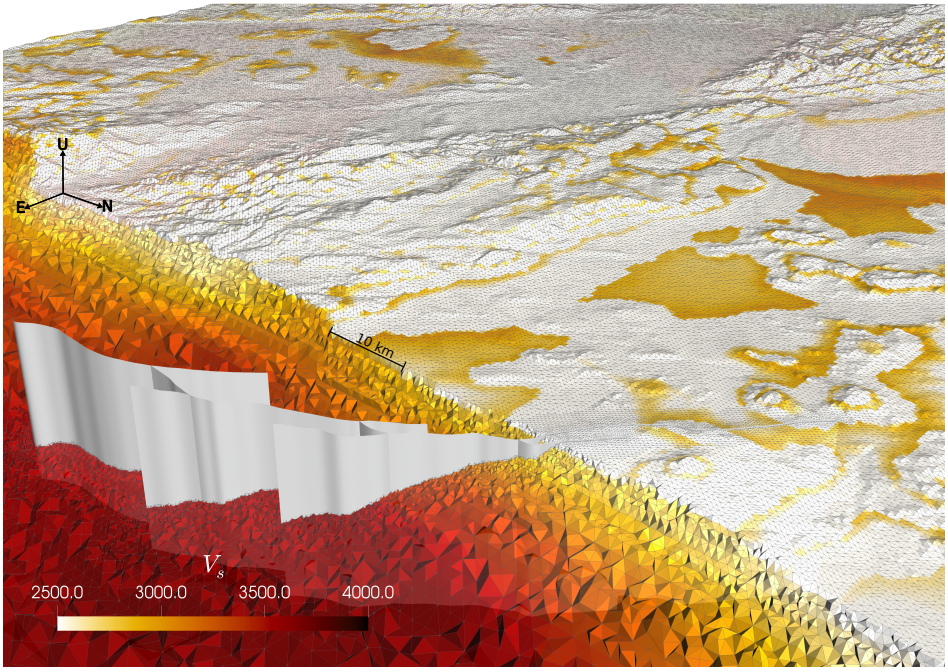

Figure 3.2: Structural model spatially discretized by tetrahedral computational elements. Colours represent the shear wave velocities V_s of the 3D velocity structure given by the Community Velocity Model-Harvard (CVM-H) (Shaw et al., 2015). Fault surface segments are visualized in white. Local refinement is applied in the vicinity of the faults (200 m) (Fleming et al., 1998) and the Earth's topography (500 m) (Farr et al., 2007). The fault surfaces intersect the local topography.

distances to the fault trace ranging from 0.47 km (station LUC) to 102.8 km (station SAL located on the Salton Sea Basin).

To avoid undesired reflections from the domain boundaries, while simultaneously saving computational costs, we gradually increase the element size by a factor of 6% from element to element up to an edge length of 10 km outside the high-resolution model area. Equivalent mesh-coarsening is applied in the volume at depth.

3.2.2 On-fault initial stresses

We prescribe a smoothly varying principal stress field across our modelling domain, without any small-scale or randomized heterogeneities. To this end, we combine information on the regional tectonic setting, findings of previous dynamic rupture studies, and newly conducted numerical experiments constraining the principal stress directions.

The state of stress governing the Landers mainshock is only incompletely known due to limited direct measurements of crustal stress in the Mojave block of the Eastern California Shear Zone. The region is characterized by north-west trending strike-slip faulting and a principal stress orientation of approximately N20°E (Nur et al., 1989; Hauksson, 1994). The Mojave block can be subdivided into several distinct domains based on geometry and faulting style of tectonic activity (e.g., Dokka and Travis, 1990; Unruh et al., 1994). While the central and northern part of the fault system (i.e. HVF, EF and CRF) belongs to the central Mojave block, Unruh et al. (1994) suggests that the JVF forms the eastern boundary of a distinct domain around the San Bernardino Mountains characterized by more north-striking strike-slip faults.

To understand the details of the dynamic rupture process, the principal stress orientations across the Landers fault system are particularly important. Focal-mechanism analysis of the 1975 Galway and the 1979 Homestead Valley earthquakes, as well as of background seismicity prior to the 1992 Landers main shock, yields a maximum principal stress angle of 38° to 16° NE (Hauksson, 1994). That is, the inferred principal stress directions slightly rotate northwards up to the EF.

While background seismicity is mainly observed in the southern part of the fault system, little is known about the stress state prior to the Landers earthquake of the northernmost segments (Hauksson et al., 1993). On the northern Landers fault system, an even steeper oriented maximum principal stress might be plausible, given the locally considerable higher maximum shear-strain orientation compared to the southern fault segments (Sauber et al., 1986). Aochi and Fukuyama (2002) hypothesize a northern rotation to steep angles based on the dynamically locked CRF in their simulations assuming a maximum principal stress orientation of N22°E. A steep angle of 11° NE enabled full dynamic rupture also of the northernmost segments under non-rotating, depth-dependent background stress (Heinecke et al., 2014; Wollherr et al., 2018).

In this study, we allow for smoothly varying directions of maximum principal stress, consistent with regional stress estimates (summarized in Fig. 3.1). We assume that the southern part of the fault system is contained in the San Bernardino Mountains domain (Aochi and Fukuyama, 2002; Unruh et al., 1994), whereas all other fault segments are considered part of the central Mojave block. Therefore, in the south we prescribe a maximum principal stress orientation of N33°E governing the JVF and KF. The maximum principal stress orientation changes to 20° between the KF and the HVF (Hauksson, 1994). We then smoothly decrease the principal stress direction northwards from N20°E at the HVF, consistent with the observed stress rotation postulated by Hauksson (1994).

Due to limited prior information, we perform several numerical experiments varying the principal stress orientation governing the CRF. We find that the CRF is orientated very unfavourably under any angle between 15° and 38°. However, this segment ruptured with a substantial amount of slip (Kagan and Houston, 2005). Sustained rupture across the EF and CRF occurs in our model under a locally low angle of maximum principal stress orientation of 11°, consistent with previous static and dynamic modelling studies of the full or southern-central fault system (Madden et al., 2013; Heinecke et al., 2014; Wollherr et al., 2018).

While the prescribed stress field orientation is laterally smooth, the varying fault strike orientation generates a heterogeneous initial stress state across all fault segments, leading to both favourably and misaligned portions of the fault system. The Kickapoo branch and the northern part of the HVF are the most favourably orientated segments. In contrast, the northernmost part of JVF, as well as the northernmost and southernmost parts of the EF and CRF are not well aligned with respect to the regional principal stress orientation. As a consequence, these fault segments experience only marginal or no slip (see Sec. 3.3.2).

Principal stresses are assumed to vary linearly with depth, in accordance with rock mechanics and field observations. Our prescribed intermediate principal stress component, σ_2, is purely vertical and set to the average confining pressure of the overlying rock reduced by a constant hydrostatic pore fluid pressure (e.g., Suppe, 1985), i.e.

$$\sigma_2 = (2700 - 1000)\text{kg/m}^3 \; gz \tag{3.1}$$

with gravity $g = 9.8$ m/s^2, average rock density of 2700 kg/m^3, and depth z in m. We then determine the remaining two horizontal principal stress amplitudes using $\sigma_2 = (\sigma_1 + \sigma_3)/2$.

In addition, we apply the relative pre-stress ratio R (Aochi and Madariaga, 2003) to constrain the magnitude of the deviatoric stresses. Specifically, we strive to uniquely determine the horizontal

principal stress amplitudes such that the stress field is most favourably oriented at the hypocenter (Ulrich et al., 2018), ensuring that the thus optimally oriented fault plane reaches failure before any other fault with different orientation.

For a given static and dynamic friction coefficient μ_s and μ_d, the R-ratio is defined as fault stress drop $\Delta\tau$ over breakdown strength drop $\Delta\tau_b$:

$$R = \frac{\Delta\tau}{\Delta\tau_b} = \frac{\tau^0 - \mu_d\sigma_n^0}{c + \mu_s\sigma_n^0 - \mu_d\sigma_n^0}. \tag{3.2}$$

Here, c denotes the frictional cohesion; τ^0 and σ_n^0 are the initial shear and normal stresses, respectively, at the hypocenter.

The relative level of initial stress has been found to determine rupture style and rupture properties (e.g., Gabriel et al., 2012, 2013). In our simulations, we assume $R = 0.65$ which leads to a potential stress drop of 65% of the breakdown strength drop across the entire fault. Numerical experiments, testing R-ratios in the range of $0.5 < R < 0.9$, reveal that $R = 0.65$ optimally balances reasonable values of rupture speed and final slip while sustaining rupture across all fault segments by facilitating rupture transfers.

3.2.3 Frictional properties

All frictional parameters are chosen constant across the fault system. Exceptions are the nucleation zone and the northernmost part of the fault system, where we account for palaeoseismological evidence. We further assume a smooth fault strength increase with depth.

Based on laboratory experiments (e.g., Ida, 1972) we use linear slip-weakening friction. We choose a static friction coefficient $\mu_s = 0.55$ close to Byerlee's coefficient which is consistent with regional stress inversions (Gross and Kisslinger, 1997). Under linear slip-weakening friction, a high stress drop is required to facilitate rupture transition between distinct fault segments. Correspondingly, we find a dynamic coefficient of friction of $\mu_d = 0.22$ to optimally facilitate rupture cascading. Frictional cohesion is set to 2 MPa for the entire fault system. The resulting average stress drop over all positive slip regions is approximately 12.5 MPa with a maximum stress drop of 33 MPa at 8 km depth. Surprisingly high stress drops were found for the Landers earthquake from energy to moment rate ratios (Kanamori et al., 1992; Sieh et al., 1993) and also agree with what is inferred from kinematic stress inversion (Bouchon and Campillo, 1998).

We observe a strong trade-off between rupture speed and critical slip distance D_c denoting the amount of slip over which friction drops from μ_s to μ_d. The critical slip distance also crucially affects rupture transitions by determining a critical nucleation size required to initiate spontaneous rupture via dynamic triggering. In numerical experiments, we find that $D_c = 0.62$ m ensures a balance of efficient rupture transfer between adjacent faults (in accordance with the moment rate release) and the prevention of pronounced supershear rupture.

While previous dynamic rupture simulations of the Landers earthquake choose D_c in the range of 0.8 m (Olsen, 1997; Peyrat et al., 2001), we find that lower D_c is required to sustain rupture across the here geometrically more complex fault system. Besides geometric effects, a lower D_c can be attributed to the effect of off-fault plasticity (Roten et al., 2017; Wollherr et al., 2018).

Paleoseismological evidence points to a large event occurring at the EF and CRF approximately 2000–3000 years ago, while the southern part of the fault system has not failed for 8000–9000 years (Sieh, 1996). This suggests locally lower fault strengths due to not yet recovered static friction or lower regional stresses due to the more recent stress release. While we choose a constant stress ratio across the entire fault zone, we locally decrease fault strength by choosing $\mu_s = 0.44$ instead of 0.55

at the EF and the CRF segments. Our simulations reveal that such only slightly weaker CRF and EF are crucial to facilitate dynamically triggered initiation of rupture on these segments.

Rupture is initiated using an artificial nucleation procedure within a circular patch of a 1.5 km radius. Within this zone, the friction coefficient is gradually reduced from its static to its dynamic value over a specified time of 0.5 s (Bizzarri, 2010). Outside this zone, forced rupture is smoothly overtaken by spontaneous rupture. The hypocentral depth is set to 7 km as constrained by source inversion (Wald and Heaton, 1994; Cotton and Campillo, 1995; Hernandez et al., 1999).

At depth, we account for the transition from the brittle to ductile regime between -9 km to -15 km. We linearly increase dynamic friction gradually up to static friction values which allows rupture to stop smoothly. By increasing fault strength instead of pre-stress with depth we ensure off- and on-fault stresses are equal which is necessary when accounting for off-fault plasticity.

3.2.4 Bulk properties and plasticity

Our model incorporates the 3D velocity structure of the Community Velocity Model-Harvard (CVM-H, version 15.1.0, Shaw et al. (2015)), exemplarily visualized for a cut-out in Fig. 3.2. Velocity and density information are efficiently mapped onto the parallelized computational mesh using the geoinformation server ASAGI (Rettenberger et al., 2016). The lowest shear-wave velocities of the domain and across the fault determine the wave field resolution reached in the simulation. Shear-wave velocities range from 4500 m/s to 320 m/s in the sedimentary basin around the Salton Sea. At the fault, shear-wave velocities are 2800 m/s at shallow depths, and do not exceed 3500 m/s at the bottom of the fault, determining the upper bound for subshear rupture speeds. Besides the low-velocity basins at the Salton sea and at the San Bernardino basin (minimum wave speed of 680 m/s) the lowest wave speeds within the high-resolution model domain is 900 m/s. The simulation employs viscoelastic rheologies to model intrinsic attenuation (Uphoff and Bader, 2016). We couple Q to the velocity model by using $Q_s = 50.0 v_s$ and $Q_p = 2Q_s$ following commonly used parametrization (Graves et al., 2008). We discuss the effect of attenuation on dynamically triggered rupture in detail in Sec. 3.4.4.

Additionally, our model makes use of a computationally efficient implementation of Drucker-Prager off-fault plasticity within SeisSol (Wollherr et al., 2018). To this end, a domain-wide initialization of initial stresses, bulk cohesion, and friction is required, which we base on regional observations from the Landers fault zone area. Here, equivalent initial on- and off-fault stresses are assumed, accounting for the smooth principal stress rotation between the San Bernardino Mountain Domain and the Central Mojave block.

Furthermore, the formulation of the plastic yield criterion requires the specification of bulk cohesion. Cohesion differs for different rock types, and also depends on depth and the respective damage level of the host rock. In the Landers region, the main near-surface rock type is granodiorite (Dibblee, 1967). Correspondingly, we assume a relatively undamaged granite-type rock, described as ”good quality rock” in Roten et al. (2017)) who use a Hoek-Brown model to constrain cohesion values for a given rock type and damage level. We therefore define a depth-dependent parametrization of cohesion, ranging from c = 2.5 MPa at the surface to c = 30 MPa at 6 km depth and c = 50 MPa at 14 km depth. While cohesion depends on depth, bulk friction is assumed constant in the entire model domain. We set bulk friction everywhere as equal to 0.55, resembling static friction of most fault segments. While the static friction coefficient of the northern segments is reduced (see previous section), we assume that off-fault rock properties are not considerably altered by paleoseismological events.

In case of plastic yielding, plastic strain at time t can be mapped into the scalar quantity $\eta(t)$ (e.g., visualized in Fig. 3.12) following Ma (2008):

$$\eta(t) = \int_0^t d\eta = \int_0^t \sqrt{\frac{1}{2}\dot{\varepsilon}_{ij}^p \dot{\varepsilon}_{ij}^p}. \tag{3.3}$$

with $\dot{\varepsilon}_{ij}{}^p$ being the inelastic strain rate.

3.2.5 Numerical method

We use the open-source software package SeisSol (`www.seissol.org`; freely available at `github.com/SeisSol/SeisSol`) to conduct large-scale dynamic rupture simulations of the 1992 Landers earthquake unifying all modelling ingredients described above. SeisSol is based on an Arbitrary high order DERivative-Discontinuous Galerkin (ADER-DG) approach which enables high-order accuracy in space and time (Käser and Dumbser, 2006; Dumbser and Käser, 2006). The software solves the non-linear problem of spontaneous frictional failure on prescribed fault surfaces coupled to seismic wave propagation (De la Puente et al., 2009; Pelties et al., 2012). It allows to precisely model seismic waves travelling over large distances in terms of propagated wavelengths with minimal dispersion errors (Käser et al., 2008) and features fully adaptive, unstructured tetrahedral grids that allow for complicated geometries and for rapid mesh generation (Wenk et al., 2013).

The software is verified in community benchmarks addressing a wide range of dynamic rupture problems including branched and curved faults, dipping faults, laboratory derived friction laws, and on-fault heterogeneities. (Pelties et al., 2014; Harris et al., 2018). End-to-end optimization (Breuer et al., 2014; Heinecke et al., 2014; Breuer et al., 2015, 2016; Rettenberger and Bader, 2015; Rettenberger et al., 2016) targeting high efficiency on high-performance computing infrastructure includes a ten-fold speedup by an efficient local time-stepping algorithm (Uphoff et al., 2017). Viscoelastic rheologies are incorporated using an offline code-generator to compute matrix products in a computationally highly efficient way. This poses an increase in computational cost of a factor of only 1.8 in comparison to a purely elastic model (of $\mathcal{O}6$) while resolving the full memory variables (Uphoff and Bader, 2016). Similarly, the off-line code generator is used for incorporating off-fault plasticity within a nodal basis approach (Wollherr et al., 2018). The computational overhead of off-fault plasticity falls in the range of 4.5% – 13.1% dependent on the number of elements that yield plastically and the polynomial degree of the basis functions. This relatively minor increase of costs enables the use of realistic material properties for large-scale scenarios - and we demonstrate the considerable effects of both, viscoelastic attenuation and off-fault plastic yielding on rupture dynamics and ground motion synthetics in Sec. 3.4.

The structural model created with GoCad (Emerson Paradigm Holding, 2018) is discretized using the meshing software Simmetrix by Simmodeler (Simmetrix Inc., 2017) to generate a mesh consisting of 20 million elements. For all presented simulations we use a spatio-temporal discretization of polynomial degree p= 4 ($\mathcal{O}5$). The models accounting for off-fault plasticity and attenuation run for 6:53 h on 525 nodes on supermuc phase 1. Note, that the computational costs are higher in comparison to previously presented scenarios (Wollherr et al., 2018) for a similar mesh size due to the additional costs of viscoelastic damping and a higher polynomial degree.

3.3 Results

In the following, we present a fully 3D dynamic rupture model combining complex fault geometries and off-fault plastic yielding with realistic rheology, viscoelastic attenuation and 3D subsurface struc-

ture. Our preferred model reproduces a broad range of regional (moment release, waveforms and peak ground velocities) and near-fault (slip distribution, shallow slip deficit, fault zone damage) observations. The model captures dynamic rupture transfers between fault segments and furthers our understanding of the activation of fault branches and the potential for dynamic triggering of adjacent fault segments.

3.3.1 Rupture dynamics

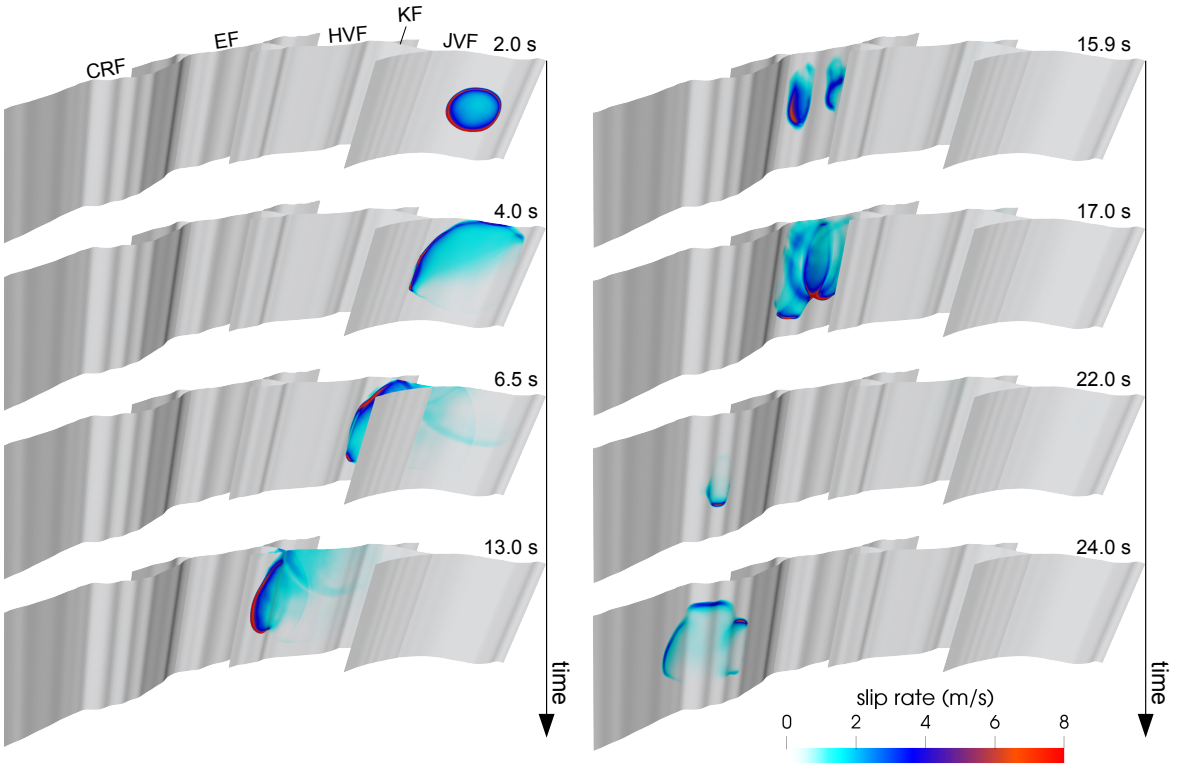

Figure 3.3: Slip rate across the fault system at selected rupture times illustrating dynamic rupture evolution and complexity. Rupture successively cascades by direct branching and dynamic triggering.

In our dynamic model rupture propagates spontaneously across five fault segments. Rupture successively cascades by direct branching and dynamic triggering. The evolution of slip-rate across the fault segments at selected time steps is visualized in Fig. 3.3. A high-resolution animation is provided in the supporting information (S1).

Our simulation features very complex rupture propagation patterns. In particular: i) we observe a variety of rupture transfer mechanisms between fault segments: direct branching, jumping by dynamic triggering, or a combination of both, in forward and reverse direction; ii) we find that dynamically triggered rupture transfer is crucial to enable sustained rupture across the entire fault system; iii) multiple rupture fronts exist at certain times that may propagate in opposite directions, and iv) rupture

speed is highly variable in correlation with the fault geometry, its orientation with respect to the pre-stress and rupture transfers.

In the following, we describe in detail the source dynamics in terms of rupture propagation through the complex fault system. Rupture smoothly nucleates within the first 0.6 s and then spontaneously propagates across the southern part of the Johnson Valley fault segment (JVF). At the fault intersection with the Kickapoo fault (KF), we observe complete rupture transfer by direct branching at high rupture speed at 4 s.

After completely rupturing the KF, slip on the Homestead Valley Fault (HVF) is initiated. However, the pronounced fault bend at the fault intersection nearly stops rupture after approximately 6.5 s rupture time creating localized small slip patches at shallow depths at its northern part. After a delay of almost 1 s, rupture re-initiates at a depth of 7–8 km and continues breaking across the full northern extent of the HVF.

At around 11.9 s, rupture is delayed upon branching into the small fault segment connecting the HVF and the Emerson fault (EF). In distinction to the Kickapoo branching, rupture here also continues along its original branch until it is stopped by the boundary of the HVF segment. The EF is first activated at shallow depth by dynamic triggering from waves originating directly from the HVF which eventually dies out. Rupture is activated for a second time just a few seconds later at depth of 6 km, while a slower propagating rupture front arrives after direct branching via the connecting segment. As a consequence, we observe multiple rupture fronts and reversely (towards the south) propagating rupture, as well as repeated slip of the KF. Parts of the HVF and the KF are dynamically re-activated due to the backward propagating rupture when multiple rupture fronts at the EF meet.

Finally, at 22.3 s rupture time, the CRF is dynamically activated at a depth of 8 km by the superimposed wave field of the subsequent failure of the northern part of the HVF (9 km from the triggered part of the CRF) and the EF (16 km from the triggered part at the CRF). Rupture propagates with a strong up-dip component across the central part of the CRF, and then dies out shortly after reaching the surface. Fault slip completely arrests after 30 s of rupture time.

Our high-resolution model allows to clearly distinguish between rupture branching and rupture (re-)nucleation by dynamic triggering. Rupture chooses to continue along secondary fault segments (branches) whenever these are more favourably orientated than the main fault segment. We observe rupture branching twice: between the JVF, KF and HVF and between the HVF and the EF. In the first case, the optimal orientation of KF towards the background stress field favours rupture propagation. Thus, rupture completely stops at the JVF and rather follows the KF branch. For the second branching transfer (between the HVF and EF), the connecting branch is less favourably oriented. Rupture only partially follows the branch while also continuing along the originating fault segment (HVF).

Dynamic stresses propagate like seismic waves from rupturing fault segments towards locked parts of the fault system, eventually nucleating rupture without requiring the direct arrival of a rupture front. Note that the main rupture front is unable to overcome the geometrical barrier between the EF and the CRF. However, unlike previous dynamic rupture scenarios, our model succeeds in rupturing the CRF by dynamic triggering. This is facilitated by a steep angle of principal stress direction governing the northern fault system, a reduced fault strength, and in particular the emitted seismic waves from the almost simultaneous failure of the northern part of the HVF and the EF. The stress changes due to failure of both fault segments are high enough to trigger fault slip over a distance of 9 km (from the EF) and 15 km (from the HVF). The abrupt deceleration of rupture in between the KF and HVF additionally triggers small patches of shallow slip at the HVF, but also at the most southern part of the EF, which eventually die out (at around 7.9-9.5s).

Rupture speed v_r is highly variable across the fault system. On average, we find $v_r \approx 2300$ m/s consistent with earlier studies (Wald and Heaton, 1994; Hernandez et al., 1999). Rupture accelerates

and decelerates in relation to changes of fault orientation and rupture transfers to adjacent segments. We observe very slow local rupture speeds at geometrical barriers, such as $v_r = 1200\ m/s$ at the transition from the KF to the HVF, and again when rupture reaches the EF.

Supershear transitions are rarely observed in nature, but due to the low resolution of the data, it remains still unclear if small supershear patches can occur locally. Small patches of supershear rupture are locally induced in our model at shallow depths. Specifically, we observe supershear due to the interaction of the rupture front with the free surface at the KF and at the HVF, as in previous dynamic rupture models (Olsen, 1997; Peyrat et al., 2001). Additionally, branching triggers local supershear episodes (cf. the JVF-KF branching at approximately 5.6 s rupture time).

Rupture termination, and the potential resultant generation of stopping phases is of specific interest when analysing rupture in complex, multi-segment fault systems (Oglesby, 2008). From a geological point of view, it was a surprising observation to find that the northern part of the Johnson Valley fault did not slip (e.g. Rockwell et al., 2000). Our dynamic rupture model provides a consistent explanation for spontaneous rupture termination on most of the principal fault segments, although fault structures in reality continue.

Rupture termination in our model is overall independent of the prescribed geometric fault endings, except for the northernmost section of the HVF. In all other cases, rupture is spontaneously stopped due to local fault geometry in conjuncture with the local principal stress orientation: First, rupture is smoothly stopped at the first fault segment in backward direction by the change of fault orientation at the most southern part of the JVF. Second, rupture completely follows the Kickapoo branch, not rupturing the northern part of the JVF. Additionally, rupture only initiates in the central part of the CRF and smoothly dies out towards the southern and northern part of the fault. These results are consistent with the rupture termination analysis by Sieh (1996) (their Fig. 8).

3.3.2 Slip distribution

Numerous studies estimated the on-fault slip distribution of the Landers earthquake (e.g., Campillo and Archuleta, 1993; Wald and Heaton, 1994; Cohee and Beroza, 1994; Cotton and Campillo, 1995; Fialko, 2004b; Milliner et al., 2015; Gombert et al., 2018). While these studies are based on different source inversion approaches and datasets, they overall agree that the largest slip is encountered on the HVF. However, the inferred slip distributions also reveal a large degree of non-uniqueness owing to inherent difficulties in finite-fault slip inversion and the resulting variations in slip models (Mai et al., 2016).

The accumulated slip of our simulation is visualized in Fig. 3.4. Fault slip is distributed over the southern part of the JVF, the KF, the central and northern part of the HVF, the central EF, and the central part of the CRF. Slip below 1-2 m is observed at the southern HVF, and also at the most southern and northern part of the EF where rupture is triggered dynamically. The northern part of the JVF is not ruptured in our simulation.

For all fault segments, slip at depth (5-10 km) is always larger than at shallow depths (less than 5 km). Slip peaks at 7 m located at 5.5 km depth of the central HVF in the vicinity to the KF branching point. At this location, the fault abruptly changes its orientation, forming a geometrical barrier that decelerates the rupture while simultaneously accumulating slip.

In the northern part of the fault system, we observe an apparent discrepancy of modelled co-seismic slip with observations. Near-surface slip on the CRF does not exceed 0.5 m in our simulation, while slip at depth reaches up to 4 m. In contrast, the imaged CRF slip values are high at shallow depth (Sieh et al., 1993; Wald and Heaton, 1994). However, Sieh (1996) and Kaneda and Rockwell (2009)

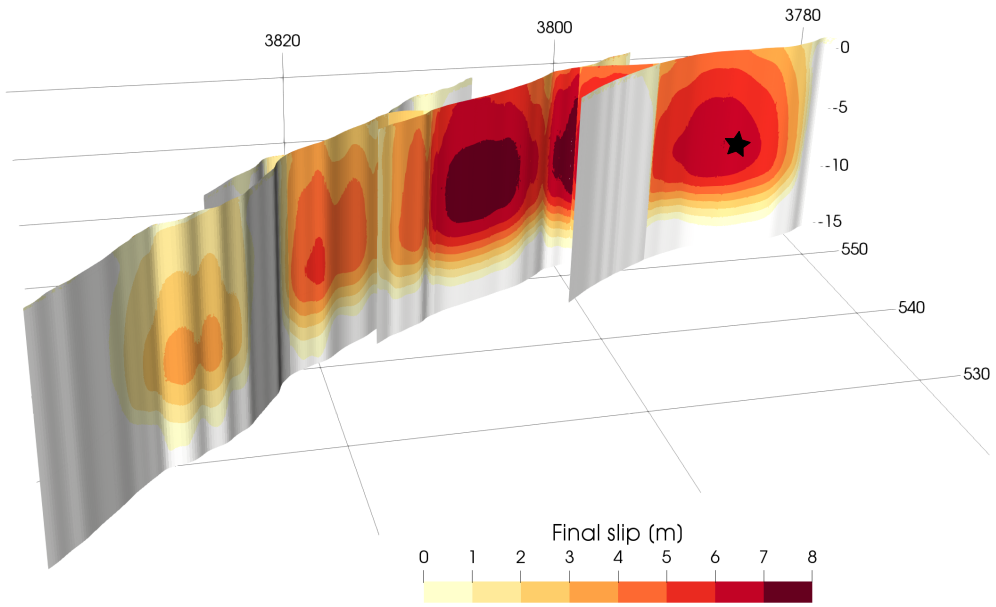

Figure 3.4: Distribution of total accumulated slip for the preferred dynamic rupture scenario. Coordinate axis are in UTM coordinates (km). The star marks the hypocenter at depth of -7 km.

suggest that the CRF might have slipped as a consequence of static stress changes shortly after the main event. We discuss this hypothesis with respect to our simulation results in Sec. 3.4.5.

3.3.3 Seismic moment rate

The Landers earthquake was the largest earthquake to strike the contiguous United States in 40 years. The event's total seismic moment has been inferred between 6.0e+19–16.0e+19 Nm (moment magnitude M_w 7.15–7.4) (Kanamori et al., 1992; Campillo and Archuleta, 1993; Sieh et al., 1993; Wald and Heaton, 1994; Dreger, 1994; Cohee and Beroza, 1994; Vallée and Douet, 2016). The seismic moment of our dynamic rupture scenario is with M_0 = 11.2e+19 Nm (M_w 7.29), in excellent agreement with previous estimates from kinematic models and geological studies.

The multi-segment character of the event reflects on the moment release over time. Most previous studies divide it into two major subevents (Campillo and Archuleta, 1993; Dreger, 1994; Cohee and Beroza, 1994), postulating that slip on the JVF and KF released approximately 20-25% of the total seismic moment, while the northern part of the fault system, including the JVF, the EF and CRF, released approximately 75-80%.

Fig. 3.5 compares the moment-release rate from our dynamic rupture simulation to three observationally inferred moment-rate functions. The optimal and average seismic moment rate of the SCARDEC database are retrieved from teleseismic body waves (Vallée and Douet (2016), grey dotted and black solid lines in Fig. 3.5). The source time function inferred from the surface slip distribution (Kagan and Houston (2005), blue in Fig. 3.5) is based on the assumption that slip to a depth of 5 km equals to $\approx$ 69% of the surface slip. Note that we use our simulation as reference time, and shift the moment rate release of the SCARDEC solution by 5 s to match the main moment rate peaks.

The seismic moment rate of our simulation well reproduces the major moment-rate peaks of the SCARDEC solution. The first is associated with rupture of the JVF and KF within the first 7 s. The

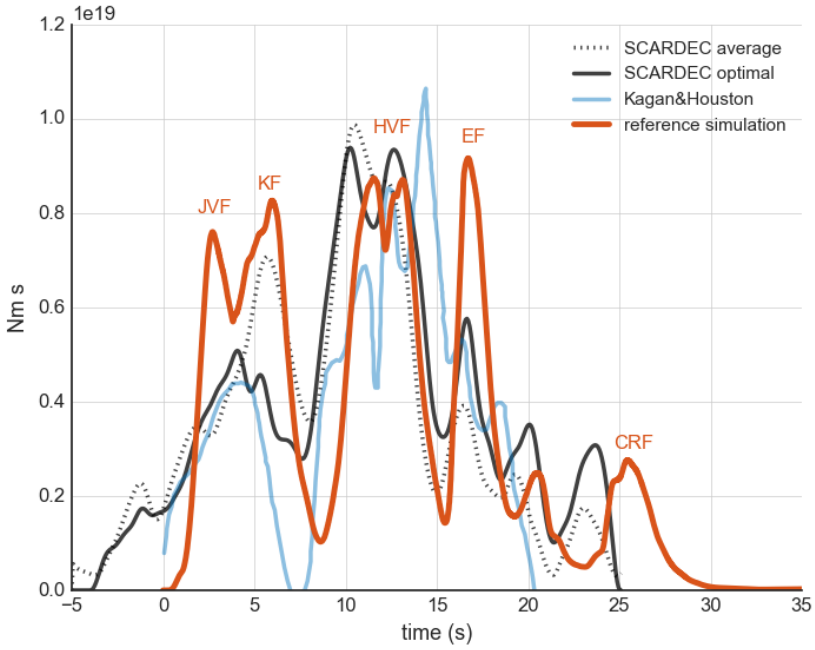

Figure 3.5: Seismic moment rate over time. Dynamic rupture simulation (orange) compared to the optimal and average moment rate of the SCARDEC database (in black and dotted light grey, Vallée and Douet (2016)) and moment rate based on the surface slip (in light blue, Kagan and Houston (2005)). The timeline is taken from our simulation, the SCARDEC solutions are shifted by -5 s accordingly to match the main moment rate peaks.

next peak between 7 s and 15 s corresponds to the failure of the HVF releasing the largest individual contribution to the overall seismic moment. Subsequently, we reproduce several distinct local peaks after 15 s that we associate with the cascading rupture of the individual northernmost fault segments (e.g. the EF and CRF).

Pronounced delays of moment-release rate in observations as well as our simulation may be correlated with rupture transferring between fault segments. Specifically, dynamic triggering (rupture jumping) has been associated with the observed segmentation of moment release. However, our dynamic rupture model reveals that dynamic triggering is not the only factor reducing the moment release significantly. Specifically, rupture deceleration due to fault geometry strongly affects the moment release, thus complicating the inference of rupture transfers from observations.

Rupture propagation along the HVF (at $\approx$ 7 s) is delayed by $\approx$ 0.5-1.0 s, in the SCARDEC solutions as well as our simulation result. The moment rate provided by Kagan and Houston (2005) even accounts for a delay of 2.0-2.5 s and a complete stop of moment release, which may correspond to the observed slip gap near the surface (Spotila and Sieh, 1995). Previous studies interpret this delay of rupture propagation as an indication of rupture jumping from the KF to the HVF(e.g., Campillo and Archuleta, 1993). However, our simulation suggests that this delay rather corresponds to a slow rupture propagation after the branching between the KF and the HVF. Rupture encounters a pronounced fault bend at the centre of the HVF and is dynamically slowed down. Rupture re-initiating is then potentially facilitated by arriving seismic waves from the failure of previous segments as discussed in Sec. 3.4.4.

The most prominent differences in the moment rate functions are found in the early rupture stage. In addition, our scenario overestimates the moment release at 17 s (rupture of the EF) with respect to the

SCARDEC solution. However, this high moment rate release at the EF could be related to the highest peak of the moment rate of Kagan and Houston (2005) at 14 s. On the other hand, peak moment rates are underestimated around 10 and 15 s (rupture of the HVF and the connecting branch between the HVF and EF). We further discuss these discrepancies in dependence of the model assumptions and artificial nucleation procedure in Sec. 3.4.1.

3.3.4 The shallow slip deficit and stress drop

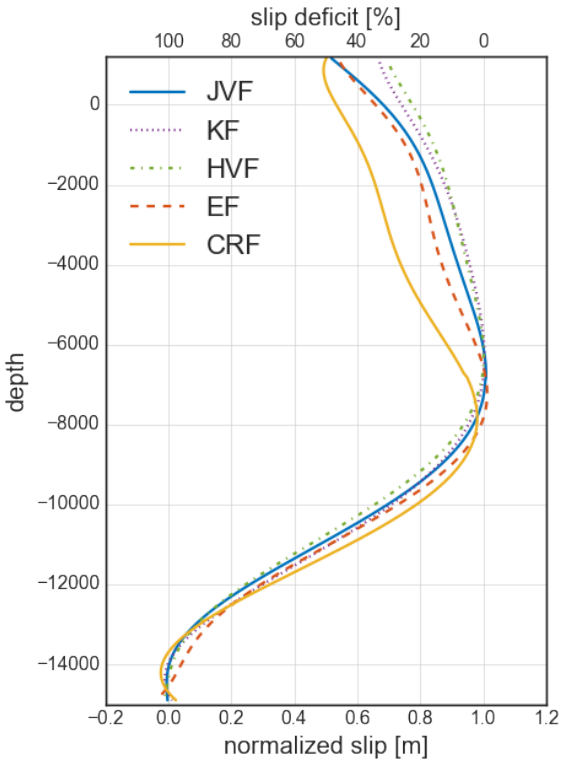

Figure 3.6: Normalized slip (bottom axis) and corresponding shallow slip deficit (top axis) for each fault segment in dependence of fault depth for the preferred Landers earthquake simulation. Each line represents the average over the corresponding fault segment.

In this section, we investigate the shallow slip deficit (SSD) - the reduction of shallow slip relative to slip at depth - in our simulation. The SSD is frequently observed in geodetic slip inversions for major strike-slip earthquakes, including the 1992 Landers event (e.g., Fialko, 2004b; Milliner et al., 2015). We show that an along-strike variability of the SSD is possible, even for laterally constant rock cohesion and bulk friction.

The SSD of the Landers earthquake is estimated to be of the order of 30-60% (e.g., Cohee and Beroza, 1994; Fialko, 2004b; Milliner et al., 2015). Recent coseismic slip models derived by a Bayesian approach suggest that the overall SSD for the Landers event is about 40%, but might vary between fault segments (Gombert et al., 2018).

The origin of the SSD is still under debate. While Xu et al. (2016) argue that the majority of inferred SSD is a result of the poor resolution of near-fault surface data in slip inversions, it is often attributed to coseismically occurring plastic deformation at shallow depths (e.g., Fialko et al., 2005; Milliner

et al., 2015). Numerical models show that shallow slip is already reduced by 18.6 % in simulations with purely elastic material properties (supplemental material of Roten et al., 2017). The SSD in their simulations is further increased when accounting for off-fault plasticity, but depends on the underlying bulk cohesion model (higher SSD with lower rock quality). The modelled SSD on a non-planar yet single fault plane model of the Landers system ranges between 42.9% (good quality rock) and 28.0% (high quality rock), consistent with slip inversion results.

Let us compare the resulting slip distribution of our dynamic rupture model (on a segmented fault system and including off-fault plasticity) to inversion results of Gombert et al. (2018) and to numerical simulations on a single non-planar fault plane (Roten et al., 2017). Recall from Sec. 3.2.4 that all material properties that influence off-fault plasticity, such as bulk cohesion and bulk friction, are constant along strike.

Fig. 3.6 shows normalized slip (bottom axis) and corresponding SSD (top axis) of our simulation. The corresponding SSD quantifies the slip reduction within the first 100 m from the surface with respect to the maximum slip, similar to the definition of Roten et al. (2017). We therefore calculate the mean slip across each fault segment in 100 m intervals, considering only slip higher than 0.1 m, and then normalize it by the segment's maximum slip at depth. Note that the SSD functions for different fault segments start at slightly different depths since the fault surfaces intersect with the changing topography.

Our derived SSDs vary between 30% and 50%, with an average SSD of 41%. The highest SSD is found at the CRF (50%). An SSD of 30% is found at the HVF while the KF depict a SSD of 31%. Surface slip on the JVF is reduced by $\approx$ 49% and on the EF by 48%. Our results indicate that variations of the SSDs within $\approx$ 20% are possible without any lateral heterogeneity of bulk cohesion. Hence, spatial variations in SSD can be attributed to different fault orientations and the resulting variations in dynamic rupture behaviour.

While our results agree well with the observational range of 30-60% Gombert et al. (2018)'s Bayesian slip-inversion suggests that the maximum SSD of 50% occurred at the HVF, which is underestimated in our model. In contrast, our SSD-values at the JVF and EF are overestimated in comparison to the probabilistic approach of Gombert et al. (2018). Additionally, their shallow slip at CRF is reduced by only 20%, while we observe a SSD of 50%.

We infer a relatively high SSD of 50% across the first rupture segments, which may be related to the inferred principal stress orientation. We assume that the hypocentral region is well oriented with respect to the principal stress orientation leading to a large amount of slip at depth. Subsequently, rupture propagates mostly along the Kickapoo branch, preventing larger surface slip at the JVF. The results are independent of the nucleation procedure initiating spontaneous rupture, as discussed in Sec. 3.4.1.

In Sec. 3.4.5 we further discuss the implications of our SSD estimates at the CRF segment in the light of recent very low SSD estimates by Gombert et al. (2018) and the hypothesis of shallow slip at the northern part of the fault system being triggered statically, shortly after the event, rather than coseismically (Sieh, 1996; Kaneda and Rockwell, 2009).

We now compare our findings to single fault-plane simulations that include frictional heterogeneity to approximate along-strike variations in fault strength (Roten et al., 2017). Their reported average SSD of 42.9% is almost identical to the inferred 41% using a similar cohesion model but more complex fault structures.

In our model, relatively high stress drops facilitate rupture transfers across geometrical complexities. The scenario features a maximum stress drop of 33 MPa at a depth of 10 km, which is slightly higher than the maximum stress drop of 25 MPa used in Landers-type simulations by Roten et al. (2017). The average stress drop over all positive slip regions is 12.5 MPa. Such overall high stress

station	name	Vs_{30} (m/s)	R_{JB}-distance (km)	azimuth (°)
LUC	Lucern	685.0	0.47	-22.57
JST	Joshua Tree	379.0	9.04	144.77
MVF	Morongo Valley	345.0	17.93	-128.53
DHS	Dessert Hot Springs	345.0	21.12	-105.14
YER	Yermo	354.0	24.37	-25.03
BRS	Barstow	371.0	33.37	-36.77
PSA	Palm Springs Airport	207.0	34.88	-98.76
PWS	Twentynine Palms	685.0	39.37	153.36
BIG	Big Bear	415.0	40.98	-85.0
H10	Silent Valley	685.0	51.32	-134.99
HSP	Hesperia	371.0	58.31	-74.41
FRT	Fort Irwin	345.0	64.97	-11.36
AMB	Amboy	270.0	67.78	57.19
H05	Hemet	339.0	69.0	-134.0
MEC	Mecca	318.0	74.58	120.6
NPA	North Shore Salton Sea	265.0	83.89	122.25
BOR	Boron	291.0	87.33	-51.49
WWS	Wrightwood	506.0	88.41	-80.56
SAL	Salton City	325.0	102.8	112.49

Table 3.1: Stations used in this study, including site name, Vs_{30}-value (used to calculate the corresponding GMPE values), Joyner-Boore distance R_{JB}, and azimuth to the fault trace. Stations are ordered with respect to R_{JB}-distance.

drops are consistent with expectations for events with long recurrence time and the inferred global averages from far-field waveforms (Sieh et al., 1993; Kanamori et al., 1992). However, stress drop estimates contain a large degree of uncertainty: Sieh et al. (1993) and Kanamori et al. (1992) report for instance 20-28 MPa inferred from the ratio of radiated energy to seismic moment. An analysis of on-fault static stress-drop estimates from kinematic source models for the Landers earthquake, using the method of Ripperger and Mai (2004), reveals stress drop averages over all positive slip regions of 6-12 MPa, and maximum stress changes of over 30 MPa within the largest asperities, consistent with our model. However, high stress drops also increase the effect of plasticity, and as a consequence the reduction of shallow slip due to plastic yielding along single fault planes (Roten et al., 2016). Our model indicates that similar SSD values are possible, even for scenarios with higher stress drop but more complex fault geometries.

3.3.5 Ground motions

In the following, we compare synthetic seismograms of our preferred dynamic rupture scenario to observed waveforms and their peak ground velocities (PGVs). The stations used for comparison are shown in Fig. 3.7. Site names, Vs_{30}-values, Joyner-Boore distances R_{JB}, and fault-station azimuths are summarized in Table 3.1. Recorded accelerograms are downloaded from the strong motion data center (`http://www.strongmotioncenter.org/`) and integrated for velocities. Note that the scope of our study is not to fine-tune the model towards detailed waveform fitting. Rather, we develop a self-consistent physics-based dynamic source model that generates the radiates seismic waves as a desired "by-product".

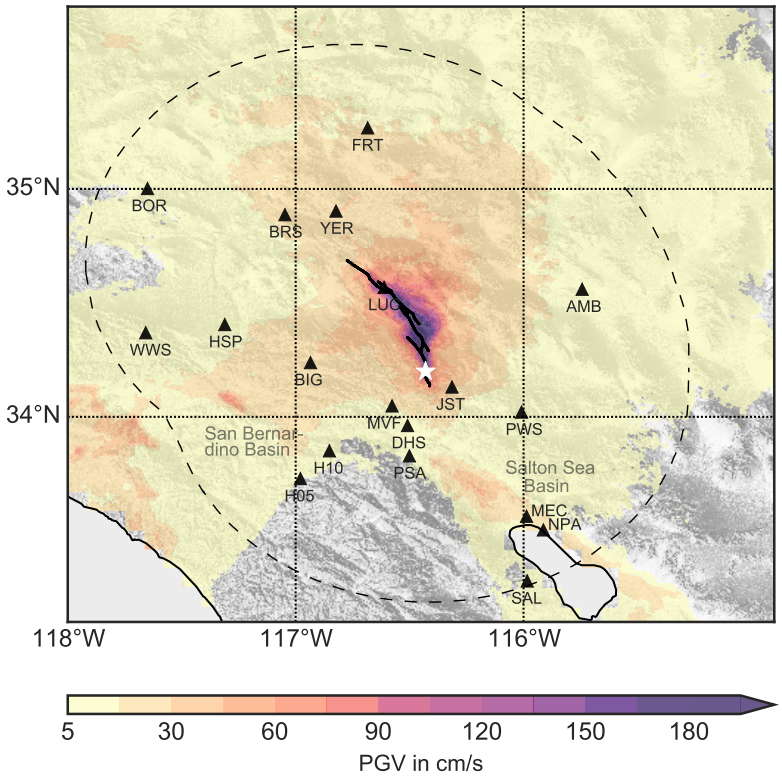

Figure 3.7: Overview map of the model domain, coloured by the simulation's peak ground motions above 5 cm/s based on GMRotD50 (Boore et al., 2006). The white star marks the epicentre of the 1992 Landers mainshock. Black triangles mark the seismic stations used for comparisons (for details see Table 3.1). The dashed line denotes the area of R_{JB}-distance of 105 km.

Peak ground velocities

The Landers event is a prominent example of a strike-slip earthquake with strong directivity effects, i.e. exhibiting large PGV variability with respect to the fault azimuth (e.g., Vyas et al., 2016). Correspondingly, we analyze the PGVs not only in dependence of R_{JB}-distance, but also with respect to azimuth to the fault.

We calculate PGVs using the sensor orientation independent measure GMRotD50 (Boore et al., 2006). Fig. 3.7 is an overview map of our high-resolution model region depicting synthetic PGVs exceeding 5 cm/s. The maximum simulated PGVs exceed 200 cm/s, and are found in the vicinity of the HVF. We observe a clear directivity effect to the north, north-north-west, while we find strong amplification of ground motions close to the Salton Sea Basin and the San Bernardino Basin due to low S-wave speeds in the subsurface model (see ground motions in Fig. 3.7).

Fig. 3.8a compares the simulated (PGV_{syn}) and the observed PGVs (PGV_{obs}) with respect to R_{JB}-distance. We include the standard deviation σ-interval (grey error bars) of the ground-motion prediction equations (GMPEs, grey diamond, Boore and Atkinson (2008)) for each station. The corresponding residuals ($\ln(PGV_{syn}/PGV_{obs})$) between the simulated and observed PGVs, as well as between GMPEs and observed PGVs ($\ln(GMPE/PGV_{obs})$) are depicted in Fig. 3.8b.

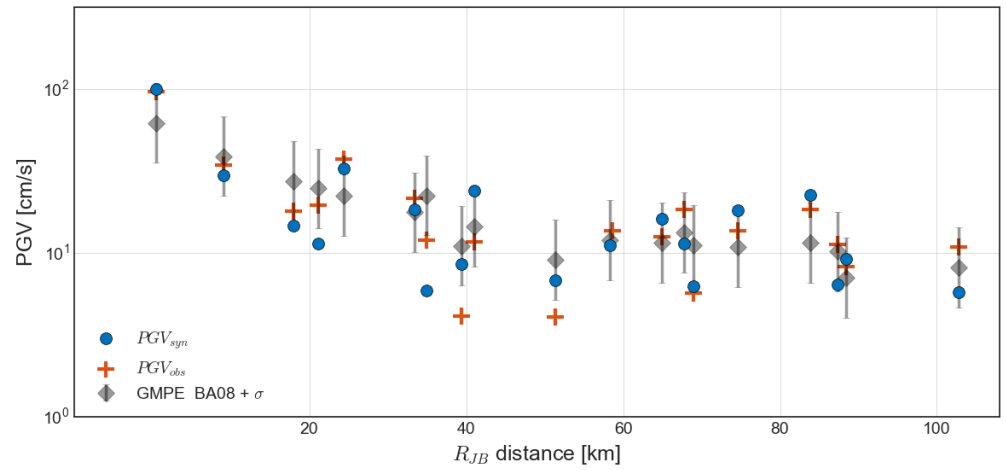

(a)

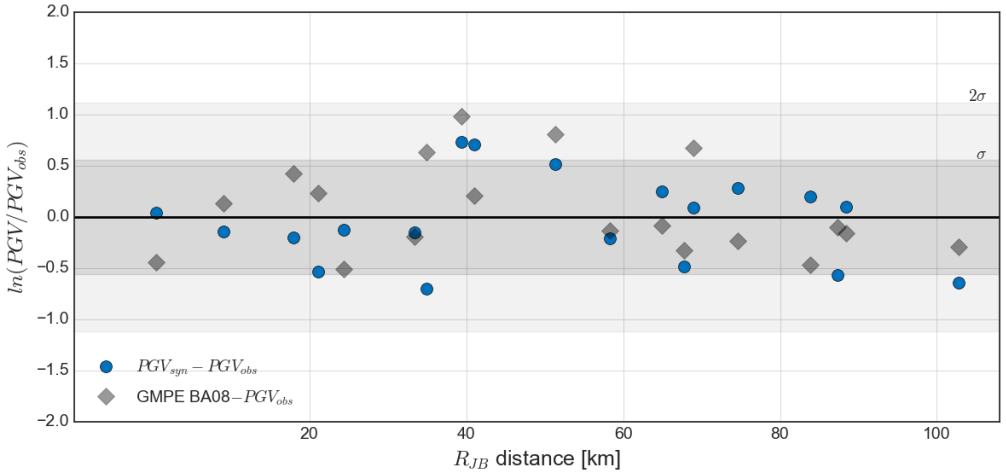

(b)

Figure 3.8: a) PGVs simulated (PGV_{syn}, blue) and observed (PGV_{obs}, orange) in dependence of Joyner-Boore distance R_{JB} for all stations in Fig. 3.7. Grey diamonds represent corresponding GMPE values (Boore and Atkinson, 2008) (including its standard deviation shown as grey bars). b) PGV-residuals, calculated as $\ln(PGV_{syn}/PGV_{obs})$ for synthetic and observed PGVs (blue dots) and $\ln(GMPE/PGV_{obs})$ for GMPE values and observed PGVs (grey diamonds). The dark and light grey shaded areas show the σ and 2σ standard deviation interval, respectively.

In general, our simulation results agree very well with the observed PGVs, as all residuals are within two standard deviations. Particular close to the fault, our simulation results agree better with the observations than the values inferred from GMPEs. The largest residuals are found for stations within 39-51 km R_{JB}-distance (stations PWS, BIG, H10, IND) for which the simulations over-predict PGV-values. These four stations are all somewhat in the backward rupture directivity direction, in particular IND and PWS. The back-propagating rupture on the HVF in our scenario may contribute to the locally larger synthetic PGVs.

To analyze a potential azimuthal trend, we plot the PGV-values and corresponding residuals with respect to fault-station azimuth (Fig. 3.9a and Fig. 3.9b. First, we clearly observe an underestimation

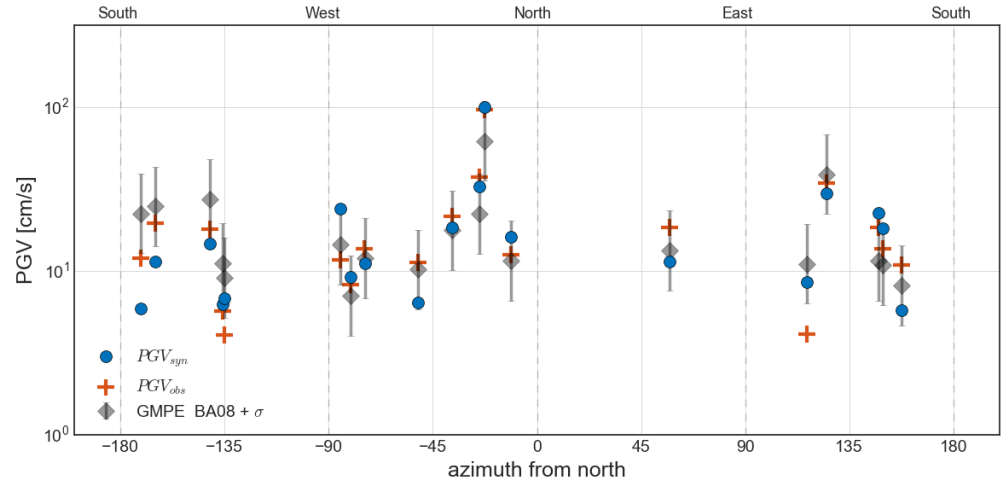

(a)

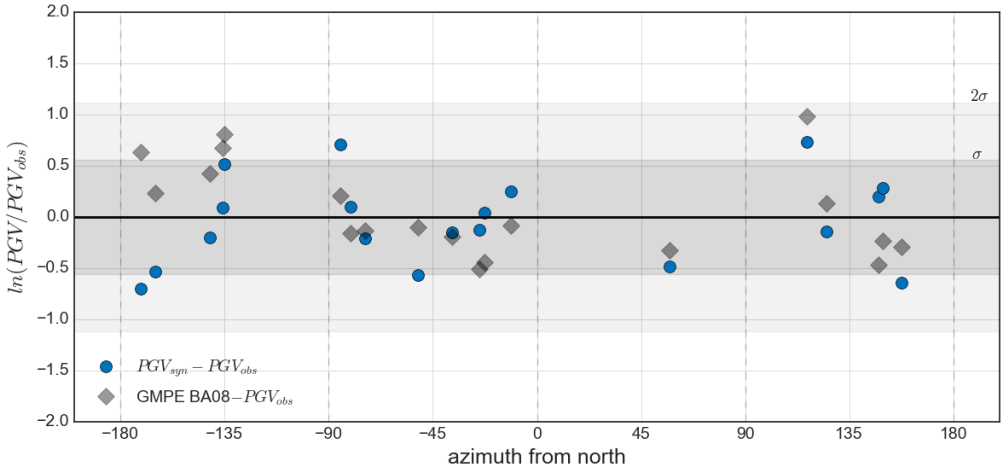

(b)

Figure 3.9: a) PGVs simulated (PGV_{syn}, blue) and observed (PGV_{obs}, orange) in dependence of fault azimuth of the stations given in Fig. 3.7. Grey diamonds represent the GMPE values (Boore and Atkinson, 2008) for each station (including its standard deviation shown as the grey bars). b) Corresponding residuals ($\ln(PGV_{syn}/PGV_{obs})$) for synthetic and observed PGVs and $\ln(GMPE/PGV_{obs})$ for the corresponding GMPE values. The dark and light grey shaded areas show the σ and 2σ standard deviation interval, respectively.

of the GMPEs in forward direction, ($\approx$ 10-39 °) as reported by Vyas et al. (2016). Our simulation results are much closer to observations than the generic GMPEs for these stations. Simulated PGVs in forward direction show very good agreement with the recorded PGVs within one standard deviation. Simulated PGVs overestimate several stations in backward direction ($>$ 110 °), as mentioned above.

In summary, the peak ground velocities from our simulation results agree well with observations, without any significant error trend with respect to R_{JB}-distance and fault-station azimuth. The specific effects of off-fault plasticity on the synthetic peak ground motions with respect to the directivity effect is described in the Discussion part (Sec. 3.4.2).

Waveforms

Next, we examine the seismic waveform characteristics of our simulations, and compare them against observations. Fig. 3.10 and Fig. 3.11 show three-component seismograms for a selection of stations in forward and backward direction, as well as perpendicular to the fault, ordered by R_{JB}-distance. All seismograms show velocities in cm/s, are bandpass filtered between 0.05 Hz and 1.0 Hz, and are normalized by their maximum value (annotated above the time series). Some of the observational strong motion recordings lack exact timing information, hence, we cross-correlate them with our synthetics for temporal alignment.

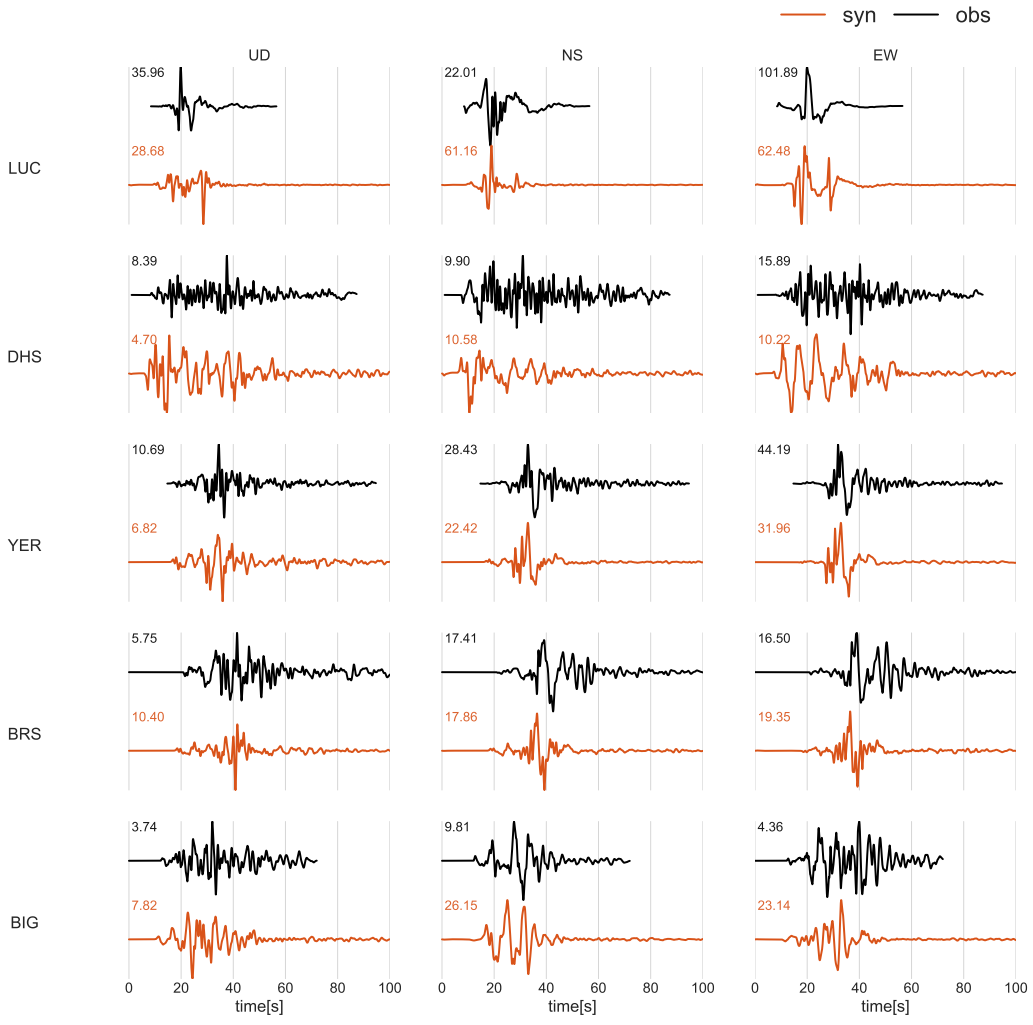

Figure 3.10: Simulated (orange) and observed (black) seismic velocities in cm/s for a selection of stations (Fig. 3.7) below 41 km R_{JB}-distance. All seismograms are bandpass filtered between 0.05 and 1 Hz. The waveforms are normalized by their maximum value (stated above each trace) to facilitate comparison and ordered by their R_{JB}-distance.

The waveform comparisons show very good agreement between simulations and observations, although not all details of the recordings are reproduced. However, this does not come as a surprise, because our study does not attempt to find an optimized source parametrization to fit waveforms (like in a source inversion study). Still, our synthetic waveforms capture the main S-wave pulses, ampli-

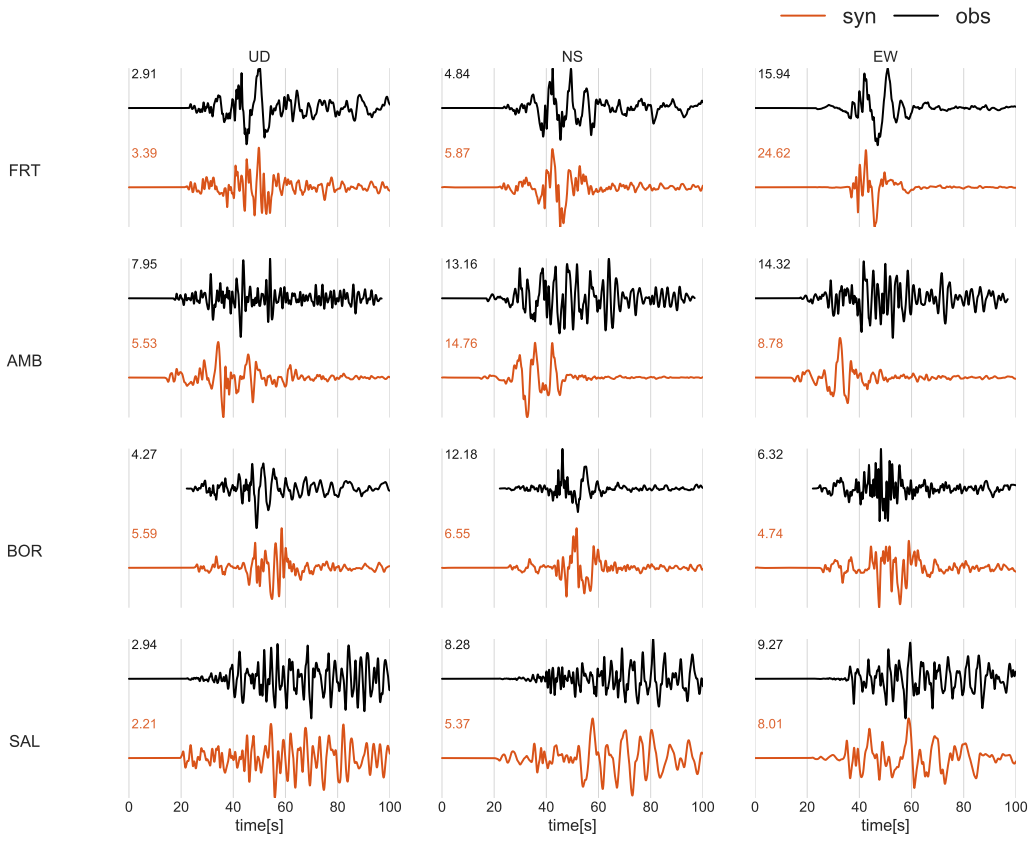

Figure 3.11: Simulated (orange) and observed (black) seismic velocities in cm/s for a selection of stations (Fig. 3.7) above 41 km R_{JB}-distance. All seismograms are bandpass filtered between 0.05 and 1 Hz. The waveforms are normalized by their maximum value (stated above each trace) to facilitate comparison and ordered by their R_{JB}-distance.

tudes, and shaking duration, indicating not only the quality of dynamic rupture model, but also of the numerical method used.

In the forward direction, the main velocity pulses at stations YER and BRS are very well reproduced. At YER, waveform characteristics and amplitudes agree very well on all three components. For BRS, both horizontal components are very consistent, while for the vertical component the synthetic waveform is substantially larger. For these two stations we also notice that our simulations are not quite able to reproduce the coda-wave behaviour following the main pulses, possibly due to the influence of unmodelled small-scale heterogeneity that leads to seismic scattering. This changes, to some extent, for the farther-away stations BOR and FRT. Both are located north of the fault but not exactly in the expected forward-directivity cone. In both cases, the synthetics well reproduce not only the dominant source-related S-wave pulses (of about 5 sec duration), but also the later part of the waveforms (at least in a statistical sense). On all three components, the amplitudes are very well matched at stations BOR and FRT.

In backward direction (i.e. to the south of the fault system), we obtain good agreement at station DHS for an $\approx$ 10 sec long source-dominated shear-wave that arrives in two distinct wave packages (spaced about 6-7 sec apart). Amplitudes match reasonably well, but coda-waves (due to scattering) are not well reproduced. A similar pattern evolves for stations to the east of the fault (e.g., AMB) and to the west (e.g., BIG). The source-dominated shear-waves are in excellent agreement (though the

amplitudes of the synthetics at BIG are higher by a factor 2-5), while the coda behaviour is not well reproduced.

Scattering caused by topography and a smooth 3D Earth model is insufficient to generate realistically scattered waves (Imperatori and Mai, 2015). Interestingly, however, the farthest recording (at SAL) demonstrates a very consistent overall waveform character, including the coda waves. Source-related wave packets are barely visible here, since regional wave-propagation effects dominate, including significant topographic changes and the sedimentary basin of the Salton Sea.

The closest station to the fault trace, Lucerne station (LUC), recorded strong motions in only 470 m distance from our modelled fault trace of the EF. We note, that the waveform in the synthetic seismogram does not align with observations, in contrast to the synthetics for other stations in forward direction (such as YER and BRS). Additionally, the amplitude on the north-south (NS) component of LUC is over-predicted by our simulations, while the east-west (EW) component is underpredicted (in each case about a factor 2). We hypothesize that parts of these discrepancies are caused by rotational components of the wave field. Particularly near-source strong motion accelerometers may be distorted by rotational motions of the sensor during coseismic slip (e.g., Graizer, 2005). This subsequently impacts recordings upon integrating to velocities.

3.3.6 Off-fault deformation

During earthquake rupture, the released energy is not only accommodated by frictional sliding on the fault and radiated seismic waves, but is also absorbed by inelastic processes such as plastic deformation in the vicinity of the fault. Off-fault deformation thus poses a key component in the energy budget of earthquakes (e.g., Rice et al., 2005; Kanamori and Rivera, 2006). Relationships between the width of the damage zone and fault displacement provide helpful insight into the associated fault growth and rupture processes (e.g., Faulkner et al., 2011).

Milliner et al. (2015) correlate pairs of aerial photographs before and after the 1992 Landers earthquake to map co-seismic off-fault deformation. The corresponding fault zone width is defined as the perpendicular extent of surface shear to either side of the fault. They find that the magnitude and width of the mapped off-fault deformation correlate with geometrical complexity of fault surface traces.

Fig. 3.12 compares the accumulated plastic strain distribution in our simulation with fault zone width (FZW) measurements (Milliner et al., 2015). Here, we focus on the qualitative characteristics of the synthetic plastic strain distribution and its relation to fault geometry, as the numerical resolution does not allow for quantitatively translating the dynamically induced plastic strain fields into mapped fault damage zones. Our simulation reproduces key features of the mapped fault zone width, in particular the drastic increase of off-fault damage in geometrically complex fault regions.

Following the fault trace from south to north, an increase of FZW for both the mapped and simulated damage zones can be observed, particularly at the southernmost part of the JVF. Close to the branching point to the KF, our model predicts an increase in plastic deformation on the extensional side of the fault which agrees with the FZW of Milliner et al. (2015). The region with highest plastic strain between 3800-3810 km UTM Northing is clearly correlated with the observed increase of the FZW. Although the southernmost part of the EF did not fully rupture in the simulation, shallow fault slip still triggers plastic deformation very narrowly around the fault trace. Both models show an increase in fault zone complexity at the transition of the HVF and EF (see inset to Fig. 3.12). In particular, the dynamic rupture scenario reveals how the accumulated plastic strain connects the ends of the HVF and the EF. The northernmost part of the fault system lacks off-fault plastic deformation, owing to the lack of shallow slip at the CRF.

An observed increase of the FZW close to the hypocentre suggests that the fault zone structure may be locally more complex than our modelled fault-surface representation. Accounting for a more complex geometry would potentially slow down rupture and/or reduce the energy release at the JVF (Zielke et al., 2017) (see also Sec. 3.4.1). Small-scale fault roughness, as observed for natural faults (e.g., Candela et al., 2012), is not included in our model, but potentially may lead to a strong signature in the simulated plastic deformation (Dunham et al., 2011b; Shi and Day, 2013).

At the transition between the HVF and EF, our model accounts only for one branch, while fault trace mapping shows two subsequent branches to the EF (Sieh et al., 1993; Milliner et al., 2015). The increase of plastic strain at the HVF results in a rapid decrease of rupture speed in the vicinity of its geometrical barrier (fault bend). Interestingly, this plastic strain exactly connects the HVF and EF where the second branch is observed. Hence, this connection may have been created or enhanced during the 1992 Landers event.

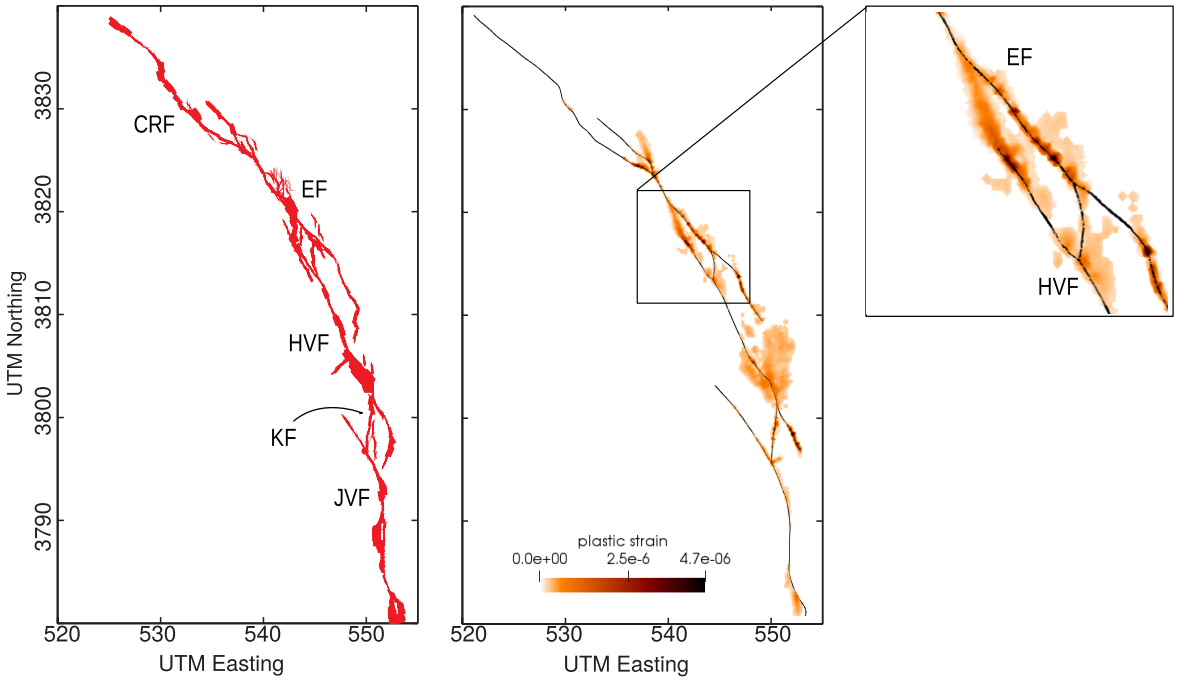

Figure 3.12: Fault zone width (FZW) compiled by Milliner et al. (2015) from aerial photograph correlations (left) in comparison to the accumulated plastic strain from the presented dynamic rupture simulation (middle). The right figure shows an inset at the transition from the HVF to EF.

3.4 Discussion

Sustained rupture along the geometrical complex fault of the 1992 Landers earthquake provides strong constraints on the model parametrization such as stress orientation, stress amplitudes, and friction. Our source model shows excellent agreement with estimated moment-release rate, recorded PGV's, and key features of the observed off-fault deformation patterns. We discuss in the following further implications, potential improvements, but also the sensitivity to variations in prior assumptions of the preferred dynamic rupture model (hereafter named the reference simulation).

3.4.1 Early moment release and earthquake initiation

The presented Landers earthquake scenario slightly overestimates moment release within the first 10 s (Fig. 3.5) compared to the SCARDEC solutions (Vallée and Douet, 2016). The higher moment release occurs during nucleation, rupture across the JVF and branching into the KF. We here discuss potential reasons and improvements specifically with respect to earthquake nucleation and the parametrization of the first segments of the fault system.

Dynamic rupture simulations are initiated by an artificial nucleation procedure on a pre-defined nucleation patch (see Sec. 3.2.3). In our simulation, this leads to a rapid start of rupture, which is further enhanced by the favourable orientation of the hypocentral fault region with respect to the regional stress field. However, observations indicate that rupture started gradually during the first 3 seconds, likely due to a small foreshock in the vicinity of the epicentre (e.g., Campillo and Archuleta, 1993; Abercrombie and Mori, 1994).

In our modelling, we find that rupture dynamics and associated moment release remain robust across the first fault segment when varying nucleation patch size, forced rupture time or forced rupture speed within the nucleation patch. This allows to also examine if the prescribed nucleation procedure affects spontaneous rupture behaviour at the JVF. Spontaneous rupture is delayed but still initiates for radii as small as 0.5 km. For larger radii (up to 4.5 km), rupture initiates faster, however, the moment-release rate remains unchanged. Similar behaviour is found for varying the time of the forced nucleation t_{nuc}: for shorter nucleation times (0.2 s) rupture initiates faster, but spontaneous rupture outside the nucleation patch is identical. We find that rupture speed and moment-release rate outside the nucleation patch are not changed by varying the forced rupture speed within the nucleation patch v_{nuc} in the range of 2000 m/s to 3300 m/s.

Mapped surface traces and off-fault deformation distributions indicate that structural complexity is enhanced close to the hypocentre (Liu et al., 2003; Milliner et al., 2015). The rapid rupture initiation could potentially be delayed by considering fault structures more complex than the curved, yet purely strike-slip fault geometry used in our simulation. Including small-scale geometrical roughness may additionally slow down rupture and limit the stress drop (Dunham et al., 2011b; Shi and Day, 2013; Zielke et al., 2017; Mai et al., 2017), while simultaneously increasing off-fault damage.

The 5 km short connecting Kickapoo fault (KF) plays a crucial role for early moment release by linking the Johnson Valley (JVF) and Homestead Valley (HVF) faults. Despite its short length, it slipped with a maximum of nearly 3 m, and may have hosted the initiation of the March 15, 1979, Homestead Valley earthquake (Hill et al., 1980; Sowers et al., 1994). However, local principal stress orientations are not well constrained, since it is debated whether this fault branch is part of the San Bernardino or the Central Mojave domain.

We observe a second relatively high peak of moment-release rate at around 6 s (see Fig. 3.13) related to slip at the KF. Decreasing the angle of principal stress orientation acting on this fault step-over branch reduces this peak. In our reference model (Sec. 3.2.2), the KF experiences an equivalent angle of maximum compressive stress (33°) as the JVF. However, if the KF already constitutes the transition between the San Bernardino and the Central Mojave domains, its local stress orientation might be steeper.

Therefore, we test two variations in stress orientations across the KF, which respectively vary its strength. First, background stresses smoothly rotate from 33°, starting at the beginning of the KF and reaching 20° at the intersection with the HVF (model variation 1). The black line in Fig. 3.13 demonstrates the reduced moment-release rate between 4-7 s, related to rupture on the KF, for this case. However, subsequently rupture is coming to a complete halt at the JVF, and thus is unable to propagate across the remaining fault segments.

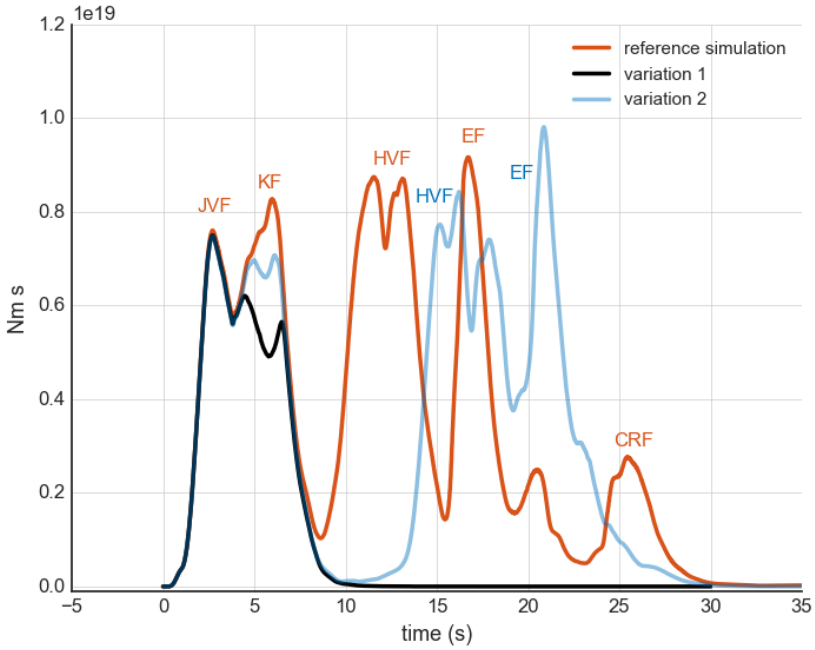

Figure 3.13: Seismic moment rate of the reference simulation (orange) in comparison to two models with changed principal stress orientation governing the Kickapoo Fault: Model variation 1 (black) assumes a linear transition of the stress regime of the JVF to the HVF (33° to 20°) starting at the beginning of the KF and ending at the intersection with the HVF. Model variation 2 (light blue) features the same transition to 20° at the HVF but starting in the centre of the KF.

Second, we test the hypothesis that the initial part of the KF is favourably oriented (33°, to promote branching), while stresses start to rotate to 20° only in the centre of the KF (model variation 2, light blue line in Fig. 3.13). In this case, the moment-release rate between 4-7 s is still decreased with respect to the reference model, but not as pronounced as for model variation 1. Rupture initiation at the HVF is drastically delayed - by 5.5 s in comparison to the reference model. After re-initiation, rupture overcomes the fault-bend barrier and breaks the entire fault system. The rupture path is very similar to the reference model, highlighting the robustness of the source dynamics described in Sec. 3.3.1.

Our numerical experiments therefore suggest a locally steeper angle of principal stress orientation in order to better match the estimated moment-release rate within the first 10 s of rupture. However, such principal stress orientation may require other mechanisms facilitating rupture transfers, such as: i) more complex fault geometries, including additional connecting fault segments as seen in fault traces by Liu et al. (2003), ii) fault weakening mechanisms, such as strong velocity-weakening friction or the effect of thermal pressurization, since there is evidence of a fluid-saturated upper crust, (Fialko, 2004a), iii) compliant fault zones with reduced rigidity promoting rupture propagation (Finzi and Langer, 2012a). Investigating the effects of these physical mechanisms on the dynamic rupture process of the Landers earthquake will be hopefully addressed in future work, but is beyond the scope of this study.

3.4.2 The effect of off-fault plasticity on rupture transfer and moment rate

In nature, high stresses during earthquake rupture are accommodated by inelastic processes near the crack tip, but also in the bulk, such as plastic deformation of the host rock. Wollherr et al. (2018)

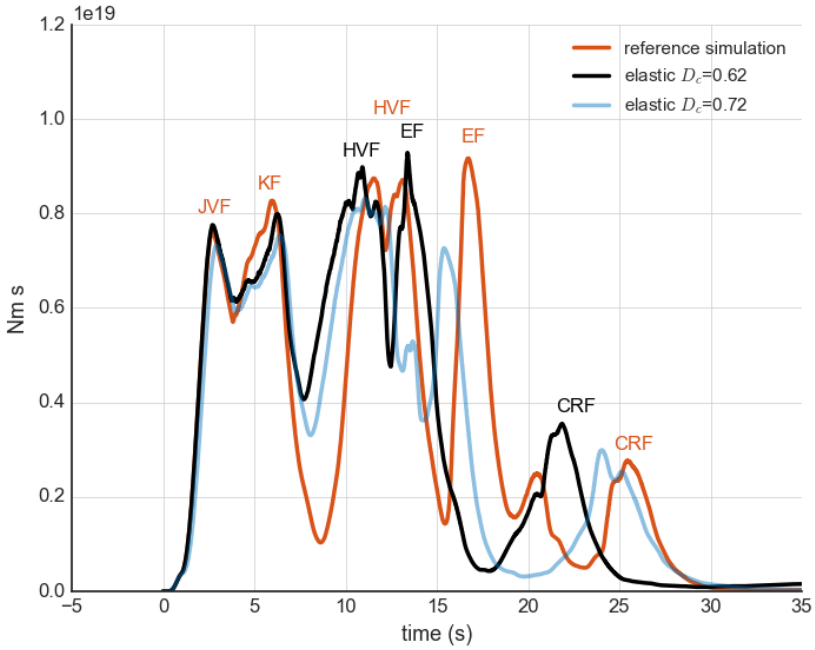

Figure 3.14: Seismic moment rate of the reference simulation including off-fault plasticity (orange), compared to an identically parametrized but purely elastic simulation (black), and an elastic simulation with a higher critical slip distance D_c (light blue).

demonstrate the influence of non-elastic material behaviour on the spatio-temporal rupture transfer processes across the geometrical complexities of the Landers fault system. Plastic strain accumulates when the rupture path deviates from planarity, e.g., at changes of fault strike orientation, branching, or segment endings, and is associated with strong reduction in peak slip rate (up to 50%). Off-fault plasticity also delays rupture arrivals across the entire fault, even to a larger extent than reported for scenarios on planar faults (Roten et al., 2015). In direct comparison of purely elastic scenarios and those including plasticity, slip is found to be locally higher but more concentrated. As a result, moment magnitudes are comparable with and without plasticity, even though the rupture path differs dynamically.

We now compare the results of our reference model that includes off-fault plasticity to simulations with purely elastic material properties, and discuss the effect of off-fault deformation on moment-release rate and rupture transfer on this complex-fault system. Fig. 3.14 depicts the moment-release rate of our reference simulation (orange) to an equivalent scenario assuming purely elastic material response (black, labelled with D_c=0.62). The model parametrization is otherwise exactly the same. The resulting seismic moment is M_0^{ela} = 11.102e+19 Nm (M_w^{ela} 7.292), compared to M_0 = 11.106e+19 Nm (M_w 7.293) of the reference simulation with off-fault plasticity.

While the overall seismic moment is almost identical for both cases, the moment release is distributed slightly differently during the intermediate rupture stage: We find that rupture transfers across geometrical barriers are generally enhanced if off-fault plasticity is neglected. The rupture transfer between the KF and the HVF is facilitated by the purely elastic material response (at 11 s in Fig. 3.14), and rupture also transfers faster between the HVF and EF, leading to a smaller gap in moment rate

release (at 12 s). Consequently, rupture at the CRF is initiated ≈ 5 s earlier than in the simulation with off-fault plasticity (compare the last moment rate peak for both scenarios).

Interestingly, our numerical tests reveal that fully elastic simulations can at least partially emulate the reference simulation when increasing the critical slip distance D_c. In this case, moment-release rate and rupture transfer dynamics are preserved, but exhibit slower rupture speeds and longer delays when transferring to adjacent segments due to an increased critical size (e.g., Ampuero et al., 2002; Bizzarri, 2010; Galis et al., 2014) to initiate self-sustained rupture by dynamic triggering.

For simulations based on linear slip-weakening friction including off-fault plasticity (i.e. the reference case), we find that both, relatively high stress drops and a relatively low critical slip distance of $D_c = 0.62$, are required to sustain rupture along the segmented faults. In particular, the geometrical barrier at the centre of the HVF, as well as the transition between the HVF and the EF, pose strong boundary conditions for sustained rupture. When increasing only as much as to $D_c = 0.64$ we observe rupture delays of more than 5 s between the KF and the HVF. For values of $D_c > 0.64$ we observe a complete stop of rupture before breaking all segments.

In the corresponding elastic simulations, rupture transfers are facilitated by the lack of plastic deformation in the vicinity of geometrical barriers (e.g., Wollherr et al., 2018). For example, by increasing D_c to 0.72 in the elastic simulation (i.e. increasing the fracture energy by 16%), rupture and the transition between distinct fault segments are distinctly slowed down (see light blue line in Fig. 3.14). However, the resulting seismic moment of M_0^{ela} = 10.057e+19 Nm (M_w^{ela} 7.279) is very similar to the seismic moment of the reference simulation.

3.4.3 The effect of off-fault plasticity on peak ground motions

Let us examine the effects on peak ground motions for these three scenarios. Ground motions in seismic hazard assessment are typically described by Ground Motion Prediction Equations (GMPEs) that depend mainly on event magnitude, source-to-site distance, and site-effects (e.g. the Vs_{30}-value), but other source- and path-related effects may be important, too. However, standard GMPEs fail to describe ground motions of earthquakes with strong directivity effects, varying rupture speed or 3D velocity structures including low-velocity basins (e.g., Graves et al., 2008; Spudich and Chiou, 2008; Ramirez-Guzman et al., 2015). Therefore, dynamic rupture simulations like ours are useful to possibly complement GMPEs by exploring physically possible parameter spaces.

Ground motions in dynamic rupture simulations on single faults are reduced by off-fault plastic yielding (Roten et al., 2014, 2015), however, the combined effects of plastic deformation, physics-based dynamic rupture transfers, and directivity on the ground motion properties for complex-geometry faults has not yet been analysed. For this purpose, we examine the mean peak ground motions and their variability for the three scenarios discussed above. The corresponding PGV maps can be found in Sec. 3.C.

Azimuthal dependence of PGVs

First, we analyze the dependence of peak ground velocities (PGVs) on receiver-epicentre azimuth to help understand directivity effects in our simulations. Off-fault plasticity reduces the mean PGVs mainly in forward direction, while they are increased in backward direction. This effect can be only partially mitigated by decreasing the rupture speed (e.g., by increasing D_c) in purely elastic simulations.

We calculate the PGVs of 250 000 synthetic stations distributed within 1 km and 105 km R_{JB}-distance of the fault trace using GMRotD50 (Boore et al., 2006). These stations are binned with

respect to their azimuth to the epicentre with bin width of 15°, resulting in at least 7000 stations per bin.

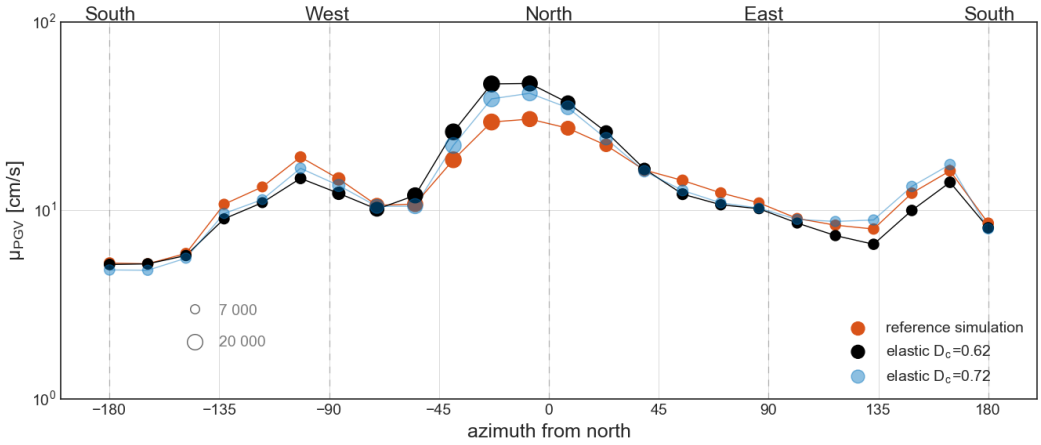

Figure 3.15: Azimuthal dependence of a) mean PGV denoted as μ_{PGV} for the reference simulation (orange), the corresponding elastic simulation (black), and the elastic simulation with increased D_c (light blue) for all stations between 1 km and 105 km R_{JB}-distance (bin width = 20 km). The circle radii represent the number of stations in each bin.

Fig. 3.15 shows the azimuthal dependence of the mean value of PGVs μ_{PGV} calculated for each bin and for all three scenarios. We observe differences in absolute PGVs between our scenarios, especially in the forward and backward directions. The purely elastic simulation with D_c = 0.62 (black) exhibits the highest μ_{PGV} reaching up to 47.1 cm/s in forward direction (between -30° and -15°). The increase of D_c from 0.62 to 0.72 m decreases μ_{PGV} by up to 11% in forward direction. Plasticity reduces μ_{PGV} by up to 35% compared to an identical elastic simulation with D_c = 0.62 m However, the directions between -90° and -45° and 45° and -135° experience very similar μ_{PGV} for all three scenarios. In backward direction (between 150° and 165°), μ_{PGV} is elevated and peaks for the simulation with off-fault plasticity and the elastic simulation with increased D_c.

While some of the increase of μ_{PGV} in backward directivity is attributed to the low velocity basin around the Salton Sea that generates basin-amplification effects (see Fig. 3.7), we can also attribute our results to the geometrical complexity of the fault system. Rupture propagation is slowed down at geometrical barriers or fault branches by the occurrence of plastic yielding which leads to an increase of reversely propagating rupture. We observe that lower rupture speeds and longer delays at geometrical barriers lead to more backward travelling seismic waves which further increase PGVs in backward direction.

We conclude that the effect of plasticity can only be partially emulated by a rupture speed decrease (e.g. increasing D_c) in purely elastic simulations - at least when D_c is constant along the fault: the simulation with plasticity and the elastic simulation with increased D_c show similar μ_{PGV} between -180° and -45° and 45° and 180°, but the purely elastic simulation still overestimates the directivity effect between -45° and 45°.

Distance dependence of PGVs

Let us now investigate the distance dependence of the mean PGVs μ_{PGV} for the three simulations. Plastic yielding primarily appears in the vicinity of the fault, but corresponding PGV maps show PGV reductions (beyond the standard geometrical spreading) over large distances (Roten et al., 2014).

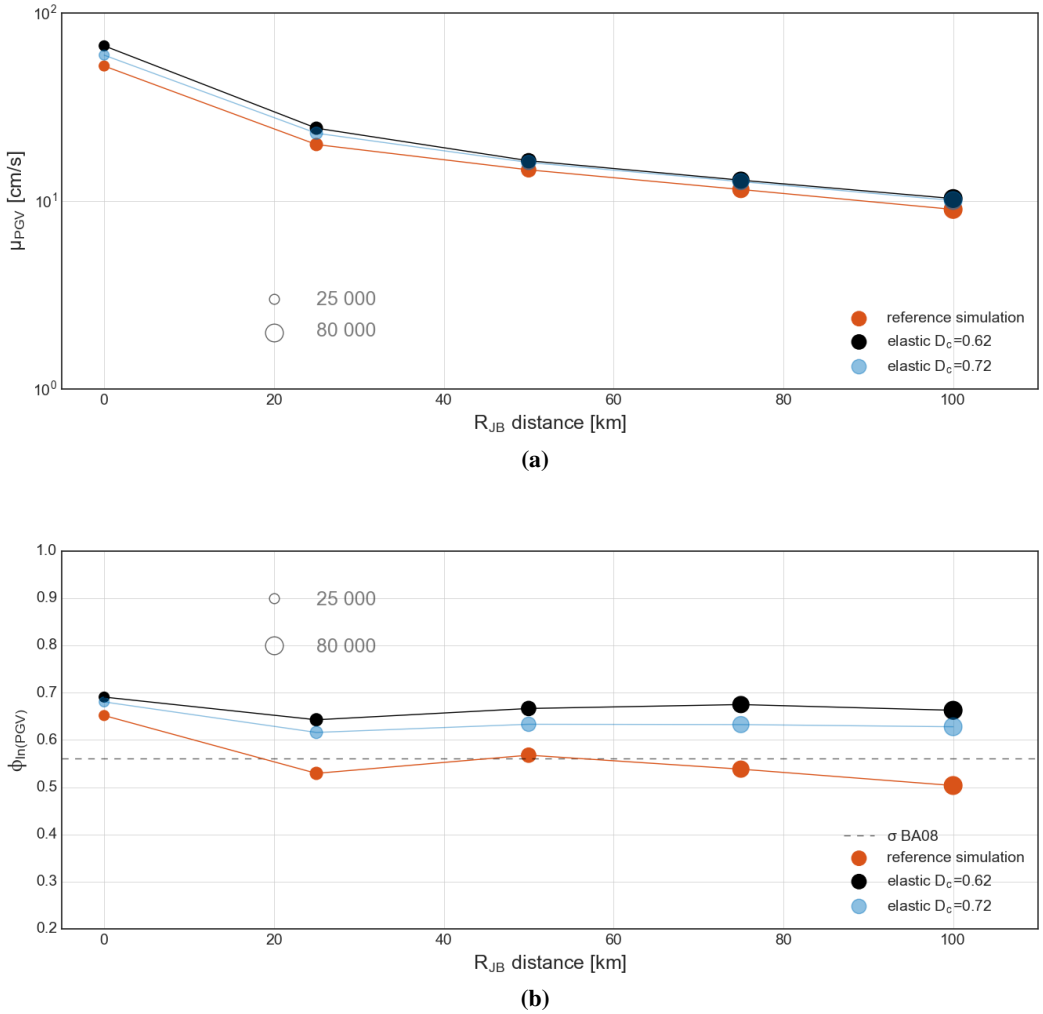

Figure 3.16: Distance dependence of a) the mean PGV μ_{PGV} and b) standard deviation $\phi_{\log(PGV)}$ for the reference simulation with plasticity (orange), the corresponding elastic simulation (black), and the elastic simulation with increased D_c (light blue) for all stations between 1 km and 105 km R_{JB}-distance (bin width = 20 km). The circle size represents the number of stations in each bin. The dashed line in b) represents the constant standard deviation of the GMPE of Boore and Atkinson (2008).

Interestingly, this effect has not yet been analysed systematically. For this purpose, stations are binned with respect to their R_{JB}-distances using a bin widths of 20 km (at least 25 000 stations per bin). Fig. 3.16a shows the mean PGV μ_{PGV} for each of these bins.

In general, the elastic simulations show higher μ_{PGV} over all distances in comparison to the reference simulation with plasticity. Larger differences are visible close to the fault where plasticity reduces μ_{PGV} by 21.9% within the first 20 km, while μ_{PGV} is reduced by on average 12.4% between 85 km and 105 km R_{JB}-distance. By increasing D_c in the purely elastic simulations, μ_{PGV} is reduced by 10.8% within the first 50 km (still 12.4% difference to the simulation with plasticity), but shows almost identical behaviour for larger distances compared to the elastic simulation with D_c = 0.62 m.

GMPEs commonly assume a constant ground motion variability (Boore and Atkinson, 2008), independent of the distance to the fault. However, a distance-dependent variability is found for kinematic

simulations of the Landers earthquake assuming purely elastic material properties (Vyas et al., 2016). Different ground motion variability values might have a significant impact on the results of seismic hazard analysis (e.g., Restrepo-Velez and Bommer, 2003; Bommer and Abrahamson, 2006; Strasser et al., 2009). Here, we additionally investigate the distance dependence of ground motion variability in dynamic rupture simulations on complex faults including off-fault plasticity.

Fig. 3.16a shows the standard deviation of the logarithmic PGVs $\phi_{\log(\mathrm{PGV})}$ for each bin in comparison to the constant value of 0.56 used by the GMPE of Boore and Atkinson (2008). The variability is in general higher than 0.56 for the purely elastic simulations although $\phi_{\log(\mathrm{PGV})}$ is already reduced by 4.4% on average when we increase D_c. The simulation with plasticity shows the smallest ground motion variability, ranging from 0.65 (0-20 km bin) to 0.50 (85-105 km bin), very close to what is used in GMPEs by Boore and Atkinson (2008). In the simulation with plasticity, high stresses are limited by plastic yielding, which results in a reduction and smoothing of on-fault slip rates (e.g., Wollherr et al., 2018). As a consequence of the smoother peak slip rates, the resulting ground motions have lower variability.

Overall, we observe only a small distance dependence of ground motion variability for the simulations using purely elastic rock properties, in contrast to what is reported by Vyas et al. (2016). However, they employ kinematic source models of the 1992 Landers earthquakes using a second-order accurate generalized finite-difference code (Ely et al., 2008). They find that the variability is much higher close to the fault (on average 0.79), and reduces to a constant value of 0.6 only at 100 km distance (Fig. 5 in Vyas et al. (2016)).

We argue that the smoother final slip distribution of our dynamic rupture source models is responsible for the lower variability of simulated ground motions. In our model, the highest slip is always located at depth, and it is very smoothly distributed across the fault segments (Fig. 3.4). In contrast, Vyas et al. (2016) use kinematic source models of Cotton and Campillo (1995); Hernandez et al. (1999); Zeng and Anderson (2000); Wald and Heaton (1994) and Cohee and Beroza (1994) which all feature very heterogeneous slip distributions, that is, slip occurs in isolated patches. Also, four out of their five models contain zones of large near-surface slip that may lead to increased variability of ground motions in the vicinity of the fault. Vyas et al. (2016) observe the lowest distance dependence of variability for the kinematic source model of Zeng and Anderson (2000) that has its highest slip at depth, similar to our simulations.

In contrast to the purely elastic simulation, ground motion variability close to the fault for the reference simulation with plasticity is increased by 29.4% with respect to variability between 85 km and 105 km R_{JB}-distance. Localized plastic deformation (see Fig. 3.12) additionally alters PGVs very heterogeneously in the vicinity of the fault, therefore further increasing the variability within the first 20 km.

We conclude that mean peak ground motions are stronger reduced in the vicinity of the fault when accounting for off-fault plastic yielding, but the reduction is still visible at 100 km R_{JB}-distance. Additionally, ground motion variability for the reference simulation using off-fault plasticity is close to what is commonly used in GMPEs (Boore and Atkinson, 2008), and in general lower than in the elastic simulations. Due to the heterogeneous distribution of near-fault plastic yielding, ground motion variability in the simulation with off-fault plasticity are slightly increased within 20 km to the fault.

3.4.4 The effect of attenuation on dynamic triggering

Viscoelastic attenuation is an important physical mechanism that describes the gradual damping of high-frequency seismic waves with propagation distance. Our reference scenario accounts for viscoelastic-plastic rheology. We clearly observe decreasing peak velocities with increasing travel

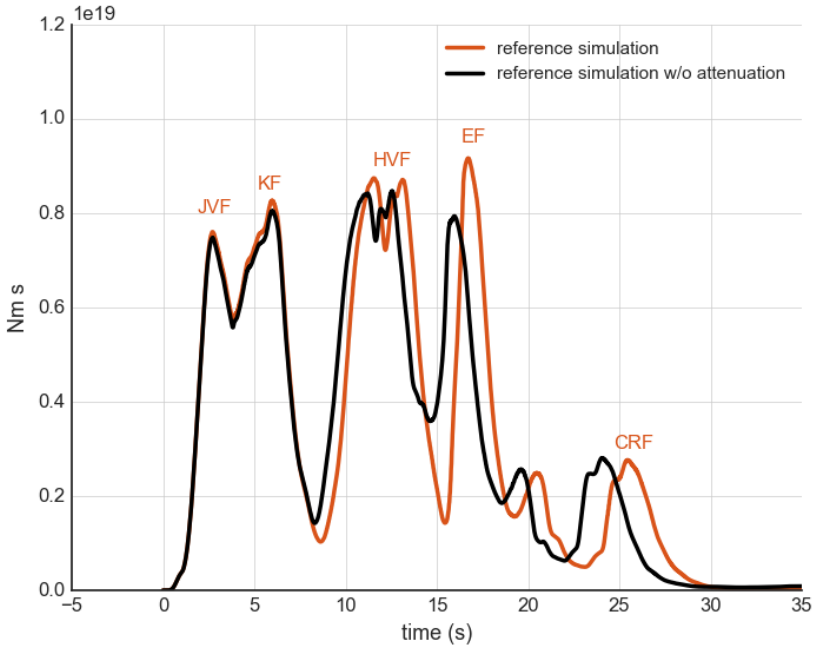

Figure 3.17: Seismic moment rate of the reference model including off-fault plasticity and viscoelastic attenuation (orange) in comparison to the corresponding simulation accounting for off-fault plasticity but not for viscoelastic attenuation (black).

distances in comparison to a setup without attenuation (see Fig. 3.D.1 in Sec. 3.D for synthetic PGVs of all seismic stations without and with accounting for seismic attenuation). However, as a consequence of the damping of the high-frequency seismic waves, seismic attenuation also affects rupture dynamics, specifically the dynamically triggered rupture transfers and re-initiation.

We find that all rupture transfer processes of our extended fault system are affected by the energy the seismic waves carry - no attenuation meaning more seismic energy and thus facilitation of dynamic triggering. Fig. 3.17 shows the moment rate over time of the reference simulation (orange) compared to the same simulation but without accounting for seismic attenuation (black). Within the first 8 s rupture propagation and moment rate release are identical. At 8.1 s, after the rupture delay at the HVF central fault bend, we observe faster rupture re-initiation in the simulation without attenuation. Additionally, rupture is dynamically triggered at the EF at an earlier time (at 15 s). With attenuation, rupture jumping to the CRF is additionally delayed (from 17.9 to 22 s).

The faster rupture initiation after the bend at the centre of the HVF in the simulation without attenuation suggests that rupture transfer is facilitated by the non-damped arriving seismic waves. We note, that dynamic triggering in a segmented fault system is highly non-linear and may bridge distances larger than expected from simplified setups (Harris and Day, 1993; Oglesby, 2008; Finzi and Langer, 2012b). For instance, at the northernmost segments which are affected by seismic waves travelling more than 50 km from the hypocentre remote triggering is delayed with attenuation. Still, the resulting slip distribution and moment magnitude is in both cases identical (M_w 7.29). A detailed analysis of the frequency bands responsible for remote triggering of rupture at adjacent fault segments will be considered in future work.

Without off-fault plasticity, rupture dynamics are less altered by ignoring attenuation. This suggests, that near fault plastic deformation here considerably increases the uniqueness of conditions

allowing sustained rupture; as a consequence dynamic triggering, and exact modelling of the emanated seismic wave field and its interaction with the fault system is crucial. The spatial extent of the Landers fault system leads to dynamic triggering effects over large distances, distances large enough to be affected critically by seismic attenuation.

3.4.5 Shallow slip at the Camp Rock fault

It is to-date under debate whether the shallow part of the CRF slipped co-seismically or if it was triggered by static stress changes shortly after the event (Sieh, 1996; Kaneda and Rockwell, 2009). A lack of aftershock recordings (Hauksson et al., 1993; Sieh et al., 1993) as well as the asymmetric right-lateral slip pattern indicate that slip may have been induced by static stress changes due to the failure of the EF (Sieh, 1996; Kaneda and Rockwell, 2009). Interestingly, slip inversion results based on GPS data (Wald and Heaton, 1994; Hernandez et al., 1999; Gombert et al., 2018) show higher shallow slip in the northernmost part of the fault system than inversions based on seismic recordings (Cohee and Beroza, 1994; Cotton and Campillo, 1995). However, due to the restriction of most inversion methods to simplified fault surfaces, it is difficult to assign the shallow slip non-ambiguously to either the EF and CRF.

The here presented dynamic rupture model of the Landers earthquake does not create large shallow slip at the northernmost fault segment. The central part of the CRF is dynamically triggered at a depth of ≈ 8 km. Rupture dies out quickly when it reaches the surface, without inducing large surface slip. Specifically interesting is the variance in SSD we infer for the CRF compared to all other fault segments (Fig. 3.6).

The here assumed regional stress field in conjuncture with the fault geometry at the CRF inhibits large surface slip. Dynamic rupture experiments varying stress orientations and stress amplitudes reveal that considerably higher surface slip is not possible to generate while breaking the full fault system and generating reasonable amount of slip at the southernmost fault segments. Thus, our dynamic rupture models align with the hypothesis of statically triggered shallow rupture.

Kaneda and Rockwell (2009) investigate the CRF in detail by analysing tectonic-geomorphic features along this fault segment. The 1992 rupture at the CRF differs distinctly from the characteristics of the penultimate and long-term ruptures. In particular, the vertical motion is almost opposite to previous ruptures. They conclude that the fault geometry might include a small dipping component at the centre of the fault segment which shows a reverse-slip motion induced by static stress changes. In contrast, our dynamic rupture model uses a vertical fault geometry for the entire fault system. Future work could investigate whether a dipping fault geometry at the centre of the CRF facilitates dynamic rupture activation and propagation at shallow depth or if shallow slip can only be induced by static stress changes.

3.5 Conclusions

We present a mechanically viable dynamic rupture scenario of the 1992 Landers earthquake, which sheds light on the physical mechanisms of rupture transferring between adjacent fault segments. Our model is characterized by a high degree of realism leading in turn to a high degree of uniqueness and reproduces a wide range of observations.

The model accounts for high-resolution topography, complex fault system geometries, 3D subsurface structure, viscoelastic attenuation, off-fault plasticity, and depth-dependent cohesion. Earthquake rupture is able to interconnect all geometrically complex segments of the fault system under the as-

sumption of smoothly varying fault stress and strength conditions. The simulation reproduces far-field and near-field observations, such as the total moment rate, final fault slip, seismic waveforms, and respective peak ground motions, as well as off-fault deformation patterns. Our dynamic rupture earthquake scenario allows detailed analysis of the mechanical sustainability of dynamic rupture transfer with respect to the interplay of tectonic stress and local fault strength conditions.

Sustained dynamic rupture of all Landers fault segments poses a strong constraint on model parametrization. Specifically, the facilitation and timing of rupture transfers between the principal fault segments determine the amplitude and orientation of initial fault stresses and friction. Scenarios succeeding in rupture across the entire fault system feature very robust slip distribution under variation of nucleation patch sizes and frictional parameters - however timing of rupture transfers are highly sensitive.

Importantly, the resulting source dynamics depict a variety of rupture transfer mechanisms, including dynamic triggering and direct rupture branching and a combination of both; both mechanisms are crucial to drive rupture across the entire fault system. Large stress changes due to the subsequent, or almost simultaneous, failure of the HVF and EF enables dynamic triggering of the CRF over distances much larger than previously suggested.

Our dynamic rupture model reveals that dynamic triggering - often associated with the observed segmentation of moment release - is not the only feature reducing the moment release. In particular, rupture deceleration due to complex fault geometry strongly affects the moment-release rate, thus complicating the inference of rupture transfer mechanisms from observations.

In distinction to previous models (Aochi and Fukuyama, 2002; Aochi et al., 2003b), we find that a steeply oriented regional stress field (maximum principal stress close to north) is crucial to allow the northernmost part (CRF) to rupture. Interestingly, large shallow slip of the CRF is dynamically inhibited in our scenario, supporting the hypothesis of statically triggered shallow rupture at the CRF shortly after the main event (Sieh, 1996; Kaneda and Rockwell, 2009). We find that it is impossible to generate considerably higher surface slip by variations in stress orientations and stress amplitudes while simultaneously breaking the entire fault system and creating reasonable amount of slip at the southernmost fault segments.

Rupture termination in our model is overall independent of the geometrically prescribed fault endings, with exception of the northernmost section of the HVF. Rupture is stopped smoothly corresponding to fault orientation towards the principal stress orientation. Our dynamic rupture model therefore provides a consistent explanation for spontaneous rupture termination on most of the principal fault segments, although fault structures in reality continue.

We show that an along-strike variability of the SSD of up to 20% is possible, even for laterally constant rock cohesion and bulk friction. These variations can be attributed to different principal stress directions and complex fault geometry. Relatively high SSDs (up to 50%) are possible for good quality rock without the presence of pre-existing fault-damage zones if stress drop is high. We observe dramatically increased off-fault deformation in the vicinity of fault bends and intersections, in excellent agreement with recent maps of fault-zone width (Milliner et al., 2015). Good agreement of synthetic waveform characteristics and associated peak ground velocities with observations include capturing of the main S-wave pulses, amplitudes, and shaking duration, indicating not only the quality of dynamic rupture model, but also of the numerical method used.

In contrast to a purely elastic simulation, our viscoelastic-plastic scenario reduces the mean PGVs in forward direction by up to 35%, while ground motions perpendicular to the fault are very similar. Rupture transfer and moment rate of the simulation with plasticity can be partially emulated by an elastic simulation with increased critical slip distance D_c that leads to slower rupture speeds and longer delays for transferring rupture to adjacent segments. However, the elastic simulation with decreased rupture speed still overestimates PGVs in forward rupture direction by 11%. Consequently,

the increase of D_c can only partially explain the effects of plasticity – at least when we use constant D_c.

Ground motion variability with respect to fault distance is in general lower for the simulation with off-fault plasticity, and found to be close to the commonly used value of 0.56 (e.g., Boore and Atkinson, 2008). However, the simulation accounting for plastic yielding creates higher ground motion variability close to the fault, presumably due to the heterogeneous distribution of near-fault plastic yielding.

We find that the complex source dynamics of the Landers fault system induce dynamic triggering over large distances, which are large enough to be strongly affected by seismic attenuation. The effect of attenuation on dynamic triggering is pronounced for models including off-fault plastic deformation. This suggests that our chosen model ingredients considerably increase the uniqueness of conditions allowing sustained rupture;

We demonstrate that physics-based modelling of realistically constrained, in-scale earthquake scenarios may successfully complement and augment earthquake source observations. An improved understanding of earthquake source physics can be achieved when combining various representations of natural complexities.

Acknowledgements

We thank Christopher Milliner for providing the left part of Fig. 3.12 which is similar to Fig. 7 in Milliner et al. (2015). All data used are listed in the chapter. Simulation results were obtained using the open-source software package SeisSol, freely available at github.com/SeisSol/SeisSol. Computing resources were provided by the Leibniz Supercomputing Centre (LRZ, projects no. pr45fi and pr63qo on SuperMUC). The work presented in this paper was supported by the German Research Foundation (DFG) (projects no. KA 2281/4-1, GA 2465/2-1, BA 3529/6-1), by the Bavarian Competence Network for Technical and Scientific High Performance Computing (KONWIHR), project GeoPF (Geophysics for PetaFlop Computing), by the Volkswagen Foundation (project ASCETE – Advanced Simulation of Coupled Earthquake-Tsunami Events, grant No. 88479), by the European Union's Horizon 2020 research and innovation program under grant agreement No. 671698 and by King Abdullah University of Science and Technology (KAUST) in Thuwal, Saudi Arabia, under grant ORS-2016-CRG5-3027-04 and OSR-CRG2017-3389. P. M. Mai is sponsored through KAUST research fund BAS/1339-01-01.

Additional information

3.A Cohesive zone width

Wollherr et al. (2018) find, that the cohesive zone width can vary considerably across geometrically complex fault systems. The authors suggest that its minimum should pose the inherent length scale to be resolved instead of an average value. Additionally, a measured cohesive zone width may vary with underlying (coarse) fault discretization. Only for sufficiently high resolutions of the fault, one can determine a correct ("numerically converged") cohesive zone width. Higher resolutions need to be considered to determine whether the cohesive zone width reached a stable value (i.e. converged) or if the solution is still changing with mesh refinement.

To calculate the cohesive zone width, we determine the time of the onset of rupture (RT), as well as the time when shear stresses reach their dynamic value (DS). Using the rupture speed v_r, the cohesive zone is then defined by the formula $(DS-RT)v_r$. For our preferred model the minimum cohesive zone width is measured as 155 m located at the HVF at a depth of 8 km. For a given on-fault resolution of 200 m, the minimum cohesive zone is then resolved by 0.775 mesh elements (or 4.56 sub-elemental Gaussian integration points for polynomial degree p = 4.). Note, that due to the different principal stress amplitudes and orientations used in this model, the rupture path varies from the scenarios in Wollherr et al. (2018) and consequently the cohesive zone width is slightly smaller than reported therein.

The convergence rates in Wollherr et al. (2018) help to determine the potential error level with respect to a high-resolution reference solution given the minimum cohesive zone width resolution and a polynomial degree p. For $p = 4$, the 200 m on-fault resolution corresponds to a mean error of 0.16% for peak slip rate time, 4.16% for peak slip rate, 0.15% for rupture arrival and 0.94% for final slip. These values are sufficiently small to accurately resolve the source dynamics (Day et al., 2005).

3.B Resolved frequencies

We analyze the distance-dependent frequency content of synthetic velocity recordings to determine the maximum resolved frequency content of the wave field in our simulation. Fig. 3.B.1 shows the normalized frequency spectrum of the observed and simulated seismic velocities for a selection of seismic stations. The stations locations are visualized in Fig. 3.7. Their full name, R_{JB}-distance, and corresponding Vs_{30}-value and can be found in Table 3.1.

The highest resolved frequencies are determined by evaluating the maximum frequency for which the synthetic spectra align with the expected ω^{-1} frequency decay. In particular close to the faults, our simulation reaches very high frequencies without modelling small-scale roughness or pre-stress heterogeneities. The station LUC, which is the closest station to the fault traces (0.47 R_{JB}-distance), shows frequencies reaching up to 4.0 Hz. The stations YER (24.37 km R_{JB}-distance) in forward direction includes frequencies up to $\approx$ 3.0 Hz. With increasing distance the resolved frequency content increasingly deviate from an ideal ω^{-1} decay: Stations FRT (64.97 km R_{JB}-distance) and BOR (87.33 km R_{JB}-distance) reach up to 2.0 Hz and 1 Hz, respectively. In the low velocity basin of the Salton Sea, station SAL (102.8 km R_{JB}-distance) only resolves a maximum frequency of 1.0 Hz. Therefore, to assure consistent frequency ranges of all synthetics, we bandpass filter all stations in Sec. 3.3.5 in between 0.1 and 1.0 Hz.

3.C Peak ground motions maps

We here show a close-up of the PGVs of the three presented simulations in Sec. 3.4.2: the reference simulation with plasticity (Fig. 3.C.1a), the corresponding elastic simulation (Fig. 3.C.1b) and the corresponding elastic simulation with increased D_c (Fig. 3.C.1c). Consistent with the findings for the mean PGVs with respect to the distance or azimuth bins in Sec. 3.4.2, we find that the directivity effect is much more pronounced in the elastic simulations. However, an increase of D_c in the elastic simulation drastically reduces the PGVs in forward direction while the PGV in the Salton Sea Basin are slightly increased due to the slower rupture which results in more backward propagating rupture. Still, ground motions in the plastic simulation differ, in particular in the forward direction.

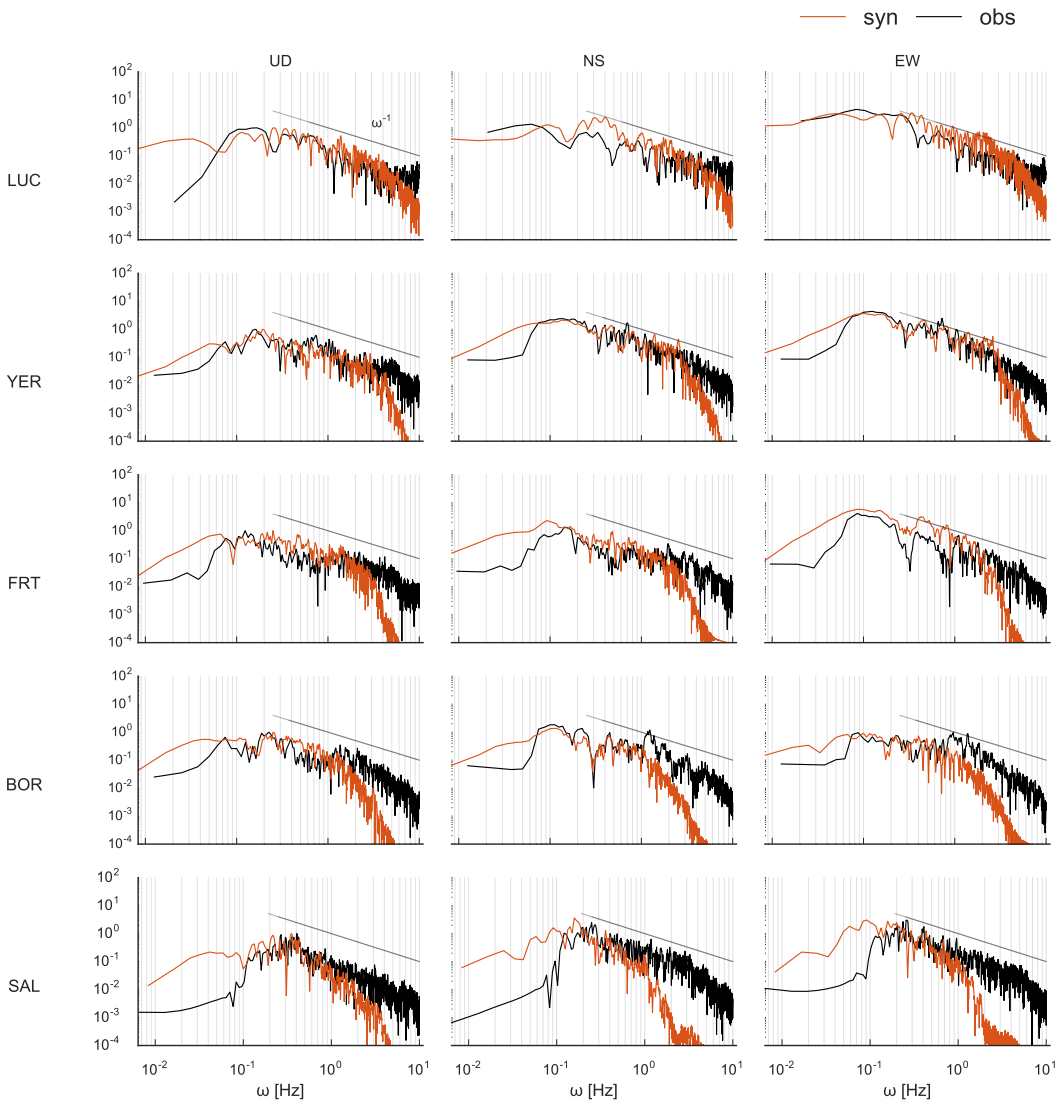

Figure 3.B.1: Normalized frequency spectra for observed (orange) and simulated (black) seismic velocities for a selection of stations listed in Table 3.1. The stations are ordered by their R_{JB}-distance. The black line indicates the ideally expected frequency decay of ω^{-1}. The frequencies are cut at their respective Nyquist frequency.

3.D Effect of attenuation on peak ground motions

We discuss in Sec. 3.4.4 the effect of attenuation on source dynamics, in particular on dynamic triggering. Fig. 3.D.1 shows how attenuation affects the the simulated PGVs for the stations listed in Sec. 3.3.5 and visualized in Fig. 3.7. While PGVs are almost identical for near-fault stations up to 20 km R_{JB}-distance, we observe a clear decrease in PGVs for greater distances due to the attenuation of seismic waves with propagation distance.

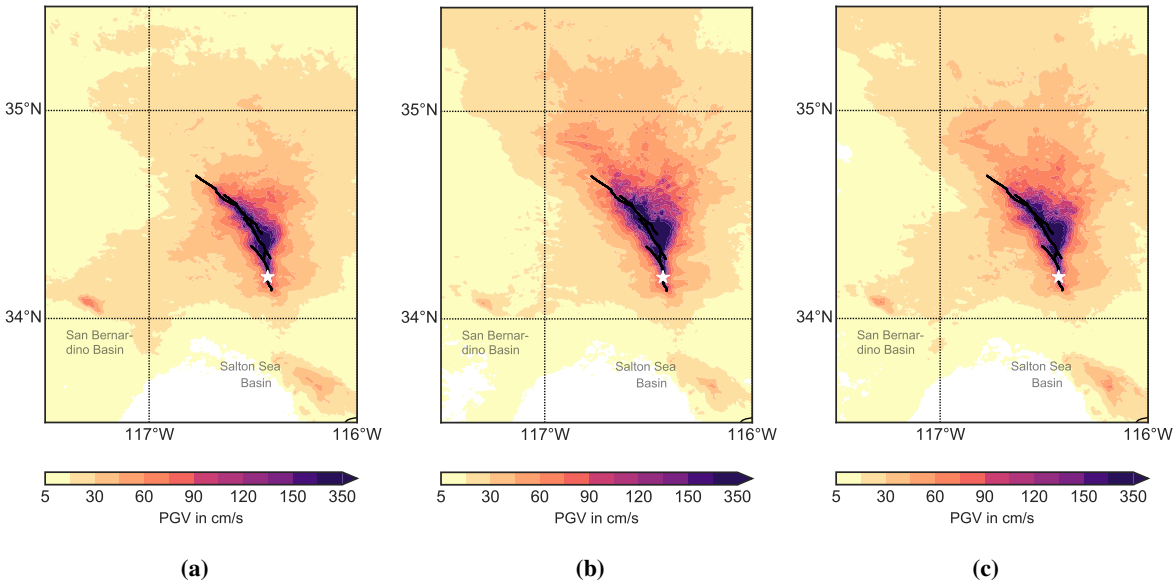

Figure 3.C.1: Simulated GMRotD50 (Boore et al., 2006) PGVs above 5 cm/s for the a) reference simulation with plasticity, b) the corresponding purely elastic simulation and b) for the purely elastic simulation with increased D_c. The white star marks the epicenter of the 1992 event.

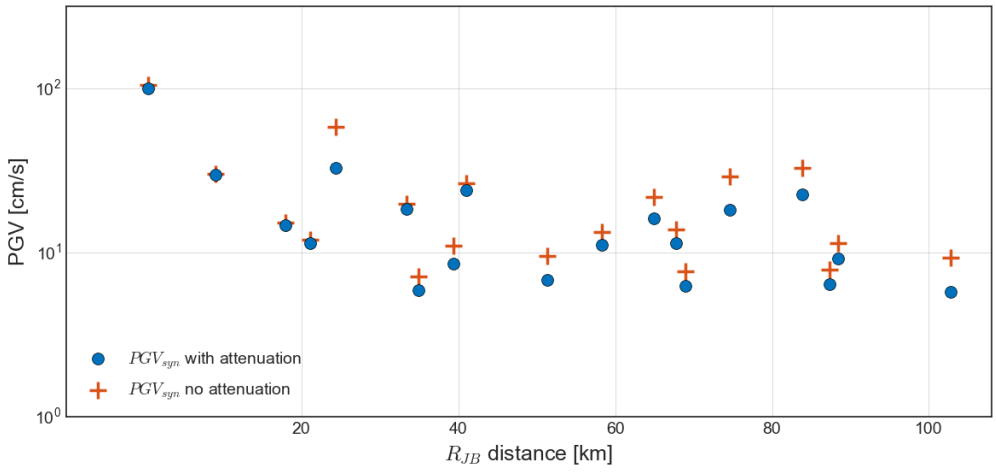

Figure 3.D.1: Simulated PGVs with (blue circles) and without attenuation (orange crosses) in dependence of R_{JB}-distance of the stations given in Table 3.1.

4

Off-fault plasticity in a large-scale dynamic rupture model of the 2004 Sumatra-Andaman earthquake

Abstract

The 2004 Sumatra-Andaman earthquake was one the biggest earthquakes of the last century and was followed by a series of devastating tsunamis that affected people in over 14 countries. The underlying source dynamics are still not completely understood since near-field data is sparse and different studies have not reached full agreement regarding its total moment and slip distribution. Dynamic rupture models provide physically-consistent source dynamics and the associated seafloor displacement that might shed light on the conditions that caused the deadly tsunamis.

While the 2004 Sumatra-Andaman model presented in Uphoff et al. (2017) was based on purely elastic material properties, we investigate for the first time the influence of off-fault plastic material response on source properties and surface displacement in a 3D large-scale dynamic rupture scenario. The model features a complex, low dipping fault geometry, splay faults, and rotating horizontal initial stress conditions. We find a clear correlation between the angle Ψ that forms between the orientation of the horizontal principal stress and the fault strike and the increase or decrease of on-fault slip when accounting for off-fault plasticity. As a consequence of the changed on-fault slip, the vertical uplift is altered along the entire trench. The results highlight the need for realistic material properties in subduction zone models for correctly assessing the potential tsunami hazard of megathrust earthquakes.

This chapter extends the model presented by Uphoff, C., Rettenberger, S., Bader, M., Madden, E. H., Ulrich, T., **Wollherr S.** and Gabriel, A.-A. (2017): Extreme Scale Multi-Physics Simulations of the Tsunamigenic 2004 Sumatra Megathrust Earthquake (in *Proceedings of the International Conference for High Performance Computing, Networking, Storage and Analysis (SC'17)*) which received the Best Paper Award. The here presented work will eventually be published as part of a second joint article focusing on the geophysical analysis of the Sumatra-Andaman setup and a more detailed parameter study.

4.1 Introduction

The Sunda megathrust is located at the convergent tectonic boundaries where the Indian and Australian plates descend beneath the Sunda plate. The megathrust stretches across a length of 5500 km and is associated with a high seismic activity. On December 26, 2004 the Sumatra-Andaman earthquake ruptured approximately 1200- 1500 km of the northernmost part of the Sunda megathrust, the greatest length of any recorded earthquake (Shearer and Bürgmann, 2010). With an estimated magnitude of 9.0-9.3 (Lay et al., 2005; Stein and Okal, 2005; Banerjee et al., 2005), the earthquake was also one of the largest with respect to its released seismic energy. Even at distances of up to 4500 km from the epicentre, static offsets at GPS stations were observed (Banerjee et al., 2005).

The earthquake was followed by a sequence of devastating tsunamis that most severely impacted the Aceh region (northern part of Sumatra) where wave heights reached 30 m along the western Aceh coast (Shearer and Bürgmann, 2010). They also affected the shores of a great part of the Indian Ocean, particularly the coastlines of Indonesia, Thailand, Sri Lanka, India, and the Maldives. The tsunamis rather than the ground motions associated with the earthquake itself killed more than 200 000 people in 14 countries, and even more lost their houses and properties.

The earliest tsunami waves reached the Andaman and Nicobar islands already minutes after the earthquake causing major destructions of the island environment. However, it took over 2 hours until the tsunami waves reached more distant shores such as the coastlines of Sri Lanka. Many lives could have been saved if tsunami early warning was more developed at the time (Sieh, 2006). Driven by this event, tsunami early warning, local disaster management, and disaster precautions training around the Indian Ocean were initiated and improved. In addition, researchers have been investigated the source dynamics of the earthquake to find explanations how such devastating tsunamis form (Lay et al., 2005; Plafker et al., 2006; Geist et al., 2007; Dean et al., 2010).

The earthquake source characteristics of the 2004 Sumatra-Andaman earthquake are still not understood in detail since different studies have not reached full agreement regarding its total moment and slip distribution (and references therein Shearer and Bürgmann, 2010). Large uncertainties also remain concerning the exact geometry of the ruptured subduction interface including its depth and dip angle and whether or not the rupture reached the seafloor (Quentin et al., 2016). However, studies of the 2004 Sumatra-Andaman earthquake agree that the earthquake is in general associated with a low rupture speed of 2.1-2.8 km/s (e..g., Ni et al., 2005; Stein and Okal, 2005; Krüger and Ohrnberger, 2005) and a total rupture duration between 8 and 10 minutes. Due to the large tsunami waves observed in the Aceh province, rupture along the megathrust might have been accompanied by rupture along splay faults, steeply dipping from the main megathrust fault (Plafker et al., 2006; Sibuet et al., 2007; Waldhauser et al., 2012).

To study the earthquake-induced tsunami generation, tsunami models often use kinematic dislocation models for fault slip that are translated into a static seafloor displacement using Okada's solution (Okada, 1985, 1992). However, the exact slip distribution is often not known or difficult to constrain (Ammon et al., 2005; Poisson et al., 2011). Further, static displacements might be an oversimplification for tsunami sources, in particular for earthquakes with such a spatial and temporal extend as the Sumatra-Andaman earthquake (Poisson et al., 2011). Dynamic earthquake models of spontaneous earthquake rupture are able to provide a physically consistent slip distribution by modelling frictional sliding along a fault and the associated ground deformations. The results of these dynamic rupture simulations can be used as spatio-temporal input for tsunami modelling tools which will help to reduce uncertainties associated with the tsunami sources.

Realistic model ingredients are key to quantify the related tsunami hazard of an earthquake. While Okada's solution is restricted to the linear elastic half-space, it is found that plastic deformation during earthquake rupture absorbs part of the released seismic energy altering ground motions (Roten et al., 2014, 2015), rupture transfers in complex fault system (Wollherr et al., 2018) and reducing shallow slip (Roten et al., 2017). In asymmetric fault geometries of subduction zones, these implications likely change final seafloor displacement and hence the tsunami genesis of an earthquake. Dynamic rupture simulations on planar dipping faults show that plastic yielding in the overriding wedge locks the upper part of the fault which results in a distinct, more vertical seafloor uplift (Ma, 2012; Ma and Hirakawa, 2013). However, all previous studies of subduction zones including plasticity were restricted to 2D. Here, we investigate for the first time the influence of off-fault plastic material response on source properties and surface displacement for the example of the complex 3D subduction zone model of the 2004 Sumatra-Andaman earthquake.

From a numerical point of view, this model is extremely challenging. Due to the long duration and the large spatial extent of that earthquake in addition to the on-fault high-resolution that is required to accurately model the frictional sliding process, numerical models quickly exceed millions of mesh elements. In addition, the geometric complexity of subduction zones, specifically faults intersecting the bathymetry at shallow angles, may lead to small in-sphere radii of the mesh elements. As a consequence, the required time step for stability is reduced and computational costs will drastically increase when all elements use the minimum required time step dictated by the smallest element. Computational costs further increase due to the incorporation of new modelling features such as off-fault plasticity which is associated with additional non-linear equations.

To handle these extreme-scale simulations within a reasonable amount of computational time, we use the dynamic rupture software SeisSol which is optimized for the efficient use on high-performance computing infrastructure. The up-to-date largest and longest dynamic rupture simulation has been made possible by incorporating a local time-stepping algorithm (Uphoff et al., 2017) amongst other recent optimization efforts (Heinecke et al., 2014; Breuer et al., 2014; Rettenberger et al., 2016). Uphoff et al. (2017) present the first dynamic rupture simulation of the 2004 Sumatra-Andaman earthquake which reproduces some of the main observed characteristics of the event such as magnitude and measured GPS displacements. However, their model assumed purely linear elastic material properties. Due to the efficient implementation of plasticity, using optimized matrix-vector multiplications (Wollherr et al., 2018), we are able to investigate the effect of more realistic material behaviour in this large-scale simulation of the 2004 Sumatra-Andaman earthquake with only a few percentages of additional computational costs.

The work is structured as follows: in Sec. 4.2 we first summarize the model of the 2004 Sumatra-Andaman earthquake which comprises layered material properties, varying fault strike, and rotation of the initial background stress, as well as a non-planar, low dipping fault, and splay faults following the model presented in Uphoff et al. (2017). The model is extended to account additionally for off-fault plastic processes. Sec. 5.4 then focuses on a detailed comparison between the purely elastic simulation and the simulation with off-fault plasticity with respect to on-fault dynamics and surface displacements. The results suggest that the effect of inelastic off-fault processes is more complex than previously inferred from 2D simplified setups which postulate an increase in vertical uplift when accounting for plasticity (Ma, 2012).

4.2 Model

In the following, we shortly summarize observational constraints and the initial conditions used for the dynamic rupture model of the 2004 Sumatra-Andaman earthquake. To create a highly realistic model of the Sumatra-Andaman region, we combine a bent fault geometry constrained from independent and complementary datasets, topography and bathymetry, local velocity structure, and stress conditions based on inversion studies. The here presented model is identical with the structural model and geometry used in the Sumatra setup of Uphoff et al. (2017) but additionally accounts for off-fault plasticity.

4.2.1 Structural model, fault geometry, and discretization

Subduction zones are characterized by their complex structure which is formed by the subduction of the heavier plate below a lighter plate at convergent tectonic plate boundaries. In the case of the Sunda megathrust, which partially ruptured during the 2004 Sumatra-Andaman earthquake, the Australian and Indian plates are subducting below the Sunda and Burma plates. Our conceptual 3D velocity model of the Sumatra-Andaman region features a 1D layered structure for the overriding continental crust as well as several bent layers of oceanic crust which follow the dip of the subduction zone interface (Fig. 4.1a). Each layer depicts a distinct velocity and density structure, visualized by different colours and their respective p-wave velocity in Fig. 4.1a. The material properties for the three continental and four oceanic layers are averaged from the velocity model of Crust1.0 (Laske et al., 2013). P-wave velocities for each domain range between 8.1 km/s below the oceanic crust (dark blue) up to 5.0 km/s in the uppermost layer of the oceanic crust (light blue).

The model incorporates 30 arc-second resolution bathymetry and topography data from GEBCO (Weatherall et al., 2015). The dataset is subsampled to the actual mesh resolution of 4 km within a refinement area denoted by the pink box in Fig. 4.2 where we resolve frequencies up to 0.33 Hz. Outside this area, the mesh discretization is coarsened by 15% (corresponding to a gradation rate of 0.3 for the meshing software Simmodeler by Simmetrix (Simmetrix Inc., 2017)) to save computational costs.

The geometry of the megathrust is based on the community model collection Slab1.0 (Hayes et al. (2012)) which combines several independent datasets ranging from historic seismicity to active seismic profiles. Since no data is available for the northernmost part of the Sunda megathrust, the Slab1.0 geometry is extended to the north by sweeping the northernmost depth profile of Slab1.0 along the known trench location. Besides this first-order geometry, little is known about whether the megathrust rupture actually reached the seafloor during the 2004 Sumatra earthquake (Quentin et al., 2016). Here, we assume that rupture went all the way up to the trench and extend the fault geometry such that it intersects with the seafloor. The extension (5 to 15 $^\circ$ dip) is steeper than the upper part of Slab1.0, which is mostly flat, mimicking a likely short splay fault at the tip of the megathrust interface. The fault is completely embedded in the velocity layer with the lowest P-wave speed of 5000 m/s (the first layer of oceanic crust).

The role of splay faults with respect to the tsunami genesis is still under debate. Splay faults with steeper dipping angles than the megathrust generate high vertical seafloor uplift more efficiently (e.g., Moore et al., 2007; Wendt et al., 2009). Seismic reflection data, as well as relocated seismicity, suggests that there exist several thrust faults branching from the megathrust (Sibuet et al., 2007; Singh et al., 2008; Chauhan et al., 2009; Lin et al., 2009) which might have been the driving force of the tele-tsunami source (e.g., Waldhauser et al., 2012). We incorporate three splay faults, one forethrust, and two backthrust faults located to the west of northern Sumatra, synchronized from the datasets

mentioned above, to investigate the effect of plasticity on the vertical seafloor uplift of the splay fault. The splays intersect the top layer of the oceanic crust as well as all layers of the continental crust. Fig. 4.2 visualizes a top-view of the resulting megathrust including the three splay faults while Fig. 4.1a presents a close-up to the splay fault geometries. The fault surfaces are discretized by elements of 400 m edge length to ensure the accurate resolution of the fault dynamics (see Sec. 4.2.4 below).

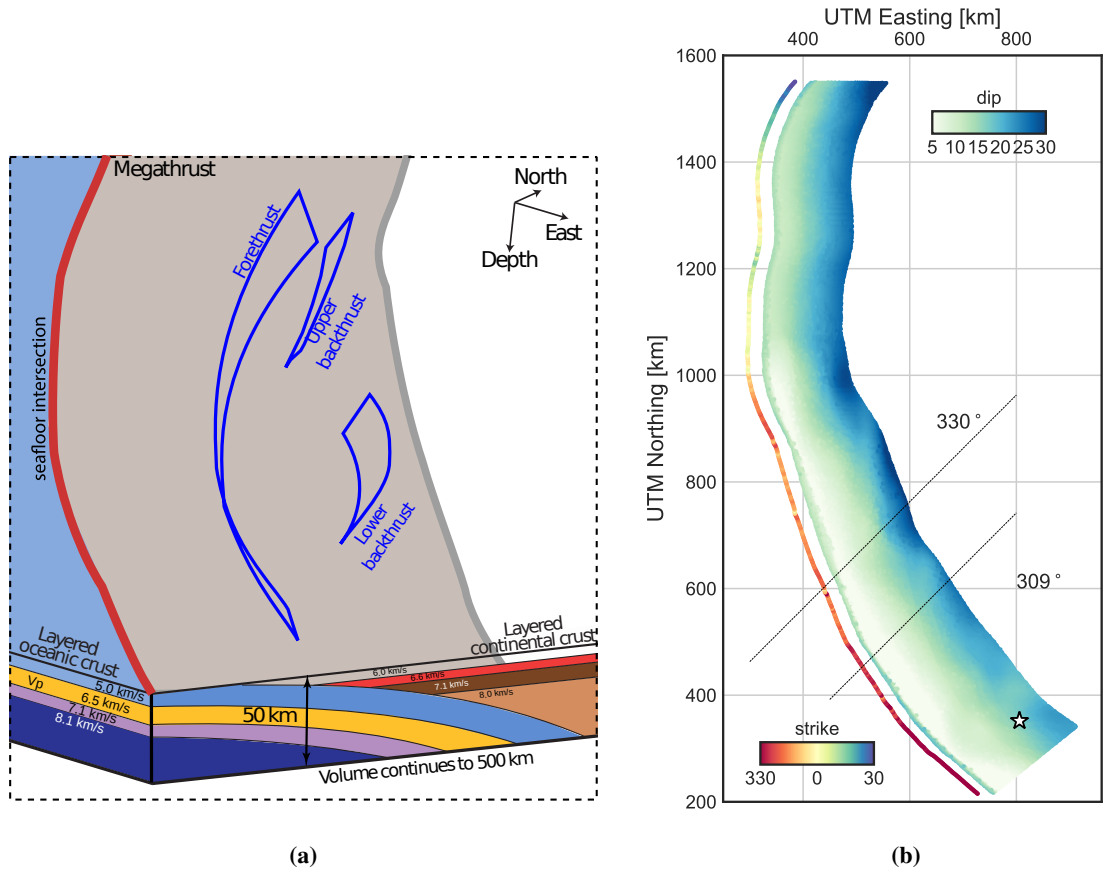

Figure 4.1: a) 3D geometry of the region marked by the black dotted box in Fig. 4.2. The structural model includes different layers characterized by different P-wave speeds. Red curves mark the megathrust trench and blue the splay faults. The megathrust fault surface is embedded in the lowest velocity layer (light blue). The figure is adapted from Fig.1 in Uphoff et al. (2017). b) Strike and dip variation of the megathrust geometry. The strike angle of the trench is plotted with an offset from the trench while the fault surface is coloured by its dip angle. The area between the solid lines represents the transition zone in which the orientation of the second principal stress smoothly rotates from 309° in the south to 330° in the north. The hypocenter is marked by a white star.

Fig. 4.1b inspects the variation in strike angle of the megathrust at the trench as well as the dip angle along-strike and along-depth. Note, that the megathrust trench is located to the west and that fault depth increases towards the east. The strike variation of the trench is plotted with an offset from the trench while the fault surface is coloured by its dip angle. The bent megathrust interface dips almost horizontally in the shallow part of the fault (with the notable exception of the extension toward the trench, previously commented) and is much steeper (up to 46 ° dip) at 50 km depth. For locations above 1000 km UTM Northing (above 10° latitude), fault dip slightly increases in its shallowest part.

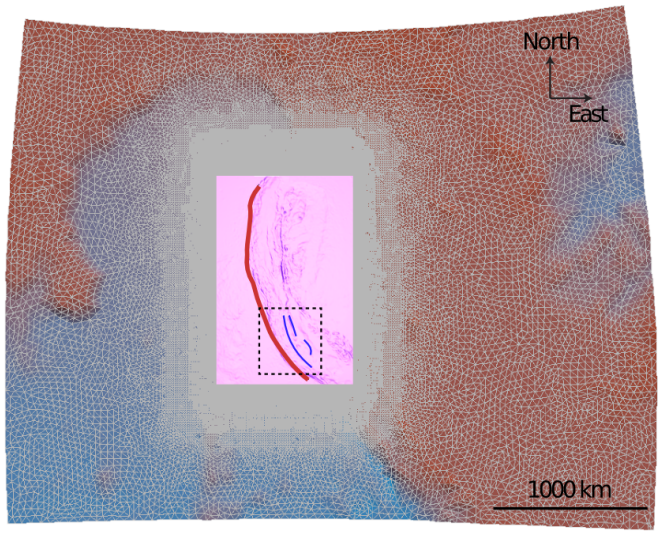

Figure 4.2: Unstructured tetrahedral mesh of the modelling domain including a refinement area (pink box) with higher mesh resolution of the 30 arc-second topography from GEBCO (Weatherall et al., 2015). Blue curves are splay fault traces and red the megathrust trench (adapted from Fig.1 in Uphoff et al. (2017)). The dashed lines mark an inset that is visualized in Fig. 4.1a.

Fault strike rotates almost gradually from 321 ° in the south to 32 ° in the north. Implications of this fault geometry on the rupture dynamics will be discussed in Sec. 5.4.

4.2.2 Initial stresses and friction

Dynamic rupture simulations are crucially dependent on their assumed initial conditions in terms of stresses and friction; it determines whether rupture can be sustained along the fault and the amount of total slip generated during coseismic rupture. This section describes the principal stress orientations, the stress field amplitudes, and assumed frictional parameters for the 2004 Sumatra-Andaman setup.

Following Hardebeck (2012), we define a non-andersonian stress state, in which the second principal stress is horizontal, roughly pointing in the strike direction. The horizontal principal stress is orientated at 309° in the south and gradually rotates to 330° within the transition zone between 450 km and 620 km UTM Northing, as suggested by stress inversions (Hardebeck, 2012) and by the orientation of the ground displacement data. The distinct zones are marked by solid lines in Fig. 4.1b and for reference in all following figures in the results section. The plunge of the maximum and minimum principal stresses, σ_1 and σ_3, is 8°, within the range of uncertainty denoted by Tsai et al. (2005) and Hardebeck (2012). The confining stress varies linearly with depth, in accordance with rock mechanics theory and field observations.

Following Aochi and Madariaga (2003) and Ulrich et al. (2018), we constrain the magnitude of the deviatoric stresses by prescribing the relative pre-stress ratio R (here 0.7) and the stress shape ratio $\nu = (\sigma_2 - \sigma_3)/(\sigma_1 - \sigma_3)$, where $\sigma_1 > \sigma_2 > \sigma_3$ are the principal stresses magnitudes (here $\nu = 0.5$). R is defined as fault stress drop $\Delta\tau = \tau^0 - \mu_d\sigma_n^0$ over breakdown strength drop $\Delta\tau_b = c + (\mu_s - \mu_d)\sigma_n^0$ for given static and dynamic friction μ_s, μ_d, frictional cohesion c, and initial on-fault shear and normal stresses τ^0 and σ_n^0.

In crystalline rocks, fluid pore pressure P_f can be assumed to be hydrostatic, i.e. $P_f(z) = 1000.0\,\rho_{avg}z$ Pa for depth z and ρ_{avg} being the average density of the overlying rock at that depth. However, in clas-

sic continental margins, fluid pore pressure appears to be overpressured below some critical depth (Suppe, 2014). Here, we assume fluid pore pressure to linearly increase from hydrostatic to close to lithostatic ($P_f(z) = 2000.0\ \rho_{avg} z$) between 5 km and 10 km depth.

Subduction zones are characterized by considerably lower friction than what is commonly assumed for intraplate earthquakes (Suppe, 2007, 2014). Here, we parametrize the frictional boundary (fault) using a linear slip weakening constitutive relation(Ida, 1972; Okubo and Dieterich, 1981; Andrews, 1985), in which the friction coefficient drops linearly from its static value μ_s = 0.3 to its dynamic value μ_d = 0.2 over a critical slip distance D_c = 0.8 m.

The shallowest part of subduction zones is considered to be an aseismic area due to the presence of unconsolidated material and smectites that depicts velocity-strengthening frictional properties (e.g., Marone and Scholz, 1988; Vrolijk, 1990). To mimic a velocity-strengthening behaviour in the shallow region of the megathrust, frictional cohesion at the fault is linearly increased from its constant value of 0.4 MPa at a depth of 10 km to 1.4 MPa at a depth of 0 km. In that manner, the strength of the fault is increased which hampers rupture propagation. Starting at a depth of 25 km, we account for the transition from the brittle to ductile regime by linearly decreasing deviatoric stresses to zero which allows rupture to stop smoothly.

4.2.3 Off-fault plasticity

Off-plasticity is incorporated in SeisSol using a Drucker-Prager yield criterion (Wollherr et al., 2018) which requires the specification of initial stresses, bulk cohesion c_{bulk}, and internal rock friction ϕ for the entire simulation domain.

Initial stresses are assumed to be the same as the one acting on the fault (described in Sec. 4.2.2), including the rotation from 309° in the south towards 330° in the northernmost part of the megathrust. Bulk cohesion c_{bulk} depends on rock type, but also on depth as it might be proportional to the vertical forces acting on the rock (Wang and Hu, 2006). We follow Ma (2012) and couple c_{bulk} to the effective vertical stress $\bar{\sigma}_{zz} = \sigma_{zz} - P_f$ with $c_{bulk} = 0.1008\ \bar{\sigma}_{zz}$. Minimum cohesion values reach 0.85 MPa at the surface and cohesion increases up to 52.0 MPa at depth of 50 km, consistent with commonly assumed depth-dependent values derived by Hoek-Brown parameter conversions (e.g., Roten et al., 2016). Note that the vertical stress $\bar{\sigma}_{zz}$ is independent of the horizontal principal stress orientation and hence, cohesion is laterally homogeneous. The internal friction ϕ is constant and equal to the static friction of 0.3 throughout the simulation domain.

For the plastic calculations, stresses σ_{ij} are adjusted whenever the second invariant of deviatoric stresses $\sqrt{I_2}$ overcomes the elastic yield limit τ_c (i.e. $\sqrt{I_2} \geq \tau_c$). We can determine the closeness of plastic failure (CF) prior to the simulation by evaluating $\sqrt{I_2}$ and τ_c for the assumed initial stresses σ^0_{ij}:

$$\text{CF} = \frac{\sqrt{I_2}}{\tau_c} = \frac{\sqrt{0.5 \sum_{ij} s^0_{ij} s^0_{ji}}}{c_{bulk} \cos(\phi) - \sigma^0_m \sin(\phi)}, \tag{4.1}$$

with initial deviatoric stresses s^0_{ij} and initial mean stress $\sigma^0_m = 1/3 \sum_i \sigma^0_{ii}$. The closer CF is to 1, the closer are the initial conditions to plastic failure.

As a consequence of the rotation of the horizontal principal stress from 309° to 330°, CF slightly changes between these three different stress regimes with the highest CF in the region with 330° (see Fig. 4.1b). CF linearly increases from 0.56 for the stress orientation of 309° to 0.63 for the stress orientation of 330° in the uppermost 25 km. CF decreases for all three cases starting at a depth of

25 km when differential stresses are linearly tapered to zero. Minimum CF values reach 0.47 to 0.53 for principal stress directions of 309° and 330°, respectively.

In contrast to what is assumed by the numerical models which are based on the critical wedge theory (Wang and Hu, 2006), the here presented scenario is initially not very close to plastic failure (CF=1). Simplified 2D scenarios on planar dipping faults with an accretionary wedge very close to failure (CF= 0.9-0.99) show high effects of plasticity on seafloor deformations and rupture dynamics (Ma, 2012; Ma and Hirakawa, 2013). In this work, we investigate the effect of plasticity for a realistic 3D subduction geometry with a more moderate CF.

Note that in contrast to the on-fault shear and normal stresses, stresses for the plastic calculations do not dependent on the fault geometry. However, the evolving rupture dynamics and as a consequence the dynamic stress change is dependent of the fault geometry and the background stress orientation which influence the occurrence of plastic deformation (e.g., Templeton and Rice, 2008; Wollherr et al., 2018).

Plastic strain at time t is mapped into the scalar quantity $\eta(t)$ (e.g., visualized in Fig. 4.10) following Ma (2008):

$$\eta(t) = \int_0^t d\eta = \int_0^t \sqrt{\frac{1}{2}\dot{\varepsilon}_{ij}^p \dot{\varepsilon}_{ij}^p}. \tag{4.2}$$

with $\dot{\varepsilon}_{ij}^p$ being the inelastic strain rate.

4.2.4 Simulation software and computational costs

The spatial extent (1500 km long fault surface) and temporal duration (over 400 s of rupture) of the 2004 Sumatra event make it indispensable to use massively parallel high-performance computing infrastructure. For the up-to-date largest and longest dynamic rupture simulation, we use the highly-efficient open-source software package SeisSol (www.seissol.org; freely available at github.com/SeisSol/SeisSol). The software exploits an Arbitrary high order DERivative-Discontinuous Galerkin (ADER-DG) method which enables high-order accuracy in space and time (Käser and Dumbser, 2006; Dumbser and Käser, 2006). Dynamic rupture is incorporated by solving the non-linear problem of spontaneous frictional failure on a prescribed fault surface (De la Puente et al., 2009; Pelties et al., 2012, 2014). On-fault slip is simultaneously coupled to seismic wave propagation such that we are able to produce the full seismic wave field including synthetic seismograms and ground displacements. The software is specifically suited for complex fault geometries due to the use of unstructured tetrahedral grids which facilitates mesh generation for shallow dipping subduction zones.

Recent optimization addresses the efficient calculation of matrix operations (Breuer et al., 2014; Heinecke et al., 2014; Breuer et al., 2014), as well as the optimization of large-scale in- and output (I/O) structures (Rettenberger et al., 2014; Rettenberger and Bader, 2015; Rettenberger et al., 2016), and the incorporating of an efficient local time-stepping algorithm (Uphoff et al., 2017). Enabled by these optimizations, SeisSol handles the extreme-scale simulation of the 2004 Sumatra earthquake within a reasonable amount of time. The mesh size of the extreme-scale run in Uphoff et al. (2017) is decreased from 221 million mesh elements to only 14 million mesh elements by decreasing the fault resolution and increasing the coarsening rate of the mesh away from the fault. Such a smaller mesh still allows to resolve the rupture dynamics but dissipates more quickly the high frequencies seismic waves emanated from the fault. In that way, we are able to run the setup on a couple of hundred of nodes instead of 3072 nodes, corresponding to the full machine of Munich's supercomputer SuperMUC phase 2. The purely elastic model requires about 2 h on 300 nodes on SuperMUC phase 1. Computational costs increase by only 7.2% when accounting for off-fault plasticity.

To accurately resolve the rupture dynamics, numerical models need to resolve the cohesive zone width. While the average cohesive zone width is highly increased when the model accounts for plasticity, the minimum cohesive zone width for both simulations is 760 m (neglecting the zone where we tapper the stresses at depth). The minimum value is reached at the trench at the northernmost part of the fault. For the given fault discretization of 400 m, the minimum cohesive zone width is resolved by 1.9 mesh elements, corresponding to 9.5 sub-elements for the spatio-temporal discretization of polynomial degree p= 3 (order of accuracy $\mathcal{O}4$). This corresponds to a mean error of 0.02% for peak slip rate time, 2.59% for peak slip rate, 0.02% for rupture arrival and 0.22% for final slip for the elastic simulation. The mean error of the corresponding simulation with plasticity is 0.08% for peak slip rate time, 2.4% for peak slip rate, 0.08% for rupture arrival and 0.5% for final slip (Wollherr et al., 2018). In both cases, the resolution is sufficiently high to accurately capture the fault dynamics (Day et al., 2005).

4.3 Results

In the following, we compare the rupture dynamics in terms of rupture speed, moment release rate and final slip, as well as seafloor displacement between the purely elastic model of the 2004 Sumatra-Andaman earthquake and the model that accounts for off-fault plasticity. We are in particular interested in knowing under which conditions plasticity alters seafloor displacement which potentially will influence the tsunami genesis.

4.3.1 Earthquake source dynamics

Moment release rate

Fig. 4.3 visualizes the moment release of the 2004 Sumatra-Andaman model over time for the purely elastic simulation (blue) and the simulation with plasticity (orange). Within the first 40 s of rupture, moment rate is identical for both models. At 45 s we unexpectedly observe a higher moment release rate in the case of plasticity. For the rest of the simulated time, the moment rate is always higher in the purely elastic model. Overall, rupture is delayed by up to 30 s due to the occurrence of plastic yielding. The corresponding moment magnitude is M_w 9.23 for the purely elastic model and is minimally decreased to M_w 9.20 for the model accounting for off-fault plasticity. Both values are in the commonly inferred range of 9.1-9.3 (Lay et al., 2005; Stein and Okal, 2005; Banerjee et al., 2005).

Rupture speed

For the Sumatra-Andaman earthquake, rupture speeds between 2300-2500 km/s were inferred (Ni et al., 2005; Ammon et al., 2005). Fig. 4.4 a) shows the inferred rupture speed of the simulation with purely elastic material properties while Fig. 4.4 b) displays rupture speed for the simulation with plasticity. The trench of the megathrust is located to the west while fault depth increases towards the east. After rupture is initiated at the very south of the fault (marked by a white star) rupture spontaneously propagates towards the north with an average rupture speed of 3150 m/s in the purely elastic model. Rupture speed is almost constant along depth. The highest values are reached at the nucleation zone and again at the most northernmost parts (1200 km and 1500 km UTM Northing) where it exceeds s-wave speed. In contrast, average rupture speed is decreased to 2980 m/s when the model accounts for plastic deformation. Rupture speed is mainly reduced in the uppermost part of the fault where the influence of plastic yielding is highest (see plastic strain accumulation in Fig. 4.10,

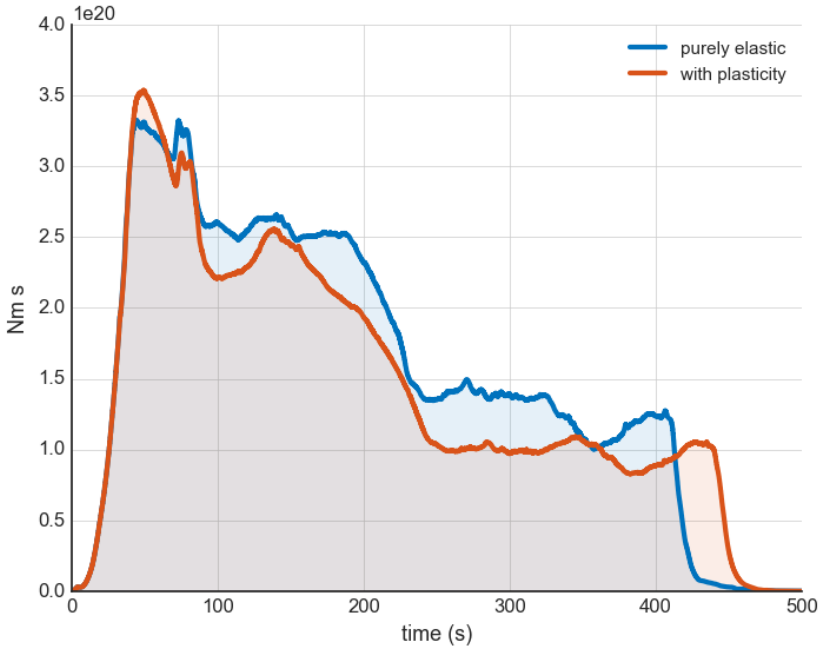

Figure 4.3: Moment release rate over time for the purely elastic model (blue) and the model with plasticity (orange).

discussed below). Rupture speed in the shallowest part is as low as 2500 m/s while it reaches almost constant values of 3200 m/s between a depth of 2.5 km and 33 km. Supershear rupture is still visible at the nucleation patch in the south, but rupture speed is highly reduced towards the northernmost parts when the model accounts for plasticity.

Both simulations slightly overestimate the average observed rupture speed of the earthquake. However, our results indicate that more realistic material properties such as the ability of the host rock to deform plastically can decrease rupture speed, in particular at shallow depths where plastic deformation predominantly occurs. These results confirm previous findings of 2D planar fault setups Ma (2009); Kaneko and Fialko (2011); Ma (2012); Finzi and Langer (2012a); Gabriel et al. (2013) and 3D strike-slip fault scenarios (e.g., Wollherr et al., 2018). Interestingly, rupture speed is decreased along the entire fault when the model accounts for plasticity, independent of whether plasticity increases or decreases the moment release.

High rupture speed close to the hypocenter in both simulations may be related to the artificial nucleation procedure together with the assumption of the well-orientation of the megathrust in the hypocentral area with respect to the regional stress which needs to be further investigated in future simulations.

Final slip distribution

Fig. 4.5 a) shows the final slip distribution of the elastic simulation and Fig. 4.5 b) the residual between the simulations with plastic and elastic material properties ($\Delta\text{slip} = \text{slip}_{pla} - \text{slip}_{ela}$). Slip in the elastic simulation is highest close to the trench reaching up to 40 m, specifically between 600 km and 800 km UTM Northing. Towards the northernmost part, slip is decreased reaching up to 20 m at

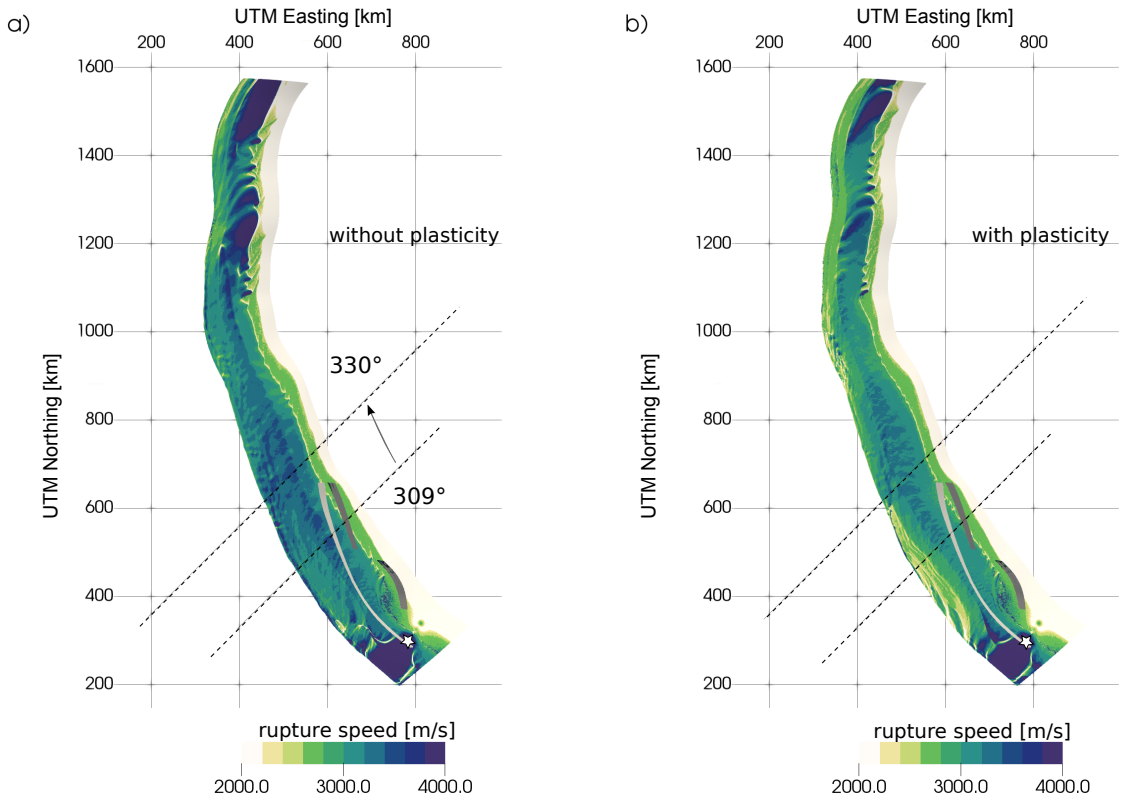

Figure 4.4: Rupture speed of the Sumatra simulation with purely elastic material response (a)) and the simulation with plasticity (b)). The hypocenter is marked by a white star. The principal stress orientation is smoothly rotated from 309° in the south to 330° in the north within the transition zone between the dashed lines.

the intersection of the fault with the seafloor. In addition, the lower backthrust splay fault is activated during earthquake rupture reaching up to 7.5 m slip (not visible at the scale of Fig. 4.5).

In comparison to the elastic simulation, final slip is altered along the entire fault when the model accounts for plasticity. In general, the highest difference between the elastic simulation and the simulation with plasticity are found at the shallowest part of the fault. When inspecting Fig. 4.5 b), we observe three distinct regions: First, plasticity mainly increases slip in the southernmost part (close to the nucleation) where the horizontal stress orientation is assumed to be 309°. The increase in slip corresponds to the increased moment release within the first 45 s in Fig. 4.3. The maximum increase in that region is 4 m (15%) in comparison to the elastic simulation. At shallow depth between 350 km and 450 km UTM Northing, there is a small localized patch of slip reduction within that region of increased slip. Second, at the shallowest depth of the middle part of the fault (600 km to approximately 1000 km UTM Northing), slip is drastically reduced by up to 15 m (25%) when accounting for plasticity. In the northernmost part of the fault, starting at 1000 km UTM Northing, slip is overall reduced by 4 m (corresponding to 14%). Maximum slip along the lower backthrust splay fault is increased by 0.9 m (12%) due to off-fault plasticity, as well as the area where fault slip reaches the maximum value.

For the following analysis we use the quantity Ψ which determines the angle between the maximum horizontal principal stress and fault strike as defined by Templeton and Rice (2008). Previous studies

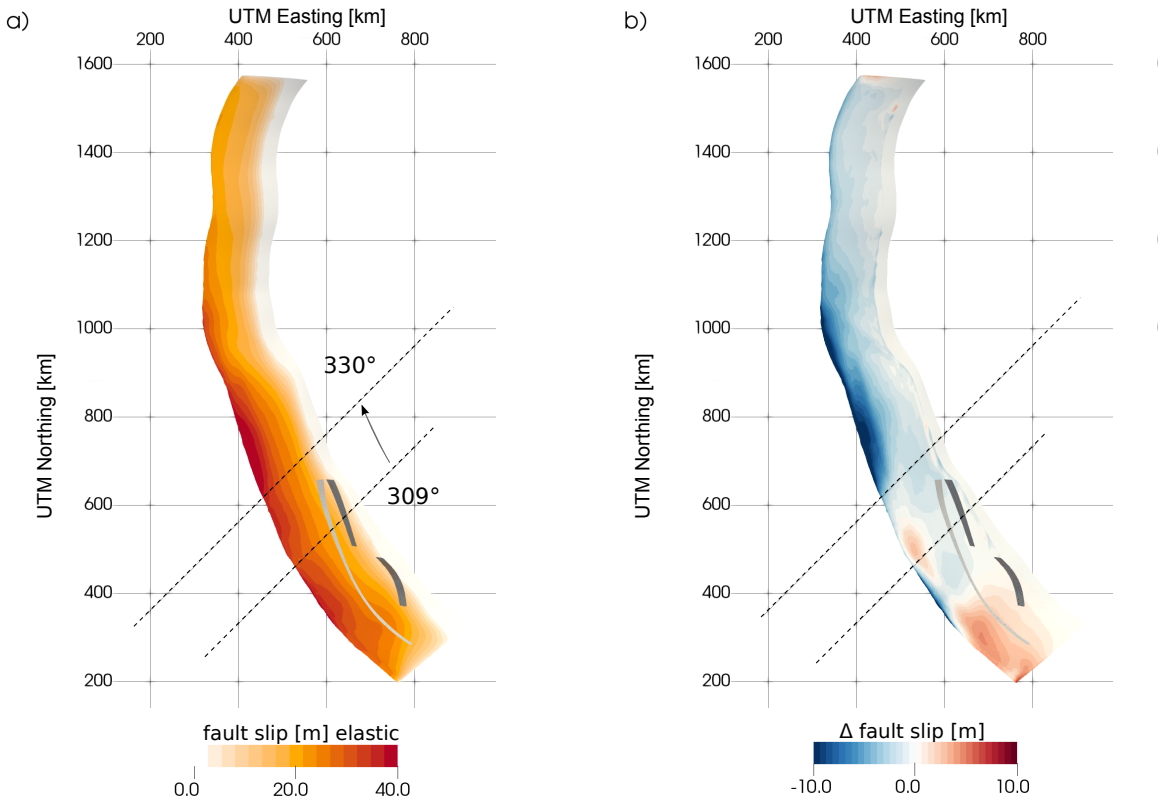

Figure 4.5: a) Final slip distribution for the Sumatra model with purely elastic material properties. b) Residual between fault slip of the simulation with plasticity and the simulation with purely elastic material properties ($\Delta\text{slip} = \text{slip}_{pla} - \text{slip}_{ela}$). Negative values (blue) represent a reduction of slip while positive values (red) represent an increase in slip. The principal stress orientation is smoothly rotated from 309° in the south to 330° in the north within the transition zone between the dashed lines.

on 2D strike-slip faults found that rupture style and plastic strain distribution is dependent of Ψ (Templeton and Rice, 2008; Gabriel et al., 2013). Here, we investigate for the first time the dependence of the final slip and seafloor displacement (in the next section) on Ψ for a 3D subduction zone scenario.

Fig. 4.6 visualizes the variation of Ψ along UTM Northing coordinates. The non-smooth behaviour results from the intersection of the megathrust surface with the local bathymetry. Colours are in correspondence to the increase (red) and decrease (blue) of final slip for the simulation with plasticity in comparison to the elastic simulation. In dependence of Ψ, we can divide the fault into distinct regions: First, for the megathrust with strike lower than 330° and a horizontal stress field orientation of 309°, plasticity increases fault slip (southernmost part). In that case, Ψ is between 15° to 30°. Within the same stress regime, the localized patch of slip reduction close to the trench can be explained by the localized exceedance of 330° fault strike. As a consequence, Ψ exceeds 30° (see Fig. 4.6 at 400 km UTM Northing). Within the area where the stress field is gradually rotated, the megathrust strike slowly increases as well. Here, Ψ lies between 20° and 30° which leads again to an increase with plasticity.

In the middle part of the fault, slip is drastically decreased due to the changed orientation of the horizontal principal stress (330°) in addition to an increase in fault strike. Ψ is on average below 20°. Fault slip is less decreased with plasticity in the northernmost part due to the notable change in fault

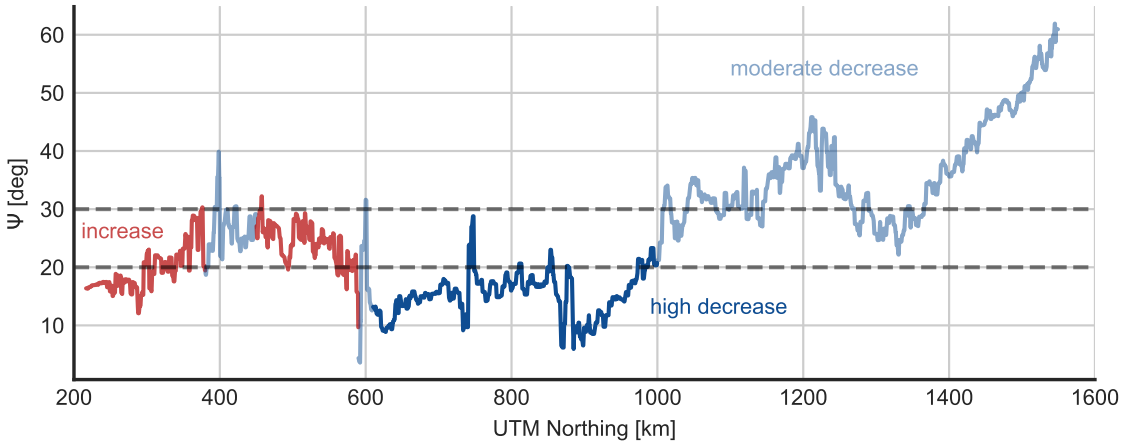

Figure 4.6: Variation of Ψ, the angle between the maximum compressive horizontal stress orientation and fault strike, along UTM Northing coordinates.

strike (from 330° to 20°) while the stress orientation stays constant. As a consequence, Ψ exceeds 30° and reaches up to 60° at the northernmost end of the fault surface.

Our results show that fault slip is considerably altered when we include off-fault plasticity, in strong dependence of Ψ. We find that fault slip is mainly increased with plasticity whenever Ψ is between 20° and 30°. For Ψ below 20°, slip is highly reduced while there is a moderate reduction above 30°. These results show the importance of accurately constraining fault geometry and initial stress orientations in order to generate reliable simulation results. We note that these variations in strike and stress orientation can exclusively be captured in 3D simulations of subduction zones highlighting the need to extend previous 2D dipping fault simulations (Ma, 2012; Ma and Hirakawa, 2013) to 3D.

4.3.2 Ground displacements

Tsunamis are generated by a sudden dislocation of the water column which can result from the displacement of the seafloor during an earthquake. Dynamic rupture scenarios provide a unique possibility to test physically consistent earthquake sources and provide the corresponding spatio-temporal seafloor displacement that can be inserted into tsunami modelling tools. In the following, we compare the impact of off-fault plasticity on the simulated ground displacements. Our findings from the previous section regarding the change in slip distribution can directly be translated into the change in displacements.

Horizontal displacements

Fig. 4.7 a) displays the accumulated horizontal displacement of the simulation with purely elastic material properties. In general, horizontal displacement along the fault is always highest at the trench where the fault intersects with the seafloor. A maximum displacement of 40 m is found between 600 km and 800 km UTM Northing and 400 km and 500 km UTM Easting. When comparing the results of the simulation with plasticity to the simulation without plasticity (Fig. 4.7 b)), horizontal displacement is first increased by up to 8.4 m (27%) in the southernmost part of the fault (309° stress orientation) and later decreased by up to 10.5 m (26%) when the stress orientation changes to 330°.

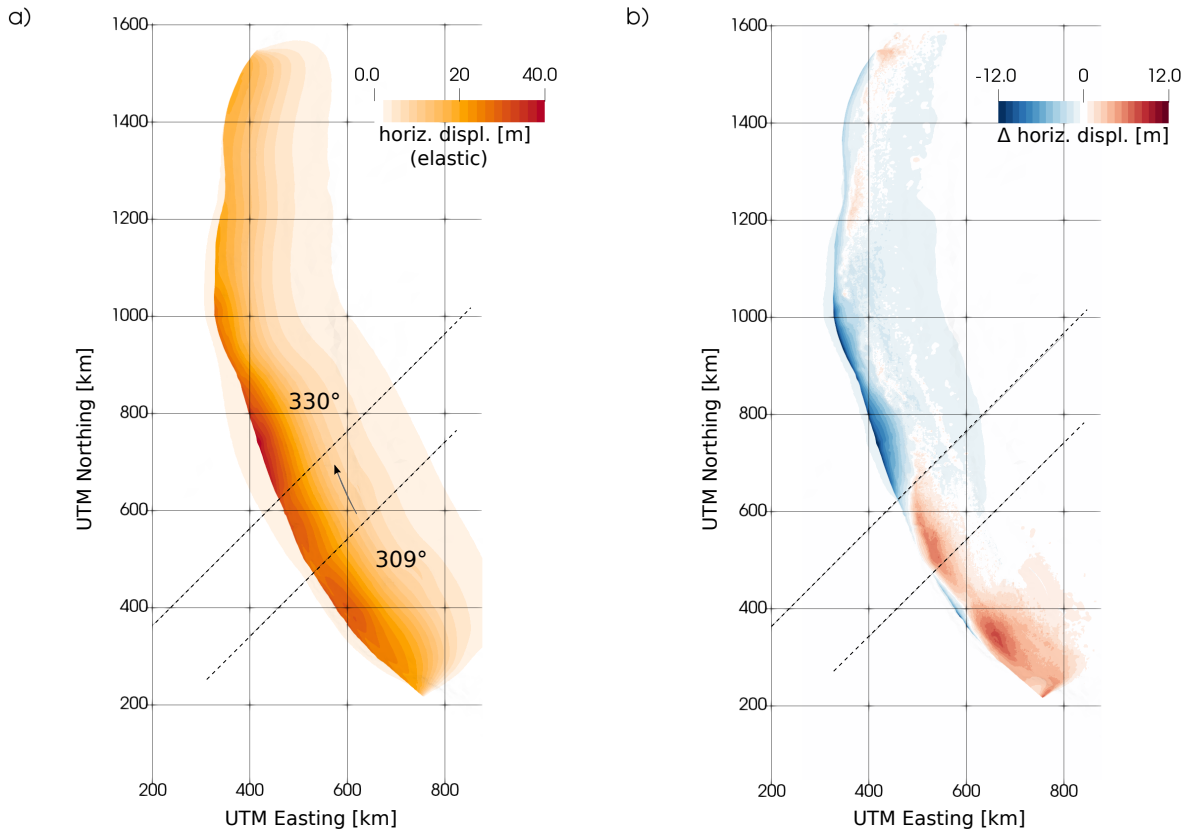

Figure 4.7: a) Horizontal surface displacement for the simulation with purely elastic material properties. b) Residual of the horizontal surface displacement between the simulation with plasticity and the simulation with purely elastic material properties (Δhoriz.displ. = horiz.displ.$_{pla}$ − horiz.displ.$_{ela}$). Negative values (blue) represent a reduction of the horizontal displacement while positive values (red) represent an increase in horizontal displacement.

Notably, in the northernmost part of the fault, there are two small patches of increased displacement (1-2 m or 5-8%) when the model accounts for plasticity.

In general, horizontal displacement is positively correlated with fault slip. When comparing the simulation with plasticity to the simulation with purely elastic material properties, the highest change in displacement is found close to the trench, in particular where fault dip is lowest. Specifically, we note that Ψ correlates with a change in displacement, in the same manner as observed for the fault slip. For Ψ between 20° and 30° (southernmost part), the horizontal displacement is increased with plasticity while it is reduced for Ψ <20° and Ψ >30°.

An exception forms the northernmost part of the fault since the first patch of increased horizontal displacement at 1250 km UTM Northing is not associated with an increase of fault slip when plasticity is included. However, we observe a slight change of fault strike at the location of that patch which decreases Ψ to values just below 30° (see Ψ between 1200 km and 1300 km Northing in Fig. 4.6). Although values of Ψ between 20° and 30° increase fault slip in the southernmost part of the fault, the very localized drop of Ψ at this location is not sufficient to increase fault slip, but it obviously influences the horizontal displacement.

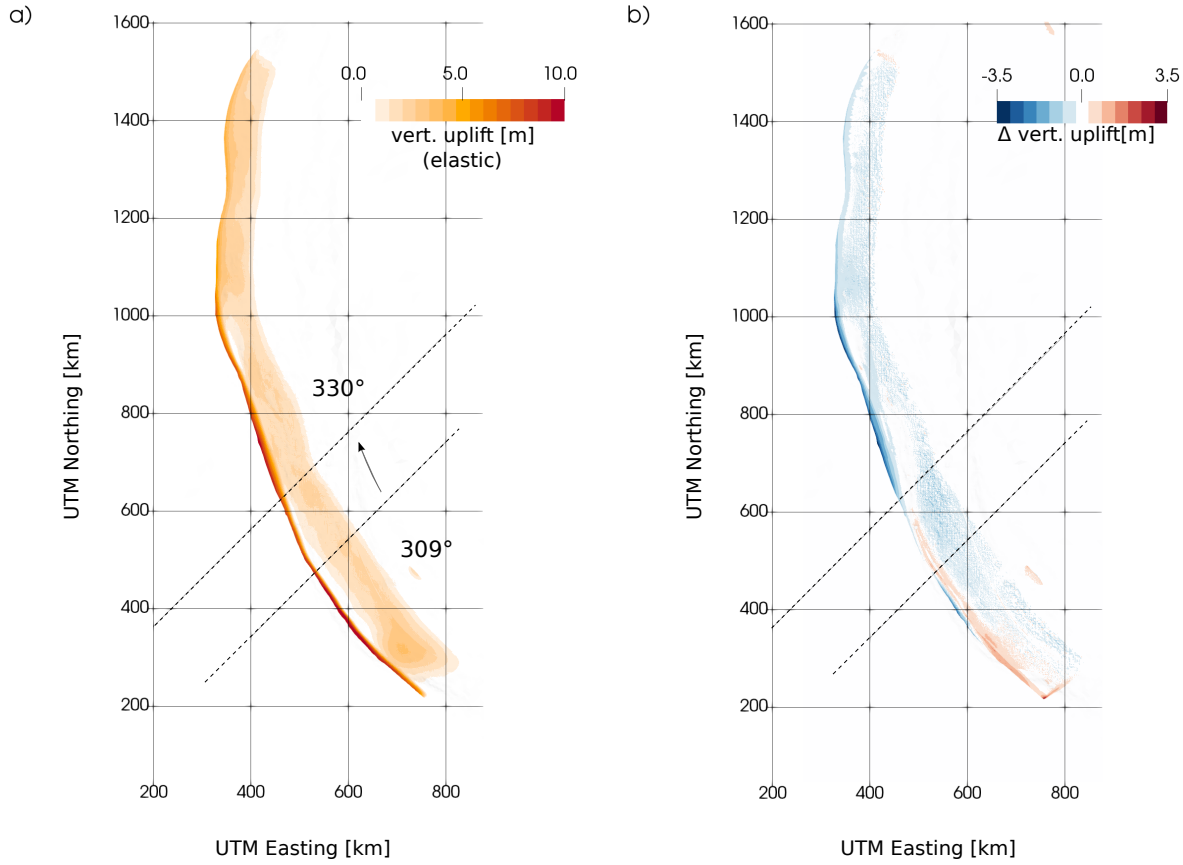

Figure 4.8: a) Vertical surface uplift for the simulation with purely elastic material properties. b) Residual of the vertical surface uplift between the simulation with plasticity and the simulation with purely elastic material properties (Δvert.uplift = vert.uplift$_{pla}$ − vert.uplift$_{ela}$). Negative values (blue) represent a reduction of vertical uplift while positive values (red) represent an increase in vertical uplift.

Vertical uplift

The coseismic vertical uplift is most important when quantifying the tsunami potential of an earthquake. Fig. 4.8 a) shows the vertical uplift (positive vertical displacements) of the purely elastic simulation. The highest vertical uplift of 11 m is found near the trench in the southernmost and middle part of the megathrust. The uplift at the trench decreases for the northernmost part of the fault. In relation to fault slip of only 7.5 m, a remarkably amount of vertical uplift of 1.8 m is found above the activated splay fault (480 km UTM Northing and 730 km UTM Easting).

In comparison to the elastic simulation, the simulation with plasticity depicts an overall reduction of vertical uplift of the seafloor above the entire megathrust. The vertical uplift is reduced by up to 3 m (45%). The only exceptions are found in the vicinity of the trench in the southernmost fault. At this location, vertical uplift is enhanced by 1 m in contrast to almost zero vertical uplift in the elastic case. Notably, we also observe an increase of 0.5 m (27%) in vertical uplift at the activated splay when the model accounts for off-fault plasticity.

The highest vertical uplift at the trench in the southernmost and middle part of the megathrust is clearly attributed to the sudden increase in fault dip towards the trench (see Fig. 4.1b). In contrast,

fault dip is almost constant above 25 km depth in the northernmost part, which leads to less uplift at these locations.

Previous simulations of 2D planar dipping faults find that plasticity solely enhances the vertical uplift (Ma, 2012; Ma and Hirakawa, 2013). Interestingly, the here presented 3D scenario with varying fault strike and rotating horizontal stress field suggest that the interplay between rupture dynamics and off-fault plasticity is far more complex. Accounting for plastic deformation changes the vertical uplift. The regions of increase and decrease of vertical uplift at the trench correlate with the inferred changes in slip in dependence of Ψ.

The increase of vertical uplift at the splay fault is explained by the increase of fault slip at that location. Our results confirm that splay faults have a high potential for generating vertical uplift, which is even enhanced when we account for inelastic off-fault processes. To evaluate the potential tsunami risk of an earthquake, numerical models need to account for realistic material properties such as off-fault deformation, as well as the full complexity of the regional stress field and the fault geometry in 3D.

Comparison with GPS observations

As mentioned above, the largest differences in displacements are found in the vicinity of the trench. However, the closest seismic recordings and GPS stations during the 2004 Sumatra earthquake were located at the islands of Andaman and Nicobar (see Fig. 4.9). Measurements closer to the trench do not exist. Due to the small differences in vertical uplift away from the trench, GPS measurements of vertical uplift at more distant stations depict almost similar results for the simulations with elastic and plastic material properties. In contrast, the differences in horizontal displacement are much wider spread and also visible at the distant stations. In the following, we focus on the comparison of the simulated horizontal displacement with respect to observations.

Fig. 4.9 shows the comparison of observed (black) and simulated horizontal GPS without (blue) and with plasticity (orange). As already shown in (Uphoff and Bader, 2016), the simulated elastic horizontal displacement shows great agreement with observations with respect to the direction and the amount of displacement, in particular at the stations in the south located at the Sumatra island.

Within that region, the simulated displacement is almost identical for the elastic simulation and the simulation with plasticity, although we find an increase of displacement up to 10 m close to the trench for the model accounting for plasticity. Besides the two stations located at 8°N and 9°N, we observe a slight overestimation of the purely elastic displacement in comparison to observations. In these cases, plasticity decreases the horizontal displacement which improves the agreement between simulated and observed displacement. Interestingly, while the direction of displacement is almost identical between the two simulations for stations below 10.5°N, plasticity slightly alters the direction of displacement for some stations located above 10.5°N.

4.3.3 Plastic deformation

Fig. 4.10 visualizes the accumulated plastic strain during the 2004 Sumatra-Andaman simulation including plasticity. The model volume is exemplarily clipped at 850 km UTM Northing, within the region characterized by a stress orientation of 330° where slip and ground displacements are reduced when accounting for plasticity. Plastic strain accumulates within the shallow part of the accretionary wedge and along the seafloor. This distribution is similar along the entire megathrust, independent of the region of increased or decreased slip. Zoom 1 in Fig. 4.10 shows accumulated plastic strain clipped at 421 km UTM Northing highlighting the plastic deformation in the vicinity of the activated

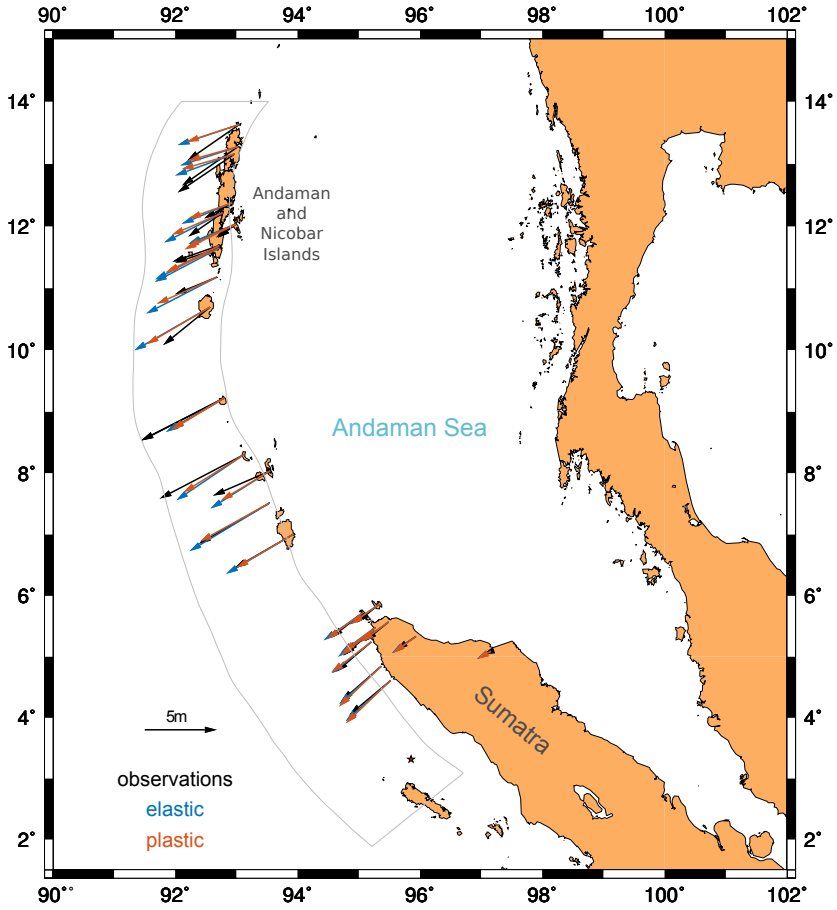

Figure 4.9: GPS comparison between observed (black) and simulated horizontal displacement. The results from the elastic simulation are denoted in blue and the simulations results with plasticity in orange. The fine grey line represents the boundary of the megathrust that is located below the seafloor.

splay fault in the 309° stress regime. Plastic strain is mainly found at the free surface and at locations where the splay intersects with the different velocity layers. Further up north, zoom 2 in Fig. 4.10 shows the plastic strain at the end of the splay fault segment (clipped at 490 km UTM Northing). In this region, plastic deformation forms on the extensional side of the steeply dipping splay fault in a flower-like structure, i.e. with increasing deformation width towards the surface.

Our results show that similar plastic strain distribution along the megathrust can both generate an increase or decrease of fault slip and displacements in dependence of the stress field and the fault geometry. Notable, no systematic change in plastic strain is found that would correlate with a change of slip and ground displacements.

The activated splay fault shows almost no plastic deformation in the direct vicinity of the fault, but only at the ground surface. However, plastic strain forms the typical plastic strain pattern of strike-slip faults (Wollherr et al., 2018) at locations where rupture is stopped by the boundary of the fault surface.

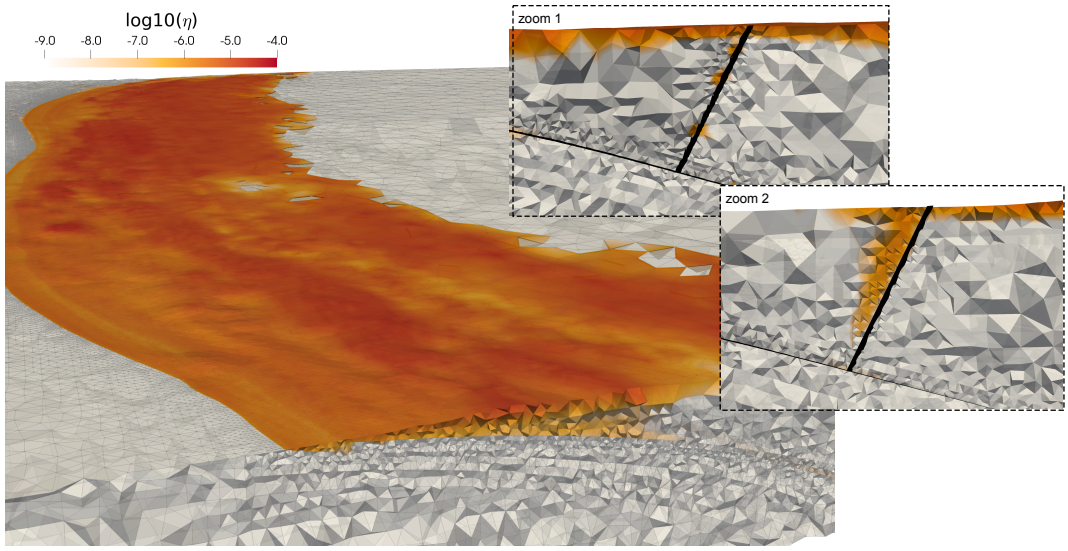

Figure 4.10: Accumulated plastic strain of the 2004 Sumatra simulation. The plastic strain output is clipped at 850 km UTM Northing within the region characterized by a stress orientation of 330°. The insets display plastic strain around the activated splay fault in the middle of the splay (zoom 1, at 421 km UTM Northing) and at the end of the splay (zoom 2, at 490 km UTM Northing).

4.4 Discussion

4.4.1 Comparison to results from simplified 2D setups

We present the first 3D simulation of rupture along a realistic subduction zone fault including off-fault plasticity. Earlier studies with plasticity are based on 2D simplified setups (planar dipping fault geometries) and homogeneous material (Ma, 2009, 2012; Ma and Hirakawa, 2013). In contrast, simulations of subduction zones with more realistic bending faults did not account for inelastic off-fault processes (Kozdon et al., 2012; Uphoff et al., 2017; Lotto et al., 2018). As a consequence, the 3D simulation of the 2004 Sumatra-Andaman earthquake provides a unique insight into the effect of off-fault plasticity under realistic initial conditions.

Previous work in 2D on planar dipping faults shows that plastic strain is asymmetrically distributed, mainly found in the hanging wall (accretionary wedge of the subduction zone) and along the free surface (seafloor) (Ma, 2009). We find a similar distribution in Sec. 4.3.3 although the initial closeness to plastic failure CF is much lower for the presented Sumatra simulation (CF = 0.56 - 0.63). Ma (2012) and Ma and Hirakawa (2013) assume that the entire wedge is on the verge of Coulomb failure (CF=0.99) prior to the earthquake. In contrast to their 15° planar dipping fault geometry, the shallow part of the Sumatra megathrust dips almost horizontally in the southernmost and middle part of the fault and has dip angles lower than 15° in the northernmost part. Our results show that extensive plastic failure within the wedge is possible even for lower CF when accounting for realistic (bent and shallow dipping) fault geometries.

High-resolution 2D simulations on strike-slip faults suggest that Ψ controls the extent and the location of plastic strain (Templeton and Rice, 2008). This dependence was never systematically investigated for dipping fault geometries. Although Ψ various considerably in our models (between 8° and 63°), we do not observe any systematic changes in the plastic strain distribution. However, we note

that the minimum resolution of 400 m on the fault (and even coarser away from the fault) might not be sufficient to capture fine difference in plastic strain patterns. While the 2004 Sumatra-Andaman earthquake provides insight into the first-order effects of plasticity, its resolution is to some extent restricted by the spatial and temporal extent of that earthquake. Future investigations need to consider higher resolutions up to several meters to re-evaluate the correlation of Ψ with the amount and distribution of plastic strain.

In comparison to purely elastic setups, plasticity is found to enhance the vertical uplift leading to a higher potential of a devastating tsunami in 2D simplified models (Ma, 2012; Ma and Hirakawa, 2013). Our 3D results only partially reproduce these findings: in dependence of the fault strike and applied horizontal principal stress orientation, plasticity is able to increase but also to decrease vertical uplift in the 3D simulation. Naturally, 2D simulations cannot account for along-strike variations. Future work thus needs to extend the simplified 2D setups into three dimensions to investigate in a systematic way how rupture dynamics, plasticity and the resulting ground displacement is influenced by these 3D effects.

According to 2D simulations on planar dipping faults, inelastic failure and the resulting vertical uplift is even more enhanced when accounting for dynamic fluid pressure changes during coseismic slip (Ma and Hirakawa, 2013). Pore pressure around the fault highly increases during up-dip rupture which leads to extensive plastic yielding in the wedge. Our current model does not account for a change in pore pressure. Including dynamic pore fluid pressure changes in a future model might be a crucial extension and may further alter our simulation results. It might also limit rupture speed (Ma, 2012) which is currently overestimated in our simulation in comparison to observations, even when we account for plasticity.

4.4.2 Initial stress conditions

The presented model of the 2004 Sumatra-Andaman earthquake suggests a strong correlation between the assumed stress field and the reduction or increase of fault slip and hence ground displacements. Constraining initial conditions for elastic dynamic rupture simulations is highly challenging but becomes increasingly difficult when we include off-fault plasticity. In addition to the stresses acting on the fault, stresses need to be parametrized throughout the entire simulation domain for the plastic calculations. Regional stresses are typically inferred from focal mechanisms of past earthquakes and from existing geological structures that formed due to tectonic loading (e.g., Pollard et al., 1993; Hauksson, 1994; Hardebeck, 2012, 2015). However, stress orientations can only be determined for fault structures with sufficient data of seismic activity and depict a high degree of uncertainty. In particular at convergent plate boundaries, the stress field might be more complex than the typically assumed linear dependence of depth (e.g., Petricca and Carminati, 2016).

One possibility to constrain initial stresses is the use of seismic cycling models that provide self-consistent stresses that evolve over millions of years due to tectonic loading (e.g., Lapusta et al., 2000; Kaneko and Fialko, 2011; Erickson et al., 2017). These stresses can be readily used as initial conditions in dynamic rupture simulations. However, most of these models are restricted to simplified or no free surface boundary condition and homogeneous, elastic material properties Lapusta et al. (2000); Noda and Lapusta (2013); Cubas et al. (2015). Both features are crucial ingredients when considering subduction zone scenarios (e.g., Ma, 2009; Kozdon and Dunham, 2013). Additionally, even models that account for plasticity require the fault geometry as prescribed input (e.g., Erickson et al., 2017). A more consistent workflow coupling the initial stress in addition to the fault geometry of a long-term seismic cycling model (Van Dinther et al., 2013b,a) to a dynamic rupture simulation is presented in the next chapter.

4.5 Conclusions

We investigate for the first time the effect of off-fault plasticity on source dynamics and seafloor deformations in a 3D subduction zone model. The model of the 2004 Sumatra-Andaman earthquake features a complex, low dipping fault geometry, splay faults, and rotating horizontal initial stress conditions.

Off-fault plasticity alters the fault dynamics along the entire megathrust. When the model accounts for inelastic processes, rupture speed is overall decreased, with the highest reduction in the shallowest part where plastic deformation predominantly occurs. We find a clear correlation between the angle Ψ that forms between the orientation of the horizontal principal stress and the fault strike and the increase or decrease of fault slip when accounting for off-fault plasticity. For Ψ between 20° and 30°, fault slip is mainly increased (up to 15%) such as at the southernmost part of the subduction zone. In the middle part, Ψ is below 20° which leads to a drastic decrease of on-fault slip of up to 25%. A moderate decrease of up to 14% is found in the northernmost part where Ψ is above 30°.

As a consequence of the altered slip, we observe an increase of horizontal displacement as well as vertical seafloor uplift in regions where slip is increased and vice versa for regions with decreased fault slip. These results are in contrast to 2D simulations of simplified subduction zone setups that find that plasticity solely increases the vertical uplift (Ma, 2012).

The highest differences between the simulation with elastic material properties and the one with plasticity are visible at the trench. Vertical uplift at the activated splay fault is enhanced with off-fault plasticity which highlights the requirement for realistic material properties to evaluate the potential tsunami hazard of splay faults.

Plastic deformation is found in the entire accretionary wedge for a moderate initial closeness of plastic failure between 0.56 - 0.63. In the vicinity of the activated splay fault, plastic strain is mainly accumulated at the surface. The analysis of plastic strain indicates that there is no systematic correlation between the change in on-fault slip or ground displacement and the distribution of accumulated plastic strain.

GPS comparisons of horizontal displacement show a slight reduction in amplitudes when the model accounts for off-fault plasticity. This enhances the agreement with observations at some stations as the elastic simulation results slightly overestimate the amount of horizontal displacement above 6°N (600 km UTM Northing). Plasticity further alters the direction of displacement for the northernmost stations.

The presented 2004 Sumatra-Andaman model shows the importance of i) considering realistic fault geometries and ii) properly constraining the initial regional stress within a 3D domain. A possible workflow to constrain these initial conditions more consistently is presented in the next chapter. In addition, future work will compare the emitted seismic waves with recordings on teleseismic stations, as well as to tsunami data by inserting the displacement as spatio-temporal source into a tsunami modelling tool.

5

Geomechanically constrained dynamic rupture models of subduction zone earthquakes with plasticity

Abstract

Dynamic rupture simulations of subduction zone earthquakes based on purely elastic material response might not realistically capture the seafloor displacement and hence the tsunami hazard. Simulations that capture the complex interplay of the rupture front, the emitted seismic waves, and off-fault deformation allow us to analyze whether plastic deformation of the bulk rock is a critical rheological component for understanding subduction zone earthquakes and assessing their hazards. However, constraining initial conditions for dynamic rupture simulations in terms of fault geometry, initial fault stress, and strength – which is already challenging for purely elastic simulations – becomes increasingly difficult when accounting for off-fault plastic deformation. The use of plasticity requires additional parametrization of bulk cohesion, internal rock friction, and initial stresses in the entire simulation domain which is particularly complex for subduction zones.

Here, we present two-dimensional dynamic rupture simulations of realistic subduction zones with off-fault plasticity and complex material layers constrained by long-term seismo-thermo-mechanical (STM) modelling. The STM model provides a self-consistent slab geometry, as well as initial stress and strength conditions which evolved according to the tectonic stress build-up and the temperature-dependent strength of the rocks. We describe the coupling approach and the challenges when using the simulation results of the STM model as initial conditions for dynamic rupture models with plasticity. The imported initial conditions suggest an initial state that is relatively close to plastic failure within the uppermost part of the accretionary wedge. While the purely elastic simulation succeeds in rupturing the velocity-strengthening region at shallow depth, plastic deformation completely stops rupture within the transition to the velocity-strengthening region. The corresponding vertical coseismic seafloor uplift is increased by the occurrence of plastic strain within the accretionary wedge. The

This chapter presents the extension of the elastic coupling approach by van Zelst, I., **Wollherr, S.**, Gabriel, A.-A., Madden, E. H. and van Dinther, Y. (2018): A coupled method for realistic initial conditions of megathrust earthquakes in dynamic rupture simulations (*in preparation for Geophys. J. Int.*) to account for off-fault plasticity. It will be eventually submitted to the *Pure and Applied Geophysics* Topical Volume "Physics of Megathrust Earthquakes".

complex initial conditions lead to pronounced rupture pulses which are smeared out when accounting for off-fault plasticity.

5.1 Introduction

Subduction is one of the most powerful and dynamic processes on Earth, where a denser plate is overridden by a lighter plate at a converging tectonic boundary. In most cases, the oceanic plate is subducted into the deep mantle beneath the continental crust. The sudden release of stress that builds up during this process causes the largest earthquakes worldwide such as the M_w 9.5 Great Chilean earthquake in 1960 (e.g., Kanamori and Cipar, 1974), the M_w 9.2 Alaska earthquake in 1964 (e.g., Wyss and Brune, 1967), M_w 9.1-9.3 Sumatra-Andaman earthquake in 2004 (e.g., Shearer and Bürgmann, 2010), and the M_w 9.0 Tohoku-Oki earthquake in 2011 (e.g. Simons et al., 2011). Still, little is known about the earthquake dynamics driving fault failure over large areas and the conditions under which subsequent devastating tsunamis evolve. Due to the lack of direct observations, physics-based dynamic rupture simulations can help to shed light on the complex source dynamics of subduction zone earthquakes by capturing the interplay of fault rupture, the emitted seismic wave field, and the Earth's surface.

To accurately represent earthquake dynamics, numerical models need to account for the complexity of subduction channels in terms of pressure, temperature, material composition, and pore fluids which highly influence frictional properties (Hyndman et al., 1997; Lay et al., 2007; Suppe, 2007; Lay et al., 2012; Suppe, 2014). These conditions determine whether rupture can be sustained along the fault or whether branches or splays are activated (e.g., Kame et al., 2003; Wang and He, 2008; DeDontney et al., 2012; Xu et al., 2015). The implications are crucial for quantifying the potential size of an earthquake and the corresponding tsunami hazard.

Accounting for a complex setup with heterogeneous material properties has been shown to influence on- and off-fault quantities. Simulations of dipping faults show that the presence of a compliant prism within a homogeneous medium enhances shallow slip and seafloor displacement (Lotto et al., 2017). Models including additional material contrasts between the continental and oceanic crust, as well as in the overriding wedge, depict a complex interaction between seismic waves reflected at material interfaces and at the Earth's surface which can lead to a re-activation of fault rupture (Kozdon and Dunham, 2013). The resulting high stress changes are able to drive rupture even through velocity-strengthening parts of the fault (Kozdon and Dunham, 2013) that are generally assumed to be stable. Both studies show the importance of accounting for heterogeneous material properties in subduction zones in order to accurately capture the coseismic dynamics. As a consequence, models in homogeneous medium (Ma, 2012; Huang et al., 2013; Galvez et al., 2014; Cubas et al., 2015) or with a 1D velocity structure (Galvez et al., 2016) might not be able to sufficiently represent the complexity of subduction zone earthquakes.

Equally important is the realistic choice of rheology such as the ability of the material to deform inelastically under high stress. Simplified subduction zone simulations on low dipping, planar faults show that the vertical surface displacement is enhanced by plastic yielding in the accretionary wedge (Ma, 2009, 2012; Ma and Hirakawa, 2013; Hirakawa, 2016). Hence, simulations based on purely elastic setups might underestimate coseismic surface displacements.

Dynamic rupture simulations are highly dependent on their initial assumptions with respect to the stress state, fault strength, material properties, and fault geometry. Typically, numerical models assume linearly increasing effective normal stress with depth (Ma, 2012; Hirakawa and Ma, 2016) or constant stresses starting at a depth where fluid pressure increases from hydrostatic to lithostatic

(Huang et al., 2013; Kozdon and Dunham, 2013; Galvez et al., 2014, 2016; Lotto et al., 2017). In addition, friction is often taken as constant along the fault interface and close to 0.6 (e.g., Ma, 2012; Huang et al., 2013; Kozdon and Dunham, 2013; Lotto et al., 2017), in accordance with Byerlee's law (Byerlee, 1978). However, friction might vary in depth due to varying stresses and temperature changes along the subduction zone (e.g., Lay et al., 2012).

Constraining these on-fault initial conditions is already difficult for purely elastic simulations but becomes increasingly challenging when accounting for off-fault plastic deformation. Models incorporating a plastic rheology require additional parametrization of bulk cohesion, bulk friction, and off-fault stresses in the entire simulation domain. These conditions determine the closeness of plastic failure prior to the earthquake and hence, control the occurrence of inelastic deformation due to stress changes induced by an earthquake (e.g., Templeton and Rice, 2008). Previous dynamic rupture models with plasticity assume an accretionary wedge very close to plastic failure prior to an earthquake (Ma and Hirakawa, 2013; Hirakawa, 2016; Hirakawa and Ma, 2016), based on the critical wedge theory (Dahlen et al., 1984). However, the true stress state is difficult to constrain since it can not be measured directly, particularly at the seismogenic zone (Hardebeck, 2015). Numerical models of long-term stress evolution due to tectonic loading might therefore help to constrain these initial conditions in a more physically consistent manner.

Here, we present 2D dynamic rupture models of subduction zone earthquakes with off-fault plasticity, complex material compositions, and initial conditions constrained by a long-term seismo-thermo-mechanical (STM) model with visco-elasto-plastic rheology. The STM model (Van Dinther et al., 2013a) provides frictional and material properties, as well as self-consistent initial stresses and a slab geometry which evolves according to the tectonic loading and temperature-dependent strength of the rocks. The dynamic rupture simulations are conducted using the software package SeisSol (De la Puente et al., 2009) which is able to account for off-fault plasticity in conjunction with complex fault geometries such as low-dipping subduction zones.

While van Zelst et al. (2018) focus on the coupling of the STM model with purely elastic DR models, we complement this coupling approach for DR models with off-fault plasticity. We constrain initial stresses, friction, and bulk cohesion for the entire simulation domain using the simulation results of the STM model.

The work is structured as follows: Sec. 5.2 gives an overview of the underlying equations of the STM and DR models. The initial setup and assumptions of the STM model are presented in Sec. 5.3.1. After the simulation of over 4 million years of tectonic loading and subduction, initial conditions prior to an exemplary event within the STM model are exported as input for the dynamic rupture simulation as described in Sec. 5.3.2. Since the two models assume different underlying equations we describe the required pre-processing steps before importing the STM output to the dynamic rupture model with plasticity. In Sec. 5.4 we analyze the geomechanically constrained simulations with purely elastic and plastic material properties with respect to rupture propagation and coseismic seafloor displacement. The initial conditions and simulation results are further discussed with respect to previous assumptions and results of simplified settings in Sec. 5.5.

5.2 Methodology

The following section gives a short overview of the underlying equations and assumptions of the long-term seismic cycling and the dynamic rupture model, as well as the numerical methods of the corresponding software packages. The main model differences and challenges in coupling both approaches are outlined in Sec. 5.2.3. We refer to Gerya and Yuen (2007) and Van Dinther et al. (2013a)

for more details on the seismic cycling model, and to Dumbser and Käser (2006), De la Puente et al. (2009) and Wollherr et al. (2018) for the dynamic rupture model.

5.2.1 Seismo-thermo-mechanical model

The 2D, continuum-based, seismo-thermo-mechanical (STM) model describes the long-term tectonics over millions of years as well as the seismic cycle down to annual time intervals for complex subduction zones (Gerya and Yuen, 2003, 2007; Van Dinther et al., 2013b). The simulation results are validated against laboratory experiments using an analogue to the thrust fault system (Van Dinther et al., 2013a).

Horizontal and vertical velocities of the material, v_x and v_z, deviatoric stresses s_{ij} and pressure P are described by a set of conservation equations (conservations of mass and momentum) including an inertia term in velocities, gravitational acceleration g, and the material's density ρ. The heat equation connects ρ in turn with pressure P, temperature T, and cohesion c_{bulk} of the underlying rock. The model assumes an incompressible medium with a Poisson's ratio of 0.5 and no volumetric changes (Van Dinther et al., 2013a).

A visco-elastio-plastic rheology is incorporated using constitutive equations connecting deviatoric stresses s_{ij} and strain rates $\dot{\varepsilon}_{ij}$ by applying linear elasticity, Newtonian viscosity, and Drucker-Prager plasticity. The strain rate is described by

$$\dot{\varepsilon}_{ij} = \frac{1}{2G}\frac{\partial}{\partial t}s_{ij} + \frac{1}{2\eta}s_{ij} + \begin{cases} 0 & \text{for } \sqrt{I_2} < \tau_c \\ \chi \frac{\partial}{\partial \sigma_{ij}}\sqrt{I_2} & \text{for } \sqrt{I_2} \geq \tau_c, \end{cases} \tag{5.1}$$

for shear modulus G, viscosity η, the second invariant of deviatoric stresses $\sqrt{I_2}$, and a plastic multiplier χ as defined in The plastic strain $\dot{\varepsilon}^p_{ij}$ (last part of Eq. (5.1)) is governed by a non-associated Drucker-Prager yield criterion defined as in (Van Dinther et al., 2013a).

$$\tau_c = c_{bulk} + \mu_{eff}\sigma_m, \tag{5.2}$$

with mean stress $\sigma_m = -P$ and effective friction $\mu_{eff} = \mu(1-\lambda_f)$ for a fluid factor $\lambda_f \in (0,1)$. Plastic yielding occurs whenever $\sqrt{I_2}$ reaches the yield strength τ_c. In case of plasticity, the visco-plastic strain rate is translated into slip rate as $V_{vp} = \tau_c/\eta$. A fault surface is not prescribed a-priori but all locations within the modelling domain are theoretically able to yield plastically.

Throughout the simulation, the friction coefficient follows a strongly rate-dependent (but not state-dependent) friction law (Ampuero and Ben-Zion, 2008; Van Dinther et al., 2013a) in dependence of V_{vp}:

$$\mu_{eff} = \mu_s(1-\gamma) + \mu_s\frac{\gamma}{1+V_{vp}/V_c}, \tag{5.3}$$

with a specified weakening rate γ, static friction μ_s, and a characteristic slip velocity V_c. The specific model parameters for the here presented STM setup are described in Sec. 5.3.

Fig. 5.1 visualizes the different boundary conditions of the STM model. The sticky-air method is used as a proxy for the topography evolution at the air-crust interface (Crameri et al., 2012). This method applies a layer of low viscosity and low density "air" on top of the model. At the right and left side of the simulation domain, the model uses a free slip boundary condition such that the material is able to move tangentially to the boundaries. With the open boundary condition at the bottom, the material can leave the simulation domain.

Numerically, the STM model makes use of a first-order accurate finite-differences method on a fully staggered Eulerian grid combined with a marker-in-cell technique to track temperature and composition advected by the velocities. The numerical method is able to resolve time steps ranging from millions of years up to annual time intervals. We refer to Gerya and Yuen (2003) and Gerya and Yuen (2007) for the full description of the numerics.

5.2.2 Spontaneous dynamic rupture model

Earthquake rupture dynamics and coupled wave propagation are modelled using the 2D version of the software package SeisSol for dynamic rupture simulations on coseismic time scales (De la Puente et al., 2009).

Stresses σ_{ij} and (seismic) velocities, v_x and v_z, are solved using the linear elastic wave equation (Dumbser and Käser, 2006). We use elasto-plastic material properties such that stresses are adjusted whenever they reach the elastic yield limit. Plasticity is incorporated using a Drucker-Prager yield criterion using the same yield limit τ_c as the STM model (Eq. (5.2)). In case of plastic yielding, the plastic strain rate is given as the differential equation

$$\dot{\varepsilon}_{ij}^{p} = \frac{1}{2GT_v} \begin{cases} 0 & \text{for } \sqrt{I_2} < \tau_c \\ s_{ij} - (\tau_c/\sqrt{I_2})\, s_{ij} & \text{for } \sqrt{I_2} \geq \tau_c, \end{cases} \tag{5.4}$$

for a viscoplastic relaxation time $T_v > 0$. In the absence of additional plastic yielding, viscoplastic regularization permits the current stress state σ_{ij} to reach the inviscid stress state after a specified time T_v.

Note that the yield criterion τ_c somewhat differs from the formulation of the dynamic rupture benchmark description of the Southern California Earthquake Center (SCEC) (Harris et al., 2011) or from the formulation in Wollherr et al. (2018). They commonly use $\hat{\tau}_c = c_{bulk}\cos(\phi) + sin(\phi)\sigma_m$ with the friction angle $\phi = \tan^{-1}(\mu_{eff})$. Here, we modify the yield criterion in the dynamic rupture simulations to match the failure criterion of the STM model. The two formulations only differ by a factor of $1/\cos(\phi)$. For low friction, τ_c is close to $\hat{\tau}_c$ ($cos(\phi)$ close to 1 and $\sin(\phi)$ close to μ_{eff}) while $\hat{\tau}_c$ is increased by 30% for friction values as high as 0.85. As a consequence, stresses within regions of high friction are allowed to be higher before plastic yielding occurs. This is mainly the case for locations outside the accretionary wedge and away from the fault (see Sec. 5.3.2 for the range of friction values we use in this work).

The closeness of plastic failure (CF) determines how close the current stresses are to the yield limit and is defined as the ratio between $\sqrt{I_2}$ and τ_c:

$$\text{CF} = \frac{\sqrt{I_2}}{\tau_c} = \frac{\sqrt{0.5\sum_{ij} s_{ij}s_{ji}}}{c_{bulk} + \mu_{eff}\ \sigma_m}. \tag{5.5}$$

We will discuss the geomechanically constrained CF for the dynamic rupture setup in Sec. 5.3.2.

Spontaneous fault rupture is incorporated as a special boundary condition using a Coulomb failure criterion at a prescribed fault surface. The fault starts to slip when shear stress τ_s overcomes the strength of the fault, i.e.

$$\tau_s > c_f + \mu_{eff}\sigma_n, \tag{5.6}$$

with fault normal stress σ_n and frictional cohesion c_f. During sliding, friction evolves according to a friction law such as linear-slip weakening or rate-and-state friction. The change of stress due to fault

movement is then coupled to the elastic wave equation solving for the emitted seismic wave field in the bulk.

The dynamic rupture software package SeisSol is based on a Discontinuous Galerkin (DG) scheme in space and an Arbitrary High Order Derivative (ADER) scheme in time (Dumbser and Käser, 2006). The simulation domain is discretized using unstructured triangular elements which makes SeisSol specifically suited for complex fault geometries. Dynamic rupture is incorporated using a modified numerical flux solving a Riemann problem across the discontinuous fault element interfaces (De la Puente et al., 2009). The 2D version is verified for a suite of benchmarks including branched and dipping faults as well as off-fault plasticity (De la Puente et al., 2009; Nerger et al., 2014; Wollherr et al., 2016).

5.2.3 Main model differences and challenges in coupling

In the following, we outline some of the main model differences between the STM model and the dynamic rupture model with respect to their equations, their assumptions and the challenges in coupling them. Details of the coupling challenges for a purely elastic dynamic rupture setup are presented in van Zelst et al. (2018). Here, we shortly summarize them but mainly focus on the challenges for a dynamic rupture setup with plasticity.

Inertia effects

While the STM model provides physically consistent initial stresses and strength conditions, as well as the time and location of a seismic event, it does not include an incompressible inertia term, i.e. no pressure waves are generated. In contrast, dynamic rupture simulations model the seismic wave field through the linear elastic wave equation. The emitted seismic wave field can dynamically trigger fault failure (”rupture jumps“) or re-activate fault slip due to the reflections at material contrasts and the Earth’s surface (e.g., Kozdon and Dunham, 2013). These dynamic effects might crucially affect the rupture dynamics and are only fully captured by dynamic rupture models.

Time scales

One of the main model differences concerns the different simulation time scales. The STM model is able to capture the evolution of strain, stress, temperature, and the distribution of different materials over millions of years up to five years, but fails to resolve coseismic time steps due to numerical restrictions. Dynamic rupture models use explicit numerical solvers in time which lead to small time steps in the millisecond range. As a consequence, the total simulation time is commonly up to a couple of minutes.

For coupling these two approaches, it is a challenge to select the appropriate time step at which initial conditions from the STM are exported to the dynamic rupture model. As described in van Zelst et al. (2018), we export initial conditions in terms of composition, stress, and friction whenever two adjacent points along the potential fault surface are at failure which ensures spontaneous earthquake nucleation in the elastic dynamic rupture simulations.

On-fault versus off-fault yielding

Another difference concerns the definition of earthquake slip and the distinction between on- and off-fault failure. Slip in the STM model is defined in terms of the visco-plastic strain rate. In that way,

slip is only coupled to the conservation equations in case of plastic failure. Theoretically, the location of plastic yielding and hence slip can occur within the entire simulation domain.

In contrast, dynamic rupture models distinguish between on-fault frictional failure and off-fault rock failure. Earthquake slip in dynamic rupture models is exclusively defined as frictional failure along a prescribed fault surface. As a consequence, all dynamic rupture models require a fixed fault geometry prior to the simulation. The change in stress due to the fault movement is coupled to the underlying wave equation and initiates seismic waves. In addition, dynamic rupture models with plasticity adjust stresses off the fault whenever they reach the elastic yield limit but the plastic strain rate is not associated with fault slip.

In this coupling approach, a potential fault surface for the dynamic rupture model is picked from the STM model as the location of the highest plastic strain during a seismic period as described in van Zelst et al. (2018).

Initial conditions at failure

Geomechanically constrained elastic dynamic rupture simulations succeed in nucleating rupture along the fault without any artificial nucleation procedures by using on-fault initial stresses that are already at failure (van Zelst et al., 2018). However, for the incorporation of plasticity, stresses are not only assigned to the fault surface but to the entire simulation domain. Initial off-fault stresses at failure would be adjusted immediately and the resulting stress change would initiate seismic waves since stresses are coupled to velocities via the wave equation. Dynamic rupture models are only designed to initiate seismic waves due to on-fault frictional sliding. As a consequence, initial conditions at immediate off-fault plastic failure are not allowed.

When importing the initial conditions from the STM model, several regions are already at plastic failure, such as the vicinity of the nucleation location. We therefore use a static pre-processing step that relaxes these stresses by adjusting them to values just below the yield criteria. However, by adjusting the stresses for the entire simulation domain, on-fault stresses are not at failure any more which prohibits spontaneous nucleation. The resulting on-fault stress differences are described in Sec. 5.3.2

5.3 Long-term subduction and spontaneous dynamic rupture model setup

We first present the initial conditions of the STM model with respect to the material composition and temperature dependent frictional regimes, as well as the model's space and time discretization. We then describe the on- and off-fault initial conditions for the DR setup that are constrained by the simulation results of the STM model.

5.3.1 Seismo-thermo-mechanical setup

The initial setup of the STM model is based on the setup presented in van Zelst et al. (2018) which we shortly summarize here. For more details we refer to Sec. 2.4 and 2.5 in van Zelst et al. (2018).

Fig. 5.1 visualizes the initial model setup. The setup in terms of thickness of the crust, size of the accretionary wedge, the temperature profile, and slab geometry is based on the Southern Chilean subduction zone. The model accounts for distinct materials (different colours in Fig. 5.1) with representative values for friction, cohesion, density, and viscosity of the upper and lower oceanic crust,

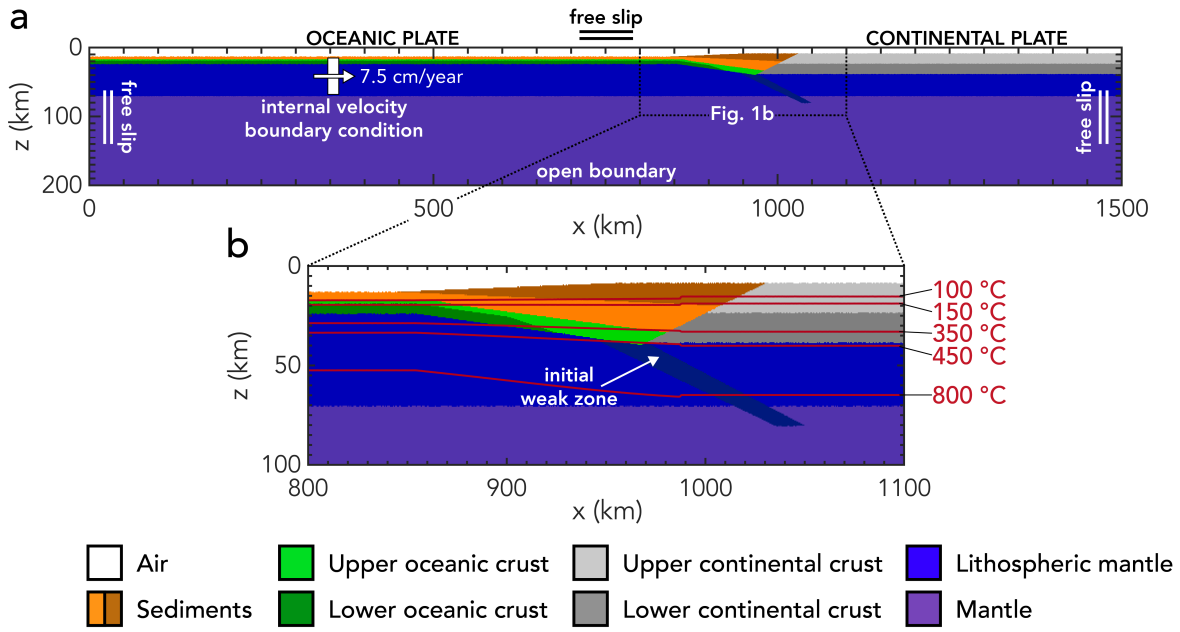

Figure 5.1: Initial setup of the STM model in terms of material (color key in the legend), boundary conditions (white labels) and isotherms (red lines and red annotations). The inset shows a zoom along the initial weak zone which controls the geometry of the subducting oceanic plate. The figure is courtesy of I. van Zelst (van Zelst et al., 2018, *in preparation*).

upper and lower continental crust, and the mantle. The parameters and references for each rock type are described in Table 5.1. A 4 km sediment layer overlies the oceanic plate and represents a mean sediment thickness of subduction zones based on the studies of Heuret et al. (2011) and Brizzi et al. (2017). The model distinguishes between fluid-rich and dry regions with a constant pore-fluid pressure ratio of $\lambda_f = 0.95$ and $\lambda_f = 0$, respectively, and a linear transition zone between $\lambda_f = 0$ and $\lambda_f = 0.4$ for the uppermost 1 km.

Frictional behaviour is governed by the temperature. The initial isotherms are visualized as red lines in Fig. 5.1. For temperatures below 100°C, sediments are assumed to display a velocity-strengthening behaviour, such that friction increases with increased slip rate. Velocity-weakening is assumed for regions with temperatures above 150°C and the model assumes a linear transition from velocity-weakening to -strengthening within the regions between 100°C and 150°C. For velocity-weakening regions, the model assumes that the dynamic friction is 30% of its initial static friction (Di Toro et al., 2011) while static friction increases by a factor of 2.5 in the velocity-strengthening regions.

To initiate and sustain subduction, a constant velocity of 7.5 cm/year is applied to the oceanic crust based on the trench-perpendicular velocity of the Nazca plate in the south of Chile (Lallemand et al., 2005). The STM model incorporates an initial zone of weakness (dark blue shading in Fig. 5.1) which is required to ensure the formation of a subducting slab but is then removed after the first 3.6 million years. Its shape also helps to control the final geometry of the subduction zone and resembles the slab geometry of the Chilean subduction zone.

Discretization and time step

The model is discretized by a fully staggered Eulerian grid with 500 m elements around the megathrust interface (inset zoom in Fig. 5.1) that gradually transitions to 2000 m elements outside that area. First,

Material (rock type)	ρ (kg/m)	G (GPa)	c_{bulk} (MPa)	μ_s	V_s (m/s)	V_p (m/s)
Sediments	2600[b]	5.0	2.5[a]	0.35[c]	1387	2401
Upper oceanic crust (Basalt)	3000[h]	12.0	5.0[b]	0.5[d]	2000	3464
Lower oceanic crust (Gabbro)	3000[b]	12.0	15.0[a]	0.85[e]	2000	3464
Upper and lower continental crust (Sandstone)	2700[f]	12.0	10.0[a]	0.72[b]	2108	3651
Mantle (Peridotite)	3300[b]	35.0	20.0[a]	0.6[g]	3257	5641

Table 5.1: Parameters for the different rock types used in the STM model that are relevant for the dynamic rupture setup. The corresponding wave velocities are calculated with a Poison's ratio of 0.25. Values are the same as in van Zelst et al. (2018) and obtained from: [a] Ranalli (1995), [b] Turcotte and Schubert (2002), [c] Den Hartog et al. (2012), [d] Di Toro et al. (2011), [e] Tsutsumi and Shimamoto (1997), [f] Dieterich (1978),Chester and Higgs (1992) and Di Toro et al. (2011), [g] Del Gaudio et al. (2009),[h] Schultz (1995).

the simulation time step dt is 1000 years until a steady-state subduction geometry is reached. After 3.6 millions years (when the zone of weakness is removed), the time step is gradually reduced to 5 years which is reached after a total time of 4.0 millions of years. The model runs then for 30 thousands years with dt=5 years and the resulting material properties, the fault geometry, and stresses just prior to an exemplary event are picked as input for the dynamic rupture model, as described in van Zelst et al. (2018).

5.3.2 Spontaneous dynamic rupture setup with off-fault plasticity

Dynamic rupture simulations require initial stress conditions and friction parametrization along a predefined fault interface. For simulations including off-fault plasticity, a plastic yield criterion is additionally checked off the fault, requiring the initialization of stresses, bulk cohesion, and internal friction for the entire simulation domain. Specifically in subduction zones, stresses and friction might be more complex than what is commonly assumed in dynamic rupture models.

In the following, we describe the geomechanically constrained initial conditions for the dynamic rupture models. We first summarize the on-fault coupling procedure for the purely elastic case, as described in detail in van Zelst et al. (2018), before focusing on the off-fault parameters used for plasticity. The initial conditions provided by the STM model are compared to commonly assumed initial conditions of dynamic rupture setups in the discussion in Sec. 5.5.

On-fault initial conditions

The location of the highest plastic strain (equal to the location of highest slip) during one coseismic period in the STM model determines the fault geometry in the dynamic rupture model (visualized as red line in Fig. 5.3). We note that the imported fault geometry does not reach the seafloor but stops at 5.46 km depth due to the rupture arrest in the STM model below the trench. All on-fault variables, such as stresses and friction, are interpolated to the additional $(p+1)$ Gaussian integration points within one fault element for the polynomial degree of approximation p.

Friction, imported by the STM model, is dependent on the underlying material, the presence of fluids, and the temperature. Fig. 5.2 visualizes the effective on-fault static friction that incorporates the effect of fluid pore pressure. Static friction varies between 0.0175 and 0.028 in the brittle regime, i.e., above a temperature of 450°C.

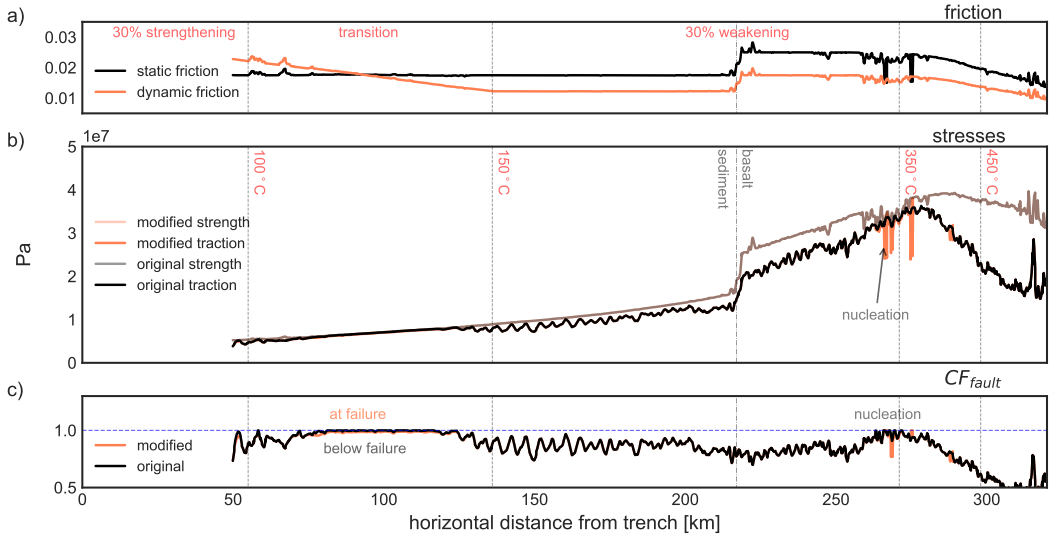

Figure 5.2: a) Effective static friction (black) imported from the STM model and the corresponding dynamic friction (orange) assuming 30% weakening or strengthening with fault slip in dependence of the temperature regimes. b) Initial traction (shear stress) τ_s and the strength of the fault ($c_f + \mu_{eff}\sigma_n$) along the horizontal distance from the trench. c) Initial closeness of fault failure CF_{fault} as the ratio between τ_c and the fault strength. Orange colors denote the modified stresses due to a preprocessing static adjustment as described in Sec. 5.2.3, while black colors show the originally imported values from the STM model. The nucleation region is located at 266 km along horizontal distance.

We approximate the velocity-weakening behaviour of the friction coefficient by a linear slip-weakening friction law, assuming 30% weakening from the initial friction over a critical slip distance D_c. Within the strengthening region, the dynamic friction increases up to 130% of the initial friction with fault slip. D_c is assumed to be 1.5 m and for simplicity, constant along the fault. Note that van Zelst et al. (2018) approximates D_c such that the fracture energy within the STM and dynamic rupture model are equal. Here, we do not infer D_c from the STM model to prevent any bias from the STM model results on the dynamic rupture behaviour. Due to this approximation, the dynamic friction coefficient and hence the fault strength increases with increasing slip in the strengthening region and fault strength decreases with fault slip in the weakening region. The dynamic friction used for the dynamic rupture models is visualized in Fig. 5.2 a) (orange line).

Initial stresses are imported from the STM model and rotated into the fault's coordinate system to determine initial normal and shear stresses (traction). The resulting traction τ_s and fault strength from the STM model are visualized in Fig. 5.2 b), denoted as original" values. The corresponding closeness of the initial conditions to fault failure (CF_{fault}), defined as the ratio between fault traction τ_c and fault strength, is visualized in Fig. 5.2 c). The blue dashed line ($CF_{\text{fault}} = 1$) represents the states at on-fault failure. The initial stresses are at failure for the shallowest part, at around 100 km horizontal distance from the trench, and at 266 km where rupture is initiated in the STM model.

While on-fault stresses at failure are used to nucleate spontaneous rupture along the fault, off-fault stresses at failure are not allowed in the plastic calculations. We therefore adjust the stresses for the entire simulation domain as described in Sec. 5.2.3. As a consequence, the on-fault stresses also change. The orange lines in Fig. 5.2 b) and c) visualizes the modified fault strength and traction. Initial traction within the nucleation area and at around 100 km horizontal distance is now below failure. We nucleate rupture by reducing the on-fault initial friction by 10% within the region where nucleation is observed in the STM model.

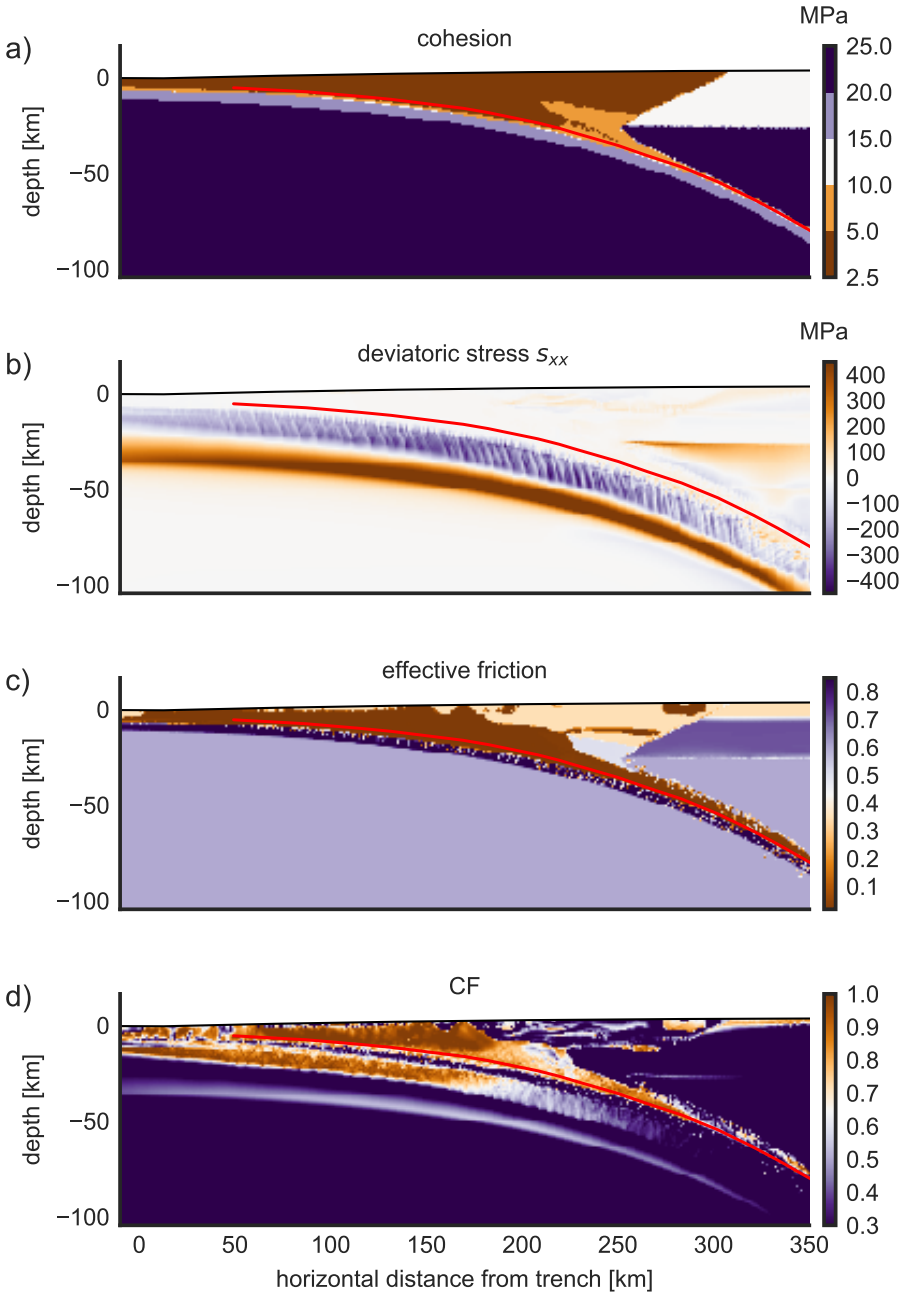

Figure 5.3: Initial conditions for the dynamic rupture simulations with SeisSol constrained by the STM model: a) bulk cohesion, b) deviatoric stress, c) effective friction and d) initial closeness to plastic failure (CF) as defined in Eq. (5.5).

Off-fault initial conditions for plasticity

In the following, we describe the off-fault initial conditions such as material properties, but also bulk cohesion, internal rock friction, and stresses that are needed for the plastic calculations in the dynamic rupture model. The presented initial conditions might serve as guidance for future dynamic rupture simulations of subduction zones with plasticity. Fig. 5.3 a)-c) visualizes bulk cohesion, deviatoric

horizontal stress s_{xx}, and internal friction. These parameters have not yet been coupled by van Zelst et al. (2018) for the entire simulation domain.

Bulk cohesion (Fig. 5.3 a)) ranges between 2.5 MPa and 20 MPa in correspondence to the values for different rock types defined in the STM model (see Table 5.1). The lowest bulk cohesion of 2.5 MPa is found in the accretionary wedge (sediments, brown). The fault is embedded in this sedimentary structure up to a depth of 26 km (corresponding to a horizontal distance of 217 km from the trench) and enters into the upper oceanic crust composed of basalt (5.0 MPa, orange) below that depth.

The horizontal deviatoric stresses s_{xx}, visualized in Fig. 5.3 b), show high extensional (positive) and compressional (negative) regimes in the bulk as a result of the tectonic loading and the subduction of the oceanic crust. The fault and the accretionary wedge are completely embedded in the compressional stress regime.

Fig. 5.3 c) shows the effective initial friction ($\mu_{eff} = (1-\lambda_f)\mu$) for the simulated domain including the pore fluid pressure factor $\lambda_f \in (0,1)$. As described in Sec. 5.3.1, λ_f does not develop dynamically during the interseismic loading in the STM model but is constant for specified regions. The presence of fluids drastically lowers friction, in particular close to the fault. The lowest value of 0.0175 is reached for the fluid filled sediment region (initial static friction of 0.35). Further, the model suggests that the upper oceanic crust is penetrated by fluids which is indicated by white and brown colors of low friction within the dark purple region of the oceanic crust with higher friction in Fig. 5.3 c).

Most insightful is the closeness of the given initial conditions to plastic failure (CF) prior the simulation as defined in Eq. (5.5). The closer CF is to 1, the closer are the initial stress conditions to plastic failure. In the vicinity of the fault, the CF ratio governs the occurrence of dynamically induced coseismic plastic strain close to the fault and hence influences rupture dynamics (Templeton and Rice, 2008; Gabriel et al., 2013). The complex structure of the stresses, cohesion, and friction results in a quite heterogeneous CF distribution (Fig. 5.3 d)). We note that due to the adjustment of stresses in the preprocessing step (see Sec. 5.2.3), initial CF values above 1 are adjusted to CF=0.99. The highest values of CF are found in the vicinity of the megathrust at 266 km horizontal distance reaching up to 0.99. This location corresponds to the nucleation region of the seismic event in the STM model. Within the accretionary wedge, CF also reaches high values between 0.95-0.99. In addition, we also observe CF between 0.9-0.95 in the oceanic crust just below the subducting slap. Outside these regions, the CF criterion is well below 0.6 and even below 0.3 for the mantle.

Discretization and time step

The model is discretized by 200 m triangular elements along the fault. In addition, the seafloor and the wedge around the fault also depict 200 m resolution, while the mesh is coarsened away from these regions of interest to save computational resources. We run the simulation with polynomial order p=4 (order of accuracy $\mathcal{O}5$) which corresponds to a sub-elemental discretization of additional 5 Gaussian integration points per element along the fault. In comparison to the STM model which uses a minimum edge length of 500 m, the dynamic rupture model depicts a much higher on-fault resolution to accurately capture the earthquake dynamics. The minimum time step is governed by a Cauchy-Friedrichs-Levy stability criterion in dependence of the fastest wave-speed and the minimum element size. The simulation runs for 200 s with a time step of 7.5e-04 s.

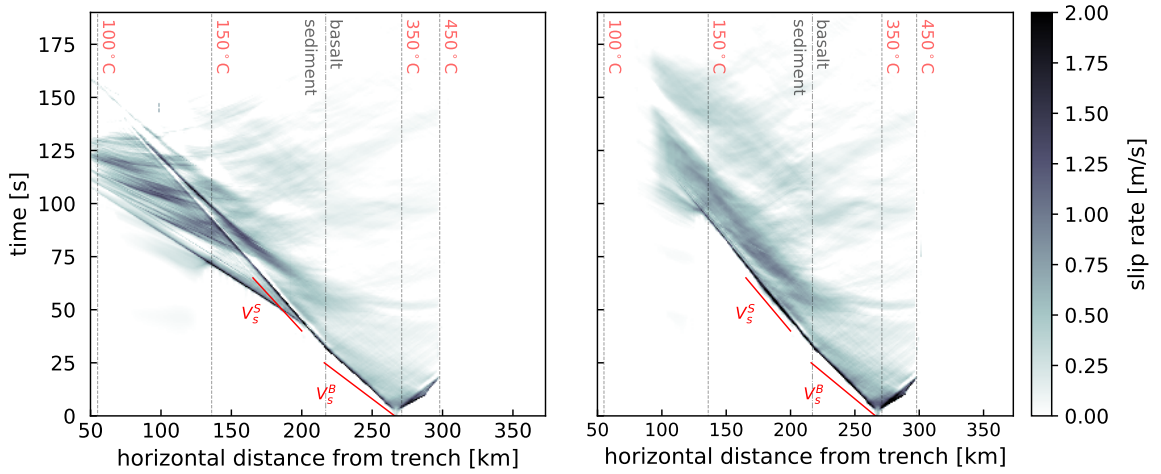

Figure 5.4: Slip rate over time for the purely elastic simulation (left) and the simulation with plasticity (right). The red lines indicate the shear-wave velocity of basalt (V_s^B) and the sediments (V_s^S). Dashed lines represent temperature or material boundaries as denoted by the annotations.

5.4 Simulation results

In the following, we analyze the simulation results of the dynamic rupture models with purely elastic and with plastic material properties using the initial conditions constrained by the STM model. We specifically investigate the combined effects of off-fault deformation, realistic geometries, and rheologies on seafloor uplift.

5.4.1 Rupture dynamics and rupture speed

Fig. 5.4 shows the slip rate along the fault over time for the elastic simulation (left) and the simulation with plasticity (right). Rupture in the elastic setup is initiated at 266 km horizontal distance from the trench at a depth of 40 km, and evolves bilaterally along the megathrust. When rupture reaches the brittle-ductile regime at around 450°C fault slip is smoothly stopped. In the up-dip direction, rupture first travels at speed of 1760 m/s, well below the s-wave speed of the basalt material (2000 m/s). Note that rupture speed is calculated using the along-fault distance and not the along horizontal distance shown in the figures of this chapter. After 43 s, a supershear daughter crack is initiated soon after the transition of the rupture from the basalt into the sediment region. This secondary rupture front enters the transition to the strengthening part (between 100°C and 150°C) after 71 s and reaches the shallow end of the fault after 105 s. Rupture in the shallowest part (less than 137 km horizontal distance to the trench) is re-activated several times and we observe distinct rupture pulses. The slower first rupture front reaches the transition to the strengthening region only at 91 s and smoothly dies out within the transition zone after 135 s. Fault slip stops completely after 157 s simulated time.

The dynamic rupture simulation with plasticity shows almost identical slip rates and rupture speed as the elastic simulation within the first 30 s. After 30 s the main rupture front travels at a reduced speed of 1380 km/s, close to s-wave speed, within the sediment layer and reaches the transition to the strengthening region after 91 s, similar to the first rupture front in the elastic case. The pronounced rupture peak diffuses and is smoothed out by the strengthening behaviour of friction. Rupture is completely stopped at 90 km from the trench, halfway within the transition from the slip-weakening

to -strengthening region. Fault slip is several times re-activated along the fault and completely stops after 174 s simulated time.

The closeness of the fault to the seafloor, as well as the different material interfaces, induce reflected seismic waves that lead to several re-activations of fault slip in both simulations. The most pronounced difference between the simulation with purely elastic material properties and the simulation with plasticity is the prevention of a secondary supershear rupture front due to plastic yielding. While the elastic simulation succeeds in rupturing through the strengthening region, shallow fault slip is always prohibited by plastic deformation. Off-fault plasticity also smears out the more distinct rupture pulses visible in the elastic simulation for distances closer than 200 km from the trench.

The interplay of increasing friction with slip and the occurrence of plastic strain (more details in Sec. 5.4.4) prohibit a continuation of fault slip along the shallowest part of the fault. Rupture in the simulation with plasticity stops exactly at the location where sliding friction is close to the initial static friction. Interestingly, this frictional barrier is easily surpassed by the supershear rupture of the elastic simulation. Accounting for more realistic material properties such as for off-fault plasticity might therefore explain why supershear rupture is rarely observed in nature, in particular in megathrust earthquakes that are often characterized by low rupture speeds (e.g., Bilek and Lay, 2018). Further, these model results provide an explanation why subduction zone earthquakes might not necessarily reach the trench, as observed for instance for the 2005 Nias-Simeulue (Sumatra) earthquake (Konca et al., 2007).

5.4.2 Final on-fault slip

The corresponding final slip along the horizontal distance from the trench is visualized in the bottom part of Fig. 5.5. Fault slip in the elastic setup reaches a maximum of 43 m located at 147 km from the trench. When the model accounts for plasticity, the maximum slip of 38 m is found at a deeper location at 190 km from the trench. Fault slip in the elastic and plastic simulation are very similar during the beginning of the rupture between 190 km and 300 km horizontal distance but fault slip is then continuously reduced by off-fault plastic yielding in the shallower part of the fault. In the case of plastic material properties, no slip is observed for distances less than 80 km from the trench while fault slip still reaches 2.2 m at the shallow part of the fault surface in the elastic simulation.

Due to the smooth rupture arrest at the transition from the slip-weakening to -strengthening region, there is no fault slip at the most shallow part of the fault for the model with off-fault plasticity. However, on-fault slip is already reduced much earlier in comparison to the elastic simulation, shortly after the formation of the supershear daughter crack at 200 km horizontal distance. This shows that the high slip for horizontal distances less than 190 km from the trench is mainly induced by the supershear rupture front in the elastic simulation. The results are further analysed with respect to the corresponding seafloor displacement in the next paragraph.

5.4.3 Surface displacements

Dynamic rupture simulations also provide the displacement along the Earth's surface or seafloor resulting from the coseismic rupture. This data helps to quantify the potential tsunami hazard associated with earthquake rupture along subduction zones.

The vertical displacement of the purely elastic simulation and the simulation with plasticity is visualized in the upper part of Fig. 5.5. The elastic simulation shows an almost continuous uplift of 3.78 m on average between 50 km and 200 km. The maximum value of 4.37 m is found at 110 km from the trench. When the model accounts for plasticity, the vertical uplift reaches up to 11.8 m at 149 km from

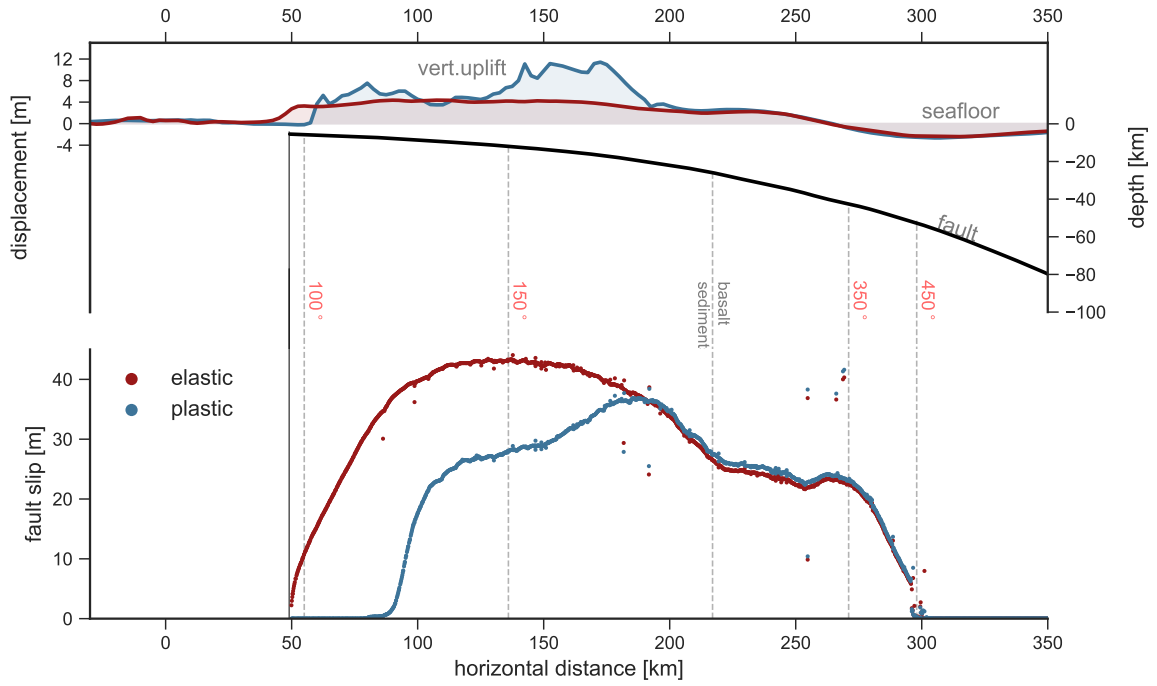

Figure 5.5: Fault slip (in m) along the megathrust and the corresponding vertical uplift of the seafloor topography (in m) for the simulations with elastic (red) and plastic (blue) material properties. Vertical lines mark the different on-fault temperature regions and material boundaries. The fault is indicated by the black line.

the trench. In comparison to the elastic simulation, plasticity increases the vertical uplift in particular between 60 km to 210 km horizontal distance. We observe two distinct regions of increased vertical uplift located at 75 km and between 140 km and 180 km. The maximum vertical uplift is increased by 70% due to plastic yielding within the accretionary wedge.

The enhanced vertical uplift for the simulation with plasticity can be explained by the corresponding on-fault slip distribution. The vertical uplift is always increased when fault rupture is slowed down or even stopped due to the occurrence of plasticity (see next paragraph for the plastic strain accumulation). The highest increase with plasticity between 115 km and 190 km corresponds to the on-fault slip decrease at these locations in comparison to the elastic simulation when plasticity prevents the occurrence of supershear. The vertical displacement is again increased when rupture along the megathrust is completely arrested within the slip-strengthening region in the shallow part of the fault.

The results imply that vertical uplift is locally highly increased by off-fault plastic yielding although total fault slip close to the trench is overall lower. These localized effects might play a crucial role in the efficient generation of tsunamis. To correctly evaluate the earthquake induced tsunami hazard, earthquake rupture models need to account for realistic material properties.

5.4.4 Plastic strain distribution

Fig. 5.6 visualizes the accumulated plastic strain η as defined by Ma (2009) after 200 s simulated time. Plastic yielding is concentrated in the shallowest part of the accretionary wedge and along the fault surface. In the accretionary wedge, plastic strain localizes into shear bands. Four distinct bands with large amounts of plastic strain stand out: The first and second splay-like structure within 150 km and

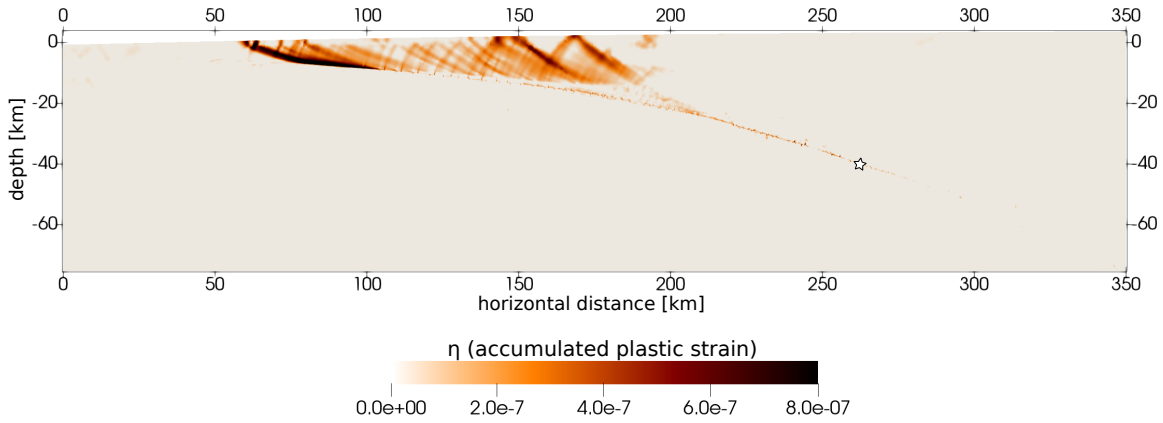

Figure 5.6: Accumulated plastic strain after 200 s simulated time. The hypocenter is marked by a white star.

200 km horizontal distance form steeply dipping between the megathrust and the seafloor. Another strain band with a high amount of plastic strain branches approximately at 100 km horizontal distance from the trench and reaches the seafloor at 78 km. The most pronounced strain band forms at 80 km horizontal distance connecting the megathrust and seafloor in a steep angle. Note that the originally prescribed fault geometry still continues up to 49 km horizontal distance from the trench but is not connected to the seafloor. Interestingly, rupture within the STM model based on a visco-elasto-plastic rheology stops along the main megathrust zone at a distance of 70-80 km from the trench, similar to the dynamic rupture model with plasticity, and further evolves along splay faults (see plastic strain accumulation in Fig. 3 d) in van Zelst et al. (2018)). The similarity between these two distinct models confirms the consistency of our coupling approach.

Plastic strain is exclusively accumulated within the accretionary wedge although the initial conditions are also close to plastic failure in the vicinity of the nucleation patch and within the oceanic crust (see Fig. 5.3 d)). The locations where the splay like structures form correspond to the regions where fault slip is reduced or completely stopped, as described in Sec. 5.4.1 and Sec. 5.4.2. These locations are in turn associated with the enhanced vertical uplift in comparison to the purely elastic simulation. The results show that plastic yielding locally enhances the vertical seafloor uplift.

5.5 Discussion

5.5.1 Initial conditions

This work focuses on constraining initial conditions for dynamic rupture models of subduction zones with plasticity by the output of a long-term seismo-thermo-mechanical model. Here, we discuss the imported initial conditions from the STM model, such as bulk cohesion and the closeness of plastic failure, with respect to previous dynamic rupture simulations of subduction zones.

Bulk cohesion in the STM model is based on the different materials that are commonly found in subduction zones. The values of each rock type (between 2.5 MPa and 25 MPa, Table 5.1) are prescribed but their location evolves with tectonic loading and associated subduction. In contrast, previous subduction zone models use bulk cohesion that is coupled to the depth-dependent vertical

stress but assume an otherwise homogeneous medium (e.g., Ma, 2012; Ma and Hirakawa, 2013; Hirakawa, 2016). For instance, cohesion ranges between 0 MPa at the seafloor to 24.7 MPa at the bottom of the accretionary wedge in the simulations of Ma (2012). In addition to the depth-dependency of cohesion, future model setups could consider using material dependent bulk cohesion to distinguish between the sediment structures in the shallow part of subduction zone and the consolidated oceanic and continental crust which might influence the occurrence of plasticity.

In terms of initial closeness of plastic failure (CF), the STM constrained initial conditions suggest that the accretionary wedge depicts a CF between 0.95-0.99, i.e. initial conditions very close to failure. Within the continuum-mechanics based STM model, CF in the shallow part of the wedge is enhanced by the assumption of velocity-strengthening material properties within that region. The strengthening behaviour hampers fault movement which leads to an increased stress build-up during tectonic loading. The resulting CF value is close to what is assumed by Ma (2012), Ma and Hirakawa (2013), and Hirakawa (2016) (CF=0.99). Their models are based on the critical wedge theory which assumes that the entire accretionary wedge is almost at failure prior to an earthquake (Dahlen et al., 1984). The self-consistent initial conditions therefore confirm the model assumptions of previous simulations.

The STM model suggests a quite heterogeneous CF distribution due to its complexity in terms of the material composition, friction, and initial stresses (Fig. 5.3 d). This is in contrast to constant or only depth-dependent CF values commonly used in dynamic rupture simulations with off-fault plasticity (e.g., Andrews, 2005; Ma, 2012; Roten et al., 2017). In particular for subduction zones, different material layers and accumulated stresses might affect CF and as a consequence the occurrence of plastic strain during coseismic slip.

As an alternative to the STM model constrained initial conditions, dynamic rupture models can be coupled with classic seismic cycling simulations that model the evolution of stress for a prescribed fault interface (Lapusta et al., 2000; Kaneko and Fialko, 2011; Erickson et al., 2017; Allison and Dunham, 2018). However, only a few of these approaches are able to account for non-elastic rheologies and most of them are restricted to planar, strike-slip fault geometries. Besides the visco-elasto-plastic rheology used by the STM model, the main advantage of the presented approach is the additional crucial information about the self-consistently evolving fault geometry and the material composition of the subduction zone channel.

5.5.2 Future extensions of the model

In the presented dynamic model, friction is approximated by a simple linear slip-weakening (and strengthening) law to mimic the velocity-weakening (and strengthening) behaviour of the underlying rocks along the subduction fault. Future work needs to extend these models to account for rate-and-state friction. This more elaborated, laboratory-based friction law describes the evolution of friction depending on the slip velocity and a state variable (Dieterich, 1979; Ruina, 1983).

Future work might also include additional on-fault weakening processes such as thermal pressurization due to the heat generation during sliding (e.g., Noda et al., 2009). This effect might facilitate rupture propagation along the fault, in particular in fluid rich regions. While thermal pressurization alters the strength of the fault, the dynamic change of off-fault pore-fluid pressure might be an important off-fault effect. Simulation results on planar fault geometries with homogeneous material already show that dynamic pore pressure influences the occurrence of plastic strain and enhances the vertical seafloor uplift even more in comparison to purely elastic simulations (Ma and Hirakawa, 2013; Hirakawa, 2016). It would be interesting to combine these effects with realistic fault geometries and complex initial conditions constrained by long-term seismic modelling.

Here, we presented dynamic rupture models that include a single megathrust geometry based on the location of the highest plastic strain during a coseismic period within the STM model (van Zelst et al., 2018). However, we can not determine a single rupture path from the STM model as plastic strain also manifests within the accretionary wedge which suggests rupture off the megathrust. Plastic yielding in our simulation develops into even more localized strain bands that resemble splay faults (see Fig. 5.6). With the current models, we cannot evaluate whether these splay would have been ruptured since they are not explicitly tagged with a friction boundary condition, Future extensions of the model could include additional splay fault geometries to investigate splay fault activation and the associated vertical uplift under realistic model assumptions.

5.6 Conclusions

We present dynamic rupture models of subduction zones with plasticity using initial conditions constrained by a long-term seismo-thermal-mechanical (STM) model. The STM model provides initial stresses, material dependent friction, and bulk cohesion as well as a fault geometry constrained by the locations of highest plastic strain within the STM model. These self-consistent initial conditions might serve as guidance for setting up future dynamic rupture models of megathrust earthquakes and increase the reliability of numerical modelling results.

To couple these two models, we describe a preprocessing step that adjusts all stresses at immediate plastic failure by a static plastic calculation. The imported initial conditions suggest that the accretionary wedge is close to plastic failure, as previously proposed by dynamic rupture models that are based on the critical wedge theory (e.g., Ma and Hirakawa, 2013). Effective friction along the fault is very low, ranging between 0.0175 and 0.028, due to the occurrence of fluids along the subduction zone interfaces.

We further analyze the simulation results of the geomechanically constrained dynamic rupture models with purely elastic and with plastic material in terms of rupture dynamics and seafloor displacement. The proximity of the fault to the seafloor and the different material interfaces induce reflected seismic waves that lead to several re-activations of fault slip along the megathrust. When the model accounts for plasticity, distinct rupture pulses that are visible in the purely elastic simulation are smeared out. Including plasticity also prevents the initiation of a daughter supershear crack after the transition from the basalt to the sediment region. The supershear front succeeds in rupturing the strengthening part of the fault in the elastic simulation while rupture in the model with plasticity is always stopped within the transition zone from the weakening to strengthening regime. Slip at the shallowest part of the fault is reduced by off-fault plastic yielding in the accretionary wedge. As a consequence, the maximum fault slip in the simulation with plasticity is located deeper along the megathrust. Still, vertical uplift is locally enhanced by 70% due to the occurrence of plastic strain at the locations where fault rupture is slowed down or arrests. These localized effects might play a crucial role in the efficient generation of tsunamis. The results highlight the underestimation of the vertical displacement and hence the tsunami hazard when dynamic rupture models do not account for realistic material properties such as off-fault plasticity.

6
Conclusions

This thesis addressed the implementation, verification, and application of off-fault plasticity in the dynamic rupture software package SeisSol. We focused on realistic multi-physics earthquake simulations along non-planar branched fault systems and shallow dipping subduction zones to investigate the complex interaction of earthquake rupture dynamics, fault geometry, and inelastic processes around the fault. This work demonstrates the need for realistic material properties in numerical models and contributes to a better understanding of the (in)elastic processes that influence earthquake source dynamics, ground motions, and surface displacements.

We first detailed the efficient implementation of off-fault plasticity that enables the use of inelastic material properties in large-scale earthquake rupture simulations. 3D refinement studies including for the first time depth-dependent initial stresses and off-fault plasticity provided essential information about the required on-fault resolution to accurately resolve the fault dynamics in realistic simulation setups. Plasticity regularizes the peak slip rate and increases the cohesive zone width such that a high resolution of the fault may be less crucial than commonly assumed. The influence of off-fault plasticity on rupture behaviour is demonstrated in a dynamic rupture simulation of the 1992 Landers earthquake including several complex fault segments connected by fault branches. Plasticity considerably alters the spatio-temporal distribution of rupture transfer, changing the location of dynamically triggered nucleation and delaying rupture arrival across the fault system. This example shows the importance of combining fully 3D dynamic modelling, complex fault geometries, and off-fault plastic yielding to realistically capture dynamic rupture transfers between fault segments.

To increase our understanding of the complex rupture transfers during the 1992 Landers earthquake, we further extended the model to account for a 3D subsurface structure, high-resolution topography, and viscoelastic attenuation in addition to the plastic material response. Sustained rupture along all fault segments poses a strong constraint on model parametrization, in particular on the amplitude and orientation of the initial fault stresses. Complex transfer mechanisms such as dynamic triggering, direct rupture branching, and combinations of both are essential to drive rupture across the entire fault system. Dynamic triggering of the segment most distant from the hypocenter is enabled by the almost simultaneous failure of preceding fault segments. Rupture jumps are thus possible over distances much larger than previously suggested and large enough to be affected by viscoelastic attenuation. The realistic modelling ingredients lead to a uniquely constrained simulation that reproduced a broad variety of observations such as moment rate function, slip distribution, seismic waveform characteristics, and peak ground velocities, as well as shallow slip deficits and off-fault damage patterns. In contrast to a purely elastic simulation, the viscoelastic-plastic scenario reduces the mean peak ground

velocities in forward direction by up to 35% due to a slower rupture transfer. The associated ground motion variability close to the fault is slightly increased with plasticity due to the heterogeneous distribution of near-fault plastic yielding. Inelastic off-fault processes are therefore not only important to realistically model rupture transfer in complex fault geometries but also for evaluating the potential ground motions in strongly unilateral earthquakes. The presented simulations demonstrate that physics-based earthquake simulations including various representations of natural complexities may successfully complement and augment earthquake source observations.

While Chapter 3 focused on the effect of off-fault plasticity on rupture transfer and ground motions in strike-slip earthquakes, we further investigated the influence of inelastic deformation on earthquake source dynamics and surface displacement in 3D subduction zone scenarios. We extended our purely elastic dynamic rupture simulation of the 2004 Sumatra-Andaman earthquake (Uphoff et al., 2017) featuring a low dipping fault geometry, splay faults, and a horizontally rotating stress field to account for inelastic deformation. We found a clear correlation between the angle that forms between the orientation of the horizontal principal stress and the fault strike, and the increase or decrease of fault slip with off-fault plasticity. Increased fault slip directly translates into an increase of horizontal and vertical seafloor displacement and vice versa for reduced fault slip. Splay faults have a high potential for generating vertical uplift, which is even more enhanced when accounting for inelastic off-fault processes. The results highlight the influence of initial modelling assumptions such as along-strike stress rotations, fault geometry, and off-fault plasticity on final fault slip and surface displacement in subduction zone models. These model ingredients are thus important when using the simulated surface displacement as spatio-temporal source input into tsunami models.

Motivated by the dependence of the simulation results on the initial assumptions, we presented a workflow that overcomes the difficulties in constraining appropriate initial conditions for 2D dynamic rupture simulations with plasticity. We used the output of a long-term seismo-thermo-mechanical (STM) model that determines stress and rheologies according to the temperature-dependent strength of the rocks and the tectonic stress build-up over millions of years (van Zelst et al., 2018). The STM model provides a self-consistent slab geometry, initial stress and strength conditions, and material information including bulk friction and cohesion. The resulting dynamic rupture models of a subduction zone earthquake depict a complex rupture evolution including several re-activations of fault slip due to the seismic waves reflected at material contrasts and at the seafloor. The initial conditions suggest that the accretionary wedge is already close to plastic failure prior to the earthquake and rupture completely stops at the transition to the velocity strengthening shallow part. These geomechanically constrained models might serve as guidance for building realistic dynamic rupture simulations of subduction zones including off-fault plasticity.

Future perspectives

This work demonstrates that current modelling features of SeisSol already enable the efficient simulation of large-scale earthquake rupture models including a high degree of realism. The output and results of these simulations can be used in various ways in future work.

The 1992 Landers simulations in Chapter 3 created a large amount of high-resolution synthetic seismograms that have only been analysed for their peak ground motions. This dataset would provide a unique opportunity to identify different signatures or characteristics in seismic signals corresponding to distinct rupture transfer mechanisms such as branching or rupture jumping. The results might help to gain more information about the earthquake source dynamics from seismic data.

While this example focused on complex large fault systems with a total length of over 80 km, SeisSol could be readily used for simulations of smaller-scale fault networks. This might be particularly

interesting for fracture networks in geo-reservoirs. They pose a potential seismic hazard due to the injected fluids that locally change the pore fluid pressure. The elevated pore pressure decreases fault strength which can lead to rupture initiation or facilitated rupture propagation. Dynamic rupture simulations can be used to analyze under which conditions these fractures are activated and cascade into bigger seismic events. A potential target site is the south of Munich where Germany's biggest geothermal power plant is currently being built. This work would help to quantify the maximum expected earthquake size associated with fracture networks within these geo-reservoirs.

Further, the output of subduction zone simulations as presented in Chapter 4 and 5 can be used to study the actual generation of tsunamis induced by the modelled earthquake. For this purpose, the spatio-temporal displacement field generated by these simulations can be inserted as physics-based earthquake source into tsunami modelling tools. This might be particularly interesting for the Sumatra-Andaman earthquake since the generation of the induced tsunami sequences is still not understood. While we showed that plastic deformation within the accretionary wedge highly alters the seafloor displacement we need to investigate how more realistic material properties affect the resulting tsunami. However, this model is quite complex due to the along-strike variation of the megathrust geometry, the rotating horizontal stress field, and the 1500 km fault length. As a first step, we could quantify the influence of stress orientation, fault dip, and different plasticity parametrizations on seafloor displacement in a detailed parameter study using a simplified 3D setup. The corresponding tsunami simulations would improve our understanding of the conditions that favour the generation of devastating tsunamis.

Constraining initial conditions for dynamic rupture simulations is quite challenging, specifically for subduction zone models. We presented in Chapter 6 a workflow for constraining initial conditions with plasticity for a single earthquake using a long-term seismo-thermo-mechanical (STM) model. The initial assumptions of the STM model were based on the characteristics of the Southern Chilean subduction zone and determined the initial zone of weakness, the thickness of the crust, the age, and hence the temperature of the slab. Future work needs to investigate how these initial conditions vary for different earthquakes within the Chilean setup, as well as for different subduction zones around the world. It would be specifically interesting to see how sediment thickness, varying rock properties, and distinct plate convergence rates influence the initial stresses and hence the closeness of plastic failure for different subduction zones. Common and distinct features could be identified and linked to a maximum expected seafloor displacement for each subduction setup. This information would improve our understanding of the stress conditions prior to an earthquake and the potential tsunami risk associated with earthquakes along megathrusts.

Although the STM model depicts a high degree of realism due to the visco-elasto-plastic rheology and the complexity of the material composition, one of the biggest drawbacks is the restriction to two dimensions. 2D simulations of subduction zones do not capture the along-strike evolution of stresses and fault geometry. The simulations of the 2004 Sumatra-Andaman earthquake in Chapter 4 confirmed that these variations lead to a distinct seafloor displacement along-strike which might affect the tsunami genesis. If we want to realistically capture the seismic and tsunami hazard these variations need to be taken into account. However, solving the nonlinear rheology equations in the STM model is computationally expensive for the wide range of involved spatial and temporal scales. Computational costs will highly increase when the model is extended to 3D. Efficient numerical techniques need to be exploited to optimize these models for the use on modern high-performance infrastructure. Current work in progress tackles that problem through scalable shared- and distributed memory parallelization and by composing a preconditioned Newton-Krylov method using the PETSc library (Pranger et al., 2018). These developments might enable constraining initial conditions also for 3D dynamic rupture models in a physically consistent way.

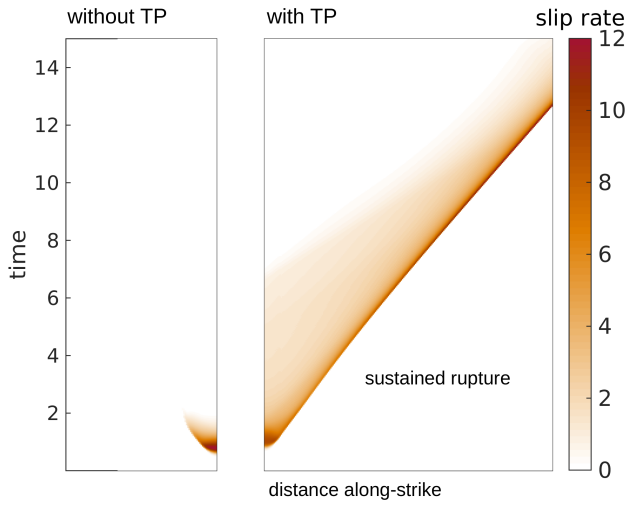

Figure 6.1: Slip rate over time and along-strike for a 2D strike-slip scenario using SeisSol (Wollherr et al., 2016). Rupture quickly dies out without thermal pressurization (TP, left) but can be sustained for the same initial conditions when we include TP (right).

Besides the current model complexities in SeisSol, the implementation of additional on-fault weakening processes in conjunction with plasticity could be considered in future work. In the presence of fluids, the generated heat during rapid coseismic fault slip increases the pore fluid pressure at the fault which effectively decreases fault strength. This process, called thermal pressurization (TP), might explain why stable creeping parts of the fault become unstable during coseismic slip as observed during the Tohoku Oki earthquake in 2011 (Noda and Lapusta, 2013). During the preparation of this thesis, we already included TP in the 2D version of SeisSol (Wollherr et al., 2016). Its extension to 3D as well as an in-depth analysis of numerically efficient schemes for incorporating TP will be part of future work. Initial results in 2D show that rupture is sustained along the fault when accounting for TP while rupture quickly dies out under the same initial conditions but without the effect of dynamically changing on-fault fluid pressure (see Fig. 6.1). These results are consistent with other 2D models: TP facilitates rupture propagation and the activation of fault branches and increases rupture speed and slip rate (e.g, Bizzarri and Cocco, 2006; Urata et al., 2013; Schmitt et al., 2015). However, previous work considered TP only in setups with purely elastic material properties. Since plasticity rather reduces rupture speed and hampers sustained rupture it would be interesting to analyze these competing effects for complex fault geometries.

Bibliography

Abercrombie, R. and Mori, J. (1994). Local observations of the onset of a large earthquake: 28 June 1992 Landers, California. *Bull. Seism. Soc. Am.*, 84(3):725. Referenced in: 3.4.1.

Allison, K. L. and Dunham, E. M. (2018). Earthquake cycle simulations with rate-and-state friction and power-law viscoelasticity. *Tectonophysics.*, 733:232 – 256. Physics of Earthquake Rupture Propagation. Referenced in: 5.5.1.

Ammon, C. J., Ji, C., Thio, H.-K., Robinson, D., Ni, S., Hjorleifsdottir, V., Kanamori, H., Lay, T., Das, S., Helmberger, D., et al. (2005). Rupture process of the 2004 Sumatra-Andaman earthquake. *Science*, 308(5725):1133–1139. Referenced in: 4.1 and 4.3.1.

Ampuero, J.-P. and Ben-Zion, Y. (2008). Cracks, pulses and macroscopic asymmetry of dynamic rupture on a bimaterial interface with velocity-weakening friction. *Geophys. J. Int.*, 173(2):674–692. Referenced in: 5.2.1.

Ampuero, J.-P., Vilotte, J.-P., and Sanchez-Sesma, F. (2002). Nucleation of rupture under slip dependent friction law: simple models of fault zone. *J. Geophys. Res.*, 107(B12). Referenced in: 3.4.2.

Ando, R. (2016). Fast Domain Partitioning Method for dynamic boundary integral equations applicable to non-planar faults dipping in 3-D elastic half-space. *Geophys. J. Int.*, 207(2):833–847. Referenced in: 2.1.

Ando, R., Imanishi, K., Panayotopoulos, Y., and Kobayashi, T. (2017). Dynamic rupture propagation on geometrically complex fault with along-strike variation of fault maturity: Insights from the 2014 Northern Nagano earthquake Crustal Dynamics. *Earth Planets Space.*, 69(1). Referenced in: 2.1 and 3.1.

Andrews, D. (1976). Rupture propagation with finite stress in antiplane strain. *Geophys. J. Int.*, 81(20):3575–3582. Referenced in: 1.1, 1.2, 2.1, and 2.6.4.

Andrews, D. J. (1985). Dynamic plane-strain shear rupture with a slip-weakening friction law calculated by a boundary integral method. *Bull. Seism. Soc. Am.*, 75(1):1. Referenced in: 1.1 and 4.2.2.

Andrews, D. J. (1999). Test of two methods for faulting on finite-difference calculations. *Bull. Seism. Soc. Am.*, 89(4):931–937. Referenced in: 1.2, 2.2.1, and 3.1.

Andrews, D. J. (2005). Rupture dynamics with energy loss outside the slip zone. *J. Geophys. Res.*, 110(1):1–14. Referenced in: 1.1, 1.2, 2.1, 2.2.2, 2.2.2, 2.2.2, 2.2.3, 2.3, 2.3.1, 2.4.4, 2.5.2, 2.6.1, and 5.5.1.

Aochi, H. and Fukuyama, E. (2002). Three-dimensional nonplanar simulation of the 1992 Landers earthquake. *J. Geophys. Res.*, 107(B2):B22035. Referenced in: 1.2, 2.1, 2.5, 2.5.1, 2.6.5, 3.1, 3.2.2, and 3.5.

Aochi, H., Fukuyama, E., and Matsu'ura, M. (2000). Spontaneous Rupture Propagation on a Non-planar Fault in 3-D Elastic Medium. *Pure Appl. Geophys.*, 157(11):2003–2027. Referenced in: 2.1.

Aochi, H. and Madariaga, R. (2003). The 1999 Izmit, Turkey, earthquake: Nonplanar fault structure, dynamic rupture process, and strong ground motion. *Bull. Seism. Soc. Am.*, 93(3):1249–1266. Referenced in: 3.2.2 and 4.2.2.

Aochi, H., Madariaga, R., and Fukuyama, E. (2003a). Constraint of fault parameters inferred from nonplanar fault modeling. *Geochem. Geophys. Geosyst.*, 4(2):1–16. Referenced in: 2.5.1.

Aochi, H., Madariaga, R., and Fukuyama, E. (2003b). Constraint of fault parameters inferred from nonplanar fault modeling. *Geochem. Geophys. Geosyst.*, 4(2):1–16. Referenced in: 3.1 and 3.5.

Atkins, H. L. and Shu, C.-W. (1996). Quadrature-free implementation of discontinuous Galerkin method for hyperbolic equations. *AIAA journal*, 36(5):775–782. Referenced in: 2.2.1.

Banerjee, P., Pollitz, F. F., and Bürgmann, R. (2005). The Size and Duration of the Sumatra-Andaman Earthquake from Far-Field Static Offsets. *Science*, 308(5729):1769–1772. Referenced in: 4.1 and 4.3.1.

Barall, M. (2009). A grid-doubling finite-element technique for calculating dynamic three-dimensional spontaneous rupture on an earthquake fault. *Geophys. J. Int.*, 178(2):845–859. Referenced in: 1.2, 2.1, 2.3.1, and 3.1.

Barall, M. and Harris, R. (2014). Metrics for Comparing Dynamic Earthquake Rupture Simulations. *Seismol. Res. Lett.*, 86(1):223–235. Referenced in: 2.2.2.

Barenblatt, G. I. (1962). The mathematical theory of equilibrium cracks in brittle fracture. In *Adv. Appl. Mech.*, volume 7, pages 55–129. Elsevier. Referenced in: 1.1.

Beeler, N., Tullis, T., and Goldsby, D. (2008). Constitutive relationships and physical basis of fault strength due to flash heating. *J. Geophys. Res.*, 113(B1). Referenced in: 1.1.

Ben-Zion, Y. and Sammis, C. G. (2003). Characterization of Fault Zones. *Pure Appl. Geophys.*, 160(3):677–715. Referenced in: 1.1 and 2.1.

Bhat, H. S., Olives, M., Dmowska, R., and Rice, J. R. (2007). Role of fault branches in earthquake rupture dynamics. *J. Geophys. Res.*, 112(B11):B11309. Referenced in: 3.1.

Bilek, S. L. and Lay, T. (2018). Subduction zone megathrust earthquakes. *Geosphere*, 14(4):1468. Referenced in: 5.4.1.

Bizzarri, A. (2010). How to promote earthquake ruptures: Different nucleation strategies in a dynamic model with slip-weakening friction. *Bull. Seism. Soc. Am.*, 100(3):923–940. Referenced in: 2.4, 3.2.3, and 3.4.2.

Bizzarri, A. and Cocco, M. (2006). A thermal pressurization model for the spontaneous dynamic rupture propagation on a three-dimensional fault: 1. Methodological approach. *J. Geophys. Res.*, 111(5). Referenced in: 1.1 and 6.

Bizzarri, A. and Das, S. (2012). Mechanics of 3-D shear cracks between Rayleigh and shear wave rupture speeds. *Earth Planet. Sci. Lett.*, 357-358:397–404. Referenced in: 2.4.2.

Boatwright, J. and Quin, H. (1986). The Seismic Radiation from a 3-D Dynamic Model of a Complex Rupture Process. Part I: Confined Ruptures. In *Earthquake Source Mechanics*, pages 97–109. Am. Geophys. Union. Referenced in: 2.3.

Bommer, J. J. and Abrahamson, N. A. (2006). Why do modern probabilistic seismic-hazard analyses often lead to increased hazard estimates? *Bull. Seism. Soc. Am.*, 96(6):1967–1977. Referenced in: 3.4.3.

Boore, D. M. and Atkinson, G. M. (2008). Ground-motion prediction equations for the average horizontal component of PGA, PGV, and 5%-damped PSA at spectral periods between 0.01 s and 10.0 s. *Earth. Spectra*, 24(1):99–138. Referenced in: 3.3.5, 3.8, 3.9, 3.16, 3.4.3, and 3.5.

Boore, D. M., Watson-Lamprey, J., and Abrahamson, N. A. (2006). Orientation-independent measures of ground motion. *Bull. Seism. Soc. Am.*, 96(4A):1502–1511. Referenced in: 3.7, 3.3.5, 3.4.3, and 3.C.1.

Bouchon, M. and Campillo, M. (1998). Stress field associated with the rupture of the 1992 Landers, California, earthquake and its implifications concerning the fault strength at the onset of the earthquake. *J. Geophys. Res.*, 103(B9):21091–21097. Referenced in: 3.1 and 3.2.3.

Brace, W. F. and Byerlee, J. D. (1966). Stick-Slip as a Mechnism for Earthquakes. *Sciene*, 153(3739):990–992. Referenced in: 1.1.

Breuer, A., Heinecke, A., and Bader, M. (2016). Petascale local time stepping for the ADER-DG finite element method. In *2016 IEEE International Parallel and Distributed Processing Symposium*, pages 854–863. IEEE. Referenced in: 2.1, 2.2.1, and 3.2.5.

Breuer, A., Heinecke, A., Rannabauer, L., and Bader, M. (2015). High-Order ADER-DG Minimizes Energy-and Time-to-Solution of SeisSol. In *Proceedings of the International Conference on High Performance Computing*, pages 340–357, Cham. Springer International Publishing. Referenced in: 2.1 and 3.2.5.

Breuer, A., Heinecke, A., Rettenberger, S., Bader, M., Gabriel, A.-A., and Pelties, C. (2014). Sustained Petascale Performance of Seismic Simulations with SeisSol on SuperMUC. In *Proceedings of the International Supercomputing Conference*, pages 1–18, Cham. Springer International Publishing. Referenced in: 1.2, 2.1, 2.2.1, 3.1, 3.2.5, 4.1, and 4.2.4.

Brizzi, S., van Zelst, I., van Dinther, Y., Funiciello, F., and Corbi, F. (2017). How long-term dynamics of sediment subduction controls short-term dynamics of seismicity. In *AGU Fall Meeting Abstracts*. Referenced in: 5.3.1.

Brodsky, E. E., Kirkpatrick, J. D., and Candela, T. (2016). Constraints from fault roughness on the scale-dependent strength of rocks. *Geology*, 44(1):19. Referenced in: 1.1.

Byerlee, J. (1978). Friction of Rocks. *Pure Appl. Geophys.*, 116:615–626. Referenced in: 1.1 and 5.1.

Campbell, K. W. and Bozorgnia, Y. (1994). Empirical analysis of strong ground motion from the 1992 Landers, California, earthquake. *Bull. Seism. Soc. Am.*, 84(3):573. Referenced in: 3.1.

Campillo, M. and Archuleta, R. J. (1993). A rupture model for the 28 June 1992 Landers, California, earthquake. *Geophys. Res. Lett.*, 20(8):647–650. Referenced in: 3.3.2, 3.3.3, and 3.4.1.

Candela, T., Renard, F., Klinger, Y., Mair, K., Schmittbuhl, J., and Brodsky, E. E. (2012). Roughness of fault surfaces over nine decades of length scales. *J. Geophys. Res.*, 117(B8). Referenced in: 1.1 and 3.3.6.

Chauhan, A. P. S., Singh, S. C., Hananto, N. D., Carton, H., Klingelhoefer, F., Dessa, J.-X., Permana, H., White, N. J., and Graindorge, D. (2009). Seismic imaging of forearc backthrusts at northern Sumatra subduction zone. *Geophys. J. Int.*, 179(3):1772–1780. Referenced in: 4.2.1.

Chen, X. (1995). *Near-field ground motion from the Landers earthquake*. PhD thesis, California Institute of Technology. Referenced in: 3.1.

Chester, F. and Higgs, N. (1992). Multimechanism friction constitutive model for ultrafine quartz gouge at hypocentral conditions. *J. Geophys. Res.*, 97(B2):1859–1870. Referenced in: 5.1.

Chester, F. and Logan, J. (1987). Composite planar fabric of gouge from the Punchbowl Fault, California. *J. Struct. Geol.*, 9(5):621 – IN6. Referenced in: 1.1.

Chester, F. M., Evans, J. P., and Biegel, R. L. (1993). Internal structure and weakening mechanisms of the San Andreas Fault. *J. Geophys. Res.*, 98(B1):771. Referenced in: 1.1 and 2.1.

Choi, J. H., Edwards, P., Ko, K., and Kim, Y. S. (2016). Definition and classification of fault damage zones: A review and a new methodological approach. *Earth-Science Reviews*, 152(November):70–87. Referenced in: 1.1.

Cockburn, B., Karniadakis, G. E., and Shu, C.-W. (2000). *Discontinuous Galerkin Methods. Theory, Computation and Applications*, volume 11. Springer, Berlin. Referenced in: 2.2.1.

Cohee, B. P. and Beroza, G. C. (1994). Slip distribution of the 1992 Landers earthquake and its implications for earthquake source mechanics. *Bull. Seism. Soc. Am.*, 84(3):692–712. Referenced in: 3.1, 3.3.2, 3.3.3, 3.3.4, 3.4.3, and 3.4.5.

Cotton, F. and Campillo, M. (1995). Frequency domain inversion of strong motions: Application to the 1992 Landers earthquake. *J. Geophys. Res.*, 100(B3):3961–3975. Referenced in: 1.2, 2.5, 3.1, 3.2.3, 3.3.2, 3.4.3, and 3.4.5.

Crameri, F., Schmeling, H., Golabek, G., Duretz, T., Orendt, R., Buiter, S., May, D., Kaus, B., Gerya, T., and Tackley, P. (2012). A comparison of numerical surface topography calculations in geodynamic modelling: an evaluation of the sticky airmethod. *Geophys. J. Int.*, 189(1):38–54. Referenced in: 5.2.1.

Cruz-Atienza, V. and Virieux, J. (2004). Dynamic rupture simulation of non-planar faults with a finite-difference approach. *Geophys. J. Int.*, 158(3):939–954. Referenced in: 2.1.

Cubas, N., Lapusta, N., Avouac, J. P., and Perfettini, H. (2015). Numerical modeling of long-term earthquake sequences on the NE Japan megathrust: Comparison with observations and implications for fault friction. *Earth Planet. Sci. Lett.*, 419:187–198. Referenced in: 4.4.2 and 5.1.

Cui, Y., Olsen, K. B., Jordan, T. H., Lee, K., Zhou, J., Small, P., Roten, D., Ely, G., Panda, D. K., Chourasia, A., Levesque, J., Day, S. M., and Maechling, P. (2010). Scalable earthquake simulation on petascale supercomputers. In *Proceedings of the International Conference for High Performance Computing, Networking, Storage and Analysis*, pages 1–20. IEEE. Referenced in: 2.1.

Dahlen, F. A., Suppe, J., and Davis, D. (1984). Mechanics of fold-and-thrust belts and accretionary wedges: Cohesive Coulomb Theory. *J. Geophys. Res.*, 89(B12):10087–10101. Referenced in: 5.1 and 5.5.1.

Dalguer, L. A. and Day, S. M. (2007). Staggered-grid split-node method for spontaneous rupture simulation. *J. Geophys. Res.*, 112(2):1–15. Referenced in: 1.2, 2.1, 2.3.1, and 3.1.

Dalguer, L. A. and Day, S. M. (2009). Asymmetric rupture of large aspect-ratio faults at bimaterial interface in 3D. *Geophys. Res. Lett.*, 36(23):L23307. Referenced in: 2.6.3.

Dalguer, L. A., Irikura, K., and Riera, J. D. (2003). Simulation of tensile crack generation by three-dimensional dynamic shear rupture propagation during an earthquake. *J. Geophys. Res.*, 108(B3):2144. Referenced in: 2.6.3.

Day, S. M. (1982). Three-dimensional finite difference simulation of fault dynamics: rectangular faults with fixed rupture velocity. *Bull. Seism. Soc. Am.*, 72(3):705–727. Referenced in: 2.1 and 2.3.

Day, S. M., Dalguer, L. A., Lapusta, N., and Liu, Y. (2005). Comparison of finite difference and boundary integral solutions to three-dimensional spontaneous rupture. *J. Geophys. Res.*, 110(B12). B12307. Referenced in: 2.1, 2.3.1, 2.3.2, 2.4, 2.4.1, 2.4.2, 2.4.3, 2.6.2, 2.6.3, 2.6.4, 2.C, 2.C, 2.C.2, 3.1, 3.2.1, 3.A, and 4.2.4.

De Borst, R., Wang, W., and Sluys, L. (1996). Interaction between material length scale and imperfection size for localization phenomena in viscoplastic media. *Eur. J. Mech.*, 15(3):447–464. Referenced in: 2.2.2.

De la Puente, J., Ampuero, J.-P., and Käser, M. (2009). Dynamic rupture modeling on unstructured meshes using a discontinuous Galerkin method. *J. Geophys. Res.*, 114(B10). B10302. Referenced in: 1.2, 2.2.1, 2.4, 3.2.5, 4.2.4, 5.1, 5.2, 5.2.2, and 5.2.2.

Dean, S. M., McNeill, L. C., Henstock, T. J., Bull, J. M., Gulick, S. P. S., Austin, J. A., Bangs, N. L. B., Djajadihardja, Y. S., and Permana, H. (2010). Contrasting Décollement and Prism Properties over the Sumatra 2004–2005 Earthquake Rupture Boundary. *Science*, 329(5988):207–210. Referenced in: 4.1.

DeDontney, N., Rice, J. R., and Dmowska, R. (2012). Finite Element Modeling of Branched Ruptures Including Off-Fault Plasticity. *Bull. Seism. Soc. Am.*, 102(2):541–562. Referenced in: 2.1, 2.6.3, 3.1, and 5.1.

DeDontney, N., Templeton-Barrett, E. L., Rice, J. R., and Dmowska, R. (2011). Influence of plastic deformation on bimaterial fault rupture directivity. *J. Geophys. Res.*, 116(B10):B10312. Referenced in: 1.2.

Del Gaudio, P., Di Toro, G., Han, R., Hirose, T., Nielsen, S., Shimamoto, T., and Cavallo, A. (2009). Frictional melting of peridotite and seismic slip. *J. Geophys. Res.*, 114(B6). Referenced in: 5.1.

Den Hartog, S., Niemeijer, A., and Spiers, C. (2012). New constraints on megathrust slip stability under subduction zone P–T conditions. *Earth Planet. Sci. Lett.*, 353:240–252. Referenced in: 5.1.

Di Toro, G., Goldsby, D. L., and Tullis, T. E. (2004). Friction falls towards zero in quartz rock as slip velocity approaches seismic rates. *Nature*, 427(6973):436. Referenced in: 1.1.

Di Toro, G., Han, R., Hirose, T., De Paola, N., Nielsen, S., Mizoguchi, K., Ferri, F., Cocco, M., and Shimamoto, T. (2011). Fault lubrication during earthquakes. *Nature*, 471(7339):494. Referenced in: 5.3.1 and 5.1.

Di Toro, G., Nielsen, S., Passelegue, F., Spagnuolo, E., Bistacchi, A., Fondriest, M., Murphy, S., Aretusini, S., and Demurtas, M. (2016). What is the earthquake fracture energy? In *AGU Fall Meeting Abstracts*. Referenced in: 1.1.

Dias da Silva, V. (2004). A simple model for viscous regularization of elasto-plastic constitutive laws with softening. *Comm. Num. Meth. Eng.*, 20(7):547–568. Referenced in: 2.2.2.

Dibblee, T. W. J. (1967). Geologic Map of the Old Woman Springs Quadrangle San Bernardino County, California. Technical report, Department of the Interior United States Gelogical Survey. Referenced in: 2.5.1 and 3.2.4.

Dieterich, J. H. (1972). Time-dependent friction in rocks. *J. Geophys. Res.*, 77(20):3690–3697. Referenced in: 1.1.

Dieterich, J. H. (1978). Time-dependent friction and the mechanics of stick-slip. In *Rock Friction and Earthquake Prediction*, pages 790–806. Springer. Referenced in: 1.1 and 5.1.

Dieterich, J. H. (1979). Modeling of rock friction: 1. Experimental results and constituve equations. *J. Geophys. Res.*, 84(B5):2161–2168. Referenced in: 1.1 and 5.5.2.

Dimmen, V., Rotevatn, A., Peacock, D. C., Nixon, C. W., and Nrland, K. (2017). Quantifying structural controls on fluid flow: Insights from carbonate-hosted fault damage zones on the maltese islands. *J. Struct. Geol.*, 101:43 – 57. Referenced in: 1.1.

Dokka, R. K. and Travis, C. J. (1990). Late Cenozoic strike-slip faulting in the Mojave Desert, California. *Tectonics*, 9(2):311–340. Referenced in: 3.2.2.

Dreger, D. S. (1994). Investigation of the Rupture Process of the 28 June 1992 Landers Earthquake Utilizing Terrascope. *Bull. Seism. Soc. Am.*, 84(3):713–724. Referenced in: 3.1 and 3.3.3.

Duan, B. (2008). Asymmetric off-fault damage generated by bilateral ruptures along a bimaterial interface. *Geophys. Res. Lett.*, 35(L14). L14306. Referenced in: 1.2, 2.2.2, 2.2.2, and 2.2.3.

Duan, B. and Day, S. M. (2008). Inelastic strain distribution and seismic radiation from rupture of a fault kink. *J. Geophys. Res.*, 113(B12). B12311. Referenced in: 2.1, 2.2.1, 2.2.2, 2.4.2, and 2.6.4.

Duan, B. and Oglesby, D. D. (2006). Heterogeneous fault stresses from previous earthquakes and the effect on dynamics of parallel strike-slip faults. *J. Geophys. Res.*, 111(B5). B05309. Referenced in: 2.1.

Dumbser, M. and Käser, M. (2006). An arbitrary high-order discontinuous Galerkin method for elastic waves on unstructured meshes II. The three-dimensional isotropic case. *Geophys. J. Int.*, 167(1):319–336. Referenced in: 1.2, 2.1, 2.2.1, 2.2.1, 2.2.3, 2.6.3, 3.1, 3.2.5, 4.2.4, 5.2, 5.2.2, and 5.2.2.

Dumbser, M., Käser, M., Titarev, V. A., and Toro, E. F. (2007). Quadrature-free non-oscillatory finite volume schemes on unstructured meshes for nonlinear hyperbolic systems. *J. Comp. Phys.*, 226(1):204–243. Referenced in: 2.6.3.

Dunham, E. M., Belanger, D., Cong, L., and Kozdon, J. E. (2011a). Earthquake Ruptures with Strongly Rate-Weakening Friction and Off-Fault Plasticity, Part 1: Planar Faults. *Bull. Seism. Soc. Am.*, 101(5):2296–2307. Referenced in: 1.2, 2.1, 2.2.2, 2.2.2, 2.3, 2.3.1, and 2.6.1.

Dunham, E. M., Belanger, D., Cong, L., and Kozdon, J. E. (2011b). Earthquake Ruptures with Strongly Rate-Weakening Friction and Off-Fault Plasticity, Part 2: Nonplanar Faults. *Bull. Seism. Soc. Am.*, 101(5):2308–2322. Referenced in: 1.2, 2.1, 2.5.2, 2.6.3, 3.3.6, and 3.4.1.

Duru, K. and Dunham, E. M. (2016). Dynamic earthquake rupture simulations on nonplanar faults embedded in 3D geometrically complex, heterogeneous elastic solids. *J. Comp. Phys.*, 305:185–207. Referenced in: 2.1, 2.4.3, 2.6.3, and 3.1.

Duru, K. C., Gabriel, A.-A., and Igel, H. (2017). A new discontinuous Galerkin spectral element method for elastic waves with physically motivated numerical fluxes. *J. Comp. Phys.* arXiv preprint arXiv:1802.06380, submitted. Referenced in: 2.1.

Duvaut, G. and Lions, J. L. (1976). *Inequalities in Mechanics and Physics*, volume 219. Springer, Berlin. Referenced in: 2.2.2.

Ely, G. P., Day, S. M., and Minster, J.-B. (2008). A support-operator method for viscoelastic wave modelling in 3-D heterogeneous media. *Geophys. J. Int.*, 172(1):331–344. Referenced in: 3.4.3.

Emerson Paradigm Holding (2018). GoCad: A computer aided design program for geological applications. `http://www.pdgm.com/products/gocad/`. Referenced in: 3.2.5.

Erickson, B. A., Dunham, E. M., and Khosravifar, A. (2017). A finite difference method for off-fault plasticity throughout the earthquake cycle. *J. Mech. Phys. Solids*, 109:50–77. Referenced in: 2.1, 2.4.3, 2.6.3, 4.4.2, and 5.5.1.

Farr, T. G., Rosen, P. A., Caro, E., Crippen, R., Duren, R., Hensley, S., Kobrick, M., Paller, M., Rodriguez, E., Roth, L., Seal, D., Shaffer, S., Shimada, J., Umland, J., Werner, M., Oskin, M., Burbank, D., and Alsdorf, D. (2007). The Shuttle Radar Topography Mission. *Rev. Geophys.*, 45(2). Referenced in: 3.2.1 and 3.2.

Faulkner, D., Mitchell, T., Healy, D., and Heap, M. (2006). Slip on 'weak' faults by the rotation of regional stress in the fracture damage zone. *Nature*, 444(7121):922. Referenced in: 1.1.

Faulkner, D. R., Mitchell, T. M., Jensen, E., and Cembrano, J. (2011). Scaling of fault damage zones with displacement and the implications for fault growth processes. *J. Geophys. Res.*, 116(B5). Referenced in: 3.3.6.

Fialko, Y. (2004a). Evidence of fluid-filled upper crust from observations of postseismic deformation due to the 1992 Mw 7.3 Landers earthquake. *J. Geophys. Res.*, 109(8):1–17. Referenced in: 3.4.1.

Fialko, Y. (2004b). Probing the mechanical properties of seismically active crust with space geodesy: Study of the coseismic deformation due to the 1992 Mw 7.3 Landers (southern California) earthquake. *J. Geophys. Res.*, 109(B3):B03307. Referenced in: 2.5, 3.1, 3.3.2, and 3.3.4.

Fialko, Y. (2015). 4.03 - Fracture and Frictional Mechanics: Theory. In *Treatise on Geophysics (Second Edition)*, pages 73 – 91. Elsevier, Oxford. Referenced in: 1.1.

Fialko, Y., Sandwell, D., Simons, M., and Rosen, P. (2005). Three-dimensional deformation caused by the Bam, Iran, earthquake and the origin of shallow slip deficit. *Nature*, 435(7040):295–299. Referenced in: 2.1, 2.5, and 3.3.4.

Finzi, Y. and Langer, S. (2012a). Damage in step-overs may enable large cascading earthquakes. *Geophys. Res. Lett.*, 39(May):1–5. Referenced in: 3.4.1 and 4.3.1.

Finzi, Y. and Langer, S. (2012b). Predicting rupture arrests, rupture jumps and cascading earthquakes. *J. Geophys. Res.*, 117(12):1–11. Referenced in: 1.2 and 3.4.4.

Fleming, R., Messerich, J., and Cruikshank, K. (1998). Fractures along a portion of the Emerson fault zone related to the 1992 Landers, California, earthquake: Evidence for the rotation of the Galway-Lake-Road block. *Geol. Soc. Am., Map and Chart Series*. MCH082. Referenced in: 2.5.1, 3.2.1, 3.1, and 3.2.

Fliss, S., Bhat, H. S., Dmowska, R., and Rice, J. R. (2005). Fault branching and rupture directivity. *J. Geophys. Res.*, 110(B6):B06312. Referenced in: 2.5 and 3.1.

Freund, L. (1979). The mechanics of dynamics shear crack propagation. *J. Geophys. Res.*, 84(B5):2199–2209. Referenced in: 1.1.

Freymueller, J., King, N. E., and Segall, P. (1994). The co-seismic slip distribution of the Landers earthquake. *Bull. Seism. Soc. Am.*, 84(3):646–659. Referenced in: 3.1.

Gabriel, A., Ampuero, J., Dalguer, L. A., and Mai, P. M. (2012). The transition of dynamic rupture styles in elastic media under velocity-weakening friction. *J. Geophys. Res.*, 117(B9). Referenced in: 3.2.2.

Gabriel, A.-A., Ampuero, J.-P., Dalguer, L. A., and Mai, P. M. (2013). Source properties of dynamic rupture pulses with off-fault plasticity. *J. Geophys. Res.*, 118(8):4117–4126. Referenced in: 1.2, 2.1, 2.2.2, 2.2.2, 2.3.1, 3.2.2, 4.3.1, 4.3.1, and 5.3.2.

Gabriel, A.-A. and Pelties, C. (2014). Simulating Large-Scale Earthquake Dynamic Rupture Scenarios On Natural Fault Zones Using the ADER-DG Method. In *EGU General Assembly Conference Abstracts*, volume 16. 10572. Referenced in: 2.1, 2.2.1, and 2.5.1.

Galis, M., Pelties, C., Kristek, J., Moczo, P., Ampuero, J.-P., and Mai, P. M. (2014). On the initiation of sustained slip-weakening ruptures by localized stresses. *Geophys. J. Int.*, 200(2):890–909. Referenced in: 2.3, 2.4, and 3.4.2.

Galvez, P., Ampuero, J. P., Dalguer, L. A., Somala, S. N., and Nissen-Meyer, T. (2014). Dynamic earthquake rupture modelled with an unstructured 3-D spectral element method applied to the 2011 M9 Tohoku earthquake. *Geophys. J. Int.*, 198(2):1222–1240. Referenced in: 1.2, 2.1, 2.3.2, 2.5.1, and 5.1.

Galvez, P., Dalguer, L. A., Ampuero, J.-P., and Giardini, D. (2016). Rupture Reactivation during the 2011 Mw 9.0 Tohoku Earthquake: Dynamic Rupture and Ground-Motion Simulations. *Bull. Seism. Soc. Am.*, 106(3):819–831. Referenced in: 2.5.1 and 5.1.

Geist, E. L., Titov, V. V., Arcas, D., Pollitz, F. F., and Bilek, S. L. (2007). Implications of the 26 December 2004 Sumatra-Andaman Earthquake on Tsunami Forecast and Assessment Models for Great Subduction-Zone Earthquakes. *Bull. Seism. Soc. Am.*, 97(1A):S249. Referenced in: 4.1.

Gerya, T. V. and Yuen, D. A. (2003). Characteristics-based marker-in-cell method with conservative finite-differences schemes for modeling geological flows with strongly variable transport properties. *Phys. Earth Planet. Inter.*, 140(4):293–318. Referenced in: 5.2.1 and 5.2.1.

Gerya, T. V. and Yuen, D. A. (2007). Robust characteristics method for modelling multiphase visco-elasto-plastic thermo-mechanical problems. *Phys. Earth Planet. Inter.*, 163(1-4):83–105. Referenced in: 5.2, 5.2.1, and 5.2.1.

Geuzaine, C. and Remacle, J. F. (2009). Gmsh: A 3-D finite element mesh generator with built-in pre- and post-processing facilities. *Int. J. Num. Meth. Eng.*, 79(11):1309–1331. Referenced in: 2.4.1.

Godunov, S. K. (1959). A difference method for numerical calculation of discontinuous solutions of the equations of hydrodynamics. *Matematicheskii Sbornik*, 89(3):271–306. Referenced in: 2.6.3.

Goldsby, D. L. and Tullis, T. E. (2011). Flash Heating Leads to Low Frictional Earthquake Slip Rates. *Science*, 334(October):216–218. Referenced in: 1.1.

Gombert, B., Duputel, Z., Jolivet, R., Doubre, C., Rivera, L., and Simons, M. (2018). Revisiting the 1992 Landers earthquake: a Bayesian exploration of co-seismic slip and off-fault damage. *Geophys. J. Int.*, 212(2):839–852. Referenced in: 3.1, 3.3.2, 3.3.4, and 3.4.5.

Graizer, V. M. (2005). Effect of tilt on strong motion data processing. *Soil Dyn. Earth. Eng.*, 25(3):197–204. Referenced in: 3.3.5.

Graves, R. W., Aagaard, B. T., Hudnut, K. W., Star, L. M., Stewart, J. P., and Jordan, T. H. (2008). Broadband simulations for Mw 7.8 southern San Andreas earthquakes: Ground motion sensitivity to rupture speed. *Geophys. Res. Lett.*, 35(22). Referenced in: 3.2.4 and 3.4.3.

Graves, R. W. and Pitarka, A. (2010). Broadband Ground-Motion Simulation Using a Hybrid Approach. *Bull. Seism. Soc. Am.*, 100(5A):2095–2123. Referenced in: 2.5.1 and 2.10.

Gross, S. and Kisslinger, C. (1997). Estimating tectonic stress rate and state with Landers aftershocks. *J. Geophys. Res.*, 102(B4):7603. Referenced in: 3.2.3.

Hardebeck, J. L. (2012). Coseismic and postseismic stress rotations due to great subduction zone earthquakes. *Geophys. Res. Lett.*, 39(21):1–6. Referenced in: 4.2.2 and 4.4.2.

Hardebeck, J. L. (2015). Stress orientations in subduction zones and the strength of subduction megathrust faults. *Science*, 349(6253):1213–1216. Referenced in: 4.4.2 and 5.1.

Harris, R. and Day, S. M. (1993). Dynamic of fault interaction: parallel strike-slip faults. *J. Geophys. Res.*, 98(No. B3):4461–4472. Referenced in: 1.2, 3.1, and 3.4.4.

Harris, R. A., Barall, M., Aagaard, B., Ma, S., Roten, D., Olsen, K., Duan, B., Liu, D., Luo, B., Bai, K., Ampuero, J., Kaneko, Y., Gabriel, A., Duru, K., Ulrich, T., Wollherr, S., Shi, Z., Dunham, E., Bydlon, S., Zhang, Z., Chen, X., Somala, S. N., Pelties, C., Tago, J., CruzAtienza, V. M., Kozdon, J., Daub, E., Aslam, K., Kase, Y., Withers, K., and Dalguer, L. (2018). A Suite of Exercises for Verifying Dynamic Earthquake Rupture Codes. *Seismol. Res. Lett.*, 89(3):1146. Referenced in: 3.2.5.

Harris, R. A., Barall, M., Andrews, D. J., Duan, B., Ma, S., Dunham, E. M., Gabriel, A.-A., Kaneko, Y., Kase, Y., Aagaard, B. T., Oglesby, D. D., Ampuero, J.-P., Hanks, T. C., and Abrahamson, N. (2011). Verifying a Computational Method for Predicting Extreme Ground Motion. *Seismol. Res. Lett.*, 82(5):638–644. Referenced in: 2.1, 2.2.2, 2.3, 2.4, and 5.2.2.

Harris, R. A., Barall, M., Archuleta, R., Dunham, E., Aagaard, B. T., Ampuero, J.-P., Bhat, H., Cruz-Atienza, V., Dalguer, L., Dawson, P., Day, S., Duan, B., Ely, G., Kaneko, Y., Kase, Y., Lapusta, N., Liu, Y., Ma, S., Oglesby, D., Olsen, K., Pitarka, A., Song, S., and Templeton, E. (2009). The SCEC/USGS Dynamic Earthquake Rupture Code Verification Exercise. *Seismol. Res. Lett.*, 80(1):119–126. Referenced in: 2.1, 2.2.2, 2.3, and 2.3.2.

Harris, R. A. and Day, S. M. (1997). Effects of a low-velocity zone on a dynamic rupture. *Bull. Seism. Soc. Am.*, 87(5):1267–1280. Referenced in: 1.2.

Hauksson, E. (1994). State of stress from focal mechanisms before and after the 1992 Landers earthquake sequence. *Bull. Seism. Soc. Am.*, 84(3):917–934. Referenced in: 3.2.2 and 4.4.2.

Hauksson, E., Jones, L. M., Hutton, K., and Eberhart-Phillips, D. (1993). The 1992 Landers earthquake sequence: Seismological observations. *J. Geophys. Res.*, 98(B11):19835–19858. Referenced in: 2.5.1, 3.2.2, and 3.4.5.

Hayes, G. P., Wald, D. J., and Johnson, R. L. (2012). Slab1.0: A three-dimensional model of global subduction zone geometries. *J. Geophys. Res.*, 117(B1):B01302. Referenced in: 4.2.1.

Heinecke, A., Breuer, A., Bader, M., and Dubey, P. (2016). High Order Seismic Simulations on the Intel Xeon Phi Processor (Knights Landing). In *Proceedings of the International Conference on High Performance Computing*, pages 343–362, Cham. Springer. Referenced in: 2.1 and 2.2.1.

Heinecke, A., Breuer, A., Rettenberger, S., Bader, M., Gabriel, A.-A., Pelties, C., Bode, A., Barth, W., and Liao, X.-K. (2014). Petascale High Order Dynamic Rupture Earthquake Simulations on Heterogeneous Supercomputers. In *Proceedings of the International Conference for High Performance Computing, Networking, Storage and Analysis*, pages 3–15. IEEE. Referenced in: 2.1, 2.2.1, 2.4, 2.5.1, 2.5.1, 3.1, 3.2.2, 3.2.5, 4.1, and 4.2.4.

Hernandez, B., Cotton, F., and Campillo, M. (1999). Contribution of radar interferometry to a two-step inversion of the kinematic process of the 1992 Landers earthquake. *J. Geophys. Res.*, 104(B6):13083–13099. Referenced in: 2.6.5, 3.1, 3.2.3, 3.3.1, 3.4.3, and 3.4.5.

Hesthaven, J. S. and Warburton, T. (2010). *Nodal Discontinuous Galerkin Methods: Algorithms, Analysis, and Applications*. Springer, New York. Referenced in: 2.2.1, 2.2.3, and 2.6.3.

Heuret, A., Lallemand, S., Funiciello, F., Piromallo, C., and Faccenna, C. (2011). Physical characteristics of subduction interface type seismogenic zones revisited. *Geochem. Geophys. Geosyst.*, 12(1):1–26. Referenced in: 5.3.1.

Hill, R., Treiman, J., Given, J., Pechman, J., McMillan, J., and Ebel, J. (1980). Geologic study of the Homestead Valley earthquake swarm of March 15, 1979. *California Geology*, 33(3):60–67. Referenced in: 3.4.1.

Hirakawa, E. and Ma, S. (2016). Dynamic fault weakening and strengthening by gouge compaction and dilatancy in a fluid-saturated fault zone. *J. Geophys. Res.*, pages 5988–6008. Referenced in: 5.1.

Hirakawa, E. T. (2016). *Poro-Elasto-Plastic Off-Fault Response and Dynamics of Earthquake Faulting*. PhD thesis, University of California, San Diego. Referenced in: 5.1, 5.5.1, and 5.5.2.

Hu, F. Q., Hussaini, M. Y., and Rasetarinera, P. (1999). An analysis of the Discontinuous Galerkin method for wave propagation problems. *J. Comp. Phys.*, 151:921–946. Referenced in: 2.2.1.

Huang, Y. and Ampuero, J.-P. (2011). Pulse-like ruptures induced by low-velocity fault zones. *J. Geophys. Res.*, 116(B12). B12307. Referenced in: 1.2 and 2.4.

Huang, Y., Meng, L., and Ampuero, J.-P. (2013). A dynamic model of the frequency-dependent rupture process of the 2011 Tohoku-Oki earthquake. *Earth Planets Space.*, 64(12):1. Referenced in: 5.1.

Hughes, T. J. R. (2000). *The finite element method: linear static and dynamic finite element analysis*. Dover Publications, New York. Referenced in: 2.3.1.

Hyndman, R. D., Yamano, M., and Oleskevich, D. A. (1997). The seismogenic zone of subduction thrust faults. *Island Arc*, 6(3):244–260. Referenced in: 5.1.

Ida, Y. (1972). Cohesive Force across the Tip of a Longitudinal-Shear Crack and Griffith's Specific Surface Energy. *J. Geophys. Res.*, 77(20):3796–3805. Referenced in: 1.1, 2.2.1, 3.2.3, and 4.2.2.

Ida, Y. (1973). The maximum acceleration of seismic ground motion. *Bull. Seism. Soc. Am.*, 63(3):959–968. Referenced in: 2.6.3.

Imperatori, W. and Mai, P. M. (2015). The role of topography and lateral velocity heterogeneiteis on near-source scattering and ground-motion variability. *Geophys. J. Int.*, 202:2163–2181. Referenced in: 3.3.5.

Irwin, G. (1957). Relation of stresses near a crack to the crack extension force. *9th Cong. App. Mech., Brussels*. Referenced in: 1.1.

Kagan, Y. Y. and Houston, H. (2005). Relation between mainshock rupture process and Omori's law for aftershock moment release rate. *Geophys. J. Int.*, 163(September):1039–1048. Referenced in: 3.2.2, 3.3.3, and 3.5.

Kame, N., Rice, J. R., and Dmowska, R. (2003). Effects of prestress state and rupture velocity on dynamic fault branching. *J. Geophys. Res.*, 108(B):2265. Referenced in: 1.2 and 5.1.

Kanamori, H. and Cipar, J. J. (1974). Focal process of the great chilean earthquake may 22, 1960. *Physics of the Earth and Planetary Interiors*, 9(2):128–136. Referenced in: 5.1.

Kanamori, H. and Rivera, L. (2006). Energy Partitioning During an Earthquake. In *Earthquakes: Radiated Energy and the Physics of Faulting Geophysical Monograph Series 170*, pages 3–13. American Geophysical Union. Referenced in: 1.1 and 3.3.6.

Kanamori, H., Thio, H.-K., Dreger, D., Hauksson, E., and Heaton, T. (1992). Initial investigation of the Landers, California, earthquake of 28 June 1992 using TERRAscope. *Geophys. Res. Lett.*, 19(22):2267–2270. Referenced in: 3.1, 3.2.3, 3.3.3, and 3.3.4.

Kaneda, H. and Rockwell, T. K. (2009). Triggered and primary surface ruptures along the camp rock fault, eastern California shear zone. *Bull. Seism. Soc. Am.*, 99(5):2704–2720. Referenced in: 3.1, 3.3.2, 3.3.4, 3.4.5, and 3.5.

Kaneko, Y. and Fialko, Y. (2011). Shallow slip deficit due to large strike-slip earthquakes in dynamic rupture simulations with elasto-plastic off-fault response. *Geophys. J. Int.*, 186(3):1389–1403. Referenced in: 2.1, 2.5, 4.3.1, 4.4.2, and 5.5.1.

Kaneko, Y., Lapusta, N., and Ampuero, J.-P. (2008). Spectral element modeling of spontaneous earthquake rupture on rate and state faults: Effect of velocity-strengthening friction at shallow depths. *J. Geophys. Res.*, 113(B9):1–17. Referenced in: 1.2, 2.1, 2.2.3, 2.3.2, 2.4, 2.4.3, and 2.6.3.

Käser, M. and Dumbser, M. (2006). An Arbitrary High Order Discontinuous Galerkin Method for Elastic Waves on Unstructured Meshes I: The Two-Dimensional Isotropic Case with External Source Terms. *Geophys. J. Int.*, 166(2):855–877. Referenced in: 1.2, 2.2.1, 3.2.5, and 4.2.4.

Käser, M., Hermann, V., and de la Puente, J. (2008). Quantitative accuracy analysis of the discontinuous Galerkin method for seismic wave propagation. *Geophys. J. Int.*, 173(3):990–999. Referenced in: 2.2.1 and 3.2.5.

Kaven, J. O. and Pollard, D. D. (2013). Geometry of crustal faults: Identification from seismicity and implications for slip and stress transfer models. *J. Geophys. Res.*, 118(9):5058–5070. Referenced in: 3.1.

King, G. C. P. and Nabelek, J. L. (1985). Role of fault bends in the initiation and termination of earthquake rupture. *Science*, 228(4702):984–987. Referenced in: 2.1.

Konca, A. O., Hjorleifsdottir, V., Song, T.-R. A., Avouac, J.-P., Helmberger, D. V., Ji, C., Sieh, K., Briggs, R., and Meltzner, A. (2007). Rupture kinematics of the 2005 Mw 8.6 Nias–Simeulue earthquake from the joint inversion of seismic and geodetic data. *Bull. Seism. Soc. Am.*, 97(1A):S307–S322. Referenced in: 5.4.1.

Kostrov, B. (1964). Selfsimilar problems of propagation of shear cracks. *J. Appl. Math. Mech.*, 28(5):1077 – 1087. Referenced in: 2.4.

Kozdon, J. E. and Dunham, E. M. (2013). Rupture to the Trench: Dynamic rupture simulations of the 11 march 2011 Tohoku earthquake. *Bull. Seism. Soc. Am.*, 103(2):1275–1289. Referenced in: 1.2, 2.4, 2.4.3, 4.4.2, 5.1, and 5.2.3.

Kozdon, J. E., Dunham, E. M., and Nordström, J. (2012). Interaction of waves with frictional interfaces using summation-by-parts difference operators: Weak enforcement of nonlinear boundary conditions. *J. Sci. Comput.*, 50(2):341–367. Referenced in: 2.1, 2.2.3, 2.6.3, and 4.4.1.

Krivodonova, L. (2007). Limiters for high-order discontinuous Galerkin methods. *J. Comp. Phys.*, 226(1):879–896. Referenced in: 2.6.3.

Krüger, F. and Ohrnberger, M. (2005). Tracking the rupture of the Mw= 9.3 Sumatra earthquake over 1150 km at teleseismic distance. *Nature*, 435(7044):937. Referenced in: 4.1.

Lallemand, S., Heuret, A., and Boutelier, D. (2005). On the relationships between slab dip, back-arc stress, upper plate absolute motion, and crustal nature in subduction zones. *Geochem. Geophys. Geosyst.*, 6(9). Referenced in: 5.3.1.

Lapusta, N., Rice, J. R., Ben-Zion, Y., and Zheng, G. (2000). Elastodynamic analysis for slow tectonic loading with spontaneous rupture episodes on faults with rate- and state-dependent friction. *J. Geophys. Res.*, 105(B10):23765–23789. Referenced in: 2.1, 4.4.2, and 5.5.1.

Laske, G., Masters, G., Ma, Z., and Pasyanos, M. (2013). Update on CRUST1.0 - A 1-degree Global Model of Earth's Crust. In *EGU General Assembly Conference Abstracts*. European Geophysical Union. Referenced in: 4.2.1.

Lay, T., Bilek, S., Dixon, T., and Moore, C. (2007). Anomalous earthquake ruptures at shallow depths on subduction zone megathrusts. *The Seismogenic Zone of Subduction Thrust Faults*, pages 476–511. Referenced in: 5.1.

Lay, T., Kanamori, H., Ammon, C. J., Koper, K. D., Hutko, A. R., Ye, L., Yue, H., and Rushing, T. M. (2012). Depth-varying rupture properties of subduction zone megathrust faults. *J. Geophys. Res.*, 117(4):1–21. Referenced in: 5.1.

Lay, T., Kanamori, H., Ammon, C. J., Nettles, M., Ward, S. N., Aster, R. C., Beck, S. L., Bilek, S. L., Brudzinski, M. R., Butler, R., DeShon, H. R., Ekström, G., Satake, K., and Sipkin, S. (2005). The Great Sumatra-Andaman Earthquake of 26 December 2004. *Science*, 308(5725):1127–1133. Referenced in: 4.1 and 4.3.1.

LeVeque, R. J. (2002). *Finite volume methods for hyperbolic problems*, volume 31. Cambridge University Press. Referenced in: 2.2.1.

Li, Y.-G., Aki, K., Adams, D., Hasemi, A., and Lee, W. H. K. (1994a). Seismic guided waves trapped in the fault zone of the Landers, California, earthquake of 1992. *J. Geophys. Res.*, 99(94):11705–11722. Referenced in: 3.1.

Li, Y.-G., Aki, K., Vidale, J. E., Lee, W. H., and Marone, C. J. (1994b). Fine structure of the Landers fault zone: segmentation and the rupture process. *Science*, 265(5170):367–370. Referenced in: 3.1.

Lin, J. Y., Le Pichon, X., Rangin, C., Sibuet, J. C., and Maury, T. (2009). Spatial aftershock distribution of the 26 December 2004 great Sumatra-Andaman earthquake in the northern Sumatra area. *Geochem. Geophys. Geosyst.*, 10(5). Referenced in: 4.2.1.

Liu, J., Sieh, K., and Hauksson, E. (2003). A structural interpretation of the aftershock cloud of the 1992 M w 7.3 Landers earthquake. *Bull. Seism. Soc. Am.*, 93(3):1333–1344. Referenced in: 3.4.1 and 3.4.1.

Lotto, G. C., Dunham, E. M., Jeppson, T. N., and Tobin, H. J. (2017). The effect of compliant prisms on subduction zone earthquakes and tsunamis. *Earth Planet. Sci. Lett.*, 458(2017):213–222. Referenced in: 5.1.

Lotto, G. C., Jeppson, T. N., and Dunham, E. M. (2018). Fully-coupled simulations of megathrust earthquakes and tsunamis in the Japan Trench, Nankai Trough, and Cascadia Subduction Zone. *submitted to Pure. Appl. Geophys.* Referenced in: 4.4.1.

Lozos, J. C., Oglesby, D. D., Brune, J. N., and Olsen, K. B. (2015). Rupture and ground-motion models on the northern San Jacinto fault, incorporating realistic complexity. *Bull. Seism. Soc. Am.*, 105(4):1931–1946. Referenced in: 1.2.

Lozos, J. C., Oglesby, D. D., Duan, B., and Wesnousky, S. G. (2011). The effects of double fault bends on rupture propagation: A geometrical parameter study. *Bull. Seism. Soc. Am.*, 101(1):385–398. Referenced in: 1.2 and 3.1.

Lyakhovsky, V. and Ben-Zion, Y. (2014). Damage-breakage rheology model and solid-granular transition near brittle instability. *J. Mech. Phys. Solids*, 64:184–197. Referenced in: 2.1.

Lyakhovsky, V., Ben-Zion, Y., Ilchev, A., and Mendecki, A. (2016). Dynamic rupture in a damage-breakage rheology model. *Geophys. J. Int.*, 206(2):1126–1143. Referenced in: 2.6.1.

Ma, S. (2008). A physical model for widespread near-surface and fault zone damage induced by earthquakes. *Geochem. Geophys. Geosyst.*, 9(11):1–9. Referenced in: 1.2, 2.1, 2.2.2, 2.3, 3.2.4, and 4.2.3.

Ma, S. (2009). Distinct asymmetry in rupture-induced inelastic strain across dipping faults: An off-fault yielding model. *Geophys. Res. Lett.*, 36(L20). L20317. Referenced in: 2.3, 4.3.1, 4.4.1, 4.4.2, 5.1, and 5.4.4.

Ma, S. (2012). A self-consistent mechanism for slow dynamic deformation and large tsunami generation for earthquakes in the shallow subduction zone. *Geophys. Res. Lett.*, 39:1–7. Referenced in: 4.1, 4.2.3, 4.2.3, 4.3.1, 4.3.1, 4.3.2, 4.4.1, 4.5, 5.1, and 5.5.1.

Ma, S. and Andrews, D. J. (2010). Inelastic off-fault response and three-dimensional dynamics of earthquake rupture on a strike-slip fault. *J. Geophys. Res.*, 115(B4). B04304. Referenced in: 2.1, 2.2.2, 2.3, 2.4, 2.5.1, and 2.6.5.

Ma, S. and Hirakawa, E. T. (2013). Dynamic wedge failure reveals anomalous energy radiation of shallow subduction earthquakes. *Earth Planet. Sci. Lett.*, 375:113–122. Referenced in: 4.1, 4.2.3, 4.3.1, 4.3.2, 4.4.1, 5.1, 5.5.1, 5.5.2, and 5.6.

Madariaga, R. (2007). *Seismic Source Theory*, volume 4, chapter 4.02, pages 59–82. Elsevier, Amsterdam. Referenced in: 1.2.

Madariaga, R., Olsen, K., and Archuleta, R. (1998). Modeling dynamic rupture in a 3D earthquake fault model. *Bull. Seism. Soc. Am.*, 88(5):1182–1197. Referenced in: 1.2.

Madden, E. H., Maerten, F., and Pollard, D. D. (2013). Mechanics of nonplanar faults at extensional steps with application to the 1992 M 7.3 Landers, California, earthquake. *J. Geophys. Res.*, 118(1):3249–3263. Referenced in: 2.5, 2.5.1, 3.1, and 3.2.2.

Madden, E. H. and Pollard, D. D. (2012). Integration of surface slip and aftershocks to constrain the 3D structure of faults involved in the M 7.3 Landers earthquake, Southern California. *Bull. Seism. Soc. Am.*, 102(1):321–342. Referenced in: 2.5 and 3.1.

Madden, E. H., Ulrich, T., and Gabriel, A.-A. (2017). Characterizing a Complex Source: The Role of Splay Faults in Seafloor Deformation During the 2004 Sumatra-Andaman Earthquake. In *EGU General Assembly Conference Abstracts*, volume 19, page 16862. Referenced in: 2.2.1.

Mai, P. M., Burjanek, J., Delouis, B., Festa, G., Francois-Holden, C., Monelli, D., Uchide, T., and Zahradnik, J. (2007). Earthquake source inversion blindtest: Initial results and further developments. In *AGU Fall Meeting Abstracts*. Referenced in: 1.2.

Mai, P. M., Galis, M., Thingbaijam, K. K., Vyas, J. C., and Dunham, E. M. (2017). Accounting for fault roughness in pseudo-dynamic ground-motion simulations. *Pure Appl. Geophys.*, 174(9):3419–3450. Referenced in: 3.4.1.

Mai, P. M., Schorlemmer, D., Page, M., Ampuero, J.-P., Asano, K., Causse, M., Custodio, S., Fan, W., Festa, G., Galis, M., et al. (2016). The earthquake-source inversion validation (SIV) project. *Seismol. Res. Lett.*, 87(3):690–708. Referenced in: 1.2 and 3.3.2.

Marone, C. and Scholz, C. H. (1988). The depth of seismic faulting and the upper transition from stable to unstable slip regimes. *Geophys. Res. Lett.*, 15(6):621–624. Referenced in: 4.2.2.

Milliner, C. W. D., Dolan, J. F., Hollingsworth, J., Leprince, S., Ayoub, F., and Sammis, C. G. (2015). Quantifying near-field and off-fault deformation patterns of the 1992 M_w 7.3 Landers earthquake. *Geochem. Geophys. Geosyst.*, 16:1577–1598. Referenced in: 2.6.5, 3.1, 3.3.2, 3.3.4, 3.3.6, 3.12, 3.4.1, and 3.5.

Mitchell, T. M., Ben-Zion, Y., and Shimamoto, T. (2011). Pulverized fault rocks and damage asymmetry along the Arima-Takatsuki Tectonic Line, Japan. *Earth Planet. Sci. Lett.*, 308(3-4):284–297. Referenced in: 1.1.

Mitchell, T. M. and Faulkner, D. (2009). The nature and origin of off-fault damage surrounding strike-slip fault zones with a wide range of displacements: A field study from the Atacama fault system, northern Chile. *J. Struct. Geol.*, 31(8):802–816. Referenced in: 1.1 and 2.1.

Moore, G. F., Bangs, N. L., Taira, A., Kuramoto, S., Pangborn, E., and Tobin, H. J. (2007). Three-Dimensional Splay Fault Geometry and Implications for Tsunami Generation. *Science*, 318(5853):1128–1131. Referenced in: 4.2.1.

Nerger, A., Pelties, C., and Gabriel, A.-A. (2014). Simulation of earthquake rupture dynamics under rate-and-state friction and effects on the generated ground motions in a dipping fault system. Master's thesis, Ludwig-Maximilians-Universität, Munich. Referenced in: 2.6.3 and 5.2.2.

Nevitt, J. M. and Pollard, D. D. (2017). Impacts of off-fault plasticity on fault slip and interaction at the base of the seismogenic zone. *Geophys. Res. Lett.*, 44(4):1714–1723. Referenced in: 2.1 and 2.5.2.

Ni, S., Kanamori, H., and Helmberger, D. (2005). Seismology: Energy radiation from the Sumatra earthquake. *Nature*, 434(7033):582. Referenced in: 4.1 and 4.3.1.

Nielsen, S. (2017). From slow to fast faulting: recent challenges in earthquake fault mechanics. *Philos. Trans. A. Math. Phys. Eng. Sci.*, 375(2103). Referenced in: 1.1.

Nielsen, S. and Madariaga, R. (2003). On the Self-Healing Fracture Mode. *Bull. Seism. Soc. Am.*, 93(6):2375. Referenced in: 2.4.

Nielsen, S., Spagnuolo, E., Violay, M., Smith, S., Di Toro, G., and Bistacchi, A. (2016). G: Fracture energy, friction and dissipation in earthquakes. *J. Seism.*, 20(4):1187–1205. Referenced in: 1.1.

Noda, H., Dunham, E. M., and Rice, J. R. (2009). Earthquake ruptures with thermal weakening and the operation of major faults at low overall stress levels. *J. Geophys. Res.*, 114(10):1–27. Referenced in: 1.1, 2.6.5, and 5.5.2.

Noda, H. and Lapusta, N. (2013). Stable creeping fault segments can become destructive as a result of dynamic weakening. *Nature*, 493(7433):518–521. Referenced in: 4.4.2 and 6.

Nur, A., Ron, H., and Scotti, O. (1989). Kinematics and mechanics of tectonic block rotations. *Slow Deformation and Transmission of Stress in the Earth, AGU Geophysical Monographs*, pages 31–46. Referenced in: 3.2.2.

Oglesby, D. (2008). Rupture Termination and Jump on Parallel Offset Faults. *Bull. Seism. Soc. Am.*, 98(1):440–447. Referenced in: 1.2, 3.1, 3.3.1, and 3.4.4.

Oglesby, D. D., Archuleta, R. J., and Nielsen, S. B. (2000). The three-dimensional dynamics of dipping faults. *Bull. Seism. Soc. Am.*, 90(3):616–628. Referenced in: 2.3.

Oglesby, D. D. and Day, S. M. (2002). Stochastic fault stress: Implications for fault dynamics and ground motion. *Bull. Seism. Soc. Am.*, 92(8):3006–3021. Referenced in: 2.3.

Oglesby, D. D. and Mai, P. M. (2012). Fault geometry, rupture dynamics and ground motion from potential earthquakes on the North Anatolian Fault under the Sea of Marmara. *Geophys. J. Int.*, 188(3):1071–1087. Referenced in: 3.1.

Okada, Y. (1985). Surface deformation due to shear and tensile faults in a half-space. *Bull. Seism. Soc. Am.*, 75(4):1135–1154. Referenced in: 4.1.

Okada, Y. (1992). Internal deformation due to shear and tensile faults in a half-space. *Bull. Seism. Soc. Am.*, 82(2):1018–1040. Referenced in: 4.1.

Okubo, K., Bhat, H. S., Klinger, Y., and Rougier, E. (2017). Modelling earthquake ruptures with dynamic off-fault damage. In *EGU General Assembly Conference Abstracts*, volume 19, page 4992. Referenced in: 2.6.1.

Okubo, P. G. and Aki, K. (1987). Fractal geometry in the san andreas fault system. *J. Geophys. Res.*, 92(B1):345–355. Referenced in: 1.1.

Okubo, P. G. and Dieterich, J. H. (1981). Fracture energy of stick-slip events in a large biaxial experiment. *Geophys. Res. Lett.*, 8(8):887–890. Referenced in: 1.1 and 4.2.2.

Olsen, K. B. (1997). Three-Dimensional Dynamic Simulation of the 1992 Landers Earthquake. *Science*, 278(5339):834–838. Referenced in: 3.1, 3.2.3, and 3.3.1.

Olsen, K. B., Day, S. M., Dalguer, L. A., Mayhew, J., Cui, Y., Zhu, J., Cruz-Atienza, V. M., Roten, D., Maechling, P., Jordan, T. H., Okaya, D., and Chourasia, A. (2009). ShakeOut-D: Ground motion estimates using an ensemble of large earthquakes on the southern San Andreas fault with spontaneous rupture propagation. *Geophys. Res. Lett.*, 36(4). Referenced in: 1.2.

O'Reilly, O., Nordström, J., Kozdon, J. E., and Dunham, E. M. (2015). Simulation of Earthquake Rupture Dynamics in Complex Geometries Using Coupled Finite Difference and Finite Volume Methods. *Commun. Compt. Phys.*, 17(2):337–370. Referenced in: 2.4.3.

Ortiz, M. and Simo, J. (1986). An analysis of a new class of integration algorithms for elastoplastic constitutive relations. *Int. J. Num. Meth. Eng.*, 23(3):353–366. Referenced in: 2.1.

Pelties, C., de la Puente, J., Ampuero, J.-P., Brietzke, G. B., and Käser, M. (2012). Three-dimensional dynamic rupture simulation with a high-order discontinuous Galerkin method on unstructured tetrahedral meshes. *J. Geophys. Res.*, 117(B2):B02309. Referenced in: 1.2, 2.1, 2.2.1, 2.4, 2.4.1, 2.4.2, 2.4.3, 2.5.1, 2.6.2, 2.6.3, 3.1, 3.2.5, and 4.2.4.

Pelties, C., Gabriel, A.-A., and Ampuero, J.-P. (2014). Verification of an ADER-DG method for complex dynamic rupture problems. *Geosci. Model Dev.*, 7(3):847–866. Referenced in: 1.2, 2.2.1, 2.3, 2.4, 3.1, 3.2.5, and 4.2.4.

Peter, D., Komatitsch, D., Luo, Y., Martin, R., Le Goff, N., Casarotti, E., Le Loher, P., Magnoni, F., Liu, Q., Blitz, C., Nissen-Meyer, T., Basini, P., and Tromp, J. (2011). Forward and adjoint simulations of seismic wave propagation on fully unstructured hexahedral meshes. *Geophys. J. Int.*, 186(2):721–739. Referenced in: 2.3.2.

Petricca, P. and Carminati, E. (2016). Present-day stress field in subduction zones: Insights from 3D viscoelastic models and data. *Tectonophysics.*, 667:48 – 62. Referenced in: 4.4.2.

Peyrat, S., Olsen, K. B., and Madariaga, R. (2001). Dynamic modeling of the 1992 Landers earthquake. *J. Geophys. Res.*, 106(B11):26467–26482. Referenced in: 1.2, 2.5, 2.5.1, 3.1, 3.2.3, and 3.3.1.

Plafker, G., Nishenko, S., Cluff, L., and Syharial, D. (2006). The cataclysmic 2004 tsunami on NW Sumatra: Preliminary evidence for a splay fault secondary source along the western Aceh basin. *Seismol. Res. Lett.*, 77:231. Referenced in: 4.1.

Platt, J. D., Viesca, R. C., and Garagash, D. I. (2015). Steadily propagating slip pulses driven by thermal decomposition. *J. Geophys. Res.*, 120(9):6558–6591. Referenced in: 2.6.5.

Poisson, B., Oliveros, C., and Pedreros, R. (2011). Is there a best source model of the Sumatra 2004 earthquake for simulating the consecutive tsunami? *Geophys. J. Int.*, 185(3):1365–1378. Referenced in: 4.1.

Pollard, D. D., Saltzer, S. D., and Rubin, A. M. (1993). Stress inversion methods: are they based on faulty assumptions? *J. Struct. Geol.*, 15(8):1045–1054. Referenced in: 4.4.2.

Power, W. L., Tullis, T. E., Brown, S. R., Boitnott, G. N., and Scholz, C. H. (1987). Roughness of natural fault surfaces. *Geophys. Res. Lett.*, 14(1):29–32. Referenced in: 1.1.

Pranger, C., May, D. A., Le Pourhiet, L., van Dinther, Y., Herrendörfer, R., Gokhberg, A., and Gerya, T. (2018). Physical and numerical ingredients of a 3D continuum seismic cycle code. In *2nd ASCETE workshop, Sudelfeld, Germany*. Referenced in: 6.

Quentin, B., Anthony, S., Junle, J., and Mark, S. (2016). A Bayesian source model for the 2004 great SumatraAndaman earthquake. *J. Geophys. Res.*, 121(7):5116–5135. Referenced in: 4.1 and 4.2.1.

Ramirez-Guzman, L., Graves, R. W., Olsen, K. B., Boyd, O. S., Cramer, C., Hartzell, S., Ni, S., Somerville, P., Williams, R. A., and Zhong, J. (2015). Ground-motion simulations of 1811–1812 New Madrid earthquakes, central United States. *Bull. Seism. Soc. Am.*, 105(4):1961–1988. Referenced in: 3.4.3.

Ranalli, G. (1995). *Rheology of the Earth*. Springer Science & Business Media. Referenced in: 5.1.

Reid, H. F. (1910). *The Mechanics of the Earthquake, The California Earthquake of April 18, 1906; Report of the State Investigation Commission*, volume 2. Carnegie Institution of Washington, Washington, D.C. Referenced in: 1.

Restrepo-Velez, L. F. and Bommer, J. J. (2003). An exploration of the nature of the scatter in ground-motion prediction equations and the implications for seismic hazard assessment. *J. Earth. Eng.*, 7:171–199. Referenced in: 3.4.3.

Rettenberger, S. and Bader, M. (2015). Optimizing Large Scale I/O for Petascale Seismic Simulations on Unstructured Meshes. In *Proceedings of the International Conference on Cluster Computing*, pages 314–317, Chicago, IL. IEEE. Referenced in: 2.2.1, 3.2.5, and 4.2.4.

Rettenberger, S., Meister, O., Bader, M., and Gabriel, A.-A. (2016). ASAGI: A Parallel Server for Adaptive Geoinformation. In *Proceedings of the Exascale Applications and Software Conference 2016*, EASC '16, pages 2:1–2:9, New York. ACM. Referenced in: 2.2.1, 2.5.1, 3.2.4, 3.2.5, 4.1, and 4.2.4.

Rettenberger, S., Smith, C., and Pelties, C. (2014). Optimizing CAD and Mesh Generation Workflow for SeisSol. In *Proceedings of the International Conference for High Performance Computing, Networking, Storage and Analysis*, New Orleans. IEEE. Referenced in: 4.2.4.

Rice, J. (1980). The mechanics of earthquake rupture. In *Physics of the Earth's Interior, edited by AM Dziewonski and E. Boschi*. Referenced in: 1.1.

Rice, J. R. (1993). Spatio-temporal complexity of slip on a fault. *J. Geophys. Res.*, 98(B6):9885–9907. Referenced in: 2.1.

Rice, J. R. (2006). Heating and weakening of faults during earthquake slip. *J. Geophys. Res.*, 111(B5). Referenced in: 1.1.

Rice, J. R., Sammis, C. G., and Parsons, R. (2005). Off-fault secondary failure induced by a dynamic slip pulse. *Bull. Seism. Soc. Am.*, 95(1):109–134. Referenced in: 3.3.6.

Ripperger, J., Ampuero, J. P., Mai, P. M., and Giardini, D. (2007). Earthquake source characteristics from dynamic rupture with constrained stochastic fault stress. *J. Geophys. Res.*, 112(4):1–17. Referenced in: 2.3.

Ripperger, J. and Mai, P. M. (2004). Fast computation of static stress changes on 2D faults from final slip distributions. *Geophys. Res. Lett.*, 31(18). Referenced in: 3.3.4.

Roache, P. J. (2002). Code verification by the method of manufactured solutions. *J. Fluids Eng.*, 124(1):4–10. Referenced in: 2.6.3.

Rockwell, T. K., Lindvall, S., Herzberg, M., Murbach, D., Dawson, T., and Berger, G. (2000). Paleoseismology of the Johnson Valley, Kickapoo, and Homestead Valley faults: Clustering of earthquakes in the eastern California shear zone. *Bull. Seism. Soc. Am.*, 90(5):1200–1236. Referenced in: 3.3.1.

Rojas, O., Day, S., Castillo, J., and Dalguer, L. A. (2008). Modelling of rupture propagation using high-order mimetic finite differences. *Geophys. J. Int.*, 172(2):631–650. Referenced in: 2.2.1, 2.4, 2.4.3, and 2.6.3.

Rojas, O., Dunham, E. M., Day, S. M., Dalguer, L. A., and Castillo, J. E. (2009). Finite difference modelling of rupture propagation with strong velocity-weakening friction. *Geophys. J. Int.*, 179(3):1831–1858. Referenced in: 2.4, 2.4.3, and 2.6.3.

Roten, D., Cui, Y., Olsen, K. B., Day, S. M., Withers, K., Savran, W. H., Wang, P., and Mu, D. (2016). High-frequency nonlinear earthquake simulations on petascale heterogeneous supercomputers. In *Proceedings of the International Conference for High Performance Computing, Networking, Storage and Analysis*, pages 82:1–82:12. IEEE. Referenced in: 1.2, 2.1, 2.2.3, 2.4, 3.3.4, and 4.2.3.

Roten, D., Olsen, K. B., Cui, Y., and Day, S. M. (2015). Quantification of fault zone plasticity effects with spontaneous rupture simulations. In *Best Practices in Physics-based Fault Rupture Models for Seismic Hazard Assessment of Nuclear Installations*, Vienna, Austria. Referenced in: 2.1, 2.3.1, 2.4, 2.10, 2.5.1, 2.5.2, 2.6.5, 2.7, 3.1, 3.4.2, 3.4.3, and 4.1.

Roten, D., Olsen, K. B., and Day, S. M. (2017). Off-fault Deformations and Shallow Slip Deficit from Dynamic Rupture Simulations with Fault Zone Plasticity. *Geophys. Res. Lett.*, pages 7733–7742. Referenced in: 1.2, 2.1, 2.4, 2.5, 3.1, 3.2.3, 3.2.4, 3.3.4, 4.1, and 5.5.1.

Roten, D., Olsen, K. B., Day, S. M., Cui, Y., and Fäh, D. (2014). Expected seismic shaking in Los Angeles reduced by San Andreas fault zone plasticity. *Geophys. Res. Lett.*, 41(8):2769–2777. Referenced in: 1.2, 2.1, 2.3.1, 2.5.1, 2.6.5, 3.1, 3.4.3, 3.4.3, and 4.1.

Ruina, A. (1983). Slip instability and state variable friction laws. *J. Geophys. Res.*, 88(B12):10359–10370. Referenced in: 1.1 and 5.5.2.

Sauber, J., Thatcher, W., and Solomon, S. C. (1986). Geodetic measurement of deformation in the central Mojave Desert, California. *J. Geophys. Res.*, 91(B12):12683–12693. Referenced in: 3.2.2.

Savage, H. M. and Brodsky, E. E. (2011). Collateral damage: Evolution with displacement of fracture distribution and secondary fault strands in fault damage zones. *J. Geophys. Res.*, 116(B3). Referenced in: 1.1.

Schmitt, S. V., Segall, P., and Dunham, E. M. (2015). Nucleation and dynamic rupture on weakly stressed faults sustained by thermal pressurization. *J. Geophys. Res.*, 120(11):7606–7640. Referenced in: 6.

Scholz, C. H. (1989). Mechanics of faulting. *Ann. Rev. Earth Planet Sci.*, 17(1):309–334. Referenced in: 1.1.

Scholz, C. H. (1998). Earthquakes and friction laws. *Nature*, 391:37–42. Referenced in: 1.1.

Scholz, C. H., Dawers, N. H., Yu, J.-Z., Anders, M. H., and Cowie, P. A. (1993). Fault growth and fault scaling laws: Preliminary results. *J. Geophys. Res.*, 98(B12):21951–21961. Referenced in: 1.1.

Schultz, R. (1995). Limits on strength and deformation properties of jointed basaltic rock masses. *Rock. Mech. Rock. Eng.*, 28(1):1–15. Referenced in: 5.1.

Shaw, J. H., Plesch, A., Tape, C., Suess, M. P., Jordan, T. H., Ely, G., Hauksson, E., Tromp, J., Tanimoto, T., Graves, R., Olsen, K., Nicholson, C., Maechling, P. J., Rivero, C., Lovely, P., Brankman, C. M., and Munster, J. (2015). Unified Structural Representation of the southern California crust and upper mantle. *Earth Planet. Sci. Lett.*, 415:1–15. Referenced in: 3.2 and 3.2.4.

Shearer, P. and Bürgmann, R. (2010). Lessons Learned from the 2004 Sumatra-Andaman Megathrust Rupture. *Ann. Rev. Earth Planet Sci.*, 38:103–131. Referenced in: 4.1 and 5.1.

Shi, Z. and Day, S. M. (2013). Rupture dynamics and ground motion from 3D roughfault simulations. *J. Geophys. Res.*, 118(3):1122–1141. Referenced in: 3.3.6 and 3.4.1.

Sibson, R. H. (2003). Thickness of the seismic slip zone. *Bull. Seism. Soc. Am.*, 93(3):1169–1178. Referenced in: 1.1.

Sibuet, J.-C., Rangin, C., Le Pichon, X., Singh, S., Cattaneo, A., Graindorge, D., Klingelhoefer, F., Lin, J.-Y., Malod, J., Maury, T., et al. (2007). 26th December 2004 great SumatraAndaman earthquake: Co-seismic and post-seismic motions in northern Sumatra. *Earth Planet. Sci. Lett.*, 263(1-2):88–103. Referenced in: 4.1 and 4.2.1.

Sieh, K. (1996). The repetition of large-earthquake ruptures. *Proceedings of the National Academy of Sciences: "Earthquake Prediction: The Scientific Challenge"*, 93(9):3764–3771. Referenced in: 3.1, 3.2.3, 3.3.1, 3.3.2, 3.3.4, 3.4.5, and 3.5.

Sieh, K. (2006). Sumatran megathrust earthquakes: from science to saving lives. *Philos. Trans. A. Math. Phys. Eng. Sci.*, 364(1845):1947–1963. Referenced in: 4.1.

Sieh, K., Jones, L., Hauksson, E., Hudnut, K., Eberhart-Phillips, D., Heaton, T., Hough, S., Hutton, K., Kanamori, H., Lilje, A., et al. (1993). Near-field investigations of the Landers earthquake sequence, April to July 1992. *Science*, 260(5105):171–176. Referenced in: 3.1, 3.2.3, 3.3.2, 3.3.3, 3.3.4, 3.3.6, and 3.4.5.

Simmetrix Inc. (2017). SimModeler: Simulation Modeling Suite 11.0 Documentation. Technical report, `www.simmetrix.org`. Referenced in: 2.3.1, 2.3.2, 2.5.1, 3.2.5, and 4.2.1.

Simo, J. C. and Hughes, T. J. (2000). *Computational inelasticity*, volume 2. New York, Springer. Referenced in: 2.6.3.

Simo, J. C., Kennedy, J. G., and Govindjee, S. (1988). Non-smooth multisurface plasticity and viscoplasticity. Loading/unloading conditions and numerical algorithms. *Int. J. Numer. Meth. Eng.*, 26(10):2161–2185. Referenced in: 2.2.2.

Simons, M., Minson, S. E., Sladen, A., Ortega, F., Jiang, J., Owen, S. E., Meng, L., Ampuero, J.-P., Wei, S., Chu, R., et al. (2011). The 2011 magnitude 9.0 Tohoku-Oki earthquake: Mosaicking the megathrust from seconds to centuries. *Science*, 332(6036):1421–1425. Referenced in: 5.1.

Singh, S. C., Carton, H., Tapponnier, P., Hananto, N. D., Chauhan, A. P. S., Hartoyo, D., Bayly, M., Moeljopranoto, S., Bunting, T., Christie, P., Lubis, H., and Martin, J. (2008). Seismic evidence for broken oceanic crust in the 2004 Sumatra earthquake epicentral region. *Nature Geoscience*, 1(11):777–781. Referenced in: 4.2.1.

Sleep, N. H. (2012). Site Resonance from Strong Ground Motions at Lucerne, California, during the 1992 Landers Mainshock. *Bull. Seism. Soc. Am.*, 102(4):1505. Referenced in: 3.1.

Sowers, J. M., Unruh, J. R., Lettis, W. R., and Rubin, T. D. (1994). Relationship of the Kickapoo Fault to the Johnson Valley and Homestead Valley Faults, San Bernardino County, California. *Bull. Seism. Soc. Am.*, 84(3):528–536. Referenced in: 3.1 and 3.4.1.

Spotila, J. A. and Sieh, K. (1995). Geological investigation of a slip gap in the surficial ruptures of the 1992 Landers earthquake, southern California. *J. Geophys. Res.*, 100(94):543–559. Referenced in: 3.1 and 3.3.3.

Spudich, P. and Chiou, B. S. (2008). Directivity in NGA earthquake ground motions: Analysis using isochrone theory. *Earthquake Spectra*, 24(1):279–298. Referenced in: 3.4.3.

Stein, S. and Okal, E. A. (2005). Speed and size of the Sumatra earthquake. *Nature*, 434(7033):581. Referenced in: 4.1 and 4.3.1.

Strasser, F. O., Abrahamson, N. A., and Bommer, J. J. (2009). Sigma: Issues, insights, and challenges. *Seismol. Res. Lett.*, 80(1):40–56. Referenced in: 3.4.3.

Stroud, A. H. (1971). *Approximate calculation of multiple integrals*. Prentice-Hall series in automatic computation. Prentice-Hall, Englewood Cliffs, NJ. Referenced in: 2.2.1 and 2.2.3.

Suppe, J. (1985). *Principles of structural geology*. Prentice Hall. Referenced in: 3.2.2.

Suppe, J. (2007). Absolute fault and crustal strength from wedge tapers. *Geology*, 35(12):1127–1130. Referenced in: 4.2.2 and 5.1.

Suppe, J. (2014). Fluid overpressures and strength of the sedimentary upper crust. *J. Struct. Geol.*, 69:481–492. Referenced in: 4.2.2 and 5.1.

Tago, J., Cruz-Atienza, V. M., Virieux, J., Etienne, V., and Sánchez-Sesma, F. J. (2012). A 3D hp-adaptive discontinuous Galerkin method for modeling earthquake dynamics. *J. Geophys. Res.*, 117(3):1–21. Referenced in: 1.2, 2.1, 2.2.1, 2.2.3, 2.4, 2.4.2, 2.5, 2.5.1, and 3.1.

Tavelli, M. and Dumbser, M. (2018). Arbitrary high order accurate space-time discontinuous Galerkin finite element schemes on staggered unstructured meshes for linear elasticity. *J. Comp. Phys.* arXiv preprint arXiv:1802.04516, submitted. Referenced in: 2.1.

Templeton, E. L., Baudet, A., Bhat, H. S., Dmowska, R., Rice, J. R., Rosakis, A. J., and Rousseau, C. E. (2009). Finite element simulations of dynamic shear rupture experiments and dynamic path selection along kinked and branched faults. *J. Geophys. Res.*, 114(8):1–17. Referenced in: 2.1.

Templeton, E. L. and Rice, J. R. (2008). Off-fault plasticity and earthquake rupture dynamics: 1. Dry materials or neglect of fluid pressure changes. *J. Geophys. Res.*, 113(B9):B09306. Referenced in: 2.1, 2.2.2, 2.3, 4.2.3, 4.3.1, 4.4.1, 5.1, and 5.3.2.

Thomas, M. Y., Bhat, H. S., and Klinger, Y. (2017). Effect of Brittle Off-Fault Damage on Earthquake Rupture Dynamics. In *Fault Zone Dynamic Processes*, pages 255–280. John Wiley and Sons, Inc., Hoboken, NJ, USA. Referenced in: 2.6.1.

Titarev, V. A. and Toro, E. F. (2002). ADER: Arbitrary High Order Godunov Approach. *J. Sci. Comput.*, 17(1-4):609–618. Referenced in: 2.2.1.

Toro, E. F. (1999). *Riemann Solvers and Numerical Methods for Fluid Dynamics, A Practical Introduction*. Springer, 2 edition. Referenced in: 2.2.1.

Tsai, V. C., Nettles, M., Ekström, G., and Dziewonski, A. M. (2005). Multiple CMT source analysis of the 2004 Sumatra earthquake. *Geophys. Res. Lett.*, 32(17). Referenced in: 4.2.2.

Tsutsumi, A. and Shimamoto, T. (1997). High-velocity frictional properties of gabbro. *Geophys. Res. Lett.*, 24(6):699–702. Referenced in: 1.1 and 5.1.

Turcotte, D. and Schubert, G. (2002). *Geodynamics*. Cambridge University Press. Referenced in: 5.1.

Ulrich, T. and Gabriel, A.-A. (2017). 3D fault curvature and fractal roughness: Insights for rupture dynamics and ground motions using a Discontinous Galerkin method. In *EGU General Assembly Conference Abstracts*, volume 19, page 18689. Referenced in: 1.2, 2.2.1, and 2.5.2.

Ulrich, T., Gabriel, A.-A., Ampuero, J.-P., and Xu, W. (2018). Dynamic viability of the 2016 Mw 7.8 Kaikura earthquake cascade on weak crustal faults. *submitted to Nature Communications*. Referenced in: 3.2.2 and 4.2.2.

Unruh, J. R., Lettis, W. R., and Sowers, J. M. (1994). Kinematic Interpretation of the 1992 Landers Earthquake. *Bull. Seism. Soc. Am.*, 84(3):537–546. Referenced in: 3.2.2.

Uphoff, C. and Bader, M. (2016). Generating high performance matrix kernels for earthquake simulations with viscoelastic attenuation. In *Proceedings of the 2016 International Conference on High Performance Computing and Simulation*, pages 908–916. IEEE. Referenced in: 1.2, 2.1, 2.2.3, 2.7, 3.2.4, 3.2.5, and 4.3.2.

Uphoff, C., Rettenberger, S., Bader, M., Madden, E. H., Ulrich, T., Wollherr, S., and Gabriel, A.-A. (2017). Extreme scale multi-physics simulations of the tsunamigenic 2004 sumatra megathrust earthquake. In *Proceedings of the International Conference for High Performance Computing, Networking, Storage and Analysis*, page 21. ACM. Referenced in: 1.2, 1.3, 3.1, 3.2.5, 4, 4.1, 4.2, 4.1, 4.2, 4.2.4, 4.4.1, and 6.

Urata, Y., Hok, Ś., Fukuyama, E., and Madariaga, R. (2013). The effect of thermal pressurization on dynamic fault branching. *Geophys. J. Int.*, 196(2):1237–1246. Referenced in: 6.

Vallée, M. and Douet, V. (2016). A new database of source time functions (STFs) extracted from the SCARDEC method. *Phys. Earth Planet. Inter.*, 257:149–157. Referenced in: 3.3.3, 3.5, and 3.4.1.

Van Dinther, Y., Gerya, T. V., Dalguer, L. A., Corbi, F., Funiciello, F., and Mai, P. M. (2013a). The seismic cycle at subduction thrusts: 2. Dynamic implications of geodynamic simulations validated with laboratory models. *J. Geophys. Res.*, 118(4):1502–1525. Referenced in: 4.4.2, 5.1, 5.2, 5.2.1, 5.2.1, and 5.2.1.

Van Dinther, Y., Gerya, T. V., Dalguer, L. a., Mai, P. M., Morra, G., and Giardini, D. (2013b). The seismic cycle at subduction thrusts: Insights from seismo-thermo- mechanical models. *J. Geophys. Res.*, 118(November):6183–6202. Referenced in: 4.4.2 and 5.2.1.

van Zelst, I., van Dinther, Y., Gabriel, A.-A., Wollherr, S., and Madden, E. H. (2017). Coupling a geodynamic seismic cycle to a dynamic rupture model with an application to splay fault propagation. In *EGU General Assembly Conference Abstracts*, volume 19, page 14004. Referenced in: 2.2.1.

van Zelst, I., Wollherr, S., Gabriel, A.-A., Madden, E. H., and van Dinther, Y. (2018). A coupled method for realistic initial conditions of megathrust earthquakes. *in preparation for Geophy. J. Int.* Referenced in: 5.1, 5.2.3, 5.3.1, 5.1, 5.1, 5.3.2, 5.3.2, 5.3.2, 5.4.4, 5.5.2, and 6.

Vermeer, P. A. and de Borst, R. (1984). Non-Associated Plasticity for Soils, Concrete and Rock. *Heron*, 29(3):1–64. Referenced in: 2.2.2.

Viesca, R. C. and Garagash, D. I. (2015). Ubiquitous weakening of faults due to thermal pressurization. *Nature Geoscience*, 8(October):875–879. Referenced in: 1.1.

Vrolijk, P. (1990). On the mechanical role of smectite in subduction zones. *Geology*, 18(8):703. Referenced in: 4.2.2.

Vyas, J. C., Mai, P. M., and Galis, M. (2016). Distance and azimuthal dependence of ground-motion variability for unilateral strike-slip ruptures. *Bull. Seism. Soc. Am.*, 106(4):1584–1599. Referenced in: 3.3.5 and 3.4.3.

Wald, D. J. and Heaton, T. H. (1994). Spatial and Temporal Distribution of Slip for the 1992 Landers, California, Earthquake. *Bull. Seism. Soc. Am.*, 84(3):668–691. Referenced in: 1.2, 2.5, 2.6.5, 3.1, 3.2.3, 3.3.1, 3.3.2, 3.3.3, 3.4.3, and 3.4.5.

Waldhauser, F., Schaff, D. P., Diehl, T., and Engdahl, E. R. (2012). Splay faults imaged by fluid-driven aftershocks of the 2004 Mw 9.2 Sumatra-Andaman earthquake. *Geology*, 40(3):243–246. Referenced in: 4.1 and 4.2.1.

Wang, K. and He, J. (2008). Effects of frictional behavior and geometry of subduction fault on coseismic seafloor deformation. *Bull. Seism. Soc. Am.*, 98(2):571–579. Referenced in: 5.1.

Wang, K. and Hu, Y. (2006). Accretionary prisms in subduction earthquake cycles: The theory of dynamic Coulomb wedge. *J. Geophys. Res.*, 111(6):1–16. Referenced in: 4.2.3 and 4.2.3.

Warburton, T. (2006). An explicit construction of interpolation nodes on the simplex. *J. Eng. Math.*, 56(3):247–262. Referenced in: 2.2.3.

Weatherall, P., Marks, K. M., Jakobsson, M., Schmitt, T., Tani, S., Arndt, J. E., Rovere, M., Chayes, D., Ferrini, V., and Wigley, R. (2015). A new digital bathymetric model of the world's oceans. *Earth Planets Space.*, 2(8):331–345. Referenced in: 4.2.1 and 4.2.

Weingärtner, M., Gabriel, A.-A., and Mai, P. M. (2016). Dynamic Rupture Earthquake Simulations on complex Fault Zones with SeisSol at the Example of the Husavik-Flatey Fault. In *Proceedings of the International Workshop on Earthquakes in North Iceland*, Husavik, Iceland. Referenced in: 2.2.1.

Wendt, J., Oglesby, D. D., and Geist, E. L. (2009). Tsunamis and splay fault dynamics. *Geophys. Res. Lett.*, 36(15). Referenced in: 4.2.1.

Wenk, S., Pelties, C., Igel, H., and Käser, M. (2013). Regional wave propagation using the discontinuous Galerkin method. *J. Geophys. Res.*, 4(1):43–57. Referenced in: 3.2.5.

Wesnousky, S. G. (1988). Seismological and structural evolution of strike-slip faults. *Nature*, 335(6188):340–343. Referenced in: 2.1.

Wesnousky, S. G. (2006). Predicting the endpoints of earthquake ruptures. *Nature*, 444(7117):358–360. Referenced in: 2.1, 2.5, and 3.1.

Wibberley, C. A. and Shimamoto, T. (2002). Internal structure and permeability of major strike-slip fault zones: The Median Tectonic Line in Mie Prefecture, Southwest Japan. *J. Struct. Geol.*, 25(1):59–78. Referenced in: 1.1.

Wibberley, C. A. J. and Shimamoto, T. (2005). Earthquake slip weakening and asperities explained by thermal pressurization. *Nature*, 436(7051):689–692. Referenced in: 1.1.

Wilcox, L. C., Stadler, G., Burstedde, C., and Ghattas, O. (2010). A high-order discontinuous Galerkin method for wave propagation through coupled elastic-acoustic media. *J. Comp. Phys.*, 229(24):9373–9396. Referenced in: 2.1.

Wilson, J., Chester, J., and Chester, F. (2003). Microfracture analysis of fault growth and wear processes, Punchbowl Fault, San Andreas system, California. *J. Struct. Geol.*, 25(11):1855 – 1873. Referenced in: 1.1.

Wollherr, S., Gabriel, A., and Igel, H. (2016). Realistic Physics for Dynamic Rupture Scenarios: The Example of the 1992 Landers Earthquake. In *AGU Fall Meeting Abstracts*. Referenced in: 5.2.2, 6.1, and 6.

Wollherr, S., Gabriel, A.-A., and Uphoff, C. (2018). Off-fault plasticity in three-dimensional dynamic rupture simulations using a modal Discontinuous Galerkin method on unstructured meshes: implementation, verification and application. *Geophys. J. Int.*, 214(3):1556–1584. Referenced in: 1.2, 3.1, 3.2.1, 3.2.2, 3.2.3, 3.2.4, 3.2.5, 3.4.2, 3.4.3, 3.A, 4.1, 4.2.3, 4.2.3, 4.2.4, 4.3.1, 4.3.3, 5.2, and 5.2.2.

Wyss, M. and Brune, J. N. (1967). The Alaska earthquake of 28 March 1964: A complex multiple rupture. *Bull. Seism. Soc. Am.*, 57(5):1017–1023. Referenced in: 5.1.

Xu, S. and Ben-Zion, Y. (2013). Numerical and theoretical analyses of in-plane dynamic rupture on a frictional interface and off-fault yielding patterns at different scales. *Geophys. J. Int.*, 193(1):304–320. Referenced in: 1.2.

Xu, S., Ben-Zion, Y., and Ampuero, J.-P. (2012). Properties of inelastic yielding zones generated by in-plane dynamic ruptures–I. Model description and basic results. *Geophys. J. Int.*, 191(3):1325–1342. Referenced in: 2.2.2 and 2.2.2.

Xu, S., Ben-Zion, Y., Ampuero, J.-P., and Lyakhovsky, V. (2015). Dynamic Ruptures on a Frictional Interface with Off-Fault Brittle Damage: Feedback Mechanisms and Effects on Slip and Near-Fault Motion. *Pure Appl. Geophys.*, 172(5):1243–1267. Referenced in: 1.2, 2.6.1, and 5.1.

Xu, X., Tong, X., Sandwell, D. T., Milliner, C. W. D., Dolan, J. F., Hollingsworth, J., Leprince, S., and Ayoub, F. (2016). Refining the shallow slip deficit. *Geophys. J. Int.*, 204(3):1867–1886. Referenced in: 2.5, 3.1, and 3.3.4.

Yu, M.-h. (2002). Advances in strength theories for materials under complex stress state in the 20th century. *Appl. Mech. Rev.* , 55(3):169–218. Referenced in: 1.1.

Zeng, Y. and Anderson, J. G. (2000). *Evaluation of numerical procedures for simulating near-fault long-period ground motions using Zeng method*. Pacific Earthquake Engineering Research Center. Referenced in: 3.4.3.

Zhang, Z., Zhang, W., and Chen, X. (2014). Three-dimensional curved grid finite-difference modelling for non-planar rupture dynamics. *Geophys. J. Int.*, 199(2):860–879. Referenced in: 2.1.

Zielke, O., Galis, M., and Mai, P. M. (2017). Fault roughness and strength heterogeneity control earthquake size and stress drop. *Geophys. Res. Lett.*, 44(2):777–783. Referenced in: 3.3.6 and 3.4.1.

Acknowledgements

This thesis would not have been possible without the contribution of the following people I wish to thank:

I thank Alice Gabriel for introducing me into the topic of earthquake rupture dynamics, guiding me through my PhD, and for her constant availability alongside all her other commitments. I thank Heiner Igel for the opportunity to work on my PhD in his group, for his inspiring and motivating workshops and for his confidence in my opinion while working on his book. I am very grateful for all the opportunities Alice and Heiner gave me to participate in numerous conferences and scientific workshops. I also thank Martin Mai for his enthusiasm, his encouraging words, and for enabling my visits to KAUST.

I highly appreciated the work of the IT service here at the institute. Thank you, Gerald and Alex, for always printing my conference posters at the last minute and thank you, Jens, for the continuous support and pleasant conversations. All the administration processes during my PhD wouldn't have gone so smoothly without the great work of Elena and Yvonne.

I further want to thank my colleagues at the institute: Sia, Thomas, Betsy, Kenneth, Chris, Edo, Lion, and Kasra, for lunch breaks and for positively contributing to the work environment. Thomas, for his perseverance in trying out and testing new features and all the useful scripts that he wrote for SeisSol. This has made our work so much easier! Betsy, for her motivating and positive attitude, for discussions on geological topics, and for proofreading. Special thanks goes to Lion who introduced me into Python and lightened my daily work during the first two years with coffee breaks, useful tools, and programming tips. I thank Sia for hanging in there with me and for joining weekend shifts.

I am also very thankful for the collaboration and continuous support of Sebastian and Carsten from TUM. SeisSol wouldn't be where it is now without you! I thank Carsten for all the constructive discussions on the numerics that have contributed to my first paper.

I was very lucky to meet great people at conferences and during my stays at Caltech and KAUST, including Josie, Ricky, Arnaud, Voon, Jorge, Maria, and Claudia. I am especially grateful that I met Sofi who enlightened many strenuous conference days with her unshakable cheerfulness and spontaneity.

I thank Iris for the collaboration, for all the scientific and non-scientific conversations that have been a significant contribution to keeping the mood and spirit high during my PhD.

Outside the geophysics world, I want to thank my friends that helped me to keep a balance, listened to my concerns, or proofread parts of the thesis: Thank you, Kamilla, Helena, Marion, Marie, and Boris.

I thank my parents and my sisters who never questioned or doubted the paths I took. Most importantly, I thank Ben for his continuous support over the last years and for his understanding whenever my work and travels were put above our time together.